



**HAL**  
open science

# Comprehension of friction and wear mechanism of DLC coatings in ZDDP-lubricated conditions

Valentin Rafael Salinas Ruiz

► **To cite this version:**

Valentin Rafael Salinas Ruiz. Comprehension of friction and wear mechanism of DLC coatings in ZDDP-lubricated conditions. Other. Université de Lyon, 2021. English. NNT : 2021LYSEC028 . tel-03696901

**HAL Id: tel-03696901**

**<https://theses.hal.science/tel-03696901>**

Submitted on 16 Jun 2022

**HAL** is a multi-disciplinary open access archive for the deposit and dissemination of scientific research documents, whether they are published or not. The documents may come from teaching and research institutions in France or abroad, or from public or private research centers.

L'archive ouverte pluridisciplinaire **HAL**, est destinée au dépôt et à la diffusion de documents scientifiques de niveau recherche, publiés ou non, émanant des établissements d'enseignement et de recherche français ou étrangers, des laboratoires publics ou privés.



ÉCOLE  
**CENTRALE** LYON

N° d'ordre: 2021LYSEC28

**THESE de DOCTORAT DE L'UNIVERSITE DE LYON**  
**opérée au sein de l'Ecole centrale de Lyon et INSA de Lyon**

**Ecole Doctorale N°34**

**Ecole Doctorale Matériaux de Lyon**

**Spécialité: Génie des matériaux**

Soutenue le 13 Juillet 2021 par:

**Valentin Rafael Salinas Ruiz**

---

**Comprehension of friction and wear mechanisms of DLC  
coatings in ZDDP-lubricated conditions.**

*Interactions mécanique et chimique du ZDDP dans la lubrification des  
revêtements DLC*

---

Devant le jury composé de:

Pr. Christophe DONNET	Université Jean Monnet	Président du jury
Pr. Robert CARPICK	Université de Pennsylvania	rapporteur
Pr. Ardian MORINA	Université de Leeds	rapporteur
Dr. Philippe MAURIN PERRIER	HEF Groupe	examineur
Dr. Laura PEÑA PARAS	Université de Monterrey	examinatrice
Dr. Maria-Isabel DE BARROS BOUCHET	Ecole Centrale de Lyon	directrice de thèse
Pr. Karine MASENELLI-VARLOT	INSA de Lyon	co-directrice de thèse
Pr. Jean-Michel MARTIN	Ecole Centrale de Lyon	co-encadrant de thèse



*“You should enjoy the little detours, enjoy them to the fullest, because that’s where you’ll find more important things than what you were looking for.”*

*-F.G.*

# ABSTRACT

For more than a decade now, Diamond-like carbon (DLC) coatings have been applied on internal combustion engine sliding components e.g. cam lobes, tappets, finger followers, and piston rings to reduce energy losses due to friction. These coatings are therefore lubricated with traditional engine oils that were originally developed for steel parts. However, the effect of certain additives, such as zinc-dialkyldithiophosphate (ZDDP), on the tribological behavior of DLCs is still unclear.

In this work, tribological tests, surface analysis techniques, and computer simulations are combined to study the friction and wear properties of several types of DLCs in ZDDP-containing solution, as well as the underlying micro/atomistic mechanisms responsible for the observed macroscopic tribological behavior.

The experiments show that for DLC/DLC contacts, the tribological behaviour in ZDDP-additivated oils can be optimized by tailoring their stiffness, surface nano-topography and hydrogen content. An optimal combination of ultralow friction and negligible wear is achieved using hydrogen-free tetrahedral amorphous carbon (ta-C) with moderate hardness. Softer coatings exhibit similarly low wear and thin ZDDP-derived patchy tribofilms, but higher friction. Conversely, harder ta-Cs undergo severe wear and sub-surface sulphur contamination. Contact-mechanics and quantum-chemical simulations reveal that shear combined with the high local contact pressure caused by the contact stiffness and average surface slope of hard ta-Cs favour ZDDP fragmentation and sulphur release. In absence of hydrogen, this is followed by local surface cold welding and sub-surface mechanical mixing of sulphur resulting in a decrease of yield stress and wear.

To further investigate the effect of sulphur on the wear of hard ta-Cs, other additive molecules with and without sulphur are tested. Wear is also observed with another sulphur-containing additive, di-ter-butyl-trisulphide (TPS), while no wear occurs and ultra-low friction is maintained in Zinc dialkylphosphate (ZP), which has a similar chemical structure to ZDDP except that the sulphur atoms are replaced by oxygen. A different solution to avoid wear is by replacing one of the DLC surfaces by steel *i.e.* switch from DLC/DLC to DLC/steel contacts. In this case wear is avoided and friction is maintained low, thus ZDDP fulfils its role of anti-wear (AW) agent. These solutions are in line with the search of reducing friction, avoiding wear, and improving fuel efficiency of ICE in passenger cars.

# ACKNOWLEDGEMENTS

This research work was carried out within the framework of a CIFRE thesis in the LTDS laboratory, at Ecole Centrale de Lyon, and MATEIS laboratory, at INSA Lyon, in partnership with HEF/IREIS company during the years 2018-2021.

I would like to start by thanking my wonderful supervisors, Dr. Maria-Isabel de Barros Bouchet, Prof. Karine Masenelli-Varlot, Dr. Christophe Héau, and Prof. Jean-Michel Martin for their constant support, dedication, guidance, and invaluable knowledge that they offered during this thesis. It was a great honor, and a pleasure working with you.

I am grateful to Dr. Takuya Kuwahara, Dr. Gianpietro Moras, and Prof. Michael Moseler from the Fraunhofer Institute for Mechanics of Materials IWM, for their great contribution of atomistic simulations to this work. I am very pleased with the results yielded from our fruitful cooperation and I learned so much from you, thank you.

My gratitude goes as well to the persons that assisted me in different ways: Dr. Jules Galipaud (XPS, but more importantly for introducing me to the incredible sport of rock climbing), Dr. Mohamed Ben Hassine (TEM), Dr. Matthieu Lenci (FIB), and Mrs. Sophie Pavan (nano-indentation).

To my colleagues in HEF/IRIES, from the laboratory, tribology department, and administration office, I thank you for your support and assistance and for your kind welcoming whenever I visited the site.

To my fellow PhD students and friends, for all the moments we shared together. The dinners in restaurants, the sport activities in campus, the football matches at Stade de Lyon, the picnics at Parc de la Tête d'Or, and so many others, thank you.

I would like to thank my mom, dad, and brother for their love and encouragement during all my life, without whom, I wouldn't have arrived here. And finally, to my beloved partner, Sofia, for her love and care which helped me immensely throughout this stage.

Sincerely,

Valentin

# Table of Contents

<b>CHAPTER 1: GENERAL INTRODUCTION</b>	<b>1</b>
<b>1.1 GENERAL CONTEXT</b>	<b>2</b>
<b>1.2 INTRODUCTION TO THE PROBLEM</b>	<b>3</b>
<b>1.3 OBJECTIVE AND RELEVANCE OF THE INVESTIGATION</b>	<b>4</b>
<b>1.4 OUTLINE OF THE THESIS</b>	<b>4</b>
<b>CHAPTER 2: BACKGROUND</b>	<b>6</b>
<b>2.1 INTRODUCTION TO DLC COATINGS</b>	<b>7</b>
2.1.1 HISTORY	7
2.1.2 CLASSIFICATION	8
2.1.3 DEPOSITION PROCESSES	11
2.1.4 NEW DLC ARCHITECTURES	14
2.1.5 INDUSTRIAL APPLICATION IN ICE ENGINES.	15
2.1.6 WEAR OF HARD TA-C COATINGS IN COMMERCIAL FULLY-FORMULATED OIL (5W30)	16
<b>CHAPTER 3: MATERIALS AND EXPERIMENTAL METHODS</b>	<b>18</b>
<b>3.1 TEST MATERIALS</b>	<b>19</b>
3.1.1 SURFACE POLISHING	20
3.1.2 SURFACE ROUGHNESS BY TACTILE PROFILOMETER	20
3.1.3 HARDNESS AND ELASTIC MODULUS BY NANO-INDENTATION	21
<b>3.2 TESTED LUBRICANTS AND ADDITIVES</b>	<b>22</b>
<b>3.3 FRICTION TESTS</b>	<b>23</b>
3.3.1 RECIPROCATING SLIDING TESTS	23
3.3.2 FRICTION REGIME ESTIMATIONS ( $\Lambda$ CALCULATIONS)	24
3.3.3 CALCULATION OF FLASH TEMPERATURES.	26
3.3.4 CALCULATION OF ROOT-MEAN-SQUARE HEIGHTS AND SLOPES	28
3.3.5 ANALYTICAL TRIBOMETER IN CONTROLLED ENVIRONMENT (ATCE)	29

<b>3.4</b>	<b>SURFACE CHARACTERIZATION TECHNIQUES</b>	<b>31</b>
3.4.1	OPTICAL INTERFEROMETER	31
3.4.2	RAMAN SPECTROSCOPY	31
3.4.3	AFM	31
3.4.4	SEM ANALYSIS	32
3.4.5	FIB MACHINING AND TEM ANALYSIS	32
3.4.6	XPS ANALYSIS	33
<b>3.5</b>	<b>COMPUTER SIMULATIONS (FRAUNHOFER INSTITUTE)</b>	<b>35</b>
3.5.1	CONTACT MECHANICS SIMULATIONS	35
3.5.2	QUANTUM CHEMICAL SIMULATIONS	36

**CHAPTER 4: INTERPLAY OF CHEMISTRY AND MECHANICS GOVERN THE WEAR OF DLC COATINGS IN ZDDP-ADDITIVATED OIL** **39**

<b>4.1</b>	<b>INTRODUCTION</b>	<b>40</b>
<b>4.2</b>	<b>FRICTION AND WEAR RESULTS</b>	<b>42</b>
<b>4.3</b>	<b>CONTACT MECHANICS CALCULATIONS</b>	<b>47</b>
<b>4.4</b>	<b>XPS SURFACE ANALYSIS</b>	<b>49</b>
<b>4.5</b>	<b>SCANNING AND TRANSMISSION ELECTRON MICROSCOPY CHARACTERISATIONS</b>	<b>54</b>
<b>4.6</b>	<b>QUANTUM CHEMICAL CALCULATIONS</b>	<b>59</b>
<b>4.7</b>	<b>DISCUSSION</b>	<b>65</b>
<b>4.8</b>	<b>SUMMARY AND CONCLUSIONS</b>	<b>68</b>

**CHAPTER 5: EFFECT OF MECHANICAL AND CHEMICAL PARAMETERS ON THE BEHAVIOR OF DLC/ZDDP SYSTEMS** **70**

<b>5.1</b>	<b>EFFECT OF SURFACE ROUGHNESS.</b>	<b>71</b>
5.1.1	INTRODUCTION	71
5.1.2	SUMMARY AND CONCLUSIONS	73
<b>5.2</b>	<b>EFFECT OF CONTACT PRESSURE AND SLIDING SPEED (LUBRICATION REGIME).</b>	<b>73</b>
5.2.1	INTRODUCTION	73
5.2.2	FRICTION AND WEAR RESULTS	75
5.2.3	DISCUSSION	78
5.2.4	SUMMARY AND CONCLUSION	79

<b>5.3</b>	<b>EFFECT OF THE COUNTERPART MATERIAL: DLC/STEEL CONTACTS.</b>	<b>80</b>
5.3.1	INTRODUCTION	80
5.3.2	FRICITION AND WEAR RESULTS	81
5.3.3	SURFACE ANALYSIS TECHNIQUES	84
5.3.4	SUMMARY AND CONCLUSIONS	88
<b>5.4</b>	<b>EFFECT OF OTHER PHOSPHORUS AND SULPHUR-CONTAINING ADDITIVES ON THE TRIBOLOGICAL PROPERTIES OF DLC COATINGS</b>	<b>90</b>
5.4.1	INTRODUCTION	90
5.4.2	FRICITION AND WEAR RESULTS	91
5.4.3	SURFACE ANALYSIS TECHNIQUES	95
5.4.4	SUMMARY AND CONCLUSIONS	101
 <b>CHAPTER 6: CONTRIBUTION OF CONTROLLED ENVIRONMENT LUBRICATION TO THE COMPREHENSION OF THE TRIBOCHEMISTRY OF S-CONTAINING ADDITIVES ON DLC SURFACES.</b>		<b>102</b>
<b>6.1</b>	<b>TA-C IN CONTROLLED GAS ENVIRONMENTS</b>	<b>103</b>
6.1.1	INTRODUCTION	103
6.1.2	FRICITION AND WEAR RESULTS	103
6.1.3	RAMAN SPECTROSCOPY	111
6.1.4	XPS ANALYSIS	112
6.1.5	DISCUSSION	116
6.1.6	SUMMARY AND CONCLUSIONS	117
<b>6.2</b>	<b>DLCs LUBRICATED IN NEAT ZDDP FILM.</b>	<b>118</b>
6.2.1	INTRODUCTION	118
6.2.2	FRICITION AND WEAR RESULTS	118
6.2.3	XPS ANALYSIS	122
6.2.4	DISCUSSION	125
6.2.5	SUMMARY AND CONCLUSIONS	125
 <b>CHAPTER 7: GENERAL CONCLUSIONS AND SUGGESTIONS FOR FUTURE WORK</b>		<b>127</b>
<b>7.1</b>	<b>GENERAL CONCLUSIONS</b>	<b>128</b>

<b>7.2</b>	<b>SUGGESTIONS FOR FUTURE WORKS</b>	<b>130</b>
	<b>REFERENCES</b>	<b>132</b>
	<b>APPENDIX A</b>	<b>139</b>

---

# Chapter 1: General Introduction

---

This first chapter aims to provide the reader a brief introduction to the general context of the topic, state the problem at hand and define the research objectives of this work.



## 1.1 General Context

The importance of environmental and energetic sustainability is rising every year worldwide. Our planet is facing major challenges such as: increasing world population, energy and resources consumption levels growing, CO<sub>2</sub> emissions increasing, and rapid progression of global warming. These are urgent matters that need to be controlled to avoid catastrophic consequences. Researchers from all over the globe are striving to find solutions to improve energy consumption efficiency, limit fossil fuel use and reduce greenhouse gas emissions to comply with the requirements established in the Kyoto and Paris Protocols on climate change.

According to Holmberg and Erdemir<sup>1</sup>, 23% of the world total energy consumption originates from tribological contacts, among which 20% is used to overcome friction and 3% is used to remanufacture worn-out parts. Energy losses could be reduced by 40% in the long term (15 years), and by 18% in the short term (8 years) by applying new tribological solutions. These savings would amount to roughly 1.4% of the GDP annually and 8.7% of total world-wide energy consumption.

In their latest report, it was estimated that almost 30% of the energy produced today is consumed by transportation vehicles and 75% of that by road vehicles alone<sup>2</sup>. The internal combustion engine (ICE) still represents 99% of all commercial vehicles<sup>3</sup>. A typical passenger car only uses 21% of the energy consumed to generate movement, while the remaining 79% is lost<sup>4</sup>, see **Figure 1. 1** . Improving the energy efficiency by reducing friction and wear-related energy losses would have positive economic and environmental impacts. In some countries, government regulations are established upon car manufacturers to limit their carbon emissions. In Europe the average emissions from passenger cars should be less than 95 g of CO<sub>2</sub>/km, severe financial penalties may apply if the objectives are not met<sup>5</sup>.

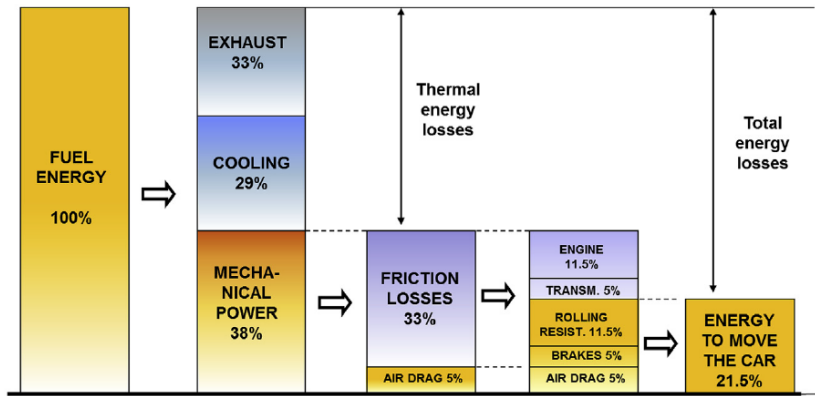


Figure 1. 1. Breakdown of energy use for ICE driven passenger cars, tank-to-wheel calculations<sup>2</sup>.

Therefore, great efforts have been made in the past decades in the academic and industrial sectors to reduce energy losses due to friction and wear in passenger cars by developing new tribological solutions e.g. ceramics and composite materials, surface treatments, lubricant additives, low viscosity oils, vapor phase lubricants, nanoparticles-based technology, surface texturing, and surface coatings.

Among these different strategies, diamond-like carbon (DLC) coatings have been applied on sliding components in ICE e.g. piston rings, cams, valve lifters and tappets to reduce friction and wear. Friction coefficients below 0.01 (the so-called super-low friction regime) have been obtained in liquid lubrication combined with certain organic additives and fatty acids. These coatings have the potential to significantly reduce the energy losses of sliding contacts in ICE and are the subject matter of this investigation.

## 1.2 Introduction to the problem

DLCs are usually lubricated with traditional engine oils suitable for ferrous surfaces (steel, cast iron). Zink dialkyldithiophosphate (ZDDP) is the most commonly used antiwear/antioxidant additive present in commercial engine oils due to its unmatched antiwear properties. However, its effects on the tribological properties and interaction mechanisms on DLCs and are still unclear despite the great number of published scientific articles on this matter. Results vary greatly between different studies and are often directly referred to as contradictory, while in fact, a more accurate assessment would be to say that they are complementary and valid in their own specific experimental conditions. There are many parameters that can explain why different studies obtain contradictory results such as: the type of DLC and additives used, counterpart material, initial surface roughness, contact

pressure, sliding speed, working temperature etc.... All of these parameters need to be rigorously controlled in order to understand their individual and combined effect on the tribological behavior of DLC/ZDDP sliding interfaces.

### **1.3 Objective and relevance of the investigation**

In this investigation, a multi-approach systematic study is carried out combining experiments, analytical measurements and computer simulations carried out for part of this work in cooperation with Prof. Michael Moseler and his colleagues from Fraunhofer Institute for Mechanics of Materials (IWM), in order to understand the effect of ZDDP and other similar additives on the friction and wear properties of different DLC coatings.

Five different DLCs lubricated with a ZDDP-containing solution are tested to study its tribofilm formation capacity, and anti-wear and friction modification properties. The experiments are coupled with computer simulations in order to better understand the underlying atomistic/nano-scale mechanisms responsible for the macroscopic tribological behavior. Other zinc-phosphate and sulphur-containing additives are also studied in order to better understand the effect of the structure and chemical composition of the additive molecules. Additionally, tribological tests are conducted in a controlled atmosphere environment using simple gas molecules without the presence of base oils and air exposure to better understand the tribochemical interactions of certain atoms with DLC surfaces.

The end goal of this investigation is to provide guidelines for developing DLC systems to effectively reduce friction and wear in ICE sliding contacts that could also be applied to other DLC/ZDDP systems such as wind turbines.

### **1.4 Outline of the thesis**

Chapter 2 provides the general context of this study as well as a brief introduction to DLC coatings for tribological applications.

Chapter 3 describes the experimental methodology and materials used in this study.

Chapter 4 studies the effect of ZDDP on the friction and wear properties of five different DLCs.

Chapter 5 investigates other mechanical and chemical parameters and their effects on the tribological behavior of DLC/ZDDP systems.

Chapter 6 presents the results obtained from tests performed in various controlled environments to study simple systems with standard molecules to further understand the tribochemistry of DLC and ZDDP.

Chapter 7 is a summary of the main conclusions from this investigation and suggestions for future works.

---

## Chapter 2: Background

---

This chapter provides an introduction to diamond-like carbon (DLC) coatings, and goes over some of their main aspects related to tribology and concludes with a brief discussion of DLCs lubricated with ZDDP and its relevance to the automotive industry.

## 2.1 Introduction to DLC coatings

Diamond-like carbon (DLC) coatings refer to a family of amorphous carbon-based thin films that contain a mixture of  $sp^2$  and  $sp^3$  coordinated bonds. It is common for them to contain hydrogen or other metal and non-metal doping elements depending on their production method. They are synthesized by different chemical vapor deposition (CVD) and physical vapor deposition (PVD) methods. One of their main advantages is that their properties can be tailored by adjusting the deposition process, therefore making them suitable for a wide range of engineering applications in the manufacturing, microelectronic, optics, space, transportation and biomedical fields.

### 2.1.1 History

In 1955, Schmellenmeier reported a black carbonaceous film derived from acetylene (a-C:H) in glow-discharge plasma<sup>6</sup>. However, it was not before 1971 that these films started to gain attention after Aisenberg and Chabot conducted a more comprehensive analysis<sup>7</sup>. By means of an ion-beam deposition technique, they were able to grow carbon films on various substrates at room temperature. For the first time these hard carbon films were referred to as “diamond-like carbon”. The films were very hard and resistant to scratching, they had high dielectric constant, high refraction index, were optically transparent, and very resistant to corrosion in strong acidic solutions. In 1973 they applied the DLC coatings on paper cutting blades and discovered that the coatings improved wear resistance and reduced friction<sup>8</sup>. This sparked the interest of other researchers and a few years later, Holland et al. reported the growth of similarly hard carbonaceous films by applying a radio frequency bias to the substrate material to generate a glow-discharge plasma<sup>9</sup>. At first it was speculated that these films were composed of crystalline diamond due to their high mechanical properties, but in the late 1970s Weissmantel et al. dispelled the uncertainty when they demonstrated that their structure was, in fact amorphous, by conducting a series of analyses by electron microscopy and electron energy loss spectroscopy (EELS)<sup>10</sup>. In 1981 King et al. reported that DLC-coated hard disks used in magnetic recording media showed higher wear resistance compared to standard overcoat materials that were used at the time. They correctly predicted that in future years the use of DLCs as protective films would greatly improve the performance of magnetic hard disks. At the same time Enke et al. studied the friction coefficient of a-C:H films against steel counterparts<sup>11,12</sup>. In low humidity conditions, the friction coefficient was  $\approx 0.01$ . In 1986 Memming et al. also performed friction tests with a-C:H/steel tribopairs in different atmospheres e.g. ultra-high vacuum, humid air, dry nitrogen and dry oxygen and began to

shed some light on the friction mechanisms of such coatings<sup>13</sup>. Their potential to reduce friction and wear in different application fields started to attract more attention and finally in the 1990s the research of DLC coatings really took off. **Figure 2. 1** shows that the number of scientific publications and patents on DLCs have been steadily rising ever since. Nowadays DLC coatings are used in a variety of industrial applications and continuous research is carried out to keep searching for new technological solutions.

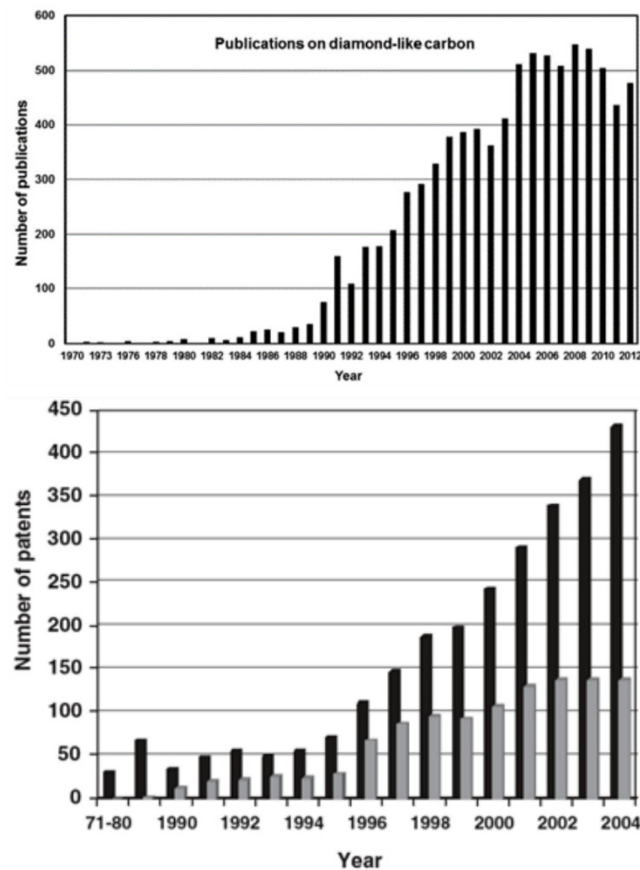


Figure 2. 1. Evolution of the number of published scientific articles (top) and issued patents in the US (bottom) of DLCs throughout the years.

### 2.1.2 Classification

DLC coatings are commonly classified based on their hydrogen content,  $sp^2/sp^3$  hybridized carbon ratio and the presence of metal or non-metal doping elements. The different types with their abbreviations are illustrated in **Figure 2. 2**.

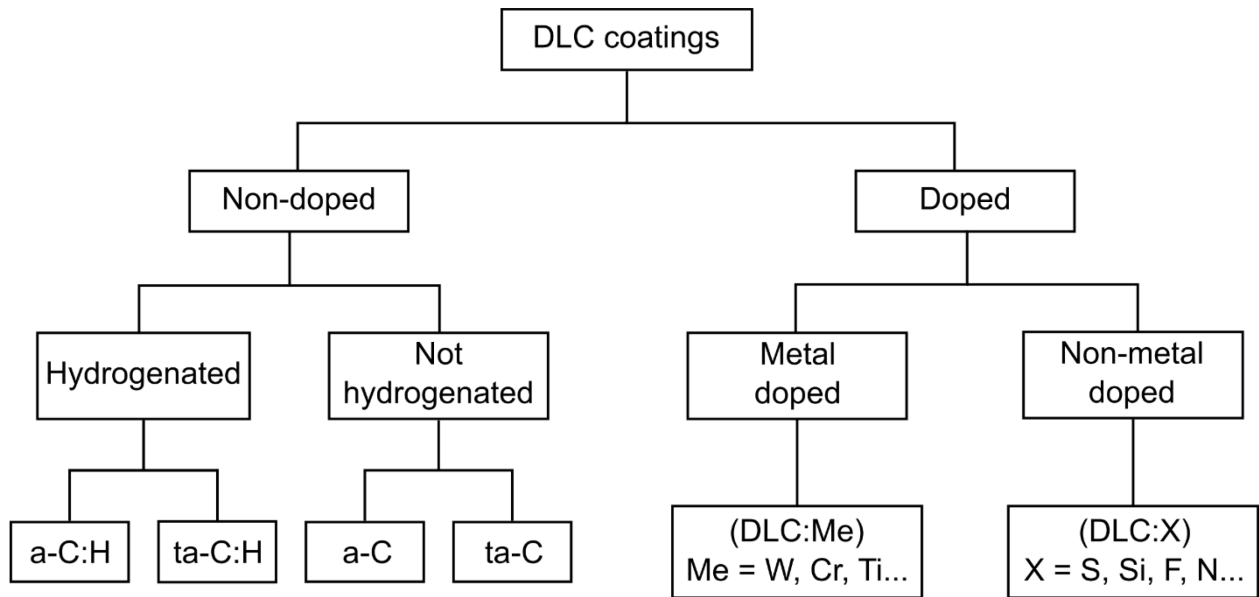


Figure 2. 2. Classification of DLC coatings.

Non-doped DLCs have been typically presented in the well-known ternary phase diagram shown in **Figure 2. 3** proposed by Robertson<sup>14</sup>. The top corner corresponds to pure  $sp^3$  carbon (like in diamond), the bottom-left corner corresponds to pure  $sp^2$  carbon (like in graphite) and the bottom-right corner represents pure hydrogen. There are four main regions labeled in this phase diagram. The first corresponds to a-Cs in the left axis. The second region corresponds to ta-Cs that are very rich in  $sp^3$  carbon. The third and fourth regions correspond to the hydrogenated DLCs, a-C:H, and ta-C:H. The mechanical properties of the designated DLCs are not given in the diagram.

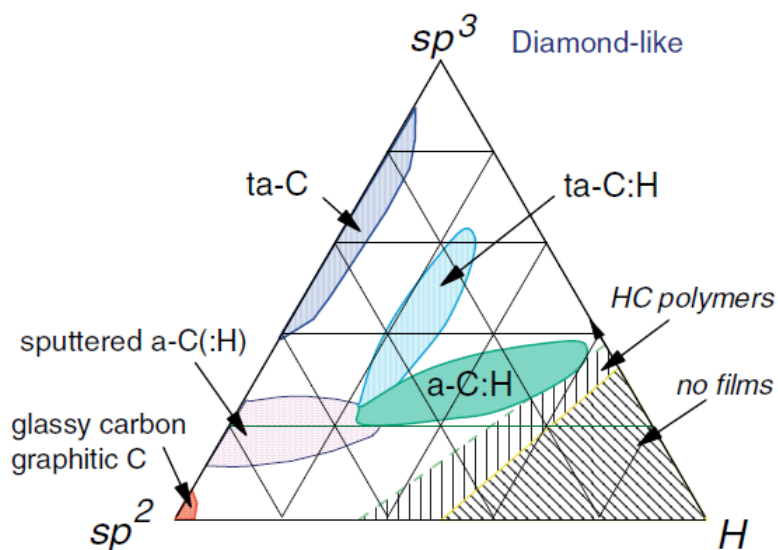


Figure 2. 3. Robertson's ternary phase diagram of DLCs<sup>14</sup>.



Vengudasamy proposed a modified classification which also includes some doped-DLCs<sup>15</sup> (see **Figure 2. 4**). The  $sp^3$  fraction and hydrogen content seem to more accurately represent modern DLCs, although some data is missing to fill in the gap between a-C and ta-Cs. There is also a very large gap between the region designated as ta-C:H and a-C:H.

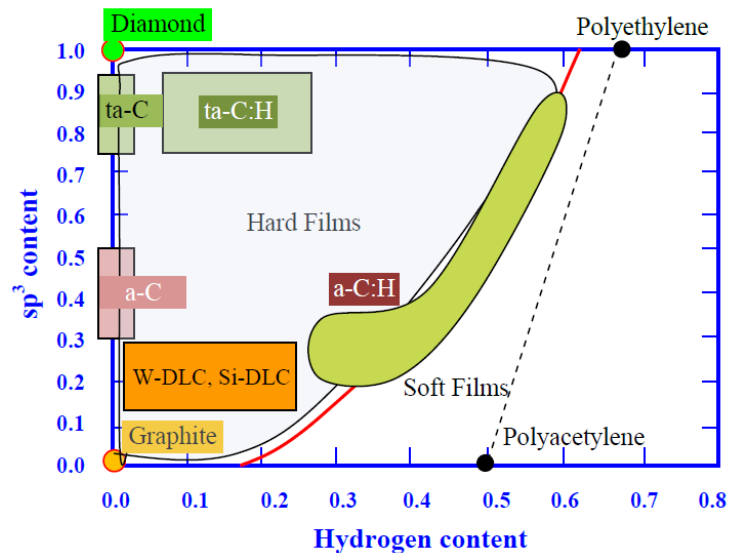


Figure 2. 4. Modified Classification of DLC coatings<sup>15</sup>.

Recently, Ohtake et al. measured the  $sp^3$  fraction, hydrogen content, hardness and other properties of 74 DLCs produced by different CVD and PVD methods<sup>16</sup>. The measured results were plotted in the ternary diagram according to their  $sp^3$  fraction and hydrogen content as before, but additionally, their hardness was included. The new diagram is presented in **Figure 2. 5**. Based on their positions on the diagram, the DLCs were designated into the four common regions: a-C, ta-C, a-C:H and ta-C:H. A summary of their properties is given in **Table 2. 1**.

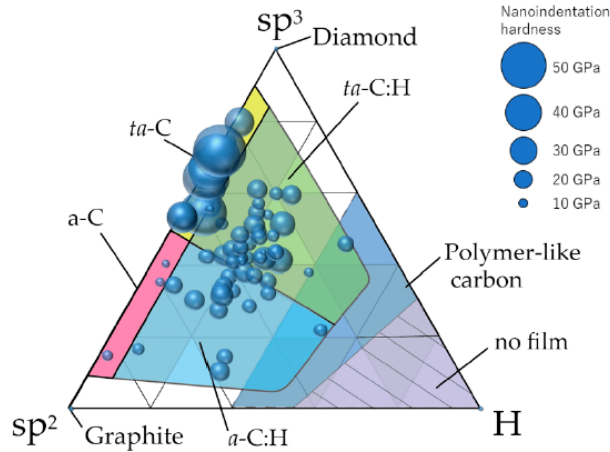


Figure 2. 5. Ternary phase diagram of 74 different DLCs. The circle diameter is proportional to their hardness obtained by nano-indentation<sup>16</sup>.

Table 2. 1. Classification of DLC films for industrial applications based on [16]<sup>16</sup>.

DLC	Sp3 fraction	Density (g/cm <sup>3</sup> )	H (at. %)	Hardness (GPa)
a-C	0.1 - 0.5	1.4 - 1.7	H < 5	9 - 25
ta-C	0.5 - 0.9	2.6 - 3.5	H < 5	25 - 90
a-C:H	0.1 - 0.5	1.4 - 2.0	5 - 50	9 - 25
ta-C:H	0.5 - 0.9	2.0 - 2.6	5 - 50	9 - 35

Although the newly proposed ternary phase diagram includes additional information (hardness), and is a step towards a better representation of DLCs, the data points distribution could be improved; there are very little a-Cs compared to the other DLCs. Additionally, the hardest ta-C was 54 GPa, when ta-Cs have been found to have hardnesses of 80 GPa. Nevertheless, it gives a good reference point of the classification of DLC coatings and is now published under the international standard ISO 20523:2017<sup>17</sup>.

### 2.1.3 Deposition Processes

There are many different PVD and CVD processes used for the production of DLC coatings. Some of the most common techniques for each type of DLC are shown in **Figure 2. 6**. By modifying the type of process and/or the deposition parameters, it is possible to obtain a wide range of DLCs with different physical and chemical properties, allowing for fine-tuning of the coating microstructure and chemical composition to fulfill specific requirements. In addition, their production is relatively cheap and convenient which allows large-scale production in different sectors such as the automotive industry.

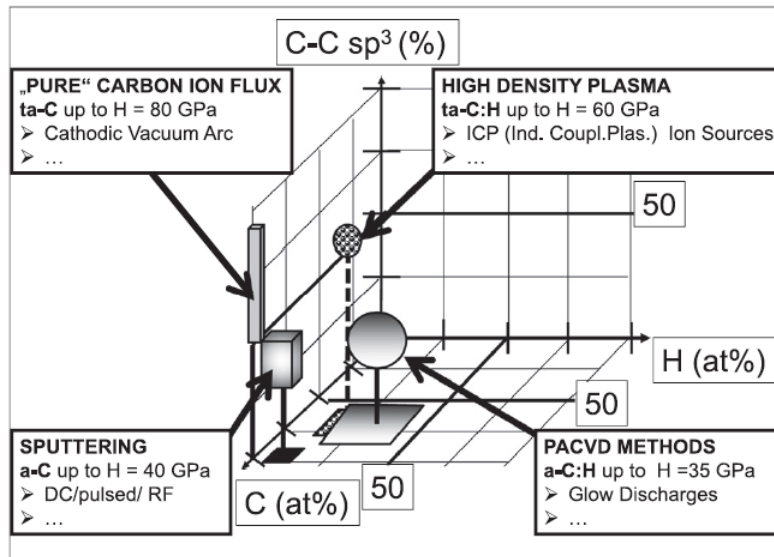


Figure 2. 6. Commonly used deposition techniques for each type of DLC coating including their carbon  $sp^3$  fraction and hydrogen atomic percentage<sup>18</sup>.

In principle the DLC film is condensed from a beam of carbon or hydrocarbon ions. The DLC properties depend heavily on the ion energy per carbon atom. To obtain a carbon  $sp^3$  rich film, the ion flux needs to have an energy close to 100 eV with low energy dispersion and the least amount of non-energized (usually neutral) species<sup>19</sup>. In general, the lower the energy is, the lower the carbon  $sp^3$  content will be. This neutral species are  $sp^2$  rich and may cause growth defects in a conical shape (also referred to as droplets) that may lead to increase surface roughness. Additionally, it is important to obtain strong interfacial bonding between the DLC coating and the substrate material in order to avoid delamination and failure. An intermediate-adhesion layer is often used between the substrate and the DLC for this purpose. Metals forming carbides or silicides, e.g. Cr, W, Si, Ti, are generally used.

For automotive applications (which is the focus of this work) the most common industrial processes used are plasma-enhanced/assisted chemical vapor deposition (PECVD, also known as PACVD) for the production of a-C:H coatings, with a hydrocarbon gas (methane, acetylene, ethylene...) used as the carbon precursor. For a-Cs and ta-Cs, cathodic vacuum arc (CVA also known as arc-PVD), and filtered cathodic vacuum arc (FCVA) deposition methods are used, the carbon precursor usually being a solid graphite target. Other noteworthy methods include magnetron sputtering, pulsed-laser deposition (PLD) technique, and inductively coupled plasma (ICP).

The CVA process consists of generating an electric arc that can be continuous or pulsed in high vacuum by using an electrode (carbon striker) that touches and releases the graphite

cathode. This will produce a high flux of energetic plasma that condensates to produce the coating. To increase the energy of the incident ions, a DC or R.F. bias voltage is applied to the substrate. Solid neutral particles can also detach from the graphite cathode and contribute to the growth of the film. FCVA is a similar technique that uses a magnetic duct to guide the plasma beam and prevent neutral particles from reaching the substrate. A schematic representation of these processes is shown in **Figure 2. 7**.

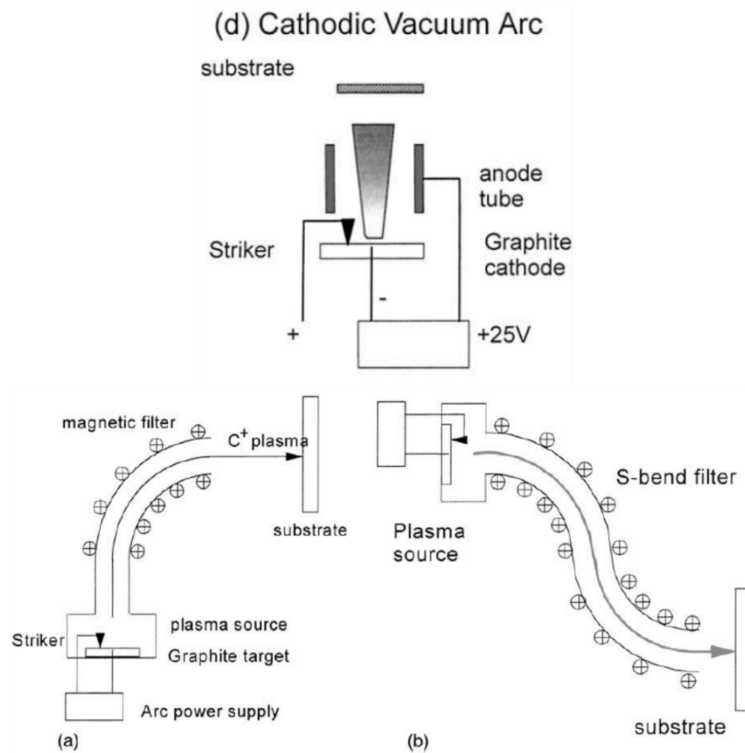


Figure 2. 7. Schematic diagrams of the CVA (top) and FCVA (bottom) processes<sup>14</sup>.

The PECVD process (illustrated in **Figure 2. 8**) uses a plasma where free highly energized electrons impact the gas molecules of the reactants (carbon precursor) to break their chemical bonds. This results in the formation of reactive radical groups that flow towards the substrate material for film growth. This method allows for lower deposition temperatures compared to traditional CVD processes that depends on thermal decomposition of the reactant.

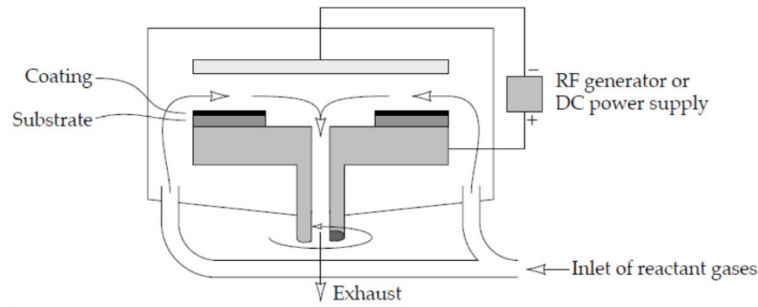


Figure 2. 8. Schematic diagram of the PECVD process<sup>20</sup>.

#### 2.1.4 New DLC architectures

Recently, Mesh and Pillar-type ta-C coatings (produced by Nippon ITF Inc.) were obtained by gradually increasing the substrate temperature above 200°C during the deposition process (arc-PVD)<sup>21</sup>. For conventional ta-Cs, the substrate temperature is maintained below 150°C. Their different structures can be observed in **Figure 2. 9**. The pillar and mesh-type ta-Cs have a crystalline graphitic structure (studied by TEM) on the top 25% of the coating thickness and therefore reduced hardness compared to the classical ta-C. These new ta-C structures were found to have higher resistance to fracture and wear (although wear on the steel counterpart was not specified), but higher friction coefficients compared to classical ta-C sliding in pure base oil against a steel counter-part.

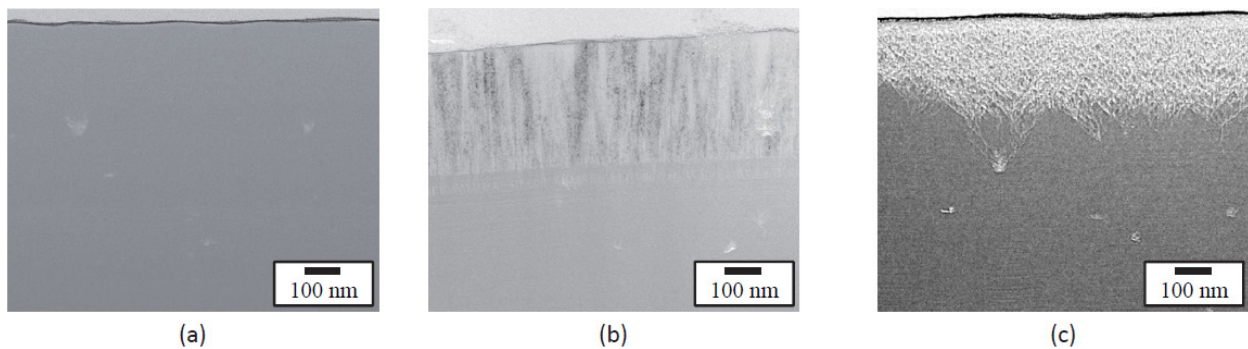


Figure 2. 9. Cross sectional cuts of conventional ta-C (a), pillar ta-C (b), and mesh ta-C (c)<sup>21</sup>.

Alternating soft and hard multilayered DLCs were produced by unbalanced magnetron sputtering technique for tribological applications under high stress<sup>22</sup>. Coatings with different number of layers were produced and it was found that the coating with 1:1 ratio that ended with the soft coating on top (see **Figure 2. 10**) gave the lowest wear rate. Multi-layered

coatings that ended with the hard coating on top actually had worse wear resistance compared to the single-layered soft coating.

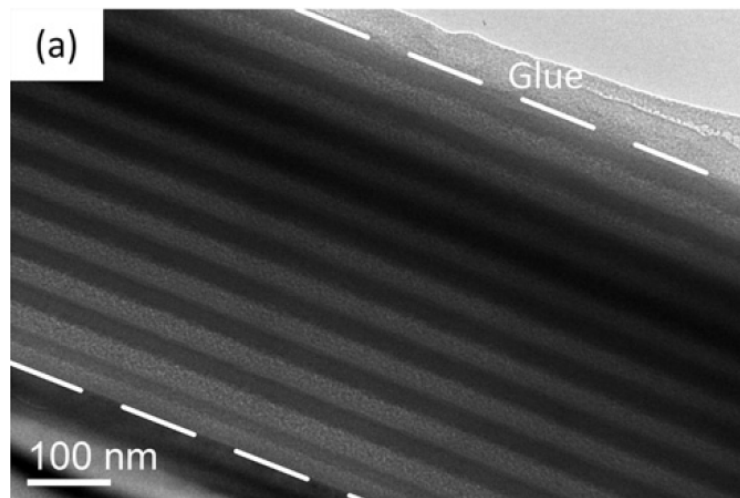


Figure 2. 10. TEM Cross-section of a multilayer DLC sample with a 1:1 soft-to-hard-layer ratio<sup>22</sup>.

Other multilayered coatings have been produced, e.g. CrN/DLC/Cr-DLC<sup>23</sup>, Cr/CrN/Cr-C/DLC<sup>24</sup>, periodic SiC/DLC layers on a copper substrate<sup>25</sup>, and Ti/Ti-DLC layers on aluminum substrates<sup>26</sup>... The authors argue that the residual stresses of the coatings are decreased by these multi-layered structures, therefore providing better adhesion and superior wear and friction properties in certain solicitation conditions. The results are interesting, but more research needs to be done with these types of coatings before definite conclusions can be made.

### 2.1.5 Industrial application in ICE engines.

For more than a decade now, DLC coatings have been applied to multiple components in ICEs. Some examples are shown in **Figure 2. 11**. The mass production and application of DLCs was strongly driven by the need to reduce carbon emissions and improve fuel efficiency due to environmental considerations. In 2006, the Nissan Motor Company started introducing ta-C coated tappets to their Skyline and Infinity G35 models<sup>27</sup>. In combination with a GMO-containing oil, this resulted in a reduction of friction torque between the cam and ta-C coated tappet of about 40%<sup>28</sup>.

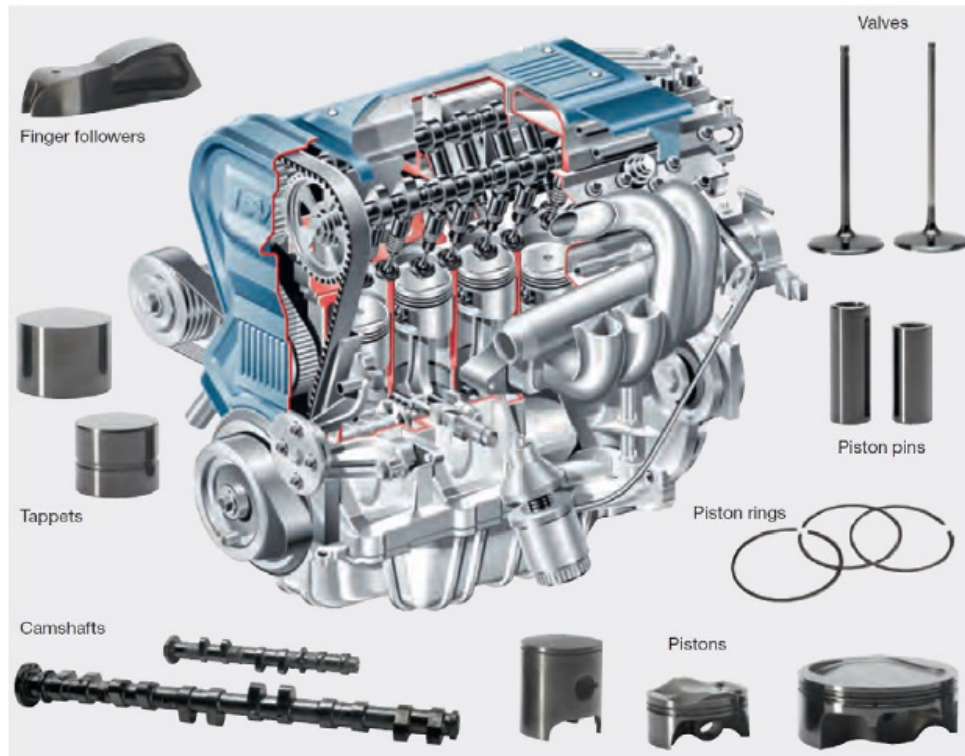


Figure 2. 11. DLC-coated engine parts in ICE<sup>18</sup>.

Other applications include<sup>29</sup>: cutting and forming tools, razor blades, data storing hard disks and recording heads, barrier films in PET bottles, IR antireflection films, dielectric layers, thin film sensors, decorative films, and biomedical components.

### 2.1.6 Wear of hard ta-C coatings in commercial fully-formulated oil (5W30)

DLCs have been applied on internal combustion engine sliding components e.g. cam lobes, tappets, finger followers, and piston rings to reduce energy losses due to friction. These coatings are therefore lubricated with traditional engine oils with complex formulations that were originally developed for steel parts.

Hydrogenated amorphous carbon (a-C:H) coatings are well established in the automotive industry in France. Its harder counterpart material, tetrahedral amorphous carbon (ta-C), is particularly interesting due to its ability to attain ultra-low and superlow friction in lubricated conditions<sup>30,31</sup>, thus potentially reducing energy consumption even more. However, at the end of 2017, tribological tests (reciprocating sliding) conducted in the research laboratory of the industrial partner of this work (HEF Group) revealed severe wear of hard ta-Cs lubricated with a fully formulated oil (5W30 provided by Total company), while no wear was observed in pure PAO base oil. For softer a-C:H coatings, wear did not occur in either lubricants. The worn ta-C samples were sent to LTDS laboratory (where most of the experiments of this work

were carried out) and XPS analysis were performed to study the surface chemistry of the wear tracks. The analysis revealed the presence of P, S, and Zn on the worn surfaces, suggesting that the AW additive ZDDP was involved in the tribochemical reactions and wear of hard ta-Cs. The tribological tests were reproduced in LTDS laboratory, but the complex 5W30 oil was replaced by a simple PAO + ZDDP solution. The concentration of ZDDP used in the solution was 1 wt.% wt, which corresponds to the amount of ZDDP in commercial oils, such as 5W30. The friction and wear results were identical to the ones obtained with the 5W30 oil, confirming that the ZDDP AW additive was at the origin of the wear of hard ta-Cs. The experimental results are available in **Figure A. 1**.

A review of the available literature at that time did not provide any explanation to the observed wear phenomena. In fact, the results from different studies about the effect of ZDDP on the tribological properties of DLCs were diverse, and even referred to as contradictory by some of the authors (discussed in the next chapters). These are the events that lead to the development of the present work, where the main focus is to study the effect of ZDDP on the tribological behaviour of DLC coatings.



---

# Chapter 3: Materials and experimental methods

---

This chapter contains the information regarding the tested DLC materials and lubricants, the test parameters used for tribological tests, and the analytical techniques used to analyze the samples.

### 3.1 Test materials

Five types of DLC coatings, labelled by a-C:H, a-C, ta-C(51), ta-C(66) and ta-C(78), were prepared by the company HEF IREIS. The numbers in between parentheses represent the hardness values of in GPa. The main properties of the DLC coatings are tabulated in **Table 3. 1** (the methods used for measuring them are given in the following sections). The coatings had a thickness of 2  $\mu\text{m}$  and were deposited onto mirror-polished steel discs, cylinders, and balls. The tests were performed in cylinder/disk, and ball/disk configuration. The steel discs had a diameter of 25 mm and a thickness of 7 mm, and were made of M2 steel (0.85% C, 6% W, 5% Mo, 4% Cr, 2% V, hardness 64 HRC). The cylinders and balls were made of 100Cr6 steel (0.95% C, 0,25% Mn, 0,15% Si, 1,5% Cr, hardness 223 HB). The cylinders had a radius of 5 mm and a length of 10 mm, and the balls had a radius of 5 mm. During the deposition process, an intermediate layer was applied onto the steel surfaces to improve the adhesion of DLC films and reduce residual stresses.

Table 3. 1. Main properties of the DLC coatings studied.

Label	Composition (at.%)		Young's modulus $E$ (GPa)	Hardness $H$ (GPa)	Density $\rho$ ( $\text{g cm}^{-3}$ )	C sp <sup>3</sup> (%)
	C	H				
a-C:H	80	20	259	27	2.07	-
a-C	> 99	< 1	287	24	2.34	31
ta-C(51)	> 99	< 1	493	51	2.77	62
ta-C(66)	> 99	< 1	572	66	2.91	73
ta-C(78)	> 99	< 1	625	78	3.01	79
	$Ra_{\text{disk}}$ (nm)	$Rq_{\text{disk}}$ (nm)	$Ra_{\text{cylinder}}$ (nm)	$Rq_{\text{cylinder}}$ (nm)	Deposition Method	
a-C:H	10 $\pm$ 1,2	12 $\pm$ 1,5	13 $\pm$ 1,7	17 $\pm$ 2,6	PACVD	
a-C	12 $\pm$ 1,6	16 $\pm$ 2,0	12 $\pm$ 1,1	16 $\pm$ 1,7	Arc-PVD	
ta-C(51)	13 $\pm$ 2,4	17 $\pm$ 3,0	11 $\pm$ 1,1	14 $\pm$ 1,4	Arc-PVD	
ta-C(66)	10 $\pm$ 2,0	13 $\pm$ 2,9	10 $\pm$ 1,5	13 $\pm$ 2,3	Arc-PVD	
ta-C(78)	12 $\pm$ 2,1	15 $\pm$ 2,6	11 $\pm$ 1,5	14 $\pm$ 1,8	Arc-PVD	

### 3.1.1 Surface polishing

In order to remove surface defects formed during the deposition process and obtain smooth surfaces to minimize friction and wear, the DLC-coated disks and cylinders were polished prior to tribological tests (the balls were not polished). There are several methods that can be used to polish DLC coatings:

- Automatic rotating steel brush: The preferred method to polish the cylinder samples due to their geometry is by brushing the surface using a rotating steel brush (tribochemical wear process involved). This method also works on flat samples, but leaves steel particles embedded on the surface that can react with the lubricant additives and could disturb the test, having an effect on friction and wear. It should be noted that brushing is a manual process so it requires experience to obtain smooth homogenous surfaces.
- SiC abrasive paper: An automatic polishing machine can be used, where the samples are pressed down onto a SiC abrasive paper that rotates at a predetermined speed. Water is used to lubricate the contact between the samples and the SiC paper. Similarly with the previous method, this procedure leaves SiC particles embedded on the sample surface which could also modify the friction and wear properties of the sample. Therefore, this method was not used for the tests presented in this work.
- Diamond particles suspension: The same automatic polishing machine is used as with the SiC paper, but instead a soft cloth covered with a diamond particle suspension is used to polish the surface. This method is the fastest and most effective way to polish the flat surfaces homogeneously with excellent reproducibility and was used for the tests presented in this work.

### 3.1.2 Surface roughness by tactile profilometer

Before each test, the surface roughness was controlled for every sample with a tactile profilometer. This technique allows rapid measurements to be made in different areas of the samples. It was used to ensure that they were properly polished and smooth surfaces were obtained. Multiple Line scans with a length = 56 mm were performed using a filter cut-off of  $\lambda_c = 80 \mu\text{m}$ . The roughness parameters:  $R_a$ ,  $R_q$ ,  $R_{vk}$ , and  $R_{pk}$  were calculated for each individual line scan and an average of all the measurements is reported with its standard deviation. These parameters were chosen to obtain information about the contribution of peaks and valleys of the surface. A typical line measurement is shown in **Figure 3. 1**.

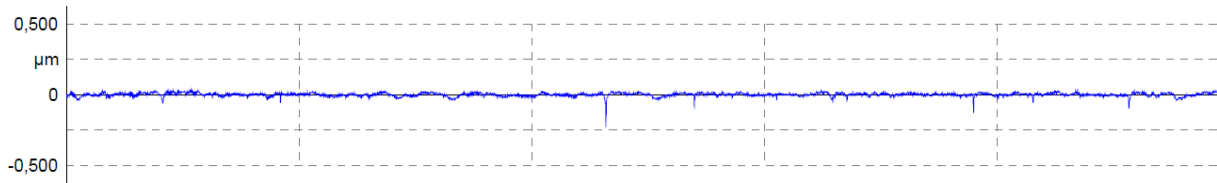


Figure 3. 1. Typical line scan measurement for roughness evaluation of the samples before sliding tests.

### 3.1.3 Hardness and Elastic Modulus by Nano-indentation

The mechanical properties of the materials were determined by nanoindentation using a Nanoindenter XP®. Indents were done with a diamond Berkovich indenter (tetrahedral geometry,  $115.12^\circ$  between edges). The maximum applied load was 450 mN assuming a Poisson's ratio of 0.20. A continuous stiffness measurement method was used. An oscillating displacement with a frequency of 32 Hz and an amplitude of 1 nm was superimposed at the continuous displacement. The tests were performed using a constant strain rate procedure. The ratio of the loading rate to the load was kept constant and was equal to  $3 \times 10^{-2} \text{ s}^{-1}$ . With a Berkovich indenter, the strain was constant during loading experiments<sup>32</sup>. Seven tests were made for each sample. Simultaneous measurements of the applied normal load, the contact stiffness versus displacement were recorded. Thus, hardness  $H$  (related to a contact pressure) and reduced elastic modulus  $E'$  were continuously calculated and analyzed versus plastic depth. For thin coatings the measurements should not exceed more than 10% of the coating thickness, otherwise the substrate material influences the results. **Figure 3. 2** shows typical  $H$  and  $E'$  measured curves versus indentation depth. It can be seen that the  $H$  and  $E'$  values decrease linearly as the indentation depth increases. Thus, the calculated  $H$  and  $E'$  values only take into account the measured points above 200 nm (10% of the coating thickness which is 2  $\mu\text{m}$ ). The mechanical properties of the DLC coatings on the cylinders are assumed to be the same as those on the discs.

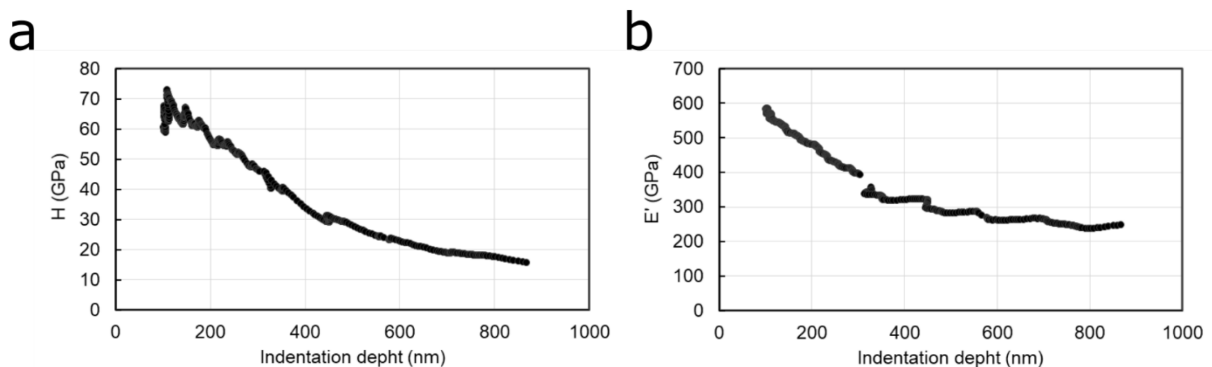

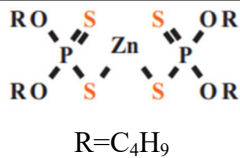
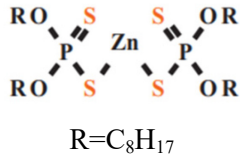
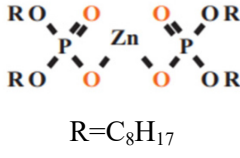
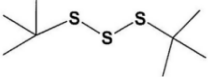


Figure 3. 2. Hardness (a) and reduced elastic modulus (b) measurements obtained by nano-indentation

### 3.2 Tested lubricants and additives

PAO-4 was used as the base oil for this work. At  $T = 100^{\circ}\text{C}$  it has a kinematic viscosity of 3.8 cSt. Different additives were mixed with the PAO base oil to obtain the lubricant solutions. The additives used in this work are shown in **Table 3. 2**. All lubricant solutions were prepared at equivalent phosphorus content (1200 ppm), which corresponds to 1.0 – 1.5 wt. % of the additive (depending on its molecular weight) in the solution. This concentration was determined to be representative of the amount of additives that can be found in commercial engine oils. To study the effect of the additive concentration, some tests were performed with smaller and larger concentrations that can also be found in the literature (800 ppm and 1600 ppm) and were found to yield similar results. The TPS additive was prepared to have an equivalent sulphur content as the one of the ZDDP additives (2400 ppm). The PAO + additives solutions were heated at  $40^{\circ}\text{C}$  and stirred during 2 hours to obtain a homogenous solution. This procedure was suggested by one of the additives suppliers, Nippon Oil.

Table 3. 2. Additives and lubricant solutions used in this work.

Label	Name	Chemical structure	Role	Lubricant Solution
PAO-4	Polyalphaolefin		Base oil	PAO
ZDDP I C4	Zinc dialkyldithiophosphate primary C4	 $\text{R}=\text{C}_4\text{H}_9$	AW	PAO + ZDDP I C4 (P = 1200 ppm) (S = 2400 ppm)
ZDDP I C8	Zinc dialkyldithiophosphate primary C8	 $\text{R}=\text{C}_8\text{H}_{17}$	AW	PAO + ZDDP I C8 (P = 1200 ppm) (S = 2400 ppm)
ZP	Zinc dialkylphosphate	 $\text{R}=\text{C}_8\text{H}_{17}$	AW	PAO + ZP (P = 1200 ppm) (S = 0 ppm)
TPS	Di-ter-butyl-trisulphide		EP	PAO + TPS (P = 0 ppm) (S = 2400 ppm)

### 3.3 Friction tests

#### 3.3.1 Reciprocating sliding tests

Cylinder-on-disc sliding tests were performed using a home-made linear reciprocating tribometer<sup>33</sup>. A 3D model of the apparatus is shown in **Figure 3. 3**. The tested conditions were chosen to resemble the real operating conditions in sliding engine components such as cam-follower systems and jacket-piston ring contacts in passenger cars. The contacting surface between the cylinder and disk (flat coupon) was immersed in 3 ml of lubricant. A good contact between the disc and cylinder was ensured for every test thanks to an auto-alignment spring system of the cylinder holder. The friction coefficient was calculated as the average of the instantaneous friction coefficient over one complete cycle (300 points per cycle). The testing conditions used are given in **Table 3. 3**.

Table 3. 3. Test parameters used in reciprocating sliding tests.

<b>Standard reciprocating sliding tests conditions</b>
Contact: cylinder-on-disk
Applied load $F_N = 23 \text{ N}$
$P_{\text{Hertz}} = 210 \text{ MPa}$
Temperature $T = 110^\circ\text{C}$
Average speed $v = 0.1 \text{ m s}^{-1}$
Stroke length $l = 10 \text{ mm}$
Test duration $t = 90 \text{ min}$ (27,000 cycles)

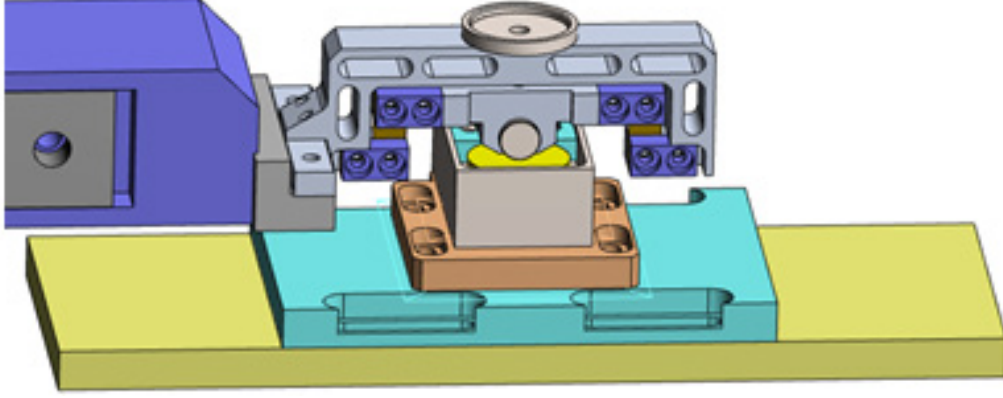


Figure 3. 3. 3D model of the reciprocating linear tribometer.

### 3.3.2 Friction regime estimations ( $\lambda$ calculations)

In reciprocating friction tests, the sliding speed  $v$  is not constant. At the edges of the stroke (where there is a change of direction),  $v$  falls to zero, whereas  $v$  reaches its maximum value ( $v \approx 0.157 \text{ ms}^{-1}$ ) in the center of the stroke. This means that at the edges of the stroke, much less lubricant is entrained in the contact zone between two contacting bodies, resulting in a transition from mixed/hydrodynamic lubrication (ML/HL) to boundary lubrication (BL). To estimate the friction regime of the sliding tests, elastohydrodynamic lubrication (EHL) film thickness calculations were made using a Moes' equation for line contacts<sup>34</sup> and calculated Tallian's lambda values<sup>35</sup>. The central EHL film thickness  $H_{\text{EHL}}$  is calculated by

$$H_{\text{EHL}} = \left[ (H_{\text{RI}}^{7/3} + H_{\text{EI}}^{7/3})^{3s/7} + (H_{\text{RP}}^{-7/2} + H_{\text{EP}}^{-7/2})^{-2s/7} \right]^{s^{-1}}, \quad (\text{S3})$$

where  $s$  is an auxiliary variable defined as  $s = \frac{1}{5}(7 + 8 \exp(-2 H_{\text{EI}}/H_{\text{RI}}))$ , and  $H_{\text{RI}}$ ,  $H_{\text{EI}}$ ,  $H_{\text{RP}}$ , and  $H_{\text{EP}}$  are also defined as  $H_{\text{RI}} = 3M^{-1}$ ,  $H_{\text{EI}} = 2.621M^{-1/5}$ ,  $H_{\text{RP}} = 1.287L^{2/3}$ ,  $H_{\text{EP}} = 1.311M^{-1/8}L^{3/4}$ , respectively. The dimensionless lubricant number  $L$  and load number  $M$  are defined as  $\alpha E' \left( \frac{\eta_0 v}{E'R} \right)^{1/4}$  and  $\frac{F}{E'R} \left( \frac{E'R}{\eta_0 v} \right)^{1/2}$ , where  $E'$  is the reduced Young's modulus ( $\frac{2}{E'} = \frac{1-\nu_1^2}{E_1} + \frac{1-\nu_2^2}{E_2}$ ),  $v$  is the sliding speed,  $\eta_0$  is the lubricant viscosity,  $\alpha$  is the viscosity pressure coefficient,  $R$  is the radius of the cylinder, and  $F$  is the normal load per unit length. The Tallian's lambda values  $\lambda$  is defined as  $\frac{H_{\text{EHL}}}{h_{\text{rms}}}$ , where  $h_{\text{rms}}$  is the composite root-mean-square roughness of the cylinder and disc (defined as  $h_{\text{rms}} = \sqrt{(h_{\text{rms,cylinder}})^2 + (h_{\text{rms,disc}})^2}$ ). Here,  $h_{\text{rms,cylinder}}$  and  $h_{\text{rms,disc}}$  are taken from

**Table 4. 2** for all DLC coatings. **Figure 3. 4** shows a visual representation of the friction regimes in the reciprocating sliding tests for a-C:H and ta-C(51). BL ( $\lambda < 1$ ) and ML ( $1 \leq \lambda < 3$ ) apply at the edges and middle of the stroke, respectively. In the a-C:H system, about 18% of the stroke are under BL, where tribochemical reactions of ZDDP with DLC surfaces occur. For ta-C(51), the BL regime accounts for 32% of the stroke.

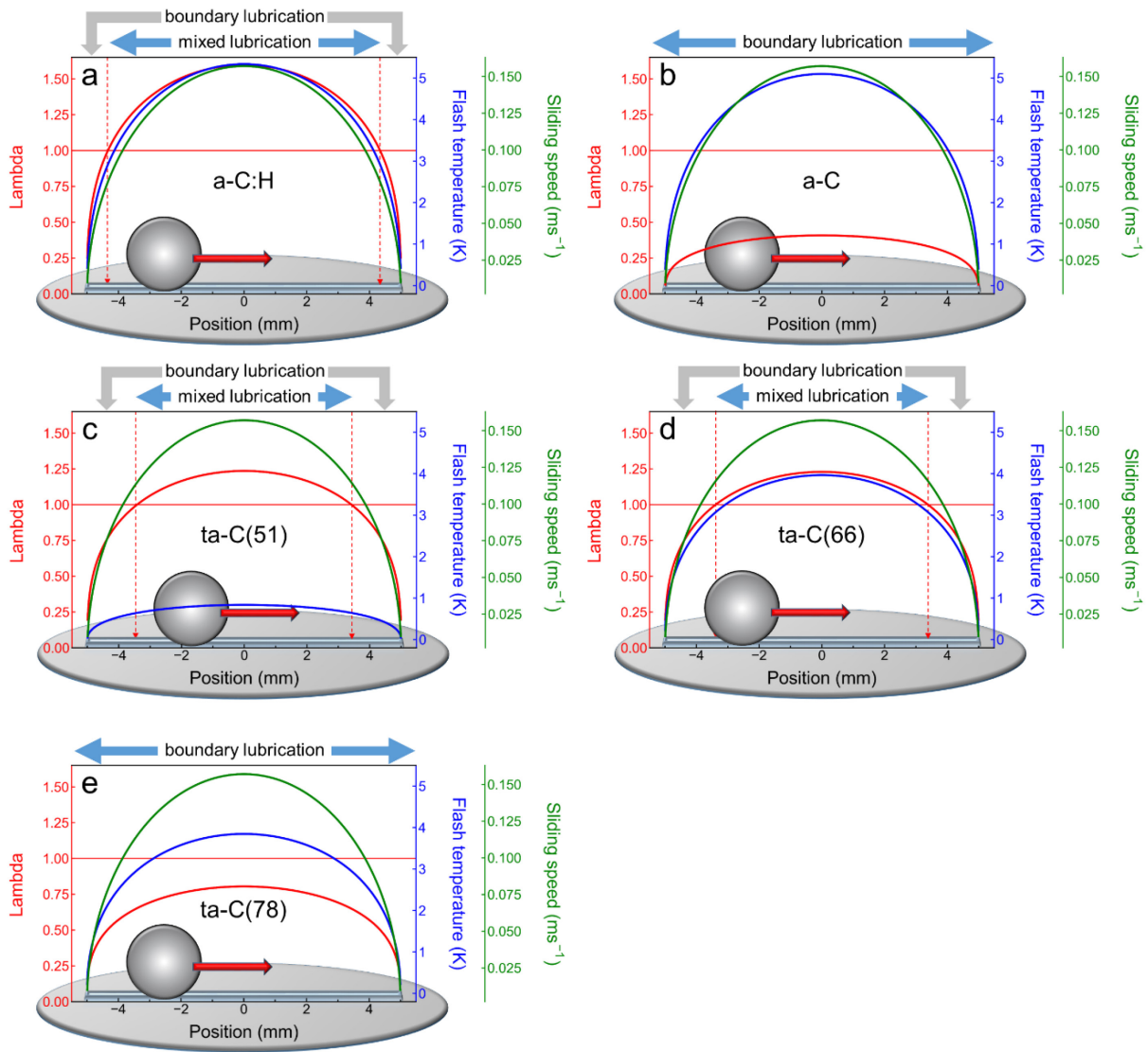


Figure 3. 4. Tallian’s lambda (red), sliding speed (green), and flash temperature (blue) as a function of the cylinder position over the stroke length ( $-0.005 \leq x \leq 0.005$  m) for (a) a-C:H, (b) a-C, (c) ta-C(51), (d) ta-C(66), and (e) ta-C(78).



### 3.3.3 Calculation of flash temperatures.

For rectangular contacts (i.e. cylinder on flat)<sup>36</sup>, the flash temperature rise ( $T_f$ ) at a dimensionless position  $X$  on a homogeneous body subject to a uniform heat flow  $\frac{\mu W |v_{\text{disk}} - v_{\text{cylinder}}|}{4bl}$  is calculated from

$$T_f(X) = \frac{2q\kappa}{\pi K v} \int_{X-L}^{X+L} e^{-\eta} d\eta \int_0^B \frac{e^{-(\eta^2+\zeta^2)^{\frac{1}{2}}}}{(\eta^2+\zeta^2)^{\frac{1}{2}}} d\zeta, \quad (1)$$

where  $l$  and  $b$  are the half width and length of the rectangular contact, respectively,  $K$  is the thermal conductivity,  $\mu$  is the friction coefficient,  $W$  is the normal load, and  $v$  is the sliding speed of the homogenous body relative to the contact. The thermal diffusivity  $\kappa$  is calculated from  $\kappa = K/\rho C_p$ , where  $\rho$  is the mass density and  $C_p$  is the heat capacity. The dimensionless parameters  $X$ ,  $B$ , and  $L$  are defined as  $\frac{vx}{2\kappa}$ ,  $\frac{vb}{2\kappa}$ , and  $\frac{vl}{2\kappa}$ .  $x$  is the position on the body along the sliding direction. First, we consider the temperature rise of a homogeneous body consisting of steel and correct for the presence of a thin DLC coating in a following step. The material parameters for 100Cr6 steel  $\rho_{\text{steel}} = 7.704 \text{ g cm}^{-3}$ ,  $K_{\text{steel}} = 26.1 \text{ W m}^{-1} \text{ K}^{-1}$ , and  $C_{p \text{ steel}} = 0.446 \text{ J g}^{-1} \text{ K}^{-1}$  are taken from the literature<sup>37</sup>.

In the following, we choose a reference frame with a stationary cylinder in contact with a moving disk. The integral in the formula for  $T_f(X)$  is evaluated numerically for the stationary situation ( $v \rightarrow 0$ ) providing the maximum temperature rise  $T_{\text{fmax,cylinder}}$  on the cylinder as well as for velocities  $|v| > 0$  providing the maximum temperature rise  $T_{\text{fmax,disk}}$  on the disk.

Now, we correct both flash temperatures for the presence of a coating. For a layered body consisting of a thin film (DLC) and substrate (steel), the maximum flash temperature for DLC  $T_{\text{fmax,DLC}}$  is calculated from the ratio of  $T_{\text{fmax,DLC}}$  to that for the homogeneous steel  $T_{\text{fmax,steel}}$ <sup>38</sup>:

$$\tau = \frac{T_{\text{fmax,DLC}}}{T_{\text{fmax,steel}}} = \frac{K_{\text{steel}}}{\alpha K_{\text{DLC}}} \left\{ 1 - \frac{2A}{1+A} f^*(A, Dp) \right\}, \quad (2)$$

for  $0.1 \leq Pe_{\text{DLC}} \leq 10.0$

$$f^*(A, Dp) = \frac{1}{1 + 2.329(1+A)^{-(0.475+0.88Dp)} Dp^{b(A)} \exp(-0.62Dp)}, \quad (3)$$

$$b(A) = 0.206 - 0.0413A + (0.0406 + 0.022A - 0.0263A^2)^{0.5}, \quad (4)$$

for  $Pe_{\text{DLC}} < 0.1$ ,

$$f^*(A, Dp) = \frac{1}{\left(1 + \frac{3.36}{(1+A)^{1.097}} Dp\right)^{b(A)}}, \quad (5)$$

$$b(A) = 1.42 + 0.399A - 0.116A^2 + 0.143A^3, \quad (6)$$

where  $Pe_{\text{DLC}} = \frac{vl}{2\kappa_{\text{DLC}}}$  and  $Pe_{\text{steel}} = \frac{vl}{2\kappa_{\text{steel}}}$  are the Peclet numbers of DLC and steel, respectively,  $A = \frac{\lambda - \alpha}{\lambda + \alpha}$ ,  $\lambda = \frac{K_{\text{steel}}}{K_{\text{DLC}}}$ ,  $\alpha = \sqrt{\frac{1 + Pe_{\text{DLC}}}{1 + Pe_{\text{steel}}}}$  for  $0.1 \leq Pe_{\text{DLC}} \leq 10.0$  and  $\alpha = 1$  for  $Pe_{\text{DLC}} < 0.1$ , and  $Dp = D^2(1 + Pe_{\text{DLC}})$ . The dimensionless thickness parameter  $D$  is defined as  $d/2l$ , where  $d$  is the thickness of a DLC coating ( $d = 2 \mu\text{m}$ ).

According to articles by Robertson and his co-workers<sup>39,40</sup>, the correlations between the density  $\rho$  and Young's modulus  $E$  of a DLC coating are given by

$$\rho = 1.37 + E^{2/3}/44.65 \text{ for a-C and ta-Cs}, \quad (7)$$

$$\rho = 0.257 + 0.011(E + 511)/44.65 \text{ for a-C:H}. \quad (8)$$

The heat capacities  $C_p$  are taken from the literature<sup>41</sup>. The thermal conductivities  $K$  for the DLCs are estimated by a linear fitting of the relation between experimental values of  $K$  and  $E$ <sup>42</sup>. A friction coefficient  $\mu = 0.02$  is used for ta-C(51) and  $\mu = 0.1$  for the other coatings.  $T_{\text{fmax}}$  is defined as a maximum  $T_f$  during the stroke.

At the end, the maximum flash temperature rise  $T_{\text{fmax}}$  must be the same for both stationary cylinder and moving disk, and can be calculated from<sup>43</sup>

$$\frac{1}{T_{\text{fmax}}} = \frac{1}{T_{\text{fmax,cylinder}}} + \frac{1}{T_{\text{fmax,disk}}}. \quad (9)$$

Most relevant are the flash temperature rise in the BL regime (i.e. at low sliding speeds near the edges of stroke) where reactions of ZDDP happen and thus our simulation models are valid. The detailed results are given in Supplementary Note 9. An average maximum flash temperature in the BL regime (18% of the stroke)  $T_{\text{fmax,BL}}$  is 2.3 °C for a-C:H. For ta-C(51), the BL regime accounts for 32% of the stroke and  $T_{\text{fmax,BL}}$  is 0.5 °C. The temperature rise is negligibly small for all DLCs, and indeed no correlations of  $T_{\text{fmax,BL}}$  with DLC properties and observed phenomena were found. For example, for a-C:H, tribo-patches form predominantly

near the ends of the stroke while  $T_f$  is larger at the middle of stroke (i.e. at higher sliding speeds) and regardless of the local temperature the hard ta-Cs undergo much more wear.

### 3.3.4 Calculation of root-mean-square heights and slopes

$20\mu\text{m} \times 20\mu\text{m}$  AFM topography maps were measured with a resolution of  $512 \times 512$  pixels. The discretization size  $\Delta l$  of our AFM data is about 39 nm – slightly above the diameter of the AFM tip ( $d_{\text{tip}} \approx 20$  nm). Note that discretization smaller than the tip size is prone to mapping errors. In contrast, increasing the grid spacing would lead to the loss of nanoscale characteristics of the surface and as a result, numerical contact mechanics calculations would give smaller local contact pressures. Since our interest lies nanoscale contact pressures, the spacing should be as small as possible without biased by AFM errors. Moreover, the RMS slope  $h'_{\text{rms}}$  is a central quantity in Persson's theory<sup>44</sup>. While  $h_{\text{rms}}$  is dominated by power-law scaling behaviour of a power spectral density at the largest wavelengths,  $h'_{\text{rms}}$  depends entirely on the surface structure at a smallest scale. A comparison of the RMS slope  $h'_{\text{rms}}$  between a  $20\mu\text{m} \times 20\mu\text{m}$  topography with  $512 \times 512$  pixels and a  $5\mu\text{m} \times 5\mu\text{m}$  topography with  $256 \times 256$  pixels (corresponding to  $\Delta l \approx 20$  nm) for a ta-C(51)-coated disc shows that the calculated values are very similar and thus indicates that the original grid size  $\Delta l \approx 39$  nm is sufficiently small. Additionally, the self-affinity of the surfaces was check by obtaining and verifying the power spectra.

**Figure 3. 5** shows AFM surface topography maps after running-in inside the wear tracks on both the cylinder and disc, which were used in our contact mechanics calculations. During running-in, large asperities are removed and thus  $h_{\text{rms}}$  and  $h'_{\text{rms}}$  decrease for the three softer DLCs (a-C:H, a-C, and ta-C(51)). For example,  $h'_{\text{rms}}$  values measured outside the wear tracks for a-C:H are about twice as large as those inside the weak tracks after running-in. In contrast, for ta-C(66) and ta-C(78), wear events are observed especially at the edge of the stroke after 2,000 sliding cycles. **Figure 3. 5 d and e** show scratches on the cylinder and disc due to wear, resulting in an increase in  $h_{\text{rms}}$  and  $h'_{\text{rms}}$ .

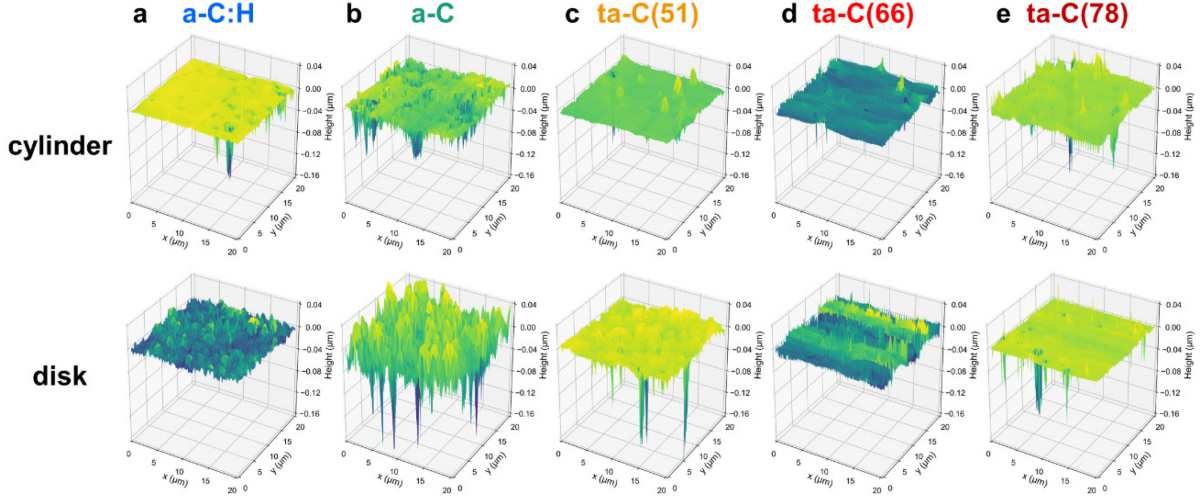


Figure 3. 5. AFM surface topography maps of DLC cylinders and disks: (a) a-C:H, (b) a-C, (c) ta-C(51), (d) ta-C(66), and (e) ta-C(78). For all panels,  $\langle h \rangle = 0.0$ .

A height map  $h_{x,y}$  of a surface topography image with  $N_x \times N_y$  grid points along the x and y axis was obtained using AFM. The root-mean-square height  $h_{rms}$  and slope  $h'_{rms}$  were computed using the following standard definitions:

$$h_{rms} = \langle |h|^2 \rangle = \sqrt{\frac{1}{N_x N_y} \sum_x \sum_y (h_{x,y} - \langle h \rangle)^2}, \quad (\text{S1})$$

$$h'_{rms} = \langle |\nabla h|^2 \rangle = \sqrt{\frac{1}{(N_x-1) \cdot (N_y-1)} \sum_x \sum_y \left( \left( \frac{\partial h_{x,y}}{\partial x} \right)^2 + \left( \frac{\partial h_{x,y}}{\partial y} \right)^2 \right)}. \quad (\text{S2})$$

We used a first-order finite-difference approximation for computing the partial derivatives in Eq. S2. The composite RMS slopes are defined as  $\sqrt{(h'_{rms,cylinder})^2 + (h'_{rms,disk})^2}$ .

### 3.3.5 Analytical Tribometer in Controlled Environment (ATCE)

Reciprocating ball-on-disk sliding tests were carried out with an Analytical Tribometer in Controlled Environment (ATCE). The samples were introduced in the load lock chamber and transferred through the radial distribution chamber into the tribometer chamber where the sliding tests are performed. Afterwards, the samples were transferred into the XPS analysis chamber without being exposed to the outside environment. The whole system pressure was kept under ultra-high vacuum (UHV) by means of primary and secondary pumping systems and managed by connecting valve gates between each separate chamber. A schematic representation of the system is shown in **Figure 3. 6**. During the sliding tests, the disk (flat

coupon) was fixed and the ball was displaced horizontally in reciprocating motion. The applied normal force was regulated to be stable throughout the test by a motor that controlled the vertical displacement of the ball. The friction coefficient  $\mu$  was calculated as the average of the acquired points for one passage (half cycle). The test parameters used for the standard reciprocating sliding tests are given in **Table 3. 4**. The parameter values were chosen taking into account practical reasons and the limitations of the tribometer. For example, to regulate well the applied normal force it is needed to use a sliding speed of only a few mm/s. It was necessary to increase the contact pressure to obtain a wear track with a diameter close to 100  $\mu\text{m}$  so it could be visible and analyzed in the XPS chamber.

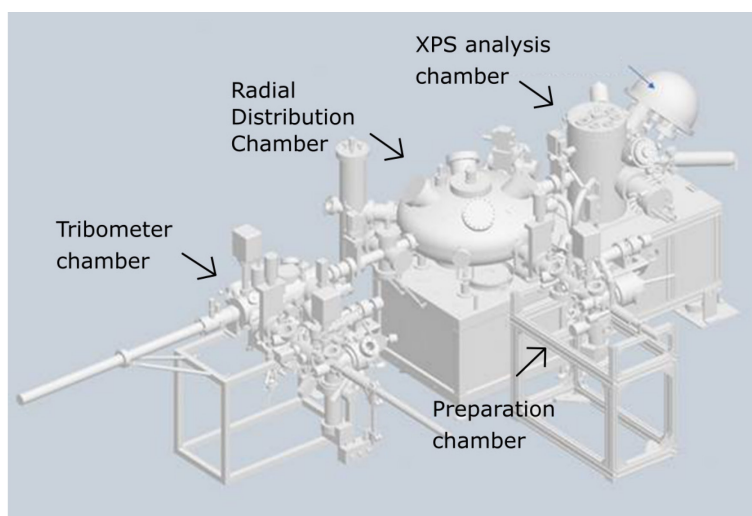


Figure 3. 6. Schematic representation of the ATCE system.

Table 3. 4. Test conditions used in the sliding experiments.

<b>Standard reciprocating sliding tests conditions</b>
Contact: ball-on-disk
Applied load $F_N = 5 \text{ N}$
$P_{\text{Hertz}} = 800 \text{ MPa}$
Temperature $T = 20^\circ\text{C}$
Average speed $v = 0.2 \text{ mm s}^{-1}$
Stroke length $l = 2$
Controlled environnement : diverse

### 3.4 Surface characterization techniques

#### 3.4.1 Optical Interferometer

The wear volumes of the samples were measured using an optical white light interferometer (Contour GT-K1, Bruker). When the wear tracks were too large to be captured in one single image (such as 4 x 10 mm wear tracks on the disks), an automatic stitching procedure was used to capture and combine multiple images to obtain the whole wear track. A terms removal (F-operator) was used to straighten the base line of the sample. **Figure 3. 7** shows the raw measurement (left) performed on a cylinder and the straightened image (right). To measure the wear (negative volume), a mask was applied to limit the analyze area close to the wear track and minimize the measurement error.

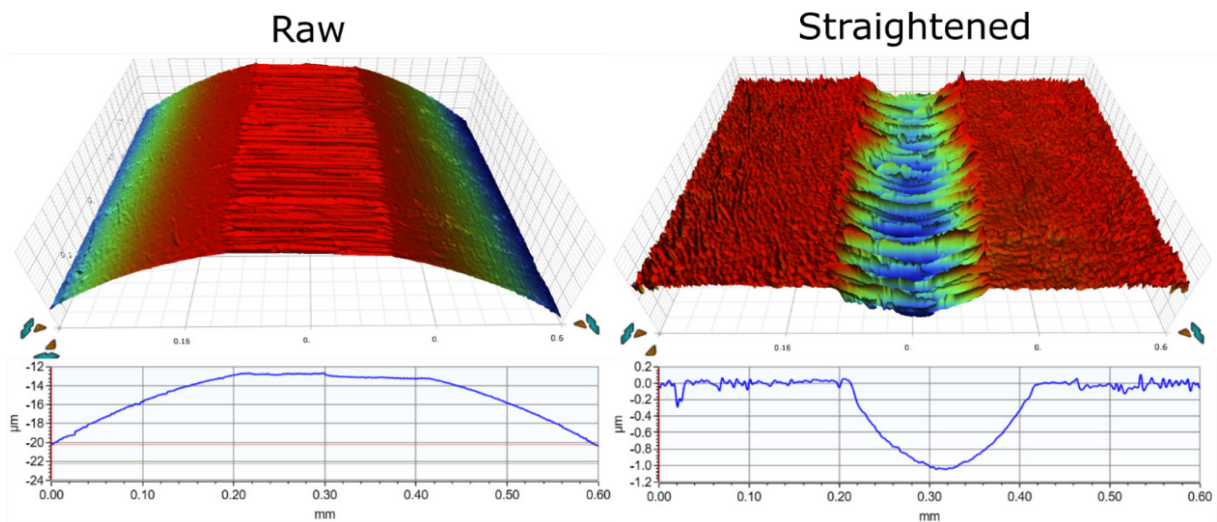


Figure 3. 7. Optical interferometer measurements of a cylinder: raw (left) and straightened (right).

#### 3.4.2 Raman Spectroscopy

The wear tracks of the DLCs samples were analyzed by Raman spectroscopy using a Renishaw inVia™ Qontor® Confocal Raman Microscope, equipped with a 50x magnification lens. The Raman spectra were recorded using a 633 nm laser with a spot size of 1.0 µm.

#### 3.4.3 AFM

To investigate the surface topography inside and outside of the wear tracks, AFM measurements were carried out with a NX 10 (Park Instruments) equipped with silicon probes having a nominal spring constant of 37 N.m<sup>-1</sup> and a nominal tip radius of 10 nm (ACTA AFM probes from App nano) and operated in standard Tapping Mode with an operational resonance

frequency  $\approx 190$  kHz after automatic calibration. Firstly, the cantilever and tip were mounted on the holder and aligned with the photodetector so the signal intensity approximated 3.0 V with lateral and vertical deviations of less than 0.1 V each. At this point, the tip could be automatically approached to the surface to begin the measurements. Firstly,  $50 \times 50 \mu\text{m}^2$  images were recorded at low resolution ( $256 \times 256 \text{ px}^2$ ) and afterwards a  $20 \times 20 \mu\text{m}^2$  high quality image ( $512 \times 512 \text{ px}^2$ ) were recorded in the region of interest. The scanning speed was kept under 0.3 Hz per line to avoid damaging the AFM tip. The data was treated (base line correction) and analyzed using Gwyddion software.

#### **3.4.4 SEM analysis**

The surfaces were observed after tribological tests to study its topography and chemical composition without any conductive coating by Scanning Electron Microscopy (SEM) using a FEI XL30-FEG equipped with an Everhardt-Thornley secondary electron detector and operating under high vacuum. The acceleration voltage was set to 2 kV or 5 kV. Chemical composition analyses were carried out by Energy Dispersive X-Ray Spectroscopy (EDS) using an Oxford Instruments X-max silicon drift detector ( $80 \text{ mm}^2$  ultra-thin window). Quantitative analysis of the EDS spectra was performed using the Aztec software.

#### **3.4.5 FIB machining and TEM analysis**

Cross-section of the flat wear track was prepared in Manutech-USD by Dual Beam Focused Ion Microscopy. A platinum gaseous precursor was first used to deposit a platinum layer onto the DLC surface, to protect it during milling and avoid any re-deposition. This layer was deposited in two steps. First, a low-energy electron beam was used to avoid damaging the DLC surface. Afterwards, a Ga ion beam was used at high energy to increase the growth rate of the protective platinum film and accelerate the process.

The a-C:H thin foils obtained were analysed by TEM using a Jeol 2010F-UHR TEM equipped with a Schottky field emission gun operating at 200 kV. Bright field images were acquired using a Gatan Orius 100 CCD camera and High-Angle Annular Dark Field (HAADF) images in the Scanning Transmission Electron Microscopy (STEM) mode. EDX ( $80 \text{ mm}^2$  silicon drift detector from Oxford Instruments) was used for local chemical analysis (spectra or elemental maps). The ta-C(66) thin foil was analysed using a FEI Titan ETEM G2 electron microscope operated at 300 keV and equipped with a Cs image aberration corrector. To avoid contamination prior to the analysis, the samples were plasma-cleaned with Argon

for 30 seconds. Compositional analyses were conducted in TEM mode with an energy dispersive X-ray spectrometer (SSD X-max 55 mm<sup>2</sup> from Oxford Instruments).

### 3.4.6 XPS analysis

After the friction tests, the samples were cleaned twice in an ultrasonic bath with n-heptane (Chimie Plus: > 99%) for 10 minutes to remove residual oil. The samples were handled with metallic tweezers without touching their surfaces. XPS analysis was performed on the samples using an ULVAC-PHI Versa Probe II spectrometer equipped with a monochromatic Al K $\alpha$  X-ray source with a beam diameter of 200  $\mu\text{m}$ . The binding energy scale was calibrated with respect to the C1s photo-peak at a binding energy of 284.8 eV. The error of binding energies is estimated as  $\pm 0.1$  eV. First, a survey spectrum was performed using a pass energy of 187.85 eV to identify all the elements present on the surface. Afterwards, narrower scans with a range of 20 eV were acquired using a pass energy of 23.5 eV to accurately identify the chemical state of each element and to perform quantitative analysis using PHI Multipack software. The contribution of the background was approximated by the Shirley method and Wagner sensitivity factors (corrected for the transmission function of the apparatus) were used for the calculation of the atomic concentrations. An Argon ion beam was used to sputter the samples surfaces at an angle of 45°. The ion beam was accelerated at 250 V with a current density of 120 nA mm<sup>-2</sup>. A digital camera was used to take pictures of the samples to identify the wear tracks. When the wear tracks were too small to be seen on the picture (often the case for ball samples), a Scanning X-ray Imaging (SXI) image was recorded to obtain a chemical contrast between the inside and the outside of the wear track (see **Figure 3. 8**).



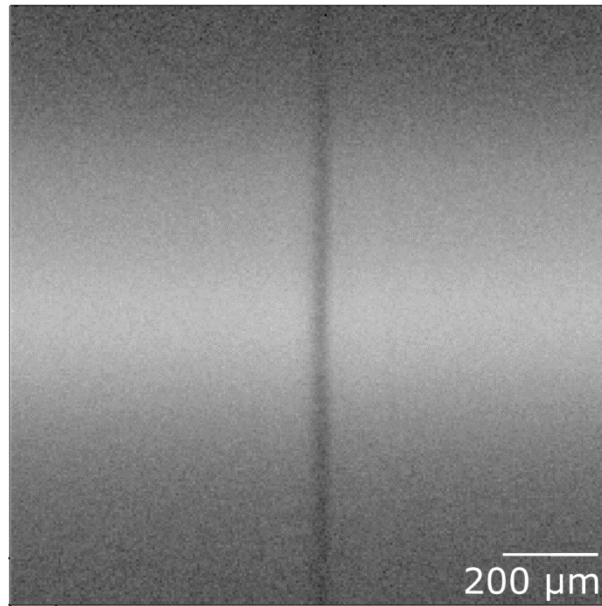


Figure 3. 8. Example SXI image showing the wear track (black line) at the center of the image.

However, when the contrast was not noticeable by this technique, narrow-range XPS spectra could be obtained using a high pass energy to record fast spectra (1 or 2 minutes per analysis point) in a determined grid-space containing up to 8 x 8 analysis points on the area where the wear track was expected to be found (on the top of the ball).

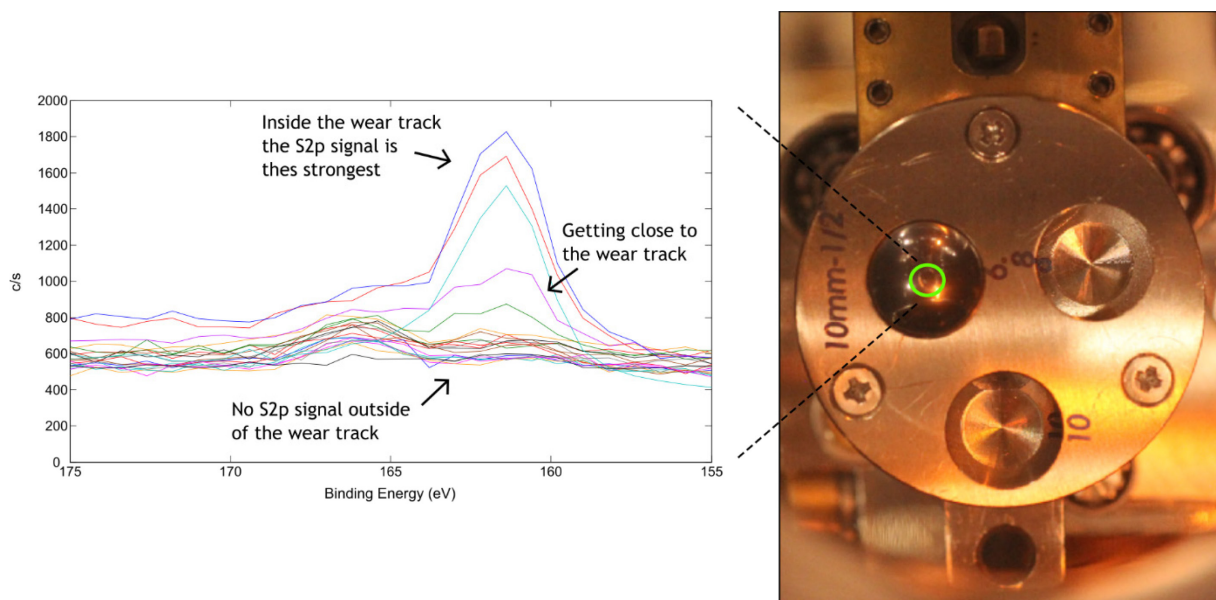


Figure 3. 9. Chemical mapping technique used to find the wear track by recording narrow-range XPS spectra using a high pass in a user-defined space-grid. The S2p signal (left) is the most intense inside the wear track and there is nothing significant outside. Picture of the ball sample where the wear track is not visible (right).

## 3.5 Computer simulations (Fraunhofer Institute)

The computer simulations were carried out Prof. Michael Moseler and his colleagues from the Fraunhofer Institute of Materials as part of a joint collaboration. For the anecdote, this collaboration started after the Tribochemistry satellite conference that took place in Hakodate on September 2019; where both parties agreed that the experimental and simulation results complimented each other very well, and so, a fruitful working collaboration began.

### 3.5.1 Contact mechanics simulations

Elastic-plastic contact of two rough DLC surfaces were modelled using experimental AFM topography maps with discrete height profiles  $h_{x,y}$  over a scan area of  $20 \times 20 \mu\text{m}^2$  (including  $512 \times 512$  data points). Local contact pressures  $p_{x,y}$  and elastic displacements  $u_{x,y}$  were calculated under an external normal pressure of 210 MPa (equal to the maximum cylindrical Hertzian contact pressure used in our experiments) using the PyCO code developed by Pastewka and co-workers. Plasticity of surface asperities was taken into account if the local contact pressure  $p_{x,y}$  went beyond the material hardness<sup>45</sup>. However, no significant differences in  $P_{l,\text{eff}}$  (defined as the median values of the pressure distribution) were observed between elastic-plastic and full elastic calculations. The details of numerical techniques used in the contact mechanics calculations are described somewhere else<sup>46–50</sup>. Young's moduli and hardness values are tabulated in **Table 4. 2** in Chapter 4. A typical value of 0.2 was used for the Poisson's ratio of DLC. For each pair, 25 contact mechanics calculations were carried out by moving a topography map with respect to the other along the x axis with a step of 20 pixels. We assumed that the load was entirely supported by asperities and no fluids were entrained in the contact zone. Thus,  $P_{l,\text{eff}}$  is only valid for boundary lubrication, i.e. at the ends of the stroke. We employed AFM topography maps measured inside the wear tracks after running-in since they are representative of DLC surfaces in a steady, low-friction state. A contact mechanics calculation of DLC topographies measured outside wear tracks showed that significant amounts of surface asperities undergo plastic deformation (corresponding to an initial high friction in **Figure 4. 1b**). However, the high friction state lasts only for the first few hundred cycles and  $\mu$  drops immediately. For example, for a-C:H, the RMS heights and slopes outside the wear track are 2–3 times larger than those inside the wear track after running-in, which results in a much larger  $P_{l,\text{eff}}$ , and no correlation between  $P_{l,\text{eff}}$  and  $E^* h'_{\text{rms}}$  was found.

### 3.5.2 Quantum chemical simulations

Bond-breaking and -forming of ZDDP in contact with DLC surfaces were studied using third-order density-functional tight-binding (DFTB3) calculations<sup>51</sup> as implemented in the Atomistica software suite<sup>52</sup>. Atomic forces were extracted from quantum chemical calculations in order to describe complicated bond-breaking and -formation processes under tribological conditions. The accuracy of Slater-Koster parameters for modelling the interactions between ZDDP and DLC surfaces was confirmed by first-principles density-functional theory (DFT) calculations (shown in **Figure 3. 10.**)

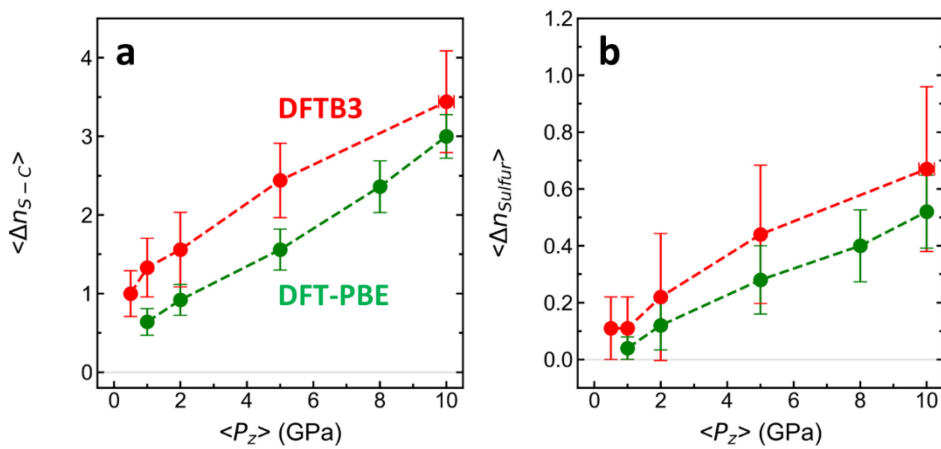


Figure 3. 10. Comparison of DFTB3 with ab-initio DFT-PBE calculations for quasi-static contact-closing of unpassivated a-C:H surfaces interacting with a ZDDP molecule. Averaged numbers of (a) S-C bonds ( $\langle \Delta n_{S-C} \rangle$ ) formed between ZDDP sulphur and DLC carbon atoms as well as (b) sulphur atoms ( $\langle n_{Sulphur} \rangle$ ) released from ZDDP to the DLC after opening the contact as a function of the contact pressure  $P_z$  for DFTB3 (red) and DFT-PBE (green). For both DFTB3 and DFT-PBE, the same a-C:H samples were employed. The error bars represent standard error of the means.

In this study, three types of DLC surfaces were considered: a-C:H with the density  $\rho = 2.0 \text{ g cm}^{-3}$  and hydrogen content  $C_H = 20 \text{ at.}\%$ , a-C with  $\rho = 2.0 \text{ g cm}^{-3}$ , and ta-C with  $\rho = 3.0 \text{ g cm}^{-3}$ . The aims of the simulations in **Figure 4. 12 and 13-15** are different. In **Figure 4. 12**, the bulk shearing of sulphur-doped DLCs aims to understand weakening of the bulk regions under shear. Thus, the three computational models were chosen to exactly correspond to experimental a-C:H, a-C, ta-C(78), respectively. In contrast, in the simulations of **Figure 4. 13-15**, we considered the former two DLC models due to the following reasons. Our focus is on understanding tribochemical reactions of ZDDP on DLC surfaces. In general, hydrostatic compression of a-C increases its density and  $sp^3$  percentage in the bulk and as a result forms ta-C with a high  $sp^3$  percentage  $p_{sp^3}$ <sup>53</sup>. However, a superimposed shear motion drives the system away from its equilibrium phase. At the sliding interface, a ta-C surface layer

undergoes  $sp^3$ -to- $sp^2$  rehybridisation resulting in a significant decrease of  $p_{sp^3}$ <sup>54</sup>. This tribolayer with  $p_{sp^3} \approx 10\%$  should be universal for any hydrogen-free DLC coatings and therefore we modelled the reactive zone on top of the ta-Cs as a low-density a-C.

All DLC samples were generated by quenching a melt from 5000 to 0 K at a constant rate of  $1 \text{ K fs}^{-1}$ . For **Figure 4. 12**, sulphur-doped ta-C samples with initial densities  $\rho = 2.0$  and  $3.0 \text{ g cm}^{-3}$  and a same initial cell size of  $14 \times 14 \times 14 \text{ \AA}^3$  were produced as starting configurations. For the DLCs in **Figure 4. 13-15**, three samples with a cell size of  $15 \times 15 \times 10 \text{ \AA}^3$  were generated. For each sample, three surfaces were then created by cutting them perpendicular to the  $z$ -axis at different  $z$  coordinates, separating the resulting slabs by 2 nm and introducing a ZDDP molecule (with ethyl groups) into the created vacuum region. Before inserting the ZDDP molecule, the DLC slabs were fully relaxed. Thus, in total, 9 independent quasi-static molecular statics contact-closing/reopening trajectories were generated for each type of DLC. During QMS simulations, the cell size  $L_z$  in the  $z$ -direction is decreased with a step  $\Delta L_z = -0.2 \text{ \AA}$  and once the system reaches a desired contact pressure  $P_0$ ,  $L_z$  is increased to the initial one ( $L_0 = 30.0 \text{ \AA}$ ) in steps  $\Delta L_z = +0.2 \text{ \AA}$ . For each step, the entire system is relaxed so that all force components are below  $5.0 \times 10^{-3} \text{ eV \AA}^{-1}$  with the FIRE algorithm<sup>55</sup>. This quasi-static contact-closing/opening simulation mimics an experimental situation in which two asperities come into contact and then detach from each other in the limit  $v \rightarrow 0 \text{ m s}^{-1}$ . However, the effect of shear stress is not explicitly taken into account within this quasi-static simulation, but is taken into account in the dynamic MD shearing simulations.

MD shearing simulations of two systems (ZDDP/DLC and sulphur-doped ta-C) were carried out with Lees-Edwards boundary conditions<sup>56</sup>. The system temperature  $T$  was kept constant at 300 K using a Peters thermostat<sup>57</sup>, and the equations of motion were integrated with a time step  $\Delta t = 0.5 \text{ fs}$  using the velocity-Verlet algorithm<sup>58</sup>. The system pressure was controlled using a Berendsen barostat<sup>59</sup>. The systems were sheared at a constant speed along the  $x$  axis, and the averaged shear stress  $\tau$  was calculated from the component  $\tau_{zx}$  of the stress tensor.

Although boundary conditions in our atomistic simulations were matched to local experimental conditions (e.g., temperature and local contact pressures), the sliding speed of  $v_{\text{MD}} = 30 \text{ m s}^{-1}$  in MD simulations is two orders of magnitude larger than the experimental values ( $v_{\text{exp}} = 0.157 \text{ m s}^{-1}$ ), as in previous MD studies<sup>60-62</sup>. The use of such high sliding speeds is necessary to simulate a long sliding distance, sufficiently sample phase space, and

especially describe tribochemical reactions and subsequent phase transitions at sliding interfaces<sup>60,63</sup>. In principle, one must keep the sliding speed well below the speed of sound in materials. The speed of sound in DLC is two or three orders of magnitude larger than our sliding speeds<sup>64</sup>. This ensures that the heat generated in the contact during sliding is rapidly dissipated from the sliding interface to surrounding materials. The criterion is a prerequisite for reliable modelling of the shear response of materials.

In addition, at low enough temperatures (when thermal activation of reactions can be neglected) the reaction products are entirely determined by the mechanochemical competition of the mechanical strength of the different chemical bonds. In this case, mechanochemical reactions observed in our MD simulations should also be independent of the sliding speed and are thus transferable to our low speed experiments. This argument is confirmed by the observation that our MD shearing simulations reveal similar results as our quasi-static calculations.

---

# Chapter 4: Interplay of Chemistry and Mechanics govern the wear of DLC coatings in ZDDP-additivated oil

---

In this chapter, the friction and wear properties of five DLCs are tested in ZDDP-solution. Combined experiments, analytical techniques, and computer simulations are carried out to provide a better understanding of the underlying mechanisms responsible for the observed macroscopic behavior of DLCs lubricated in ZDDP-solution. The results presented in this chapter were reported in a scientific paper accepted for publication at the end of May 2021 in Nature Communications journal.

## 4.1 Introduction

Diamond-like carbon is an excellent solid lubricant that exhibits high wear resistance and superlubricity (i.e., friction coefficient  $\mu$  below 0.01) under boundary<sup>63,65</sup> and mixed lubrication<sup>66</sup> with organic friction modifiers (FM), including oleic acid and glycerol. It has been increasingly applied as a protective coating in internal combustion engines, where operating conditions are extremely severe and thus the use of anti-wear (AW) additives, e.g. zinc dialkyldithiophosphate (ZDDP) and FM additives, e.g. molybdenum dithiocarbamate (MoDTC), admixed with base oils is essential for reducing wear and friction. However, it has been proven that some additives (e.g. MoDTC<sup>67</sup>) can cause massive wear of some DLCs, and especially the role of ZDDP with respect to wear in DLC/DLC contacts remains controversial<sup>68-72</sup>, since research on these additives has been mainly focused on conventional ferrous surfaces<sup>73</sup>. Consequently, a better understanding of interactions between such additives and DLC as well as an improvement of the AW performance of additives on DLC are of technological importance.

ZDDP is one of the most indispensable and effective AW additives for automotive combustion engines<sup>73</sup>. However, since sulphur and phosphorous produce environmentally hazardous waste substances and degrade catalyst converters, alternative additives have been sought to replace ZDDP with other ash- and phosphorous-free AW agents for the sake of reducing the environmental load<sup>74,75</sup>. Nevertheless, owing to its extraordinary AW properties, ZDDP is still a principal AW additive. Substantial efforts have been made to identify chemical structures and formation mechanisms of ZDDP-derived tribofilms<sup>76-79</sup>, which is necessary not only to improve the AW performance of ZDDP but also to formulate alternative sulphur- and phosphorous-free lubricants.

Particular attention is paid to whether ZDDP is effective with DLC, which has been already investigated for various types of DLC coatings<sup>68,69,72,80,81</sup>, including hydrogen-free tetrahedral amorphous carbon (ta-C) and hydrogenated amorphous carbon (a-C:H). Vengudusamy et al. carried out comprehensive experimental studies on the effect of different types of DLC coatings, such as a-C:H, a-C, ta-C, and doped DLCs<sup>68-70</sup>. They reported that ta-C lowers boundary friction, but exhibits higher wear compared with a-C:H and a-C. They concluded that the wear resistance of DLC is mainly governed by the type of DLC, and the role of ZDDP as AW agent is unclear.

Interestingly, ZDDP-derived patchy layers are likely to form on DLC surfaces, but are less thick and durable than those observed on steel probably due to weaker interactions of ZDDP with DLC surfaces<sup>70,82</sup>. The thicknesses and morphologies of these tribofilms are affected by intrinsic parameters of the DLC coatings, i.e. hydrogen content, sp<sup>2</sup>/sp<sup>3</sup> ratio, presence or absence of dopants, surface roughness and mechanical properties<sup>69,83</sup>. The former three factors would alter chemical reactivity of DLC surfaces and thus reaction rates of ZDDP, whereas the latter two factors affect the mechanical response of the system such as contact pressure and geometry, and elastic/plastic deformation of surface asperities.

Mosey et al.<sup>84</sup> simulated the cross-linking of bulk zinc phosphate precursors with ab-initio molecular dynamics (MD), showing that high hydrostatic pressures induce the formation of poly-phosphates. It would be tempting to ascribe the low quantity of ZDDP-derived polyphosphates on DLC to reduced contact pressures. However, DLCs are stiffer than steel and therefore ZDDP on DLC should experience higher contact pressures. This indicates that the chemical interactions between ZDDP and surfaces cannot be neglected in the ab-initio modelling. So far, only decomposition processes of other sulphur-<sup>84</sup> and phosphorous-containing additives<sup>86</sup> on iron surfaces have been simulated.

Here, we combine experiments and simulations to understand the reaction mechanisms of ZDDP with DLC surfaces and the role of mechanics, surface roughness and chemistry. Friction and wear of five different self-mated DLC coatings sliding in a ZDDP solution with a PAO base oil are studied. First, a combination of reciprocating sliding tests, XPS surface chemical analyses, and contact mechanical calculations suggest that wear and friction regimes are strongly affected by asperity-scale contact mechanics of two rough surfaces. The effective local contact pressure  $P_{l,eff}$  varies with the Young's modulus  $E$  and root-mean-square (RMS) slope  $h'_{rms}$  of the DLC coatings. Therefore, surface asperities on soft DLC experience lower contact pressures ( $P_{l,eff} \lesssim 3.5$  GPa) than on hard DLC ( $P_{l,eff} \gtrsim 9$  GPa). While on the former 20-nm-thick tribo-patches form and no visible wear is observed, the latter undergo severe wear accompanied by a drastic increase of the friction coefficient  $\mu$ . On hard DLCs, we observe significantly more S–C than Zn–S bonds, indicating that ZDDP is more likely to react with the hard DLC surfaces.

Second, quantum-chemical simulations reveal that the kinetics of ZDDP's chemical decomposition reactions is accelerated by an increase in  $P_{l,eff}$  and it is independent of the bulk chemical structure of DLC. However, chemical differences between DLC surfaces alter the



response of the frictional interface to shear action at high contact pressures ( $P_{1,\text{eff}} > 5$  GPa). Non-hydrogenated DLC surfaces are likely to cold-weld at high contact pressures due to lower steric hindrance and stronger attractive interactions. The cold-welded surfaces undergo chemical mixing under shear, resulting in sub-surface sulphur doping, which in turn weakens the DLC matrix (reduces its yield stress) and causes severe wear. In contrast, local contact pressures on soft DLC are small enough ( $P_{1,\text{eff}} \lesssim 3.5$  GPa) to prevent cold welding and sulphur doping. In this case, ZDDP chemisorbs and decomposes into atoms and small fragments that accumulate and cross-link to form anti-wear tribofilms on the softer DLCs.

Our study elucidates the crucial role of inter-asperity nano-mechanics and chemistry in determining the chemical reactions of ZDDP with DLC surfaces and their macroscopic tribological behaviours. In this context, the effective local pressure  $P_{1,\text{eff}}$  at asperity contacts and the hydrogen content of the coatings are the crucial mechanical and chemical factors, respectively. The former dominates the mechanochemistry of ZDDP, whereas the latter affects shear accommodation of the sliding interface. The understanding of the interplay between mechanical and chemical stimuli and the correlation between atomistic and macroscopic phenomena pave the way for prediction and control of tribological properties of DLC lubricated with ZDDP-additivated oils. The underlying concepts might be also applicable to ferrous and other non-ferrous materials in tribological contact with sulphur- and phosphorous-containing additives, and even useful for a comprehensive understanding of the formation of lubricant-derived tribofilms with enhanced anti-wear performance.

## 4.2 Friction and wear results

In order to investigate the impact of ZDDP on friction and wear of DLC coatings, reciprocating cylinder-on-disc sliding tests are performed for self-mated DLC/DLC tribopairs in both pure poly-alpha-olefin (PAO-4) base oil and PAO-4 mixed with 1 wt.% ZDDP primary-C4. The test parameters were given in **Methods section 3.3.1** and reminded in **Table 4. 1**. The tests were repeated at least 4 times each to ensure the repeatability of our experiments. Five DLC coatings with varying properties are tested under the same conditions. They are labelled as: a-C:H, a-C, ta-C(51), ta-C(66) and ta-C(78). The numbers in parenthesis represent the hardness of ta-Cs in GPa. Their main properties are reminded in **Table 4. 2**. The reported RMS heights  $h_{\text{rms}}$  and slopes  $h'_{\text{rms}}$  are average values measured inside the wear tracks of DLC-coated cylinders and discs after running-in (800 cycles for ta-C(78) and 2000

cycles for the others). The mathematical definitions of the RMS heights and slopes are available in the **Methods section 3.3.4**.

Table 4. 1. Test parameters used in the reciprocating sliding tests.

<b>Standard reciprocating sliding tests conditions</b>
Contact: cylinder-on-disk
Applied load $F_N = 23$ N
$P_{\text{Hertz}} = 210$ MPa
Temperature $T = 110^\circ\text{C}$
Average speed $v = 0,1$ m s <sup>-1</sup>
Stroke length $l = 10$ mm
Test duration $t = 90$ min (27,000 cycles)

Table 4. 2. Chemical compositions, mechanical and structural properties, and surface roughness parameters of the tested DLCs. The densities  $\rho$  and percentages of sp<sup>3</sup> carbon atoms  $p_{\text{sp}^3}$  are estimated from Young's modulus using empirical formulae suggested by Ferrari and co-workers<sup>39,40</sup>.

Label	Composition (at.%)		Young's modulus $E$ (GPa)	Hardness $H$ (GPa)	Density $\rho$ (g cm <sup>-3</sup> )	sp <sup>3</sup> C $p_{\text{sp}^3}$ (%)
	C	H				
a-C:H	80	20	259	27	2.07	-
a-C	> 99	< 1	287	24	2.34	31
ta-C(51)	> 99	< 1	493	51	2.77	62
ta-C(66)	> 99	< 1	572	66	2.91	73
ta-C(78)	> 99	< 1	625	78	3.01	79

RMS after running-in						
Label	height $h_{\text{rms}}$ (nm)			slope $h'_{\text{rms}}$ (-)		
	Cylinder	Disc	Composite	Cylinder	Disc	Composite
a-C:H	5.0±0.7	6.7±1.3	8.4±1.0	0.051±0.015	0.087±0.043	0.104±0.032
a-C	13.4±3.9	26.5±0.1	29.8±1.4	0.072±0.002	0.131±0.005	0.150±0.004
ta-C(51)	3.9±1.3	9.0±2.0	9.8±1.5	0.025±0.002	0.054±0.028	0.060±0.020
ta-C(66)	3.8±0.6	9.1±0.4	9.9±0.4	0.044±0.010	0.078±0.009	0.089±0.008
ta-C(78)	10.9±0.8	10.4±4.3	15.3±2.5	0.099±0.013	0.080±0.015	0.128±0.012

Significant differences in both friction and wear are observed between pure PAO and PAO+ZDDP lubrication. **Figure 4. 1a and b** show the evolution of the friction coefficient  $\mu$  in pure PAO and PAO+ZDDP, respectively. For a-C and a-C:H,  $\mu$  increases gradually and reaches a steady state with  $\mu \approx 0.1$  in PAO (**Figure 4. 1a**). Conversely, in PAO+ZDDP, the running-in periods are much shorter than those in PAO and  $\mu$  decreases slightly to 0.08 – 0.09 (**Figure 4. 1b**). The three ta-Cs reach rapidly a steady, ultralow friction state ( $\mu = 0.01 – 0.03$ ) in PAO. In PAO+ZDDP, the friction curve for ta-C(51) is almost the same as that in PAO. However, for harder ta-Cs, i.e. ta-C(66) and ta-C(78), the addition of ZDDP significantly changes their tribological performance. Friction increases gradually to  $\mu = 0.08 – 0.10$  after 2000 and 12000 sliding cycles for ta-C(66) and ta-C(78), respectively.

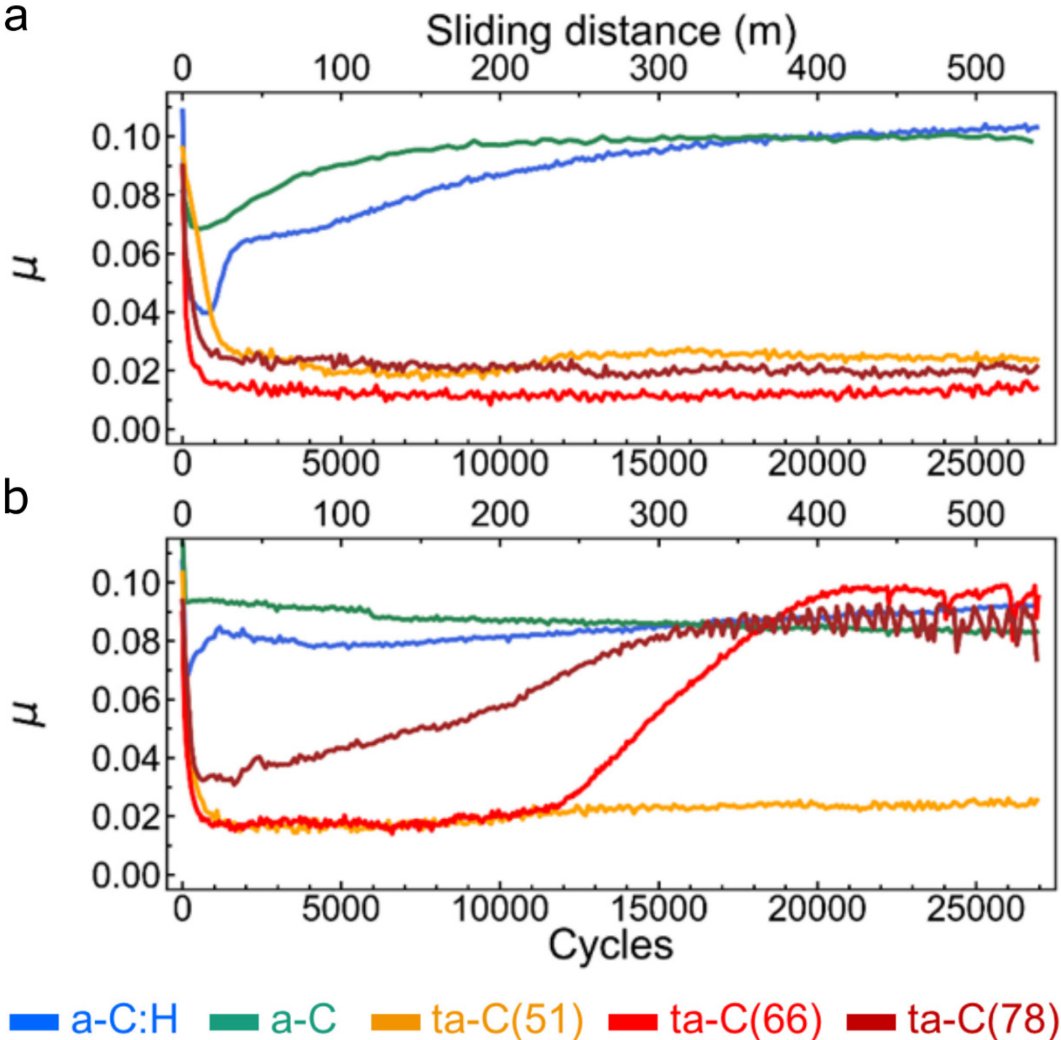


Figure 4. 1. Friction curves of five self-mated DLC tribopairs in (a) pure PAO-4 base oil and (b) a mixture of PAO-4 and 1 wt.% ZDDP.

**Figure 4. 2** shows composite wear volumes  $W$  measured on the cylinders (a) and discs (b) measured by optical interferometry. In PAO the wear volumes are not measurable for most DLCs. However, in PAO+ZDDP wear increases drastically for ta-C(66) and ta-C(78) in correlation with the increased  $\mu$  (**Figure 4. 1**). It should be noted that the wear volume of the discs (**Figure 4. 2b**) is 10 times larger than that of the cylinders (**Figure 4. 2a**).

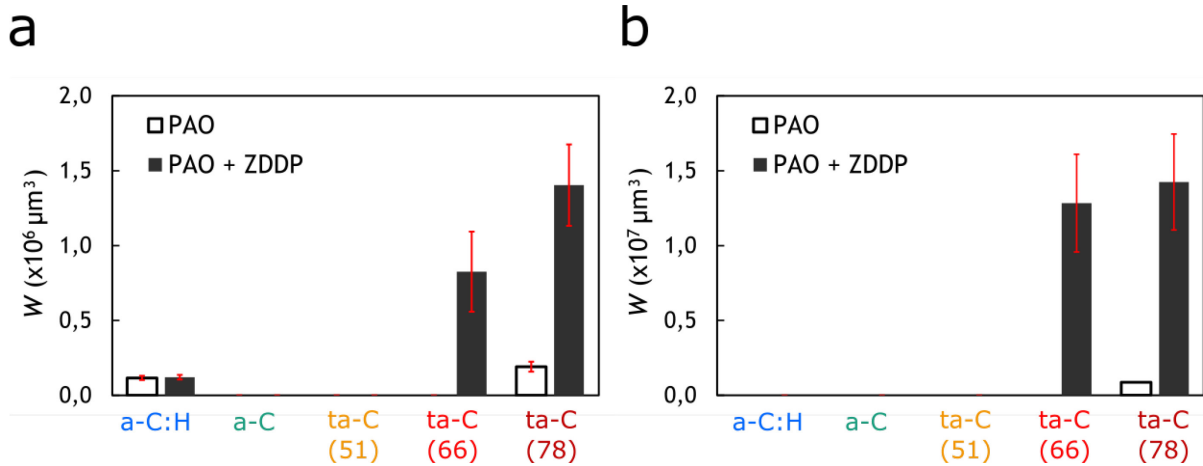


Figure 4. 2. Wear volumes of DLCs cylinders (a) and discs (b) after sliding tests in PAO and PAO + ZDDP.

Optical images of wear tracks on both cylinders and discs after sliding show deep scratches for ta-C(66) and ta-C(78) on PAO + ZDDP lubrication (**Figure 4. 3**). The rubbed surfaces are much rougher than the pristine surfaces as shown by optical interferometer images in **Figure 4. 4**. The average depths of the wear scars are about 0.5 and 1.5  $\mu\text{m}$  for the disc and cylinder, respectively (the DLC coating's thickness is 2.0  $\mu\text{m}$ ). Conversely, the wear scars of the other softer DLCs are barely visible under the same observation conditions. Thus, ZDDP has a negligible effect on the friction and wear of soft/moderate-hard DLCs but a catastrophic effect on those of harder ta-Cs.

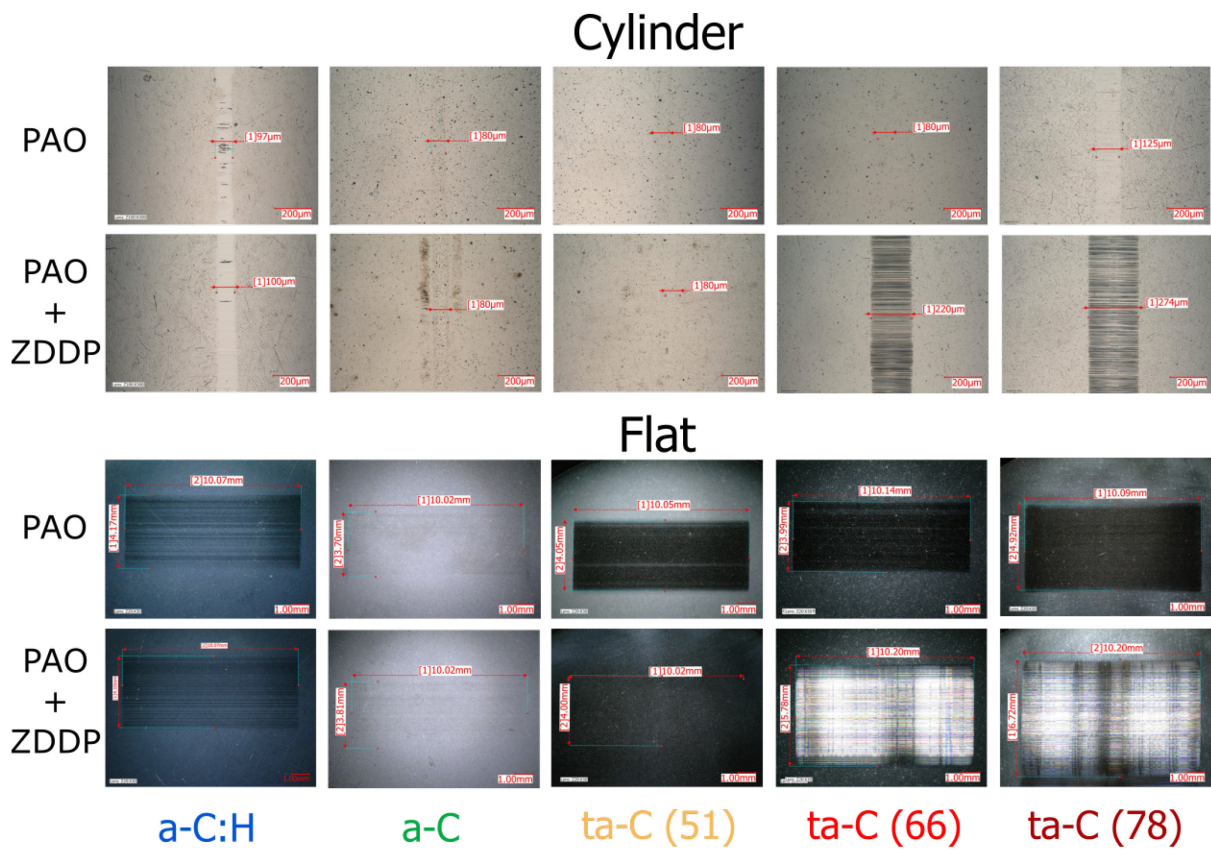


Figure 4. 3. Optical images of the wear tracks of the DLC-coated cylinders and discs after sliding tests.



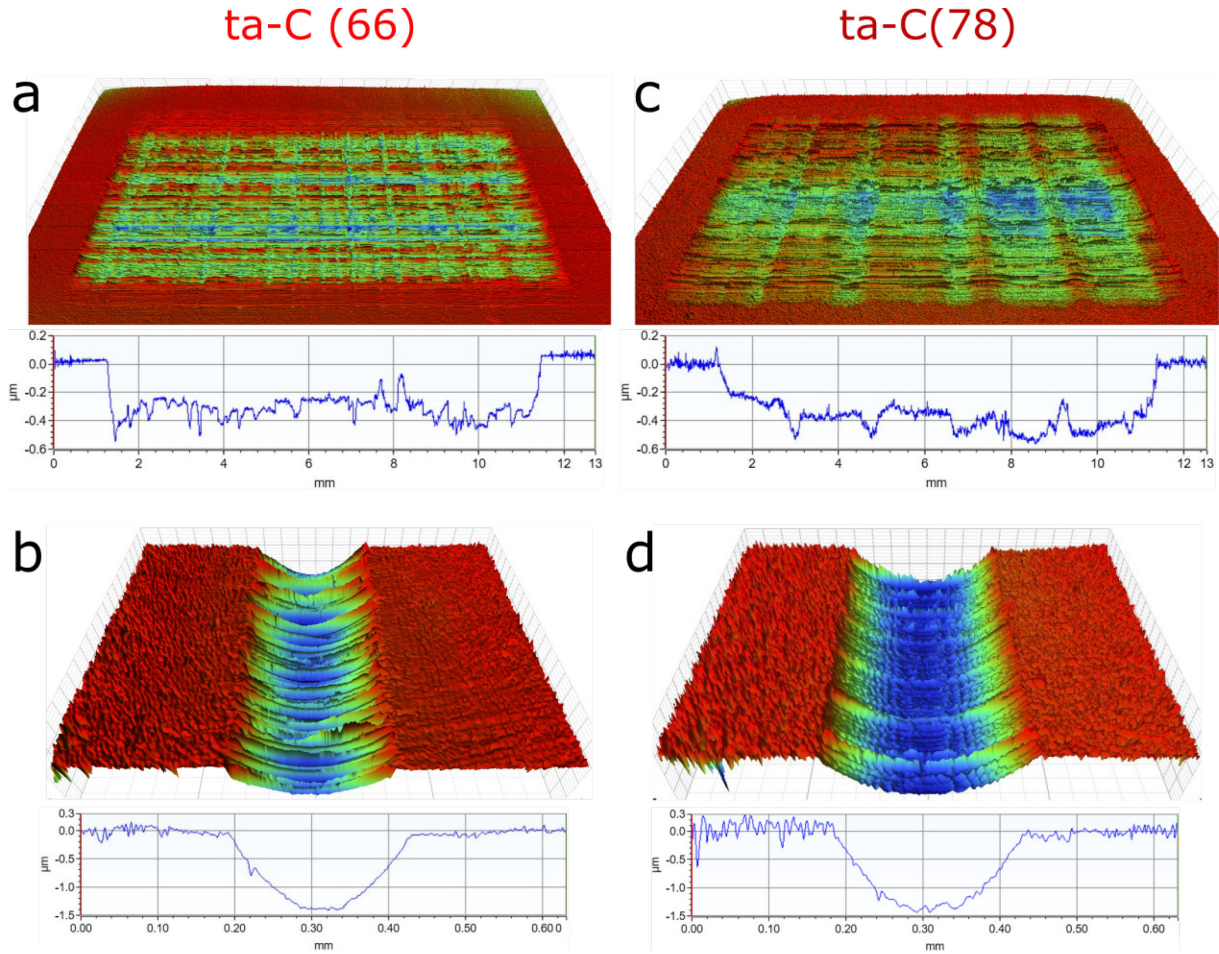


Figure 4. 4. Optical interferometer images of the wear tracks: (a-b) ta-C(66) flat and cylinder, (c-d) ta-C(78) flat and cylinder, respectively. The images of the cylinders are flattened in order to observe the wear volume.

### 4.3 Contact mechanics calculations

Our friction experiments are carried out with the same initial macroscopic cylindrical Hertzian contact pressure ( $P_{\text{Hertz}} = 210 \text{ MPa}$ ) for all tribo-pairs. However, the DLC coatings differ in their mechanical properties and surface topographies (

**Table 4. 2**) and thus local contact pressures  $P_l$  at the asperity level can be different. Here, we perform contact mechanics calculations using the numerical boundary element method with experimental surface topographies to estimate these effects at the nanoscale (see details in **Methods section 3.5.1**). Surface topographies of all five DLC coatings are measured by atomic force microscopy (AFM) with a scan area of  $20 \times 20 \mu\text{m}^2$  inside the wear tracks of the cylinders and discs after running-in. The AFM topographies of the cylinder and disc are brought into contact under an external pressure of 210 MPa. For the softer DLCs (a-C:H, a-C,

and ta-C(51)), the  $P_l$  probability density distributions have a high peak around  $P_l = 0$  and decay rapidly, with most asperities experiencing a  $P_l$  of less than a few GPa (**Figure 4.5a**). In contrast, the  $P_l$  distributions for ta-C(66) and ta-C(78) are broader and contact pressures  $P_l > 10$  GPa occur frequently.

**Figure 4.5b** shows the effective local contact pressure  $P_{l,eff}$  (as the median of the  $P_l$  distribution over all contact spots where  $P_l > 0$ ) as a function of a material parameter  $E^*h'_{rms}$  (the product of the contact modulus  $E^*$  and the RMS slope  $h'_{rms}$ , discussed later on). For ta-C(66) and ta-C(78),  $P_{l,eff}$  is 9.2 and 10.5 GPa, respectively. In contrast, for the three softer DLCs,  $P_{l,eff}$  values are in the range 1.7 – 3.5 GPa. Interestingly,  $P_{l,eff}$  for ta-C(51) is smaller than that for a-C (which has a larger  $h'_{rms}$ ). The monotonic increase in  $P_{l,eff}$  with  $E^*h'_{rms}$  indicates that  $P_{l,eff}$  is not only a function of the Young's modulus  $E$ , but also depends on surface topography.

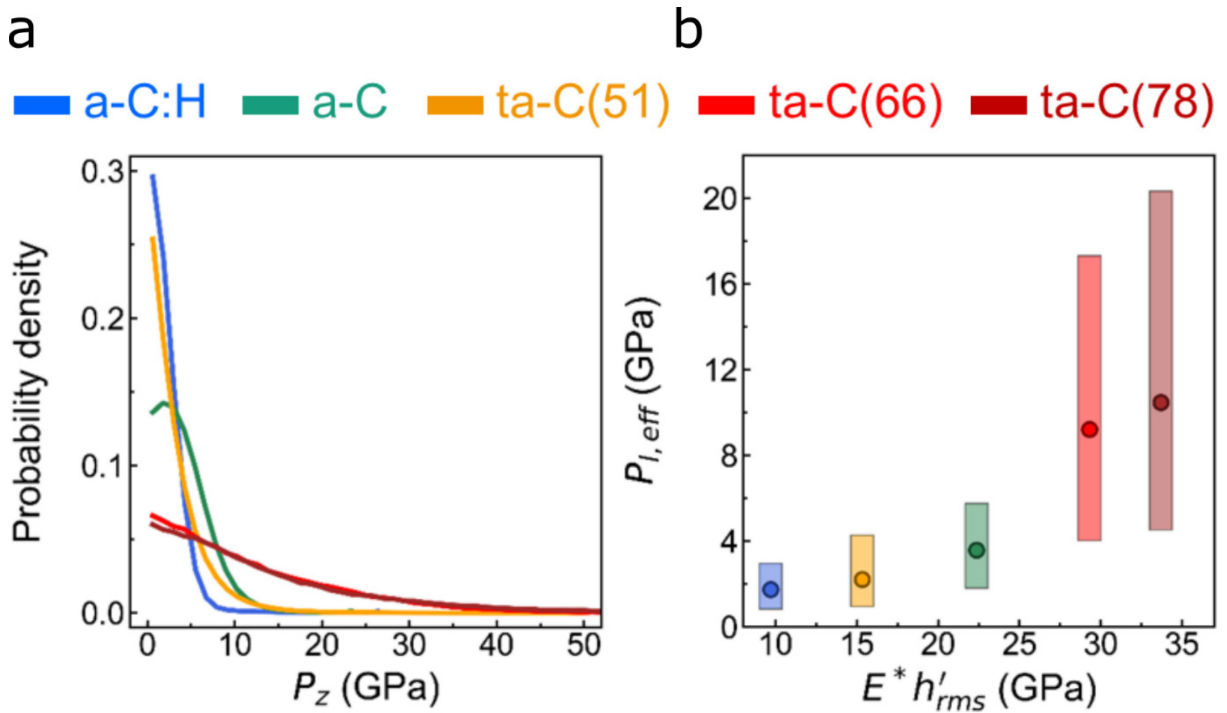


Figure 4.5: (a) Local contact pressure distributions calculated from contact mechanics calculations using AFM topographies measured inside the wear track after running-in (2000 cycles) with a scan area of  $20 \times 20 \mu\text{m}^2$ . (b) Effective local contact pressure  $P_{l,eff}$  as a function of  $E^*h'_{rms}$ , where  $E^*$  is the contact modulus and  $h'_{rms}$  is the combined root-mean-square slope between two DLC surfaces.  $P_{l,eff}$  is defined as the median over all nonzero  $P_l$  values and is obtained from a numerical boundary element solution of two experimental DLC topographies

under a normal pressure of 210 MPa. Filled circles mark the material parameter  $E^*h'_{rms}$  of each DLC coating. The boxes represent the range of the  $P_l$  distribution (limited by the 25th and 75th percentiles).

#### 4.4 XPS surface analysis

Surface chemical analyses are performed using X-ray photoelectron spectroscopy (XPS) inside and outside the wear tracks of the discs to study the mechanisms underlying the tribological behaviours of DLC surfaces under PAO+ZDDP lubrication. The binding energies (BEs) of the C1s, O1s, P2p, S2p and Zn2p<sub>3/2</sub> photo-peaks are analysed carefully (see **Methods 3.4.6** for details of the fitting procedure and XPS spectrometer). **Figure 4. 6** shows the relative chemical compositions estimated from XPS spectra in the topmost 10 nm of DLC surfaces on the discs. The ZDDP-derived elements, namely P, S, and Zn, are detected inside the wear tracks of all DLC surfaces, whereas very small traces (0.1-0.4 at. %) of these elements are found outside the wear tracks. The atomic concentrations of P, S, and Zn inside the wear tracks decrease in the order: a-C:H > a-C > ta-Cs. The precise elemental quantification results including C and O are given in **Table 4. 3**.

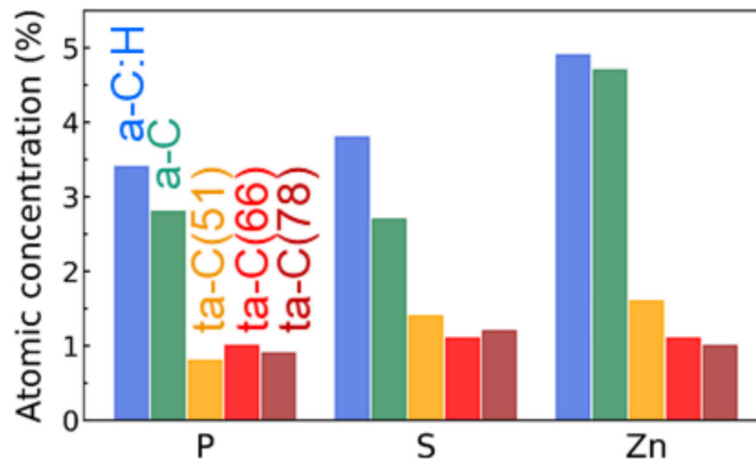


Figure 4. 6. Atomic concentrations of ZDDP-derived elements P, S, and Zn obtained from XPS spectra recorded on the DLCs flat after sliding tests in PAO+ZDDP.



Table 4. 3. Elemental quantification obtained from XPS spectra recorded on DLCs flats.

DLC	C (at. %)	O (at. %)	P (at. %)	S (at. %)	Zn (at. %)
a-C:H	73.6	14.3	3.4	3.8	4.9
a-C	77.2	14.9	2.8	2.7	4.7
ta-C(52)	86.6	9.6	0.8	1.4	1.6
ta-C(66)	87.5	9.4	1.0	1.1	1.1
ta-C(78)	87.9	9.0	0.9	1.2	1.0

The chemical states of C, O, P and Zn are practically undistinguishable between the five DLCs (see **Figure 4. 7**). C1s XPS spectra show the contribution of three types of chemical bonds: the first peak at  $BE = 284.8$  eV is attributed to both  $sp^2$  and  $sp^3$  carbon bonds in DLC as well as to adsorbed aliphatic carbon. The second and third peaks at  $BE = 286.5$  and  $288.3$ eV correspond to C–O and O–C=O bonds, respectively. O1s XPS spectra can be fitted using only two peaks: the first peak at  $BE = 531.7$  eV is attributed to non-bridging oxygen (NBO) and the second peak at  $BE = 533.0$  eV is attributed to bridging-oxygen (BO). P2p spectra are fitted with one doublet with a separation of 0.84 eV and intensity ratio of 0.5. The P2p<sub>3/2</sub> peak located at  $BE = 133.4$  eV corresponds to phosphates. The Zn2p<sub>3/2</sub> peak at  $BE = 1022.3$  eV corresponds to ZnS or Zn<sup>2+</sup> in zinc phosphates.

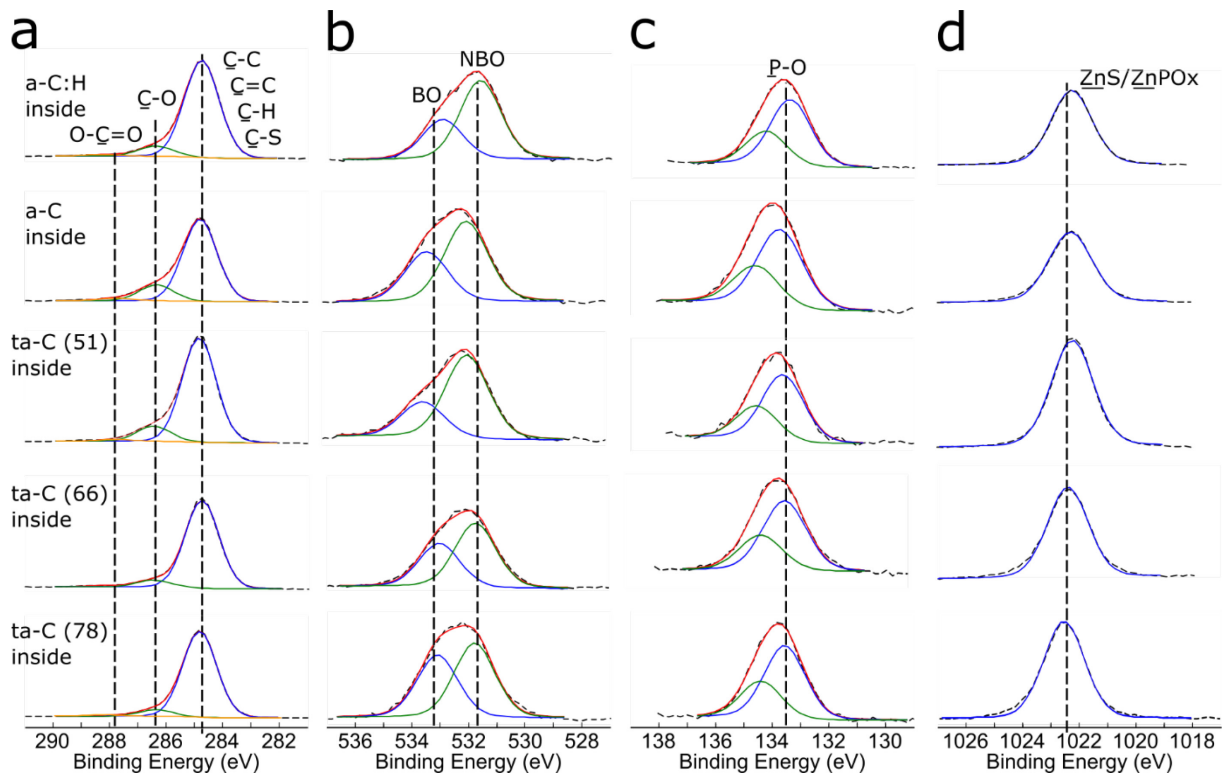


Figure 4. 7. (a) C1s, (b) O1s, (c) P2p, and (d) Zn2p<sub>3/2</sub> XPS spectra obtained from the DLCs flats after sliding tests in PAO+ZDDP.

For sulphur the situation is different, there are significant differences between the chemical states of the five DLCs. **Figure 4.8** shows the S2p XPS spectra inside and outside wear tracks on flat specimens. It should be noted that the vertical axis of the spectra are not included as the intensities of the peaks (in counts/second) between different samples are not directly comparable to one another. However, it may be observed that the raw signal (black-dashed curved) of the spectra outside the wear tracks are less smooth due to a lower signal-to-noise ratio.

Outside the wear tracks, similar S2p XPS spectra are observed for all DLC surfaces with a peak at  $BE = 162.4$  eV (right column of **Figure 4.8**), which is very close to that of sulphur in neat ZDDP ( $BE = 162.5$  eV). The other peak at  $BE = 168.5$  eV indicates the presence of sulphates (presumably due to thermal oxidation of DLC surfaces and subsequent chemisorption of ZDDP). In contrast, inside the wear track of a-C:H (left column of **Figure 4.8**), the S2p spectrum has one single component (in blue) at  $BE = 162.3$  eV corresponding to S–Zn<sup>70,87</sup>, or S–P and S=P in thiophosphates<sup>87</sup>. This peak is present also inside the wear tracks of the other DLCs, but the spectra contain another component (in red) at  $BE = 163.3$  eV corresponding to S–C bonds<sup>88</sup>. Note that C–S–H, C–S–C, or C–S–S–C bonding states are

very difficult to distinguish as their shifts in the BEs are only about 0.1 eV<sup>88</sup>. The other component for ta-Cs is attributed to a peak at  $BE = 167.9$  eV due to sulphur oxides<sup>89,90</sup>. Interestingly, the contribution from the S–C component at  $BE = 163.3$  eV is much smaller than the one at  $BE = 162.3$  eV for the a-C and ta-C(51), and thus sulphur in these coatings is preferentially bound to zinc and phosphorous (in the forms of S–P and S=P). In contrast, for ta-C(66) and ta-C(78), the red contribution at  $BE = 163.3$  eV is dominant, indicating the breaking of S–Zn, S–P and S=P bonds in the ZDDP molecule and the formation of S–C bonds. **Figure 4. 9** shows a clear correlation between the wear volume and S–C/S–Zn ratio. These results indicate that ZDDP is likely to stay intact on the softer three DLCs, whereas it undergoes decomposition on the hard ta-Cs.

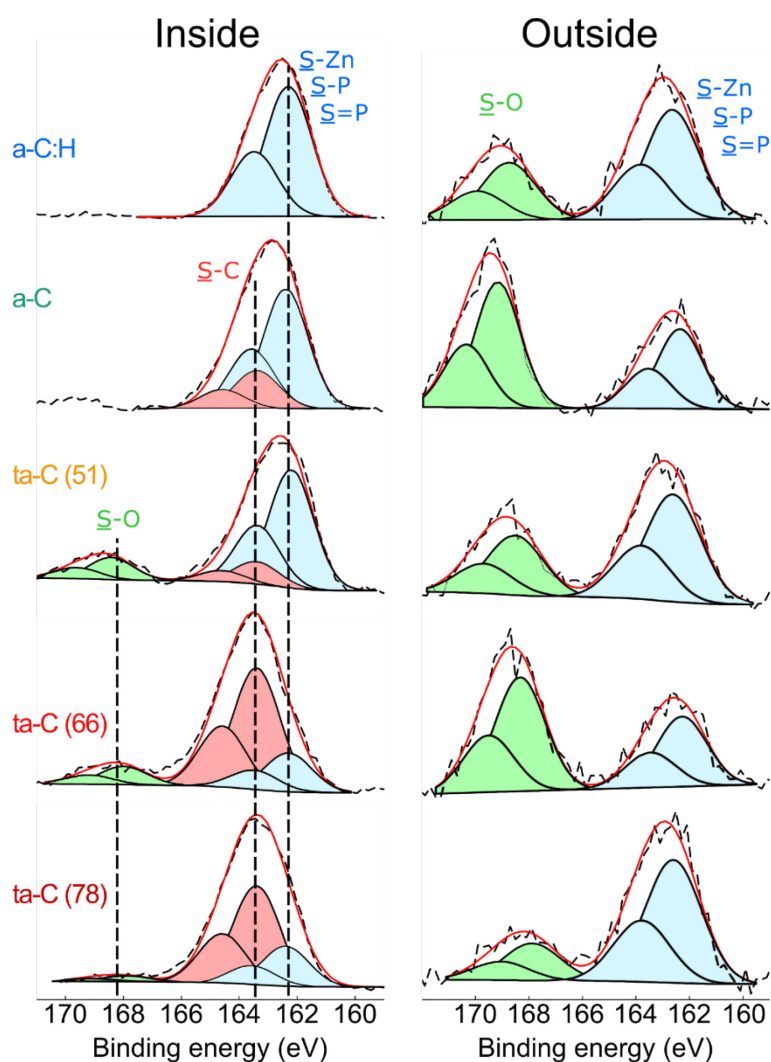


Figure 4.8. S<sub>2p</sub> XPS spectra inside (left) and outside (right) the DLCs wear tracks. They are fitted using a doublet due to spin-coupling with a separation of 1.2 eV and an intensity ratio of 0.5. Peak coloured in blue correspond to S–Zn or S–P bonds, while red and green peaks correspond to S–C and S–O bonds, respectively. The intensity of the S<sub>2p</sub> XPS spectra outside the wear tracks are magnified by a factor of 3 (for the ta-Cs) and a factor 10 (for a-C:H and a-C) to improve visibility.

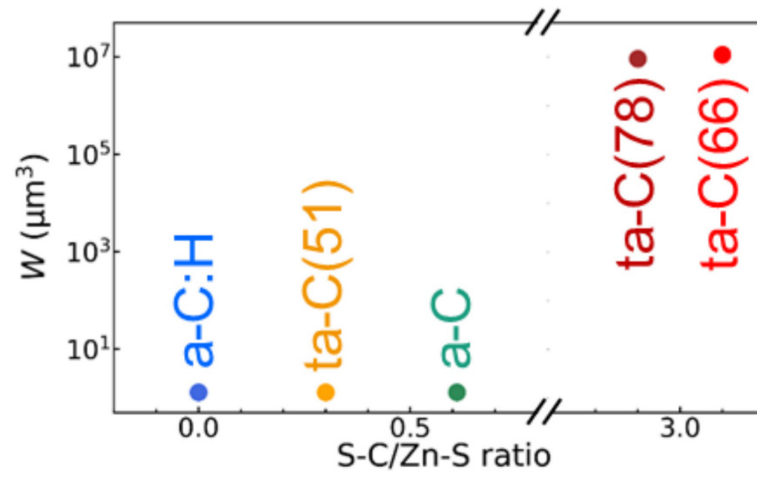


Figure 4. 9. Wear volume  $W$  as a function of the S-C/S-Zn ratio. For a critical value of the S-C/S-Zn ratio (located somewhere between 1 and 2.5) a transition from negligible to high wear can be observed.

## 4.5 Scanning and transmission electron microscopy characterisations

It is still not clear whether ZDDP-derived tribofilms form on DLC surfaces. Thicknesses, morphologies and chemical compositions of ZDDP-derived tribofilms are scrutinized using SEM, EDX and TEM (see **Methods 3.4.4 and 3.4.5**). **Figure 4. 10** shows representative SEM images of the five DLC surfaces after sliding in PAO+ZDDP solution. Tribofilms derived from ZDDP form on a-C:H, a-C, and ta-C(51) (**Figure 4. 10 a–c**), as evidenced by superimposing the chemical map of zinc (in green colour). For a-C:H, ZDDP-derived tribopatches are heterogeneous in size, ranging from 0.1 up to 5  $\mu\text{m}$  in diameter (**Figure 4. 10a**). For a-C, the tribopatches are more homogenous in size and distribution (**Figure 4. 10b**). For ta-C(51), tribopatches are found in the least amount (**Figure 4. 10c**), in agreement with the XPS results. For a-C:H and ta-C(51) the tribo-patches are found on the edges of the stroke, for a-C which is rougher the tribo-patches are formed along the entire wear track (see **Figure A. 2**). For ta-C(66) and ta-C(78), scratches are observed and no ZDDP tribo-patches are observed (**Figure 4. 10 d and e**). Instead, small ZDDP-derived particles (marked by green dots) are detected by punctual EDX spectra. EDX spectra (numbered 1-10) were recorded and are marked in green-dashed circles where tribo-patches are found and by red-dashed circles on the native DLC surface. The elemental quantification results are given in **Table 4. 4**.

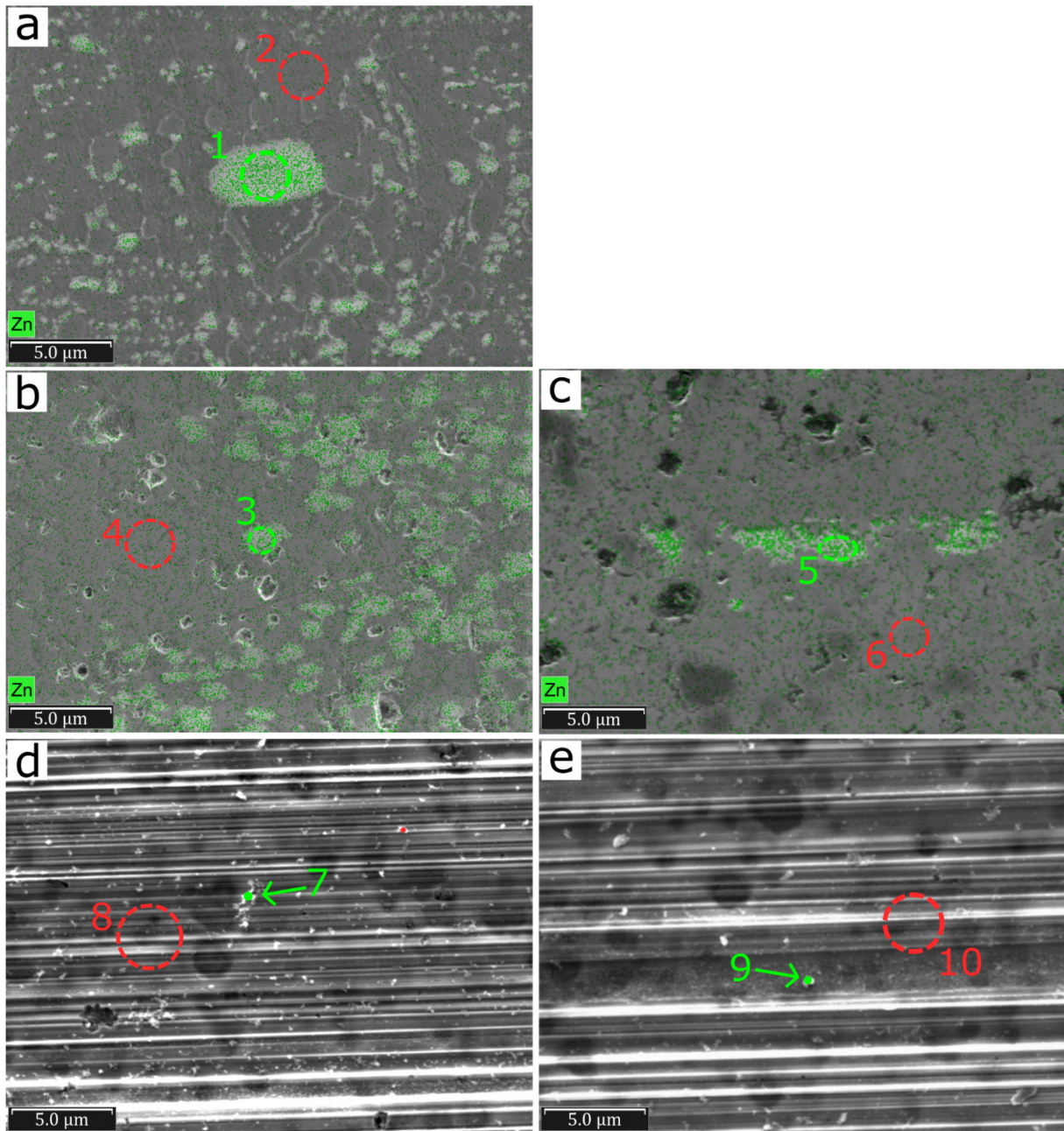


Figure 4. 10. Representative SEM images of DLC surfaces after sliding in PAO+ZDDP: (a) a-C:H, (b) a-C, (c) ta-C(51), (d) ta-C(66), and (e) ta-C(78). Zinc's chemical map is represented in green (panel a-c) and EDX spectra are indicated by green and red dashed circles or dots.

Table 4. 4. Elemental quantification obtained by EDX analysis of a-C:H and ta-C in the regions shown in Figure 4. 10 after tribological experiments in PAO+ZDDP.

Spectrum #	Chemical composition (at.%)				
	C	O	P	S	Zn

Spectrum 01	84.3	5.0	2.8	1.9	6.0
Spectrum 02	99.3	0.7	-	-	-
Spectrum 03	88.3	3.2	1.6	2.0	4.9
Spectrum 04	99.8	0.2	-	-	-
Spectrum 05	93.9	1.4	0.3	1.7	2.7
Spectrum 06	99.7	0.3	-	-	-
Spectrum 07	98.8	0.2	0.3	0.6	0.1
Spectrum 08	99.8	0.2	-	-	-
Spectrum 09	96.1	2.0	0.5	1.1	0.3
Spectrum 10	99.9	0.1	-	-	-

Cross-sections were prepared by Focus Ion Beam (FIB) and analysed by TEM and STEM. The a-C:H and ta-C(66) samples were chosen since the first exhibits no wear and the largest-tribopatches formation, while the latter undergoes severe wear and no visible tribo-patches are formed. For a-C:H, a bright-field (BF) TEM image reveals that the ZDDP-derived tribolayer (marked by a dashed green ellipse) is amorphous and discontinuous (**Figure 4. 11a**). Its thickness is about 20 nm, i.e. 5–10 times thinner than typical pad-like tribofilms on steel surfaces under similar sliding conditions<sup>77</sup>. **Figure 4. 11b** shows a high-angle annular dark-field (HAADF) image of the tribofilm and the chemical compositions in three different regions of interest (ROI) (marked by dashed boxes). The presence of O, S and Zn inside the tribofilm (ROI 1) is confirmed by elemental quantitative analyses and a combined EDX chemical mapping for Zn, Pt, and C (**Figure 4. 11c** and **Table 4. 5**). Note that phosphorus is not resolvable since its signal overlaps with the platinum signal. **Figure 4. 11d** shows a superposition of six individual BF-TEM images of the entire cross-section of the ta-C(66) sample (see **Figure A. 3** for a 2D SEM image of the area where the FIB cut was made) . There are two main features to be observed: on the right a large empty groove caused by wear and on the left a similarly large groove that has been filled by re-deposition of a wear particle that was smeared-in during sliding (both regions are indicated with arrows). There is a clear boundary line between the re-deposited wear debris and the ta-C bulk (**Figure 4. 11e**). Additionally, an asperity tip was formed by detaching from the rest of the particle due to plastic deformation (follow red-dashed arrow) and this lead to the formation and propagation of a crack (black color due to platinum infiltration during FIB preparation). Chemical information was obtained by EDX for ROI 4-8 in **Figure 4. 11f**. ROI 4-6 contain sulphur and

in fewer amounts zinc, ROI 7 and 8 contain mostly carbon and traces of oxygen, typical of the native ta-C. This indicates that sulphur is transported into the ta-C subsurface region. Interestingly, a higher magnification image (**Figure 4. 11g**) reveals that the sulphur-rich bright regions (4-6) undergo phase transformation and exhibit ordered graphitic structures (onion-like), which is consistent with a previous study by Berman et al. showing sulphur diffusion into diamond nanoparticles and subsequent formation of an onion-like structure<sup>91</sup>. Additional images of these graphitic/onion regions are given in **Figure A. 4**. Moreover, to further investigate this sulphur-doping phenomena, XPS profiles were acquired at different intervals of sputter time for a total duration of 20 minutes. For ta-C(66), the XPS spectra after 5-minute sputtering (corresponding to a sputter depth of about 0.5 nm<sup>92</sup>) remain similar to those before sputtering inside the wear track (**Figure 4.8**) and show the presence of significant amounts of S–C bonds (see **Figure A. 5**). In contrast, for a-C:H, no peaks attributed to S–C bonds are observed. This indicates that sulphur is present in the subsurface region of hard ta-Cs, but not of a-C:H.



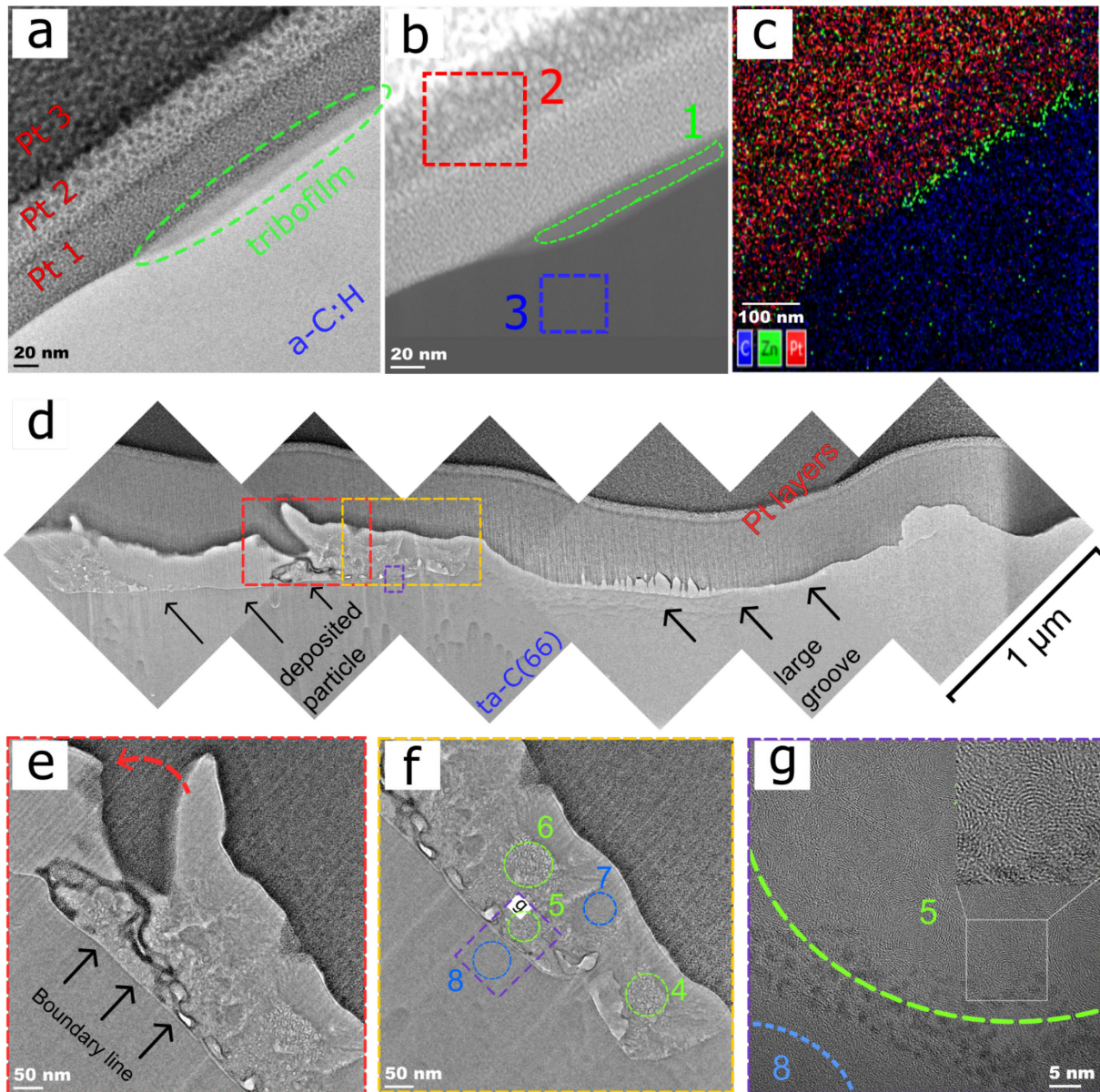


Figure 4. 11. (a) BF TEM image of the cross section of a-C:H surface after sliding. (b) HAADF image with recorded spectra from three different regions of interest (ROI). ROI 1: ZDDP-derived tribofilm, ROI 2: protective platinum layer, and ROI 3: a-C:H layer. (c) EDX map cartography superposition showing x-rays signal signatures of platinum (red), carbon (blue), and zinc (green). (d) Combined BF TEM images of the cross-section of ta-C(66) surface after sliding. (e and f) TEM images of a boundary between the smeared layer of redeposited wear debris and ta-C bulk (indicated in panel (d) by the red and yellow box for panel (e) and (f), respectively). In panel (f), the ROIs used for EDX analysis are specified. (g) A high magnification TEM image of the plastically transformed graphitic region (ROI 5) and native ta-C structure (ROI 8).

Table 4. 5. Elemental quantification of the spectra recorded in ROI 1–3 for a-C:H (Figure 4. 11b) and ROI 4–8 for ta-C(66) (Figure 4. 11f).

Label	ROI	Elemental quantification of the spectra (at.%)				
		C	O	S	Zn	Pt
a-C:H	1	65.7	22.0	5.1	5.0	2.2
	2	66.1	-	-	-	33.9
	3	100.0	-	-	-	-
ta-C(66)	4	94.7	2.8	1.2	1.3	-
	5	92.0	5.4	1.7	0.9	-
	6	93.7	4.6	1.1	0.6	-
	7	99.5	0.5	-	-	-
	8	99.3	0.7	-	-	-

## 4.6 Quantum chemical calculations

The experimental correlation between wear and the presence of S–C bonds (**Figure 4.8 and Figure 4. 11**) can be explained by weakening of ta-C matrices via incorporation of small amounts of sulphur (**Figure 4. 12**). We carry out MD homogeneous shearing simulations of sulphur-doped DLCs using a third-order density-functional tight-binding (DFTB3) method<sup>93</sup>. Lees-Edwards boundary conditions<sup>56</sup> are employed in this non-equilibrium MD simulations to impose a shear flow in a representative volume element of a bulk a-C, a-C:H and ta-C system (see **Methods 3.5.2** for the details of sample preparation).

For all three systems, the average shear stress  $\tau$  (the yield stress) decreases with increasing sulphur concentration  $C_S$  (**Figure 4. 12b**). While  $\tau$  is almost identical for a-C and a-C:H, it is larger for ta-C (as expected). For a-C:H and a-C (red and blue curves in **Figure 4. 12b**, respectively), the yield stresses at  $C_S = 0$  at.% are about 11 – 12 GPa and almost the same as that at  $C_S = 8$  at.% for ta-C (green curve in **Figure 4. 12b**). Thus, significant sulphur doping of the hardest ta-Cs can lower their yield stresses making the resulting sulphur-carbon phase much weaker than pure a-C:H and a-C.

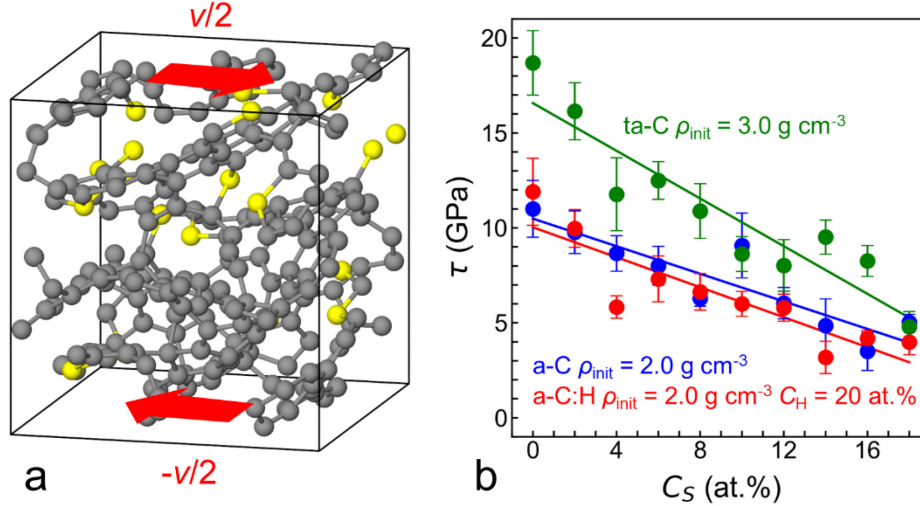


Figure 4. 12. DFTB3 quantum MD simulation of sulphur doped DLCs subject to homogeneous shear deformation. (a) Atomic configuration at  $t = 50$  ps for a-C with an initial density of  $2.0 \text{ g cm}^{-3}$  and 8 at.% S. Carbon atoms are represented by grey and sulphur atoms by yellow spheres. A shear velocity of  $v = 100 \text{ m s}^{-1}$  is imposed along the x direction (as shown by red arrows) with Lees-Edwards boundary conditions. (b) Shear stresses  $\tau$  as a function of the sulphur concentration  $C_S$  in ta-C with an initial density  $\rho_{\text{init}} = 3.0 \text{ g cm}^{-3}$ , in a-C with  $\rho_{\text{init}} = 2.0 \text{ g cm}^{-3}$ , and in a-C:H with  $\rho_{\text{init}} = 2.0 \text{ g cm}^{-3}$  and 20 at.% hydrogen.  $\tau$  is calculated every 10 ps and averaged for 50-ps MD runs. Error bars represent standard error of means.

But how does sulphur doping occur and how do reactions of ZDDP depend on coating properties such as stiffness, surface topography and chemical structure? Our experiments and contact mechanics calculations indicate that local contact pressures between surface asperities varies with the contact Young's modulus  $E^*$  and RMS slope  $h'_{\text{rms}}$  of the coatings. The differences in both the local contact pressure and surface reactivity of the DLC surfaces may trigger different mechanochemical reactions of ZDDP and thus influence the macroscopic tribological behaviour. Thus, additional simulations are performed in order to elucidate the dependence of ZDDP decomposition reactions on the contact pressure and the chemical structure of DLC coatings. Tribocontacts between DLC surfaces in presence of ZDDP are modelled using both quasi-static quantum-mechanical molecular statics (QMS) and QMD simulations (see **Methods 3.5.2** for computational details). Two types of DLC surfaces are considered: (i) an a-C:H with bulk density  $\rho = 2.0 \text{ g cm}^{-3}$  and hydrogen concentration  $C_H = 20$  at.% as well as (ii) an a-C with the same density  $\rho = 2.0 \text{ g cm}^{-3}$ . The a-C sample represents the near-surface-region of ta-C coatings, since ta-C is covered with a several-nm-thick a-C layer due to the nature of the deposition process<sup>94</sup> and a tribo-induced  $\text{sp}^3$ -to- $\text{sp}^2$  rehybridisation<sup>54</sup>.

**Figure 4. 13a** displays an initial configuration of the QMS system, where a ZDDP molecule with ethyl groups is positioned between two a-C:H surfaces. Here, unpassivated surfaces are considered since asperity collisions can remove terminating species mechanically, leaving behind reactive carbon atoms<sup>54</sup>. A full hydrogen passivation would inhibit reactions of ZDDP even under extremely high contact pressures ( $P_z > 10$  GPa) (Figure A. 6). As the two surfaces come gradually into contact, the ZDDP molecule reacts with the upper surface even at a low contact pressure ( $P_z \approx 0.1$  GPa). The reactions starts with the breaking of a Zn–S bond in the molecule and the formation of a S–C bond between the molecule and the upper surface (**Figure 4. 13b**). The second chemical bond forms between the Zn atom in the molecule and a C atom of the lower surface, resulting in the formation of a cross-linked configuration that bridges the tribogap at a slightly larger contact pressure  $P_z \approx 0.3$  GPa (Fig. 6c). At  $P_z = 5.1$  GPa, breaking of another Zn–S bond and formation of another S–C bond are observed (**Figure 4. 13d**). As the contact is reopened, the cross-linked ZDDP molecule is stretched (corresponding to negative contact pressures; see the grey line in **Figure 4. 13f**). This mechanical pulling induces breaking of a S–C bond on the lower surface and reforming of a Zn–S bond in the molecule, and eventually fragmentation of the ZDDP molecule into two smaller products (**Figure 4. 13e**). It is important to note that reactions of ZDDP on surfaces differ from those observed during simulations in the gas phase, where Zn–S bonds repeatedly break and form and ZDDP’s decomposition starts with the loss of alkyl groups<sup>95</sup>. On surfaces, breaking of Zn–S bonds is the first observed reaction because the formation of S–C bonds with C atoms on the surface prevents the reformation of the Zn–S bonds.

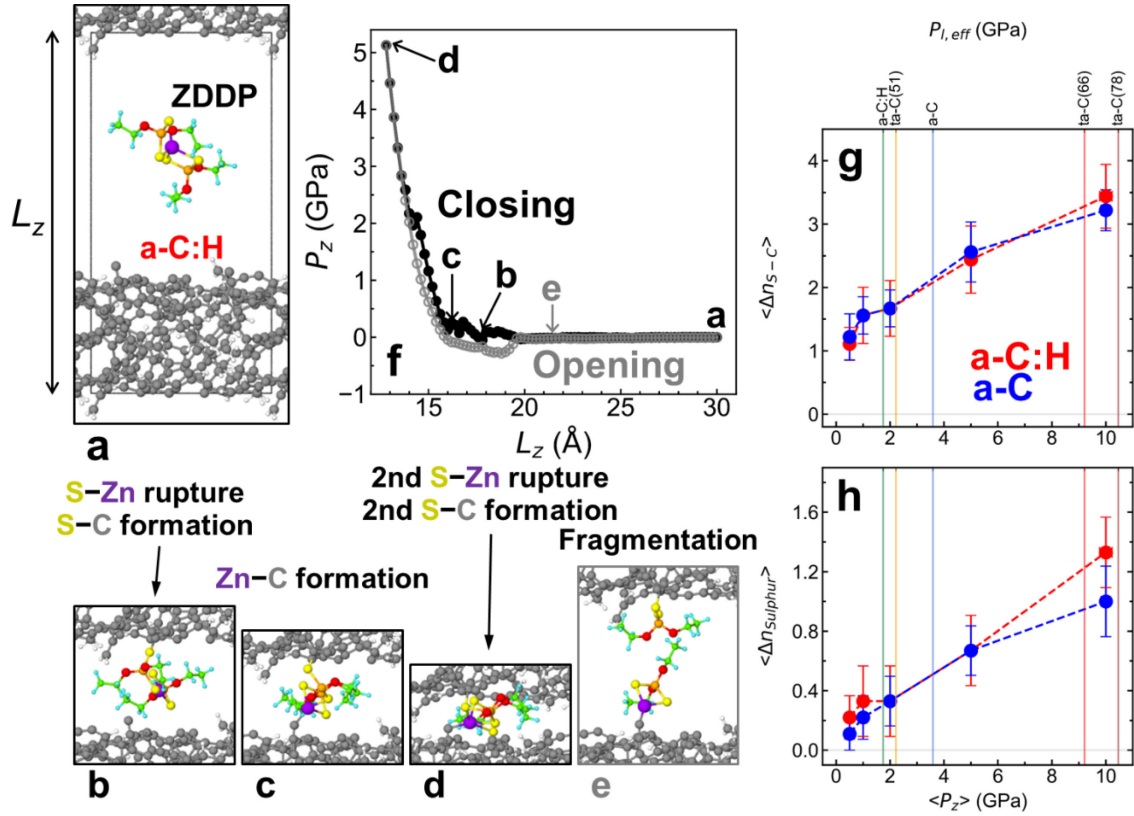


Figure 4. 13. Quasi-static contact-closing/opening simulations for a-C:H with  $\rho = 2.0 \text{ g cm}^{-3}$  and  $C_H = 20 \text{ at.}\%$  and a-C with  $\rho = 2.0 \text{ g cm}^{-3}$  in contact with a ZDDP molecule using DFTB3 quantum chemical calculations. (a) Initial configuration and (b)–(e) evolution of atomic configurations for a representative trajectory of a-C:H. (f) Evolution of the normal pressure  $P_z$  as a function of the z system dimension  $L_z$  during the closing (black discs) and opening process (grey circles). For C and H, different colours are assigned between the surface atoms (grey for C and white for H) and atoms in the ZDDP molecule (green for C and cyan for H). Zn, S, P, and O are represented by violet, yellow, orange, and red spheres, respectively. The  $L_z$  values and corresponding normal pressures of the snapshots (a)–(e) are indicated by labels in panel (f). (g) Averaged numbers of S–C bonds ( $\langle \Delta n_{S-C} \rangle$ ) formed between ZDDP sulphur and DLC carbon atoms as well as (h) sulphur atoms released from ZDDP ( $n_{\text{Sulphur}}$ ) to the DLC after reopening the contact as a function of the contact pressure  $P_z$  for a-C:H with  $\rho = 2.0 \text{ g cm}^{-3}$  and  $C_H = 20 \text{ at.}\%$  (red) and a-C with  $\rho = 2.0 \text{ g cm}^{-3}$  (blue). The error bars represent standard error of the means. The vertical lines mark the effective local contact pressures  $P_{l,eff}$  for the five experimental coatings (**Figure 4.5b**).

Bond-breaking and -forming processes of ZDDP are strongly affected by the contact pressure but not by the chemical structure of the DLC surfaces. **Figure 4. 13g** shows the contact pressure dependence of chemical reactions of ZDDP squeezed quasi-statically between two a-C and two a-C:H surfaces. The values  $\langle n_{S-C} \rangle$  on the vertical axis represents the average number of bonds between sulphur and DLC carbon atoms that remain intact after reopening the contacts. Our simulations reveal that the formation of S–C bonds is the most dominant chemical reaction, which is in agreement with our XPS results (**Figure 4.8**). While  $\langle n_{S-C} \rangle$



increases with contact pressure  $P_z$  ( $0.5 \leq P_z \leq 10$  GPa), the pressure dependence of  $\langle n_{S-C} \rangle$  in a-C:H and a-C is almost identical. For both DLC surfaces, chemical reactions of ZDDP follow the scenario described in **Figure 4. 13**. At  $P_z \lesssim 2$  GPa, most ZDDP molecules chemisorb without decomposition (**Figure 4. 13b**) or decompose into two fragments by breaking of Zn–S bonds. A further increase of the contact pressure induces decomposition of ZDDP into atoms and small fragments.

Only sulphur atoms that are effectively released onto the DLC surface are relevant to the weakening of the DLC presented in **Figure 4. 12**. Therefore, we next calculate the average number of sulphur atoms  $\langle n_{Sulphur} \rangle$  that are not bound to any atoms in ZDDP and remain chemisorbed on the DLC surface after reopening the contact (see **Figure 4. 13h**). As already observed for  $\langle n_{S-C} \rangle$ ,  $\langle n_{Sulphur} \rangle$  increases significantly with  $P_z$  and no difference between a-C:H and a-C is detectable (**Figure 4. 13h**). Even though the a-C systems used here are representative of the surface region of ta-C, which typically has a low  $sp^3$  content of about 10 %<sup>54</sup>, we performed a comparison between ta-C with high  $sp^3$  percentages  $p_{sp^3}$  (ranging from 48–67%) and a-C with  $p_{sp^3} = 2 - 9\%$  and observed that  $\langle n_{S-C} \rangle$  and  $\langle n_{Sulphur} \rangle$  are not significantly affected by the  $sp^3$  content of the hydrogen-free DLC surface (see **Figure A. 7**).

Next, we perform QMD sliding simulations to explore the role of shearing (**Figure 4. 14**). A DLC/ZDDP/DLC tribo-interface is studied at a sliding velocity of  $30 \text{ m s}^{-1}$  and various  $P_z$  values (see snapshots for  $P_z = 10$  GPa in **Figure 4. 14b and c**). After 0.2 ns sliding, the two DLC surfaces are separated quasi-statically to ensure the consistency with the QMS results. For both a-C and a-C:H  $\langle n_{Sulphur} \rangle$  increases about 2–3 times at all  $P_z$  compared with  $\langle n_{Sulphur} \rangle$  in QMS simulations and the effect of the DLC’s chemical structure on the effective number of sulphur atoms left on the surface is not significant (except for  $P_z = 2$  GPa) as shown in **Figure 4. 14a**.

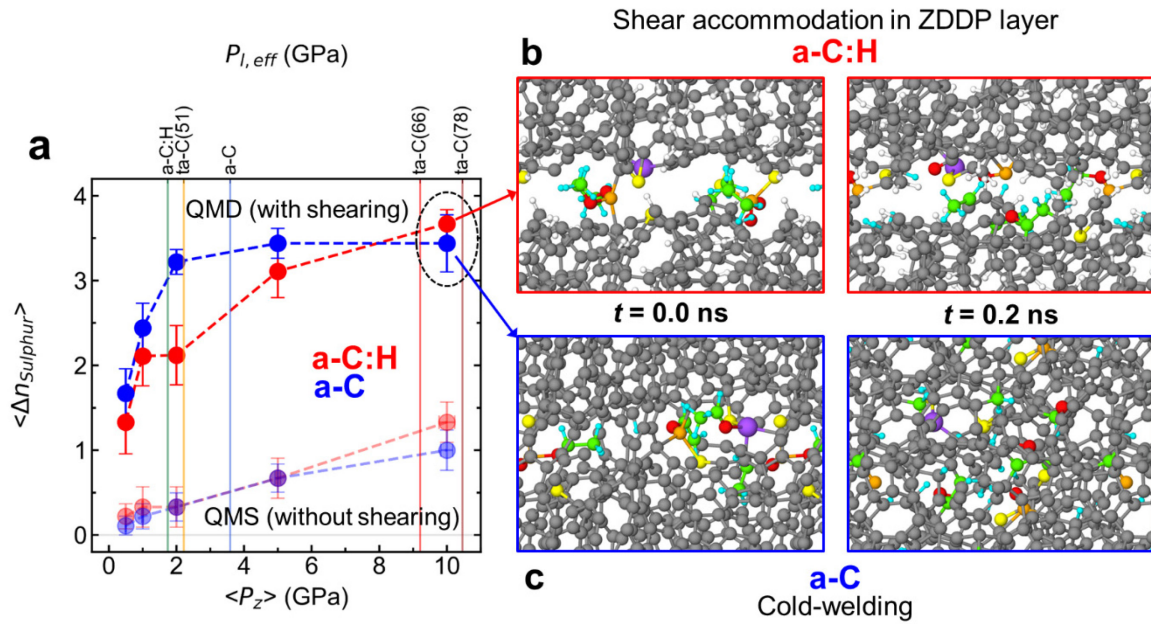


Figure 4. 14. DFTB3-MD sliding simulations of a-C:H and a-C in contact with a ZDDP molecule. A shear velocity of  $30 \text{ m s}^{-1}$  is imposed along the x direction using Lees-Edwards boundary conditions. The system temperature is kept constant at  $T = 300 \text{ K}$ . (a) Averaged numbers of sulphur atoms ( $n_{\text{Sulphur}}$ ) released from ZDDP to DLC after reopening the contact as a function of the contact pressure  $P_z$ . The error bars represent standard error of the means. The vertical lines mark the effective local contact pressures  $P_{l, \text{eff}}$  for the five experimental coatings (Figure 4.5b). As references,  $\langle n_{\text{Sulphur}} \rangle$  for quasi-static calculations with no shear (Figure 4. 13g) are depicted with semi-transparent markers. Representative snapshots of DLC surfaces at  $P_z = 10 \text{ GPa}$  for (b) a-C:H and (c) a-C. The left and right pictures in panel (b) and (c) show configurations at  $t = 0.0$  and  $0.2 \text{ ns}$ , respectively.

Thus, the chemical difference between a-C:H and ta-C, i.e. presence or absence of hydrogen, hardly affects the kinetics of ZDDP's decomposition. The local contact pressures alone determine the chemical state of sulphur on the different DLC surfaces. However, the DLC's chemical structure affects shear accommodation in the DLC/ZDDP/DLC interface at high contact pressures. Similar surfaces functionalized with ZDDP-derived fragments form at small contact pressures ( $P_z \lesssim 5 \text{ GPa}$ ) on a-C:H and a-C (Figure A. 8), whereas a clear structural difference is observed at  $P_z = 10 \text{ GPa}$  (Figure 4. 14b and c). While a layer of ZDDP-derived fragments still accommodates shear on a-C:H, the a-C surfaces are cold-welded (Figure 4. 14c and supplementary movies 1 and 2). In this case, ZDDP-derived atoms/fragments diffuse underneath the surface as a result of mechanical mixing.

Figure 4. 15 provides further statistical evidence that the chemical difference between the DLC surfaces (i.e. the hydrogen concentration) has a significant effect on the shear response of the frictional interface. First, the weakest interface in each final configuration after MD

sliding is determined and then the number of cold-welding C–C bonds  $n_{C-C}^{CW}$  within this interface is calculated. Averaging over different MD runs yields the mean density of cold-welding C–C bonds  $\langle n_{C-C}^{CW} \rangle$  for a-C:H and a-C (**Figure 4. 15a**).  $\langle n_{C-C}^{CW} \rangle$  is almost equal to zero at  $P_z \lesssim 2$  GPa for both a-C:H and a-C, indicating the presence of a sliding interface with no significant cold welding. However,  $\langle n_{C-C}^{CW} \rangle$  increases drastically for a-C at  $P_z \gtrsim 5$  GPa, which is a typical contact pressure range reached only by ta-C(66) and ta-C(78) in our experiments (as shown by the vertical lines of **Figure 4. 15a**). In this case, the cold welding and shear-induced plastic flow increase the mobility of atoms and induce chemical mixing of the contaminated a-C surfaces. **Figure 4. 15b and c** clearly show that the depth distribution (z-axis profile) of the sulphur density at  $P_z = 10$  GPa is significantly broadened for a-C, while sulphur is still localized at the surfaces for a-C:H.

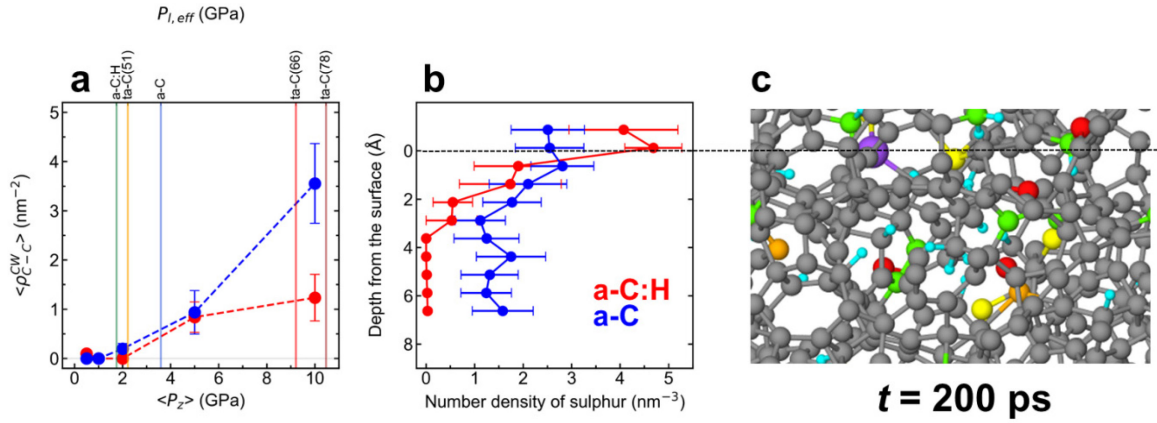


Figure 4. 15. (a) Mean bond densities of cold-welding C–C bonds  $\langle n_{C-C}^{CW} \rangle$  at  $t = 0.2$  ns. The error bars represent standard error of the means.  $n_{C-C}^{CW}(z)$  is defined as the number of C–C bonds across a x-y plane at height  $z$ . For each system, the minimum values  $n_{C-C}^{CW} = \min_z n_{C-C}^{CW}(z)$  (corresponding to a shear interface) is searched with a step of  $\Delta z = 0.5$  Å. (b) Depth profile of the number density of sulphur  $\rho_{Sulphur}$  (nm<sup>-3</sup>) averaged over the last 0.1 ns MD runs at  $P_z = 10$  GPa. (c) Example of a chemically mixed a-C layer at  $t = 0.2$  ns. The horizontal dashed line represents an initial a-C surface before sliding.

## 4.7 Discussion

In this study, a combined experimental and multiscale modelling approach reveal the crucial impact of both contact mechanics of surface asperities and chemical structure of DLC coatings on the tribochemistry of ZDDP decomposition and, in turn, on the different macroscopic tribological behaviours of DLC coatings in boundary lubrication with a ZDDP-additivated base oil (see **Figure 4. 16** for a schematic representation of our findings). While



the macroscopic cylindrical Hertzian contact pressure is identical (in all our experiments  $P_{\text{macro}} = 210$  MPa), the nanoscale mechanical response of surface asperities to the normal load varies with contact modulus  $E^*$  and RMS slope  $h'_{\text{rms}} = \langle |\nabla h|^2 \rangle$  of the coatings. According to Persson's contact mechanics theory<sup>44,96</sup>, the average local contact pressure for small  $P_{\text{macro}}$  is given by  $\langle P_l \rangle = \frac{h'_{\text{rms}} E^*}{\kappa}$  with the contact modulus  $E^* = \frac{1}{2} \frac{E}{1-\nu^2}$  and the combined RMS slope of the two surfaces  $h'_{\text{rms}} = \sqrt{(h'_{\text{rms,cylinder}})^2 + (h'_{\text{rms,disc}})^2}$ . When the pressure distribution follows a Rayleigh formula<sup>96</sup>,  $\kappa$  is equal to  $\sqrt{\frac{8}{\pi}} \approx 1.6$  and the median  $P_{l,\text{eff}}^{\text{Persson}}$  can be also analytically calculated by  $\sqrt{\frac{\ln 2}{2}} h'_{\text{rms}} E^* \approx 0.59 h'_{\text{rms}} E^*$  (irrespective of  $P_{\text{macro}}$ ). A linear fitting of  $P_{l,\text{eff}}$  obtained from our contact mechanics calculations gives a slope of 0.4 that is lower than the theoretical one. While this can be probably attributed to the lower degree of self-affinity of our DLC surfaces with respect to the theory and to overestimation of  $h'_{\text{rms}}$  due to the presence of holes, Persson's theory provides the rationale behind the results of our contact mechanics calculations. Interestingly, the ordering in  $P_{l,\text{eff}}$  between a-C and ta-C(51) is an example showing that  $P_{l,\text{eff}}$  depends on both contact stiffness and topography of the DLC surfaces. While ta-C(51) is much stiffer than a-C,  $h'_{\text{rms}}$  for ta-C(51) is almost half of that for a-C. This smaller  $h'_{\text{rms}}$  for ta-C(51) can decrease the effective local contact pressure  $P_{l,\text{eff}}$  compared with a-C, which is in excellent agreement with the experimental results in the S-C/S-Zn ratio (**Figure 4. 9**).

Our results suggest that the effective local contact pressure  $P_{l,\text{eff}}$  represents a crucial parameter to determine the kinetics of ZDDP decomposition as well as the wear and friction regime. For soft DLCs (such as a-C:H, a-C, and ta-C(51)), at  $P_{l,\text{eff}} \lesssim 3$  GPa, ZDDP chemisorbs on the surfaces by breaking of Zn-S and formation of Zn-C bonds and undergoes decomposition into zinc- and dithiophosphates (**Figure 4. 16a**). An anti-wear tribofilm, consisting of zinc polyphosphates, can grow via accumulation and subsequent cross-linking of such precursors<sup>84</sup>. During the tribofilm growth, the formation of a narrow shear zone in ZDDP-derived layers inhibits weakening of DLCs by mechanical mixing. Eventually, nanoscale patchy anti-wear tribofilms form on the surfaces. Conversely,  $P_{l,\text{eff}}$  exceeds 9 GPa on hard ta-Cs and such high local contact pressures aggressively promote fragmentation of ZDDP (**Figure 4. 16b**). Mechanochemical sulphur doping of the sub-surface region becomes prominent and weakens the carbon matrix via mixing under shear, resulting in massive wear

of ta-Cs. The difference in the wear volume between a-C:H and hard ta-Cs is consistent with previous experiments<sup>68</sup>. Interestingly, the effective local contact pressure  $P_{l,eff}$  (Fig. 1f) is consistent with contact pressures for single-asperity sliding contact of DLC/steel where tribofilm growth was observed<sup>79</sup>. Since  $P_{l,eff}$  is estimated as the median of all the local contact pressures in the real contact area from contact mechanics calculations, and thus characteristic of asperity-asperity contacts, this consistency suggests that the use of  $P_{l,eff}$  can fill the gap between atomic and macroscopic experimental scales. The effective local pressure is determined by the contact parameter  $E^*h'_{rms}$ . Therefore, a direct link between the coatings' properties and ZDDP's tribochemistry as well as the DLCs' macroscopic tribological behaviour can be established. When  $E^*h'_{rms}$  exceeds a critical value ( $\sim 25$  GPa), tribofilm formation is replaced by sulphur doping (Figure 4. 16).

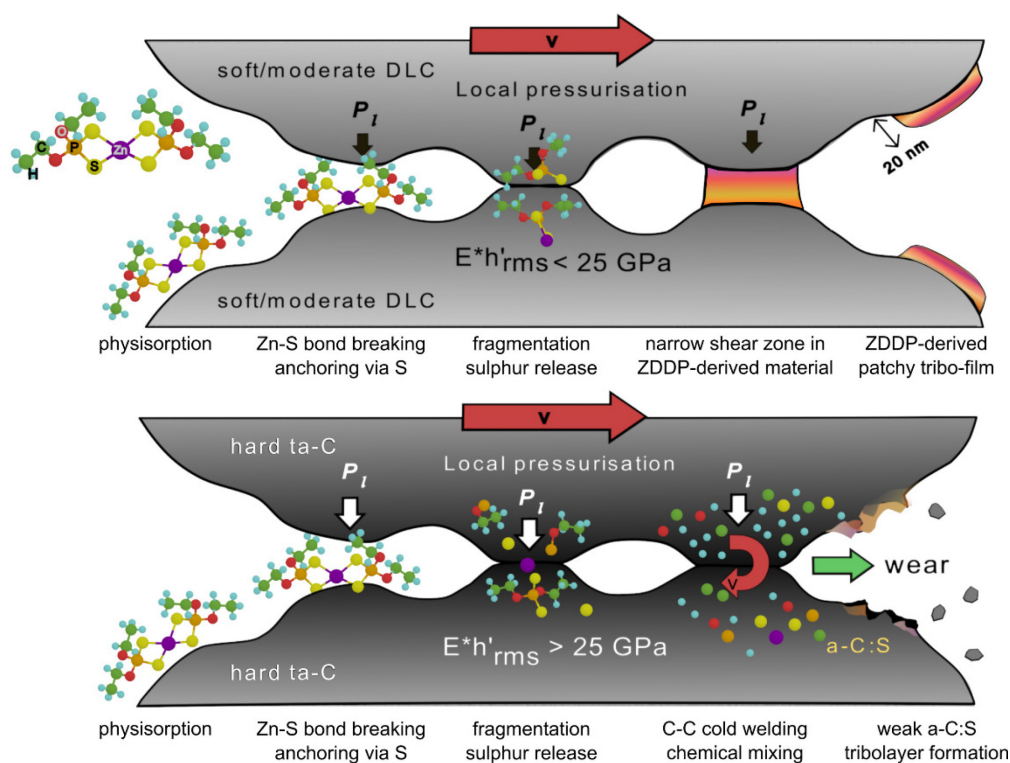


Figure 4. 16. Schematic representation of likely scenarios (a) for formation of ZDDP-derived patchy anti-wear tribofilms on soft DLC coatings (when  $E^*h'_{rms} < 25$  GPa) and (b) for wear of hard ta-C coatings lubricated by a ZDDP-additivated oil.

In addition to contact pressure, mechanical stimuli by shear stress play a decisive role in lowering the activation barrier for chemical reactions of ZDDP and increasing the accessibility of reactive sites. Moreover, shear action at high contact pressures ( $P_l > 5$  GPa) makes the effect of the DLC's chemical structure (i.e. presence or absence of hydrogen) apparent. At low contact pressures ( $P_l < 5$  GPa), irrespective of presence or absence of

hydrogen, shear can be accommodated in a narrow region consisting of ZDDP-derived species. However, at  $P_1 > 5$  GPa, for a-C and ta-Cs, the separation between two surfaces is insufficient to localize shear in the ZDDP-derived tribolayer, and cold welding via C–C bonds (bridging the two surfaces) takes place.

Under shear, mechanical mixing of the cold-welded surfaces induces sulphur doping into the subsurface regions resulting in significant weakening of the material and wear. This process is mechanically driven and leads to a non-equilibrium state with low shear resistance that accommodates the shear deformation. As typical of other mechanically driven tribological processes<sup>53,97</sup>, this metastable material is higher in energy than the original one and sulphur penetration cannot be described thermodynamically. In contrast, on a-C:H, the ZDDP chemisorbed layer is able to support the high contact pressure ( $P_1 > 5$  GPa) due to steric hindrance between surface hydrogen atoms (this would most likely occur also for a hard ta-C:H despite the high contact pressure). Thus, since  $P_{1,eff} \lesssim 3.5$  GPa for a-C:H, a-C and ta-C(51), soft DLC surfaces are likely to remain intact, and the accumulation of ZDDP-derived species can lead to the growth of anti-wear tribofilms irrespective of the chemical difference of the DLC coatings.

## 4.8 Summary and Conclusions

In summary, our friction experiments combined with surface analyses and contact mechanics calculations suggest that friction and wear of DLCs in PAO+ZDDP depend on asperity-scale contact pressures. For softer DLCs, the majority of asperities experience mild local contact pressures (less than a few GPa), which seems to be sufficient for the growth of a 20-nm-thick, patchy tribofilm but insufficient for the complete decomposition of ZDDP. In contrast, for harder DLCs, higher effective local contact pressures ( $P_{1,eff} > 9$  GPa) might promote breaking of Zn–S bonds in ZDDP and preferential formation of S–C bonds, accompanied by penetration of sulphur into the sub-surface region and massive wear.

In conclusion, this study sheds light on hitherto unknown multiscale physical processes and reveals how the interplay of mechanical, topographical and chemical factors determine the tribological behaviour of DLC coatings under lubrication with a ZDDP-additivated base oil. We find a knowledge-based design recipe for DLC coatings (hydrogen-free and of moderate

hardness) that are wear resistant in ZDDP-additivated oils while still inducing ultralow friction.

Furthermore, the insights into the fundamental mechanochemistry of ZDDP and the interplaying role of mechanics and chemistry could be transferable to ferrous or other non-ferrous/metallic lubrication systems. Hopefully, this study will pave the way for further studies aiming at finding FMs and lubrication configurations/conditions that improve the wear and friction performance of DLC/ZDDP systems and, more in general, at controlling tribochemistry of additives by tuning microscopic contact mechanics and surface chemical structure. Such studies could facilitate the alternative formulation of less harmful anti-wear additives that protect iron and DLC surfaces simultaneously.

---

# Chapter 5: Effect of mechanical and chemical parameters on the behavior of DLC/ZDDP systems

---

In the previous chapter, it was shown that hard ta-Cs exhibited severe wear and rise of  $\mu$  in ZDDP-solution, whereas soft and moderate hard DLCs did not. From the differing experimental results found in the scientific literature, it is clear that the tribological behavior of DLC coatings varies greatly depending on the environment and test conditions. In this chapter, different parameters such as surface roughness, sliding speed, contact pressure, counterpart material, and chemistry of the additives used to study their influence on the friction and wear properties of DLC/ZDDP systems to better predict and control them.

## 5.1 Effect of surface roughness.

### 5.1.1 Introduction

It is generally agreed that smoother surfaces lead to lower friction coefficient and wear. It is important to acknowledge that most DLC deposition processes lead to rough surfaces due to growth defects in the form of protrusions, often also referred to as “droplets”. During sliding, these defects may detach from the surfaces and effectively act as abrasive particles on the sliding interface between the two bodies leading to wear. It is surprising that this very important factor is often overlooked and it is not uncommon to find studies where different DLCs with different surface roughness are being compared.

To study the effect of the initial roughness of ta-C(66) coatings, sliding tests were performed with smooth and rough samples for comparison. Smooth surfaces ( $R_{a \text{ initial}} = 10 \text{ nm}$ ) were obtained by performing the standard polishing procedure of ta-C coatings described in **section 3.1.1** (lapping with diamond slurry for the flat, and industrial polishing procedure for the cylinder). “Rougher” surfaces ( $R_{a \text{ initial}} = 25 \text{ nm}$ ) were obtained by shortening the duration of the polishing procedure. The test conditions given in **Methods 3.3.1** are reminded in **Table 5.1**.

Table 5. 1. Test parameters used in the reciprocating sliding tests.

Test conditions
<ul style="list-style-type: none"><li>• Contact = cylinder-on-disk</li><li>• <math>F_N = 23 \text{ N}, 50 \text{ N}</math></li><li>• <math>P_{\text{Hertz}} = 210 \text{ MPa}, 300 \text{ MPa}</math></li><li>• <math>T = 110^\circ\text{C}</math></li><li>• <math>v = 0.1 \text{ m s}^{-1}, 0.05 \text{ m s}^{-1}</math></li><li>• <math>l = 10 \text{ mm}</math></li><li>• <math>t = 90 \text{ min (2,700 cycles)}</math></li></ul>

#### 5.1.1.1 Friction and wear results

**Figure 5. 1** shows the friction curves of ta-C(66)/ta-C(66) tribopairs in PAO base oil with different surface roughnesses. The smooth ta-C surfaces exhibit a steady friction coefficient of 0.02 after a short running-in period (a few hundred cycles). In the case of the rough surfaces,

the friction coefficient varies throughout the test. At first, it reaches a minimum value close to 0.04 – 0.05 and then it fluctuates between 0.06 and 0.08.

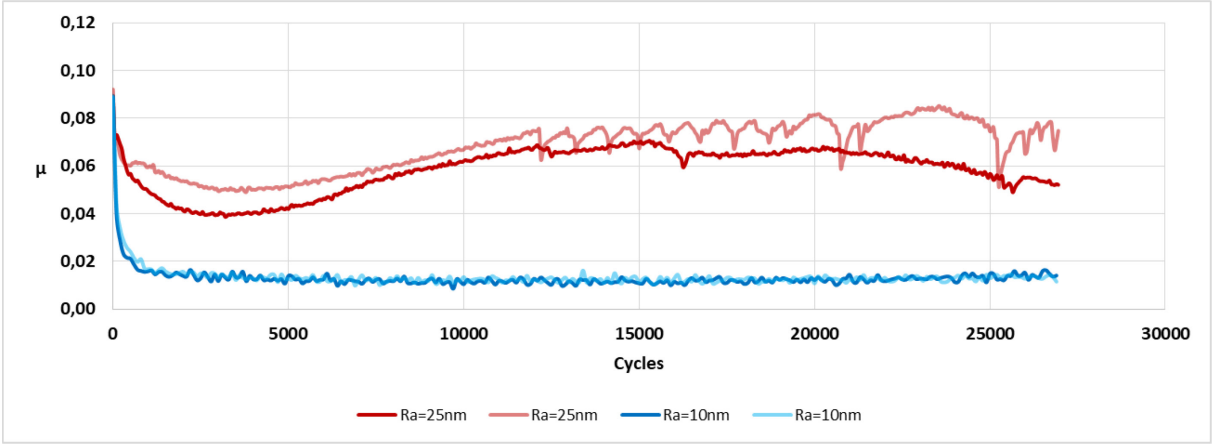


Figure 5. 1. Friction curves of ta-C/ta-C tribopairs in PAO base oil with different initial surface roughness. Smooth surfaces  $Ra_{initial} = 10 \text{ nm}$  (blue curves), and “rough” surfaces,  $Ra_{initial} = 25 \text{ nm}$  (red curves).

**Figure 5. 2** shows optical images of the wear scars of the flats and cylinders after sliding. The smooth surfaces exhibit no measurable wear, whereas the rough surfaces show horizontal scratches. **Figure 5. 3** shows optical interferometer images of the flat and cylinder. The wear scars are very rough and irregular. The wear depth of the flat and cylinder is approximately  $0.5 \mu\text{m}$  (25% of the coating thickness) and  $1.0 \mu\text{m}$  (50% of the coating thickness), respectively.

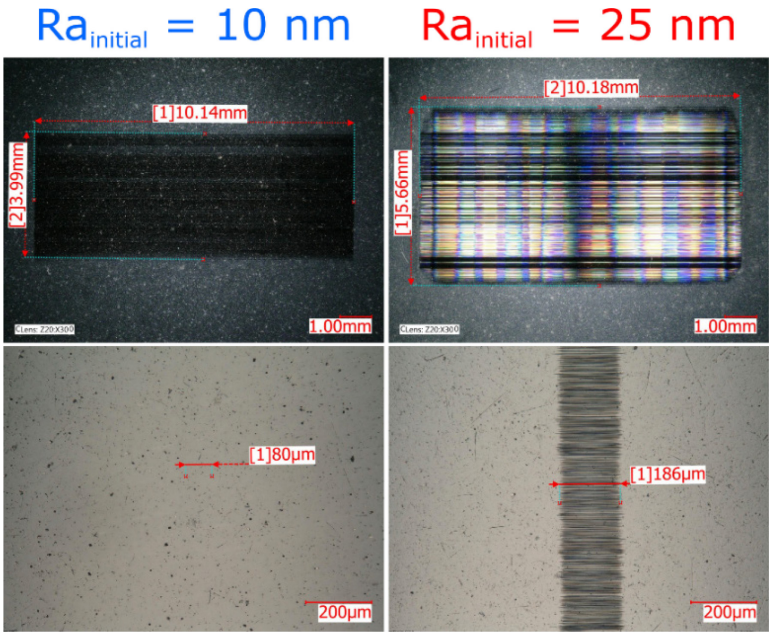


Figure 5. 2. Wear scars of disks (top) and cylinders (bottom) of ta-C/ta-C tribopairs after sliding tests in PAO base oil with smooth surfaces (left) and rough surfaces (right).

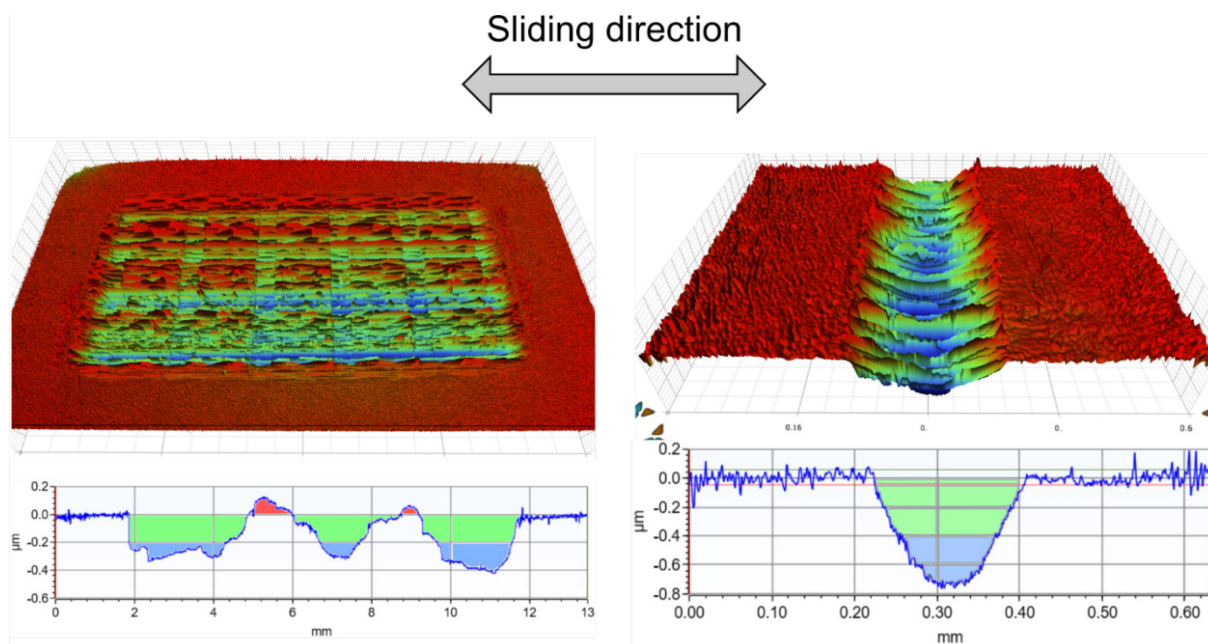


Figure 5. 3. Optical interferometer images of the rough disk (left) and cylinder (right) after sliding in PAO base oil (top) and horizontal wear profiles parallel to sliding direction (bottom). The red-colored areas are positive wear (above baseline) while the green and blue areas are deep negative wear (below baseline). The cylinder base line is straightened to observe the wear track.

### 5.1.2 Summary and Conclusions

To summarize the results, the smooth ta-C surfaces ( $R_a \approx 10$  nm) give low friction ( $\mu = 0.02$ ) and no measurable wear is observed on the wear tracks. When the polishing procedure is shortened and the ta-C surfaces are rougher ( $R_a \approx 25$  nm),  $\mu = 0.06 - 0.08$  and the surfaces undergo severe wear equivalent to 25% and 50% of the coating thickness for the disk and cylinder, respectively. To minimize friction and wear DLC surfaces must be polished close to a mirror-finish ( $R_a \approx 10$  nm).

## 5.2 Effect of contact pressure and sliding speed (lubrication regime).

### 5.2.1 Introduction

In reciprocating friction tests, the sliding speed  $v$  is not constant. At the edges of the stroke (where there is a change of direction),  $v$  falls to zero, whereas  $v$  reaches its maximum value in the center of the stroke. This means that at the edges of the stroke, much less lubricant is entrained in the contact zone between two contacting bodies, possibly resulting in a transition from mixed/elastohydrodynamic lubrication (ML/EHL) to boundary lubrication (BL). In Chapter 4, it was evidenced by SEM images that the tribofilm form on the edges of the wear



tracks of soft DLCs and not in the center. Additionally, the AFM images showed that after running-in, hard ta-Cs exhibit scratches at the edges, but not in the center of the wear track.

In this chapter, the initial contact pressure  $P_{\text{Hertz}}$  and average sliding speed  $v$  of ta-C(66)/ta-C(66) contacts was varied for four different test configurations shown in **Table 5. 2**. The other test parameters are unchanged from the previous chapter. Both parameters have an impact on the lubricant film thickness and therefore on the lubrication regime of the system. Case 1 corresponds to the typical contact pressure and sliding speed values that are commonly used in experimental studies to try to imitate the conditions in line contacts of sliding components in ICEs. Case 2, 3, and 4 are more severe since the pressure is increased and/or the sliding speed is decreased. Lambda values were calculated according to the **Methods section 3.3.2**. The percentage of the stroke length where boundary lubrication applies to case 1, 2, 3, and 4 are approximately 20%, 30%, 52% and 76%, respectively, as illustrated in **Figure 5. 4**.

Table 5. 2. Configurations of contact pressure, sliding speed and  $\lambda$  calculations for the sliding tests.

Label	$P_{\text{Hertz}}$ (GPa)	$v$ (mm/s)	$\lambda_{\text{Max}}$
Case 1	210	100	1.9
Case 2	300	100	1.7
Case 3	210	50	1.2
Case 4	300	50	1.1

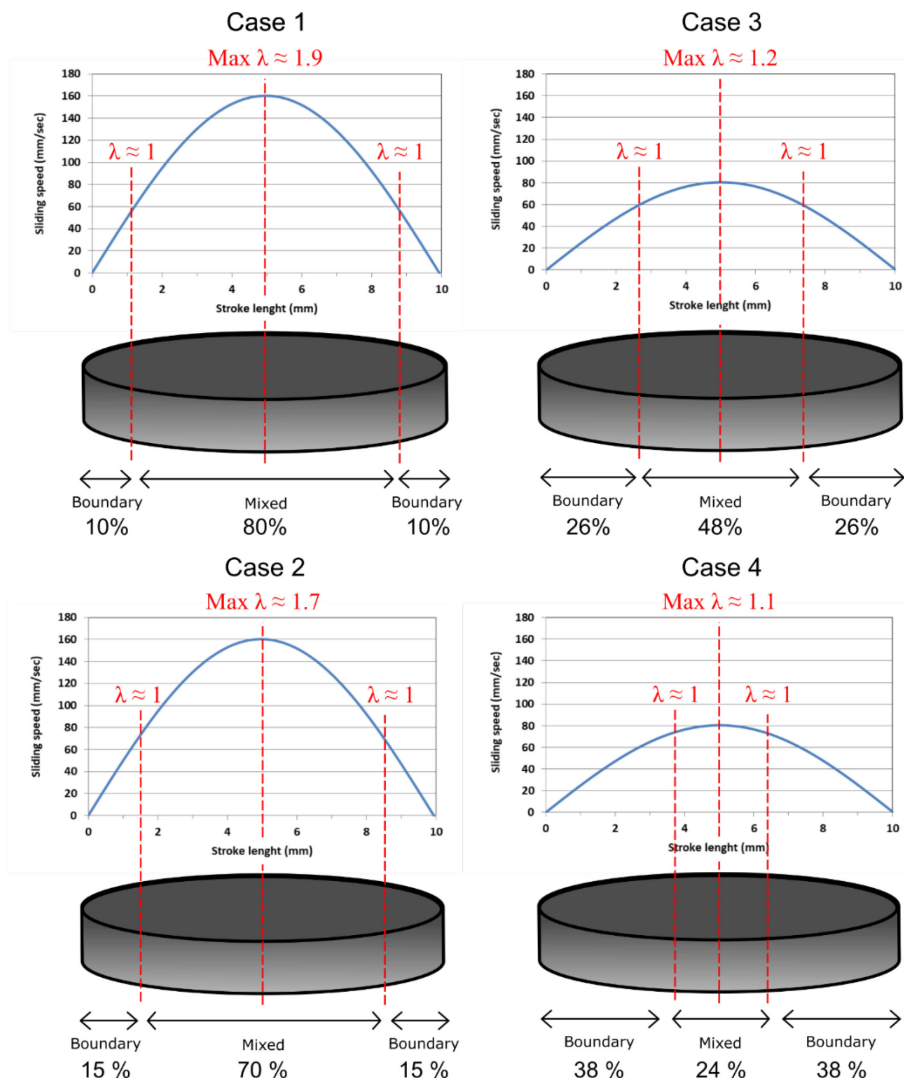


Figure 5. 4. Lambda Calculations for Cases 1 - 4. Blue curves represent the sliding speed that corresponds to the sliding distance (stroke length) on the horizontal axis.

## 5.2.2 Friction and wear results

Figure 5. 5 shows the friction curves obtained from sliding tests of ta-C/ta-C in PAO base oil. At least three tests were performed for each case. For case one, the friction coefficient is steady throughout the tests at a value of 0.02. Surprisingly, when the contact pressure is increased (Case 2) the friction coefficient decreases to 0.01. This will be discussed further ahead after examination of the wear tracks. According to Stribeck's curve it is expected that increasing the applied force will shift the lubrication regime towards the left (boundary lubrication) and increase the friction coefficient. However, this will be explained by looking at the wear tracks. For the most severe cases (3 and 4), the friction coefficient is similar to the

other tests at the beginning around (0.02), but starts to rise towards the end of the sliding test up to 0.06 – 0.07.

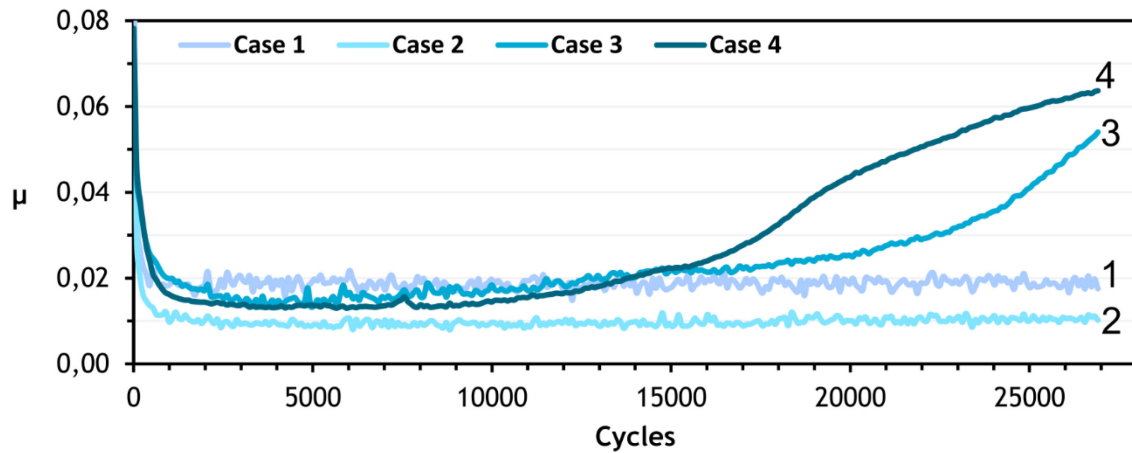


Figure 5. 5. Friction curves of ta-C(66) lubricated with PAO base oil at different combinations of contact pressure and sliding speed. Case 1:  $P_{\text{Hertz}} = 210 \text{ GPa}$ ,  $v = 100 \text{ mm/s}$ . Case 2:  $P_{\text{Hertz}} = 300 \text{ GPa}$ ,  $v = 100 \text{ mm/s}$ . Case 3:  $P_{\text{Hertz}} = 210 \text{ GPa}$ ,  $v = 50 \text{ mm/s}$ . Case 4:  $P_{\text{Hertz}} = 300 \text{ GPa}$ ,  $v = 50 \text{ mm/s}$ .

The wear tracks are shown in **Figure 5. 6**. In case 1, the height of the flat wear track is 4 mm, which corresponds to the linear surface of the cylinder. The cylinder wear track is not observable (Hertz diameter  $\approx 70 \mu\text{m}$  shown for reference). For case 2, the flat coupon has a particular shape: the height at the edges is larger than at the center of the wear track (indicated by red dash-lines), which indicates that the contact surface is larger at the edges and the surfaces are more separated towards the center. This corresponds well to the predicted lambda calculations in **Figure 5. 4** and illustrates that wear starts at the portion of the stroke length that corresponds to boundary regime (edges of the wear track). The cylinder wear track is clearly visible with a width of  $115 \mu\text{m}$ . It is mostly smooth, but some horizontal scratches (parallel to sliding) can be observed. The enlargement and smoothing of the cylinder wear track effectively decreases the applied contact pressure and can explain why  $\mu$  drops to 0.01. The wear tracks of cases 3 and 4 are much more scratched for both the flat and cylinder. This increases their surface roughness and  $\mu$  starts to increase towards the end of the sliding tests.



# Flat

# Cylinder

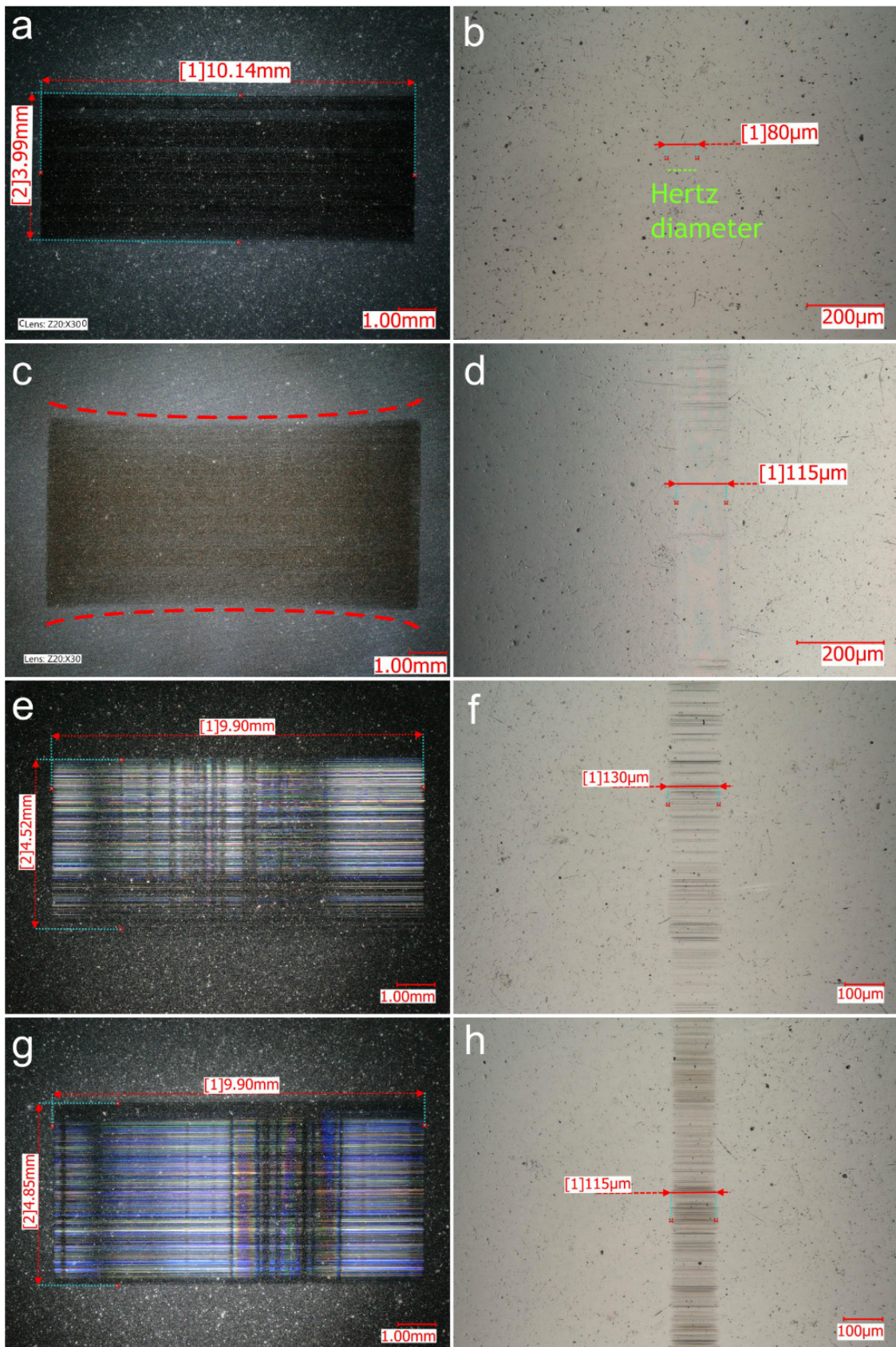


Figure 5. 6. Optical images of the wear tracks of ta-C(66) flats and cylinders after sliding tests in PAO base oil for case 1 (a-b) case 2 (c-d) case 3 (e-f) and case 4 (g-h).

The wear volumes are presented in **Figure 5. 7**. There is no measurable wear for case 1 and small wear for case 2. Cases 3 and 4 exhibit higher wear volumes and the wear of the disk is 3 - 5 times larger than that of the cylinder. This phenomena was also observed on the wear of hard ta-Cs lubricated with ZDDP in **Chapter 4.2**, although the wear volumes were 5 – 10 times larger.

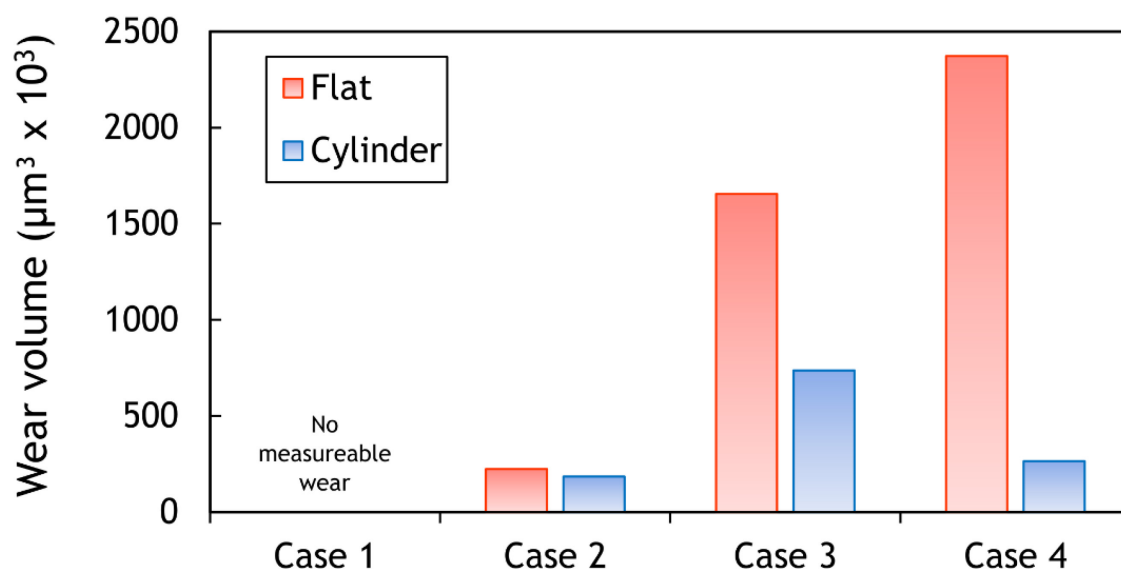


Figure 5. 7. Wear volumes of ta-C(66) flats (red bars) and cylinders (blue bars) after sliding tests in PAO base oil in four different parameter configurations.

### 5.2.3 Discussion

The use of the cylinder-on-disk reciprocating tests aim to mimic, for instance, a piston-liner system. However, in the distribution part of an engine, on the cam-latch or cam-follower contact, there is a reciprocating movement. This is not pure sliding, but the drive speed drops to 0 at the edge of the follower or at the end of the stroke of the big skate. This is one of the reasons for wear. Indeed when the driving speed drops to 0, the surfaces come into contact. On a cam, there can be wear on both sides of the nose. This also corresponds to the area where the driving speed drops to 0 and therefore the cylinder-on-disk reciprocating test is also useful for this case. Almost no tribometer is representative of real contacts in engines. To be a little more representative of the cam-follower contact, ring/plane can be explored with the sliding speed ranging from 0.6 to 2.6 ms<sup>-1</sup> and contact pressures of about 500 MPa. The real power dissipated by friction is generally around several tens of W in applications, while it is a few tens of mW in the tribometer used in this work. Nevertheless, it is important to explore

different parameter values, e.g. contact pressure, sliding speed..., to better understand the tribological systems studied.

#### **5.2.4 Summary and Conclusion**

To summarize the results presented in this chapter, four different combinations of contact pressure  $P_{\text{Hertz}}$  and sliding speed  $v$  were tested. Increasing the contact pressure and/or decreasing the sliding speed of the tests reduces the thickness of the separating lubricant film. This leads to increased contact between asperities. Moreover, a larger portion of the stroke length enters the boundary regime, which induces rougher/scratched surfaces and a rise of friction coefficient. Wear starts in the regions where boundary lubrication applies (towards the edges where the sliding speed drops to 0). As the surfaces become rougher, the wear spreads towards the center until boundary lubrication applies on the whole stroke length.

## 5.3 Effect of the counterpart material: DLC/steel contacts.

### 5.3.1 Introduction

For more than a decade, DLC coatings have been applied in automotive parts to reduce friction and wear in sliding components. There are two possible systems: both counterparts can be DLC-coated (DLC/DLC) or only one of them, in which case the other material is most often steel (DLC/steel) or another ferrous surface such as cast iron. For certain components such as cam/valve-lifter or cam/follower, it is conceivable to apply DLC coatings to both parts (already applied in the automotive industry). On the contrary, in other systems, it could be more practical to only coat one part, for example in piston-ring/liner contacts, where coating the liner can be done for competitive car racing models, but could amount to an important price raise of commercial passenger cars. Therefore, from a practical point of view, both systems are relevant to study in order to understand their tribological behavior and develop efficient systems in order to reduce wear and friction of sliding components in ICE that could also be applied to other machine elements.

Lafon Placette *et. al* performed ta-C/steel and a-C:H/steel friction tests in PAO base oil. Very little wear was observed for a-C:H coatings, while harder ta-C coatings exhibited severe tribochemical wear that was activated by temperature and followed an Arrhenius behavior<sup>98</sup>. Surface analysis revealed the formation of a carbon-rich tribofilm on the steel counterpart that did not stop the progression of wear, and the resulting ta-C wear track was very smooth (characteristic of tribochemical atomic layer by layer wear). In a different study Tasdemir *et. al* found similar results<sup>99</sup>.

Okubo *et. al* reported similar wear results in PAO base oil of DLC/steel tribopairs<sup>100</sup>. By performing in-situ Raman observations, they inferred that wear of ta-C against steel surfaces was induced by graphitization and could be reduced, but not inhibited, by adding 1 wt.% of GMO (glycerol mono-oleate) to the PAO base oil. They observed a reduction of friction coefficient and argued that the contact temperature at the sliding interface was lowered, therefore graphitization temperature for ta-C was not attained. The effect of reduced shear stress and passivation of ta-C surface by formation of a GMO-derived tribofilm was not discussed in detail, but could be of important relevance. On the other hand, Makowski *et. al* reported high wear of ta-C/steel tribopairs lubricated with with GMO compared to a fully formulated engine oil and other fatty-acids<sup>101</sup>, which is contradictory to the results obtained by Okubo. More studies on the effect of GMO on DLC/steel tribopairs is needed.

Tasdemir et al.<sup>102</sup> performed cylinder-on-disk unidirectional tests in taC/steel, taC/taC, and steel/steel configurations lubricated with PAO, and PAO + additives (ZDDP and/or GMO). For taC/steel in PAO, the initial friction coefficient was about 0.02, but increased drastically up to 0.10 due to complete wear of the taC pin and appearance of steel substrate. Wear of the ta-C pin was avoided in PAO + ZDDP due to the formation of the typical ZDDP pad-like tribofilm on the steel disk and ta-C pin and the friction coefficient was stable at 0.08. Okubo *et. al*<sup>103</sup> also reported wear inhibition of ta-C/steel in PAO + ZDDP solutions.

In summary, the literature shows that in pure base oil lubrication, hard ta-C coatings undergo severe wear against steel surfaces and a carbon transfer film can be observed on the steel wear track, however, it does not stop wear. The resulting wear track on the ta-C is smooth, hinting tribochemical wear rather than abrasive and it is aggravated by the increase of temperature. In PAO + ZDDP, the wear of ta-C is inhibited due to the formation of the typical zinc/polyphosphate tribofilm formation on the steel surface, which inhibits carbon transferring from the ta-C.

### 5.3.2 Friction and wear results

DLC/steel tribopairs in base oil and ZDDP-solutions are studied by reciprocating sliding tests using the standard test parameters as the ones given at the beginning of this chapter in **Table 5. 1**. The friction curves of ta-C/steel tribopairs lubricated with PAO base oil and PAO + ZDDP solution are shown in **Figure 5. 8**. The black curve corresponds to the typical steel/steel tribopair in PAO + ZDDP for reference. In PAO base oil  $\mu$  is approximately 0.11 for the steel<sub>cylinder</sub>/ta-C<sub>disk</sub> tribopair. When the tribopair is inversed to ta-C<sub>cylinder</sub>/steel<sub>disk</sub>,  $\mu$  is drastically reduced to 0.02. This can be explained by a carbon film that is transferred onto the steel surface (discussed in the previous studies mentioned above) resulting in an atomically smooth ta-C/ta-C<sub>transferred</sub> sliding interface. However, this is not sustainable, as after 17,000 cycles the ta-C cylinder is completely worn out. The wear of the ta-C exposes the chrome interlayer and there is a momentarily steel/chrome sliding interface, which explains the rise of  $\mu$ . Ultimately, the contact area is enlarged and displaced due to the continuous wear and again a ta-C/steel contact is attained decreasing  $\mu$  back to 0.02. In PAO + ZDDP, both steel<sub>cylinder</sub>/ta-C<sub>disk</sub> and ta-C<sub>cylinder</sub>/steel<sub>disk</sub> tribopairs exhibit a similar steady state friction coefficient close to 0.07 – 0.08, (which corresponds to a 40% reduction compared to the steel/steel tribopair). However, their running-in is different. For the ta-C<sub>cylinder</sub>/steel<sub>disk</sub> tribopair,  $\mu$  drops to 0.04 at the beginning of the test, but after a few thousand cycles ( $\approx$  5,000) it stabilizes at 0.08. For the inversed tribopair, steel<sub>cylinder</sub>/ta-C<sub>disk</sub>, this running-in procedure does not occur and  $\mu$  has been



steady since the beginning of the test (similar to the steel/steel tribopair). This difference is most likely due to the formation time of the ZDDP-derived tribofilm on the steel surface. It occurs almost immediately on the 80  $\mu\text{m}$  wide contact area of the cylinder, but requires about 5,000 cycles to form on the 10 mm long surface of the disk that has a kinematic length almost 150 times larger than the one of the cylinder.

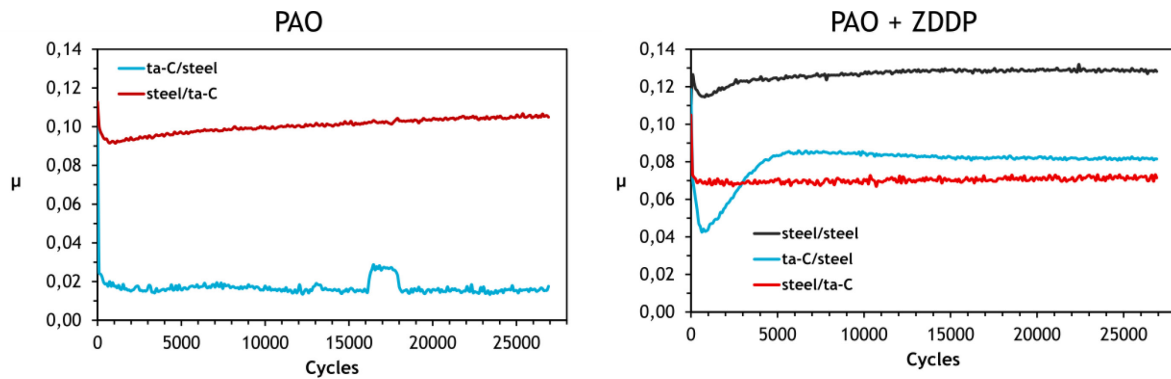


Figure 5. 8. Friction curves of ta-C(66)/steel tribopairs lubricated in PAO (left) and PAO + ZDDP (right). The black curve corresponds to steel/steel in PAO + ZDDP and serves as reference. The tribopairs designation correspond to cylinder/disk configuration.

Optical images of the wear tracks are shown in **Figure 5. 9**. In PAO base oil there is the formation of a “brownish” tribofilm on the steel<sub>cylinder</sub>/ta-C<sub>disk</sub> tribopair (**Figure 5. 9a and b**). When the tribopair is inverted (ta-C<sub>cylinder</sub>/steel<sub>disk</sub>) and the ta-C is now on the cylinder, it completely wears out and the chrome interlayer is visible (**Figure 5. 9c and d**). The kinematic length of the cylinder is 150 times shorter than that of the disk, so when the ta-C is on the cylinder the wear due to the transfer of carbon atoms is accelerated drastically. In PAO + ZDDP, there is the formation of a ZDDP-derived tribofilm (blue color) on the steel surfaces for both cases whether the steel coupon is the disk or cylinder. However, the morphology of the ZDDP tribofilms formed on steel/ta-C tribopairs is different from the typical pad and valley tribofilm formed in steel/steel contacts (**Figure 5. 9i and j**). The tribofilms formed on the steel surfaces in steel/ta-C contacts are more homogenous and continuous, with well-defined straight edges (see **Figure 5. 9e and h**).

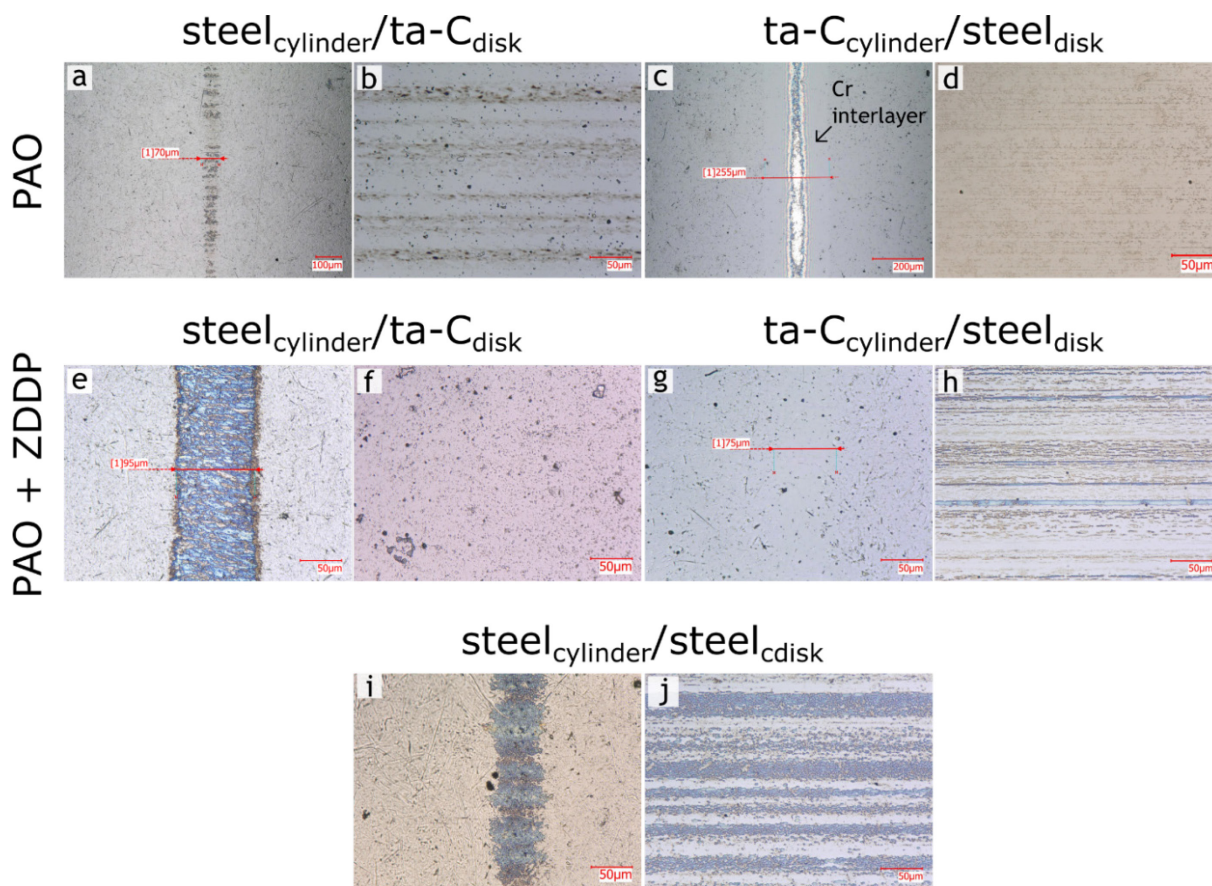


Figure 5. 9. Optical images of the wear tracks of asymmetric ta-C/steel tribopairs and steel/steel tribopair as reference after sliding tests in PAO (top) and PAO + ZDDP solution (middle).

The wear volumes of the disks and cylinders are shown in **Figure 5. 10**. In PAO base oil the ta-C cylinder is completely worn out (shown in **Figure 5. 9d**), when sliding against the steel disk. This result is in good agreement with previous studies that show that in ta-C/steel contacts the carbon atoms of the ta-C are continuously transferred to the steel surface, causing wear<sup>98,102</sup>. By inverting the tribopair (ta-C coating on the disk against steel cylinder), there is no measurable wear on the disk or cylinder (**Figure 5. 9a and b**), which provides a possible solution to prevent wear in the absence of ZDDP. When ZDDP is added to the base oil, a tribofilm is formed on the steel surface so the sliding interface becomes ta-C against ZDDP tribofilm. This prevents carbon transfer and inhibits wear of the ta-C, in agreement with previous studies<sup>102,103</sup>.

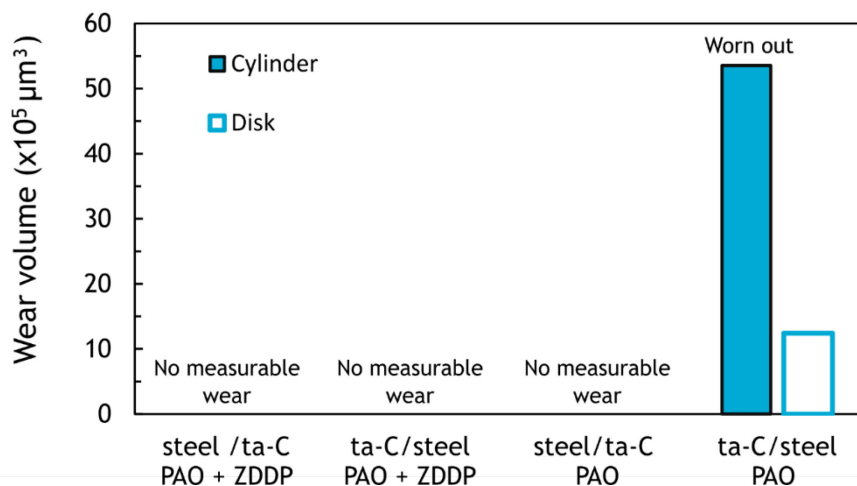


Figure 5. 10. Wear volumes of ta-C/steel tribopairs after sliding tests in PAO and PAO + ZDDP solution.

### 5.3.3 Surface analysis techniques

In Chapter 4, it was shown that ZDDP induces wear of hard ta-C/ta-C contacts. There was a strong correlation between the wear of hard ta-Cs and the chemical state of sulphur (**Figure 4. 9**), where C-S bonds (**Figure 4.8**) and diffused sulphur atoms into the ta-C matrix were observed, inducing a structural change from amorphous carbon to graphitic/onion-like structures (**Figure 4. 11**). The results presented above show that in ta-C/steel contacts, ZDDP has the opposite effect and actually fulfills its role as an anti-wear additive to protect the ta-C surface. To understand this behavior surface, chemical analysis were performed by XPS.

**Figure 5. 11a** shows the S2p spectrum obtained on the ta-C disk after sliding against the steel cylinder and an optical image of the corresponding wear track from where the spectra was obtained. The S2p spectrum is composed of 2 components: the first and most prominent one at 162.2 eV (in blue) corresponds to S-Zn, or S-P and S=P in thiophosphates. There is a second small contribution at 168.9 eV from sulphates. The correlation found in Chapter 4 between no wear and absence of S-C bonds still applies. For comparison, the S2p spectrum of ta-C disk against ta-C cylinder in PAO + ZDDP (**Figure 5. 11 b**) from chapter 4 is shown where severe wear was observed and the dominant component of the spectrum was the S-C bonds (in red).

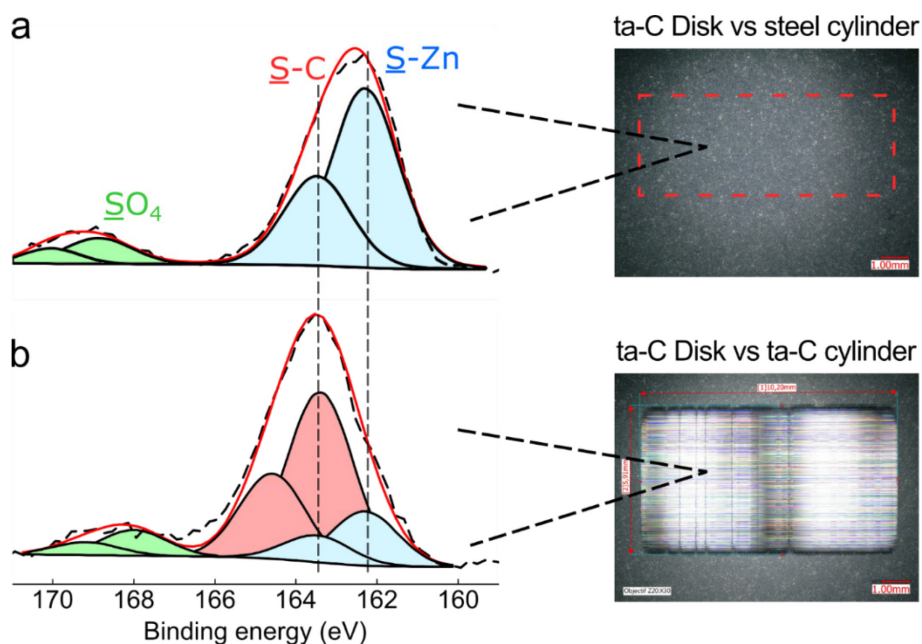


Figure 5. 11. S<sub>2p</sub> XPS spectra measured on disk samples from: (a) ta-C/steel tribopair and (b) ta-C/ta-C tribopair after sliding tests in PAO + ZDDP. Optical images of the wear tracks are shown to illustrate the difference in wear associated with the chemical state of sulphur.

The C1s, O1s, P2p, and Zn2p<sub>3/2</sub> spectra are shown in **Figure 5. 12**. The C1s photopeak is composed of three contributions: the first peak at 284.8 eV is attributed to sp<sup>2</sup> and sp<sup>3</sup> carbon bonds of the ta-C as well aliphatic carbon. The second and third peaks at 286.5 and 288.4 eV correspond to C–O and C=O bonds, respectively. The O1s spectrum can be fitted using two contributions: the first one, at 531.7 eV, is attributed to non-bridging oxygen and the second one, at 533.0 eV, is attributed to bridging oxygen. The P2p spectrum is fitted with one doublet with a separation of 0.84 eV and intensity ratio of 0.5. The P2p<sub>3/2</sub> peak located at B.E. = 133.4 eV corresponds to phosphates. The Zn2p<sub>3/2</sub> peak at B.E = 1022.3 eV corresponds to ZnS or Zn<sup>2+</sup> in zinc phosphates.

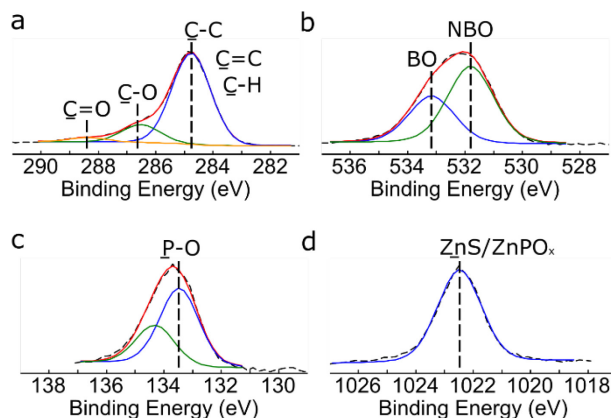


Figure 5. 12. (a) C1s, (b) O1s, (c) P2p and (d) Zn2p<sub>3/2</sub> XPS spectra obtained from ta-C disk after sliding tests against steel cylinder (steel/ta-C tribopair) in PAO + ZDDP.

**Figure 5. 13** shows the C1s, O1s, P2p, S2p, Zn2p<sub>3/2</sub> and Fe2p XPS spectra recorded on the steel disks from ta-C<sub>cylinder</sub>/steel<sub>disk</sub> and steel/steel tribopairs after sliding tests in PAO + ZDDP. Even though the optical images revealed a difference in the morphology of the ZDDP-derived tribofilms, their chemical compositions are the same. The C1s spectrum is composed of three contributions: the first one, at 284.8 eV, corresponds to aliphatic carbon, while C-O and C=O species are observed at 286.4 and 288.3 eV, respectively. The O1s spectrum is composed of two components, the first and largest one at 531.4 eV is non-bridging oxygen (NBO), while bridging-oxygen (BO) is located at 533.0 eV. The P2p<sub>3/2</sub> photopeak at 133.5 eV indicates the presence of phosphates. The S2p spectrum consists mostly of one contribution located at 162.0 eV, which corresponds to metal sulfides (ZnS) and/or S-P and S=P bonds in thiophosphates. There are two other very small contributions at 164.0 and 168.0 eV, which correspond to sulfites and sulphates, respectively. The Zn2p<sub>3/2</sub> photopeak is composed of two contributions: the first one, at 1022.1 eV, corresponds to ZnS and Zn phosphates, while the second one at 1023.8 eV corresponds to ZnO. The Fe2p spectra are also shown, although the signal/noise ratio is too low to be taken into account as a significant concentration. The atomic concentrations are given in **Table 5. 3** and the parameters used for the fitting procedure are given in **Table A. 1**.

Similarly to the XPS results presented in Chapter 4, the concentrations of the ZDDP-derived elements (P, S, and Zn) are between 1 – 2 %, confirming again that thick ZDDP-tribofilms do not form on hard ta-C surfaces in the tested conditions. The chemical composition of the ZDDP-derived tribofilms on steel surfaces contain higher amounts of P and Zn and less S, which has been shown many times in the literature. They are very rich in oxygen, which is characteristic of the well-known zinc-phosphate glass that composes the bulk of the tribofilms.

Table 5. 3. Relative chemical composition obtained from XPS spectra of steel/ta-C, ta-C/steel, and steel/steel tribopairs. The spectra are obtained from the disk samples of the tribopairs (cylinder/**disk**).

Tribopair	Elemental quantification (at. %)					
	C1s	O1s	P2p	S2p	Zn2p <sub>3/2</sub>	Fe2p
<b>Steel/ta-C</b>	78.9	15.8	1.3	1.4	2.6	0.0
<b>ta-C/Steel</b>	31.8	45.0	9.0	3.5	10.6	0.1
<b>Steel/steel</b>	31.6	45.2	8.9	3.6	10.6	0.1

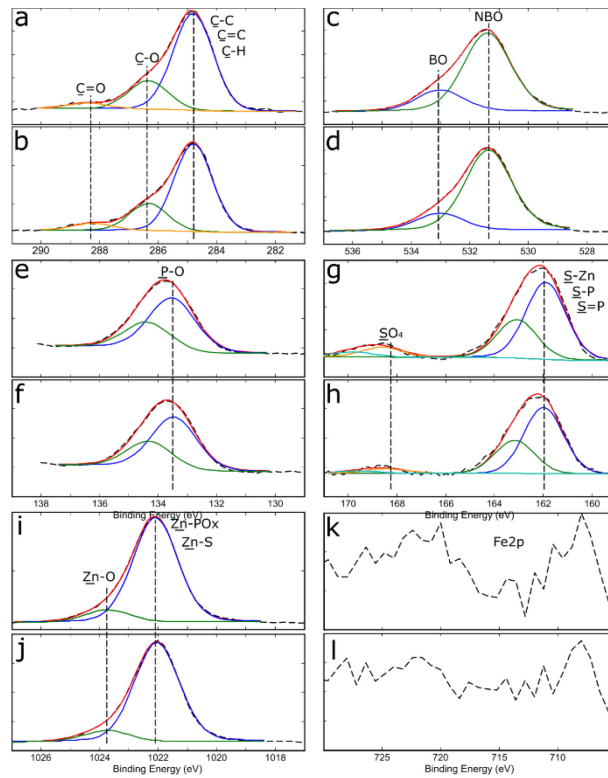


Figure 5. 13. XPS spectra obtained from steel disk vs. ta-C cylinder (a, c, e, g, i, k) and steel disk vs. steel cylinder (b, d, f, h, j, l) after sliding tests in PAO + ZDDP.

The tribofilms formed on the steel surfaces were analyzed by SEM technique. **Figure 5. 14** shows representative SEM images of the steel disks of ta-C<sub>cylinder</sub>/steel<sub>disk</sub> and steel/steel tribopairs after sliding tests in PAO + ZDDP. EDX spectra were obtained in specific regions of interest, indicated by dashed rectangles. The regions in green correspond to the ZDDP-derived tribofilm, in yellow to the steel (iron) surface and in red to tungsten precipitates. The EDX elemental quantification results are given in **Table 5. 4**. Despite the almost identical chemical composition, there is a clear difference in the morphology of the ZDDP-derived tribofilms on the steel surfaces. For the ta-C<sub>cylinder</sub>/steel<sub>disk</sub> tribopair (**Figure 5. 14a and c**) the tribofilm forms long-continuous stripes with well-defined straight edges. The tribofilms formed on the steel/steel tribopair (**Figure 5. 14b and d**) shows the typical pad and valley (so-called “pad-like”) tribofilm. Obviously, ta-C is harder and stiffer than steel, so the real contact area between steel/ta-C and steel/steel tribopairs can differ due to less elastic deformation that the ta-C asperities undergo under the same applied load and lead to different morphologies.



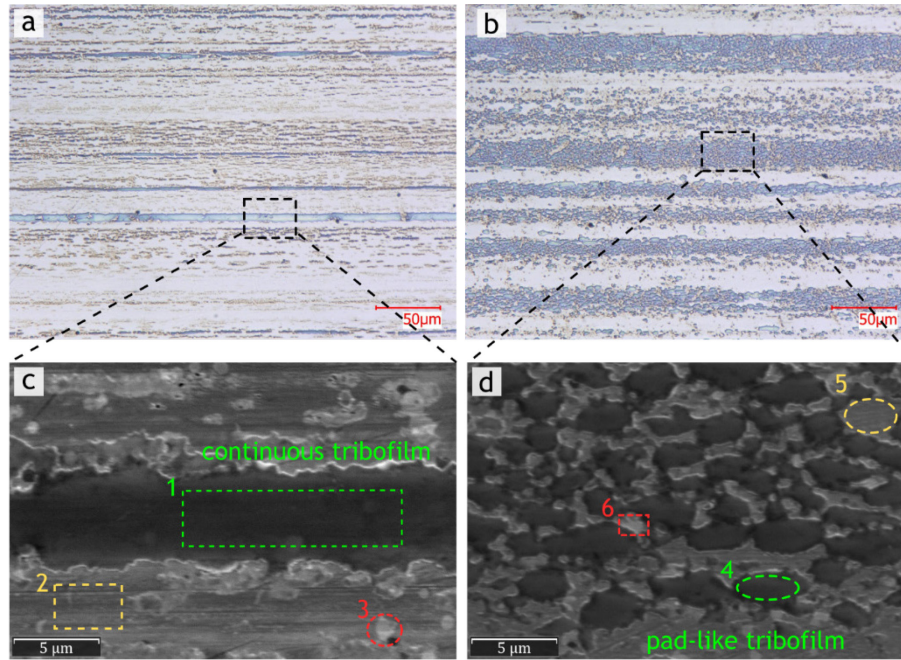


Figure 5. 14. Optical and SEM images of the wear tracks of steel disks in: (a and c) ta-C<sub>cylinder</sub>/steel<sub>disk</sub> and (b and d) steel/steel tribopairs after sliding in PAO + ZDDP. The dashed rectangles indicate the regions of interest where EDX spectra were obtained.

Table 5. 4. Elemental quantification obtained by EDX analysis of the spectra recorded in ROI 1-6 shown in Figure 5. 14.

ROI #	Elemental quantification (at. %)						
	C	O	P	S	Fe	Zn	W
1	2.1	32.6	9.0	4.6	9.9	41.4	0.4
2	3.7	12.1	2.1	3.2	67.1	9.5	2.4
3	9.4	4.5	0.9	11.0	29.0	1.2	44.1
4	1.8	32.8	9.4	4.1	13.8	38.1	0.0
5	5.1	3.9	0.2	0.7	84.9	1.4	3.9
6	6.4	6.7	2.9	9.3	28.6	5.4	40.0

### 5.3.4 Summary and Conclusions

To summarize the results obtained in this section, without a protective tribofilm the ta-C counterparts exhibits severe wear in ta-C/steel tribopairs. Wear can be greatly reduced if the ta-C coated surface is the counterpart with the longest kinematic distance i.e. on the disk. In PAO + ZDDP, the typical pad-like tribofilm is formed on the steel counterpart (but not on the ta-C surface), which protects both the steel and the ta-C surface and inhibits wear; in this case fulfilling its role as anti-wear additive. The friction coefficient of ta-C/steel tribopairs is

approximately 0.07. This represents a 40% reduction compared to a steel/steel contact, which is in line with the search of reducing friction and improving fuel efficiency of ICE in passenger cars.



## 5.4 Effect of other phosphorus and sulphur-containing additives on the tribological properties of DLC coatings

### 5.4.1 Introduction

Chapter 4 evidenced the wear of hard ta-C coatings in presence of ZDDP. The released sulphur atoms from the ZDDP molecule and subsequent sulphur doping, which weakens the ta-C material, is at the origin of the wear mechanism. In order to further understand this phenomenon, reciprocating sliding tests were performed with a-C:H and ta-C(66) coatings using different additives with and without sulphur (see **Figure 5. 15**). The description of the tribometer and test conditions are given in the **Methods section 3.3.1** and reminded in **Table 5. 5**.

Table 5. 5. Test conditions used for the reciprocating sliding tests.

Test conditions
<ul style="list-style-type: none"><li>• Contact = cylinder-on-disk</li><li>• <math>F_N = 23 \text{ N}</math></li><li>• <math>P_{\text{Hertz}} = 210 \text{ MPa}</math></li><li>• <math>T = 110^\circ\text{C}</math></li><li>• <math>v = 0.1 \text{ m s}^{-1}</math></li><li>• <math>l = 10 \text{ mm}</math></li><li>• <math>t = 90 \text{ min (2,700 cycles)}</math></li></ul>

The procedure for preparing the lubricant solutions and their concentrations is given in the **Methods section 3.2**. The ZDDP molecule used in the previous sections of this work was a primary-C<sub>4</sub> (R=C<sub>4</sub>H<sub>9</sub>). The ZP additive, with the same chemical composition as ZDDP except that the four S atoms are replaced by O atoms, was studied. However, its alkyl chain is longer (R=C<sub>8</sub>H<sub>17</sub>), so a ZDDP primary-C<sub>8</sub> (R=C<sub>8</sub>H<sub>17</sub>) additive was also studied to keep this variable equal. Finally, the TPS additive containing only H, C and S was tested to remove the influence of O, P, and Zn elements. This additive is used as an extreme-pressure (EP) in lubricant formulations in metal working fluids (MWF). To the best of the authors' knowledge, this is the first study that compares such types of additives with similar chemical structures on DLCs.

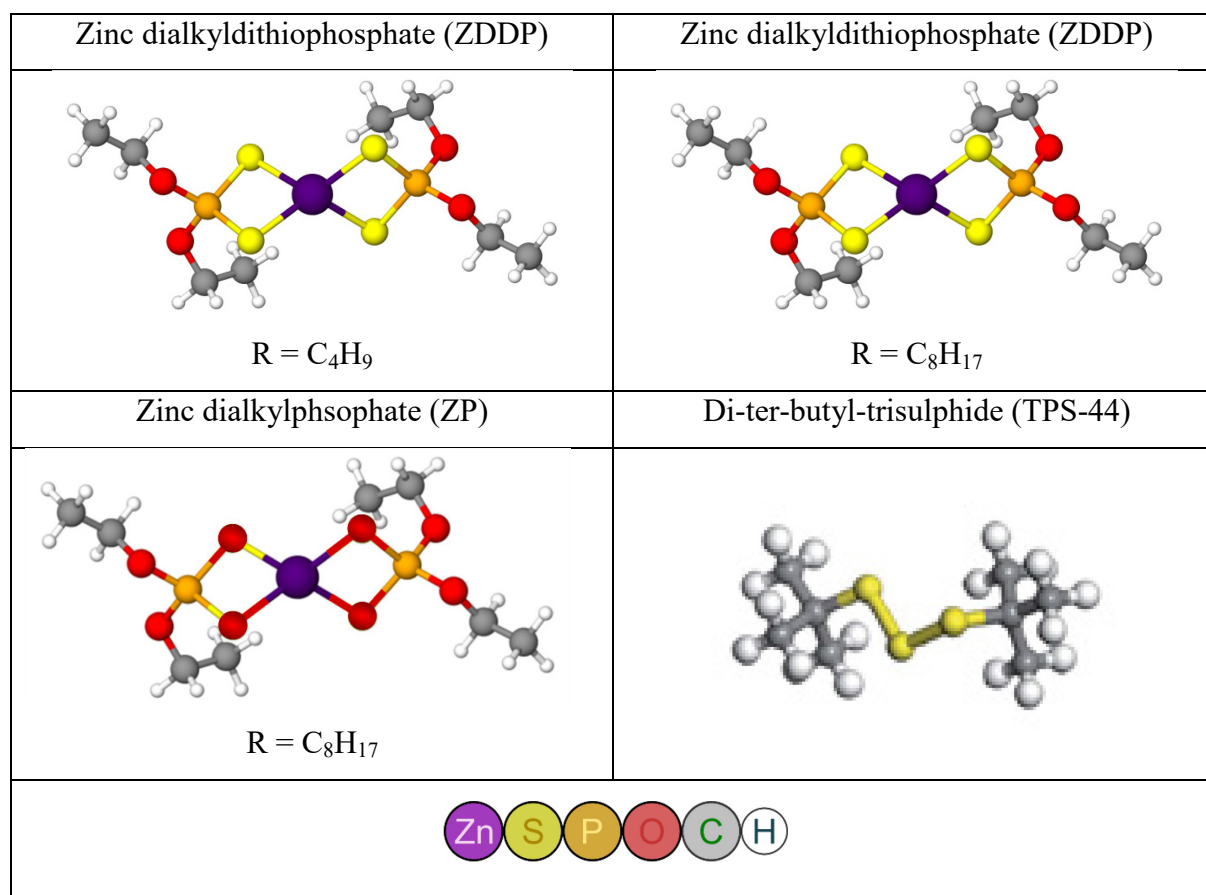


Figure 5. 15. Chemical structure of the tested additives.

#### 5.4.2 Friction and wear results

**Figure 5. 16** shows the evolution of the friction coefficient  $\mu$  obtained from sliding tests of a-C:H/a-C:H tribopairs in PAO and PAO + additives lubricants (the results with ZDDP primary-C4 were already presented in Chapter 4 and are included in this chapter to facilitate the direct comparison with the other additives). In PAO base oil,  $\mu$  reaches a steady-state value of 0.09. When ZDDP primary-C4 is added to the PAO base oil,  $\mu$  increases slightly to 0.10. In PAO + ZDDP primary-C8 and PAO + ZP primary-C8,  $\mu = 0.07$ , suggesting that even though their chemistries are different (ZDDP contains S, which is replaced by O in ZP), the length of the alkyl chain could be responsible for the friction reduction compared to the ZDDP with shorter alkyl chain length (R=C<sub>4</sub>H<sub>9</sub>). Finally, in PAO + TPS  $\mu = 0.10$ . It should be noted that for all the friction curves (except PAO base oil),  $\mu$  is lower at the beginning of the test and increases gradually throughout the test. This could be due to the progressive formation of tribofilms, which will be studied further ahead.

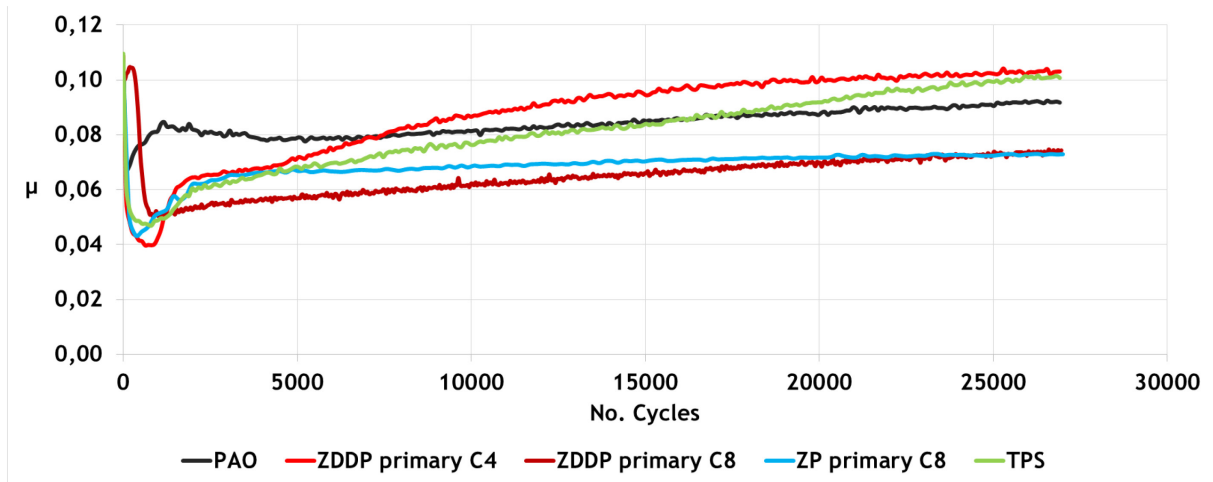


Figure 5. 16. Friction curves obtained from sliding tests of a-C:H/a-C:H tribopairs in PAO base oil and PAO + additives lubricants.

**Figure 5. 17** shows the friction curves obtained from sliding tests of ta-C(66)/ta-C(66) tribopairs in PAO and PAO + additives lubricants. In PAO and PAO + ZP,  $\mu = 0.02$  and remains steady throughout the test, indicating that ZP does not affect friction compared to PAO base oil alone. For both ZDDP additives (Primary-C4 and C8),  $\mu$  starts as with the PAO base oil at around 0.02 – 0.03, but after approximately 10,000 cycles,  $\mu$  gradually increases up to 0.10 and the signal becomes unstable (not smooth) at the end of the test. The moment at which  $\mu$  starts rising varies from one test to the other, but always occurs between 4,000 - 12,000 cycles. Finally, in PAO + TPS, there is a similar behavior of low friction at the beginning of the test ( $\mu = 0.02 - 0.03$ ) followed by a gradual increase up to 0.07.

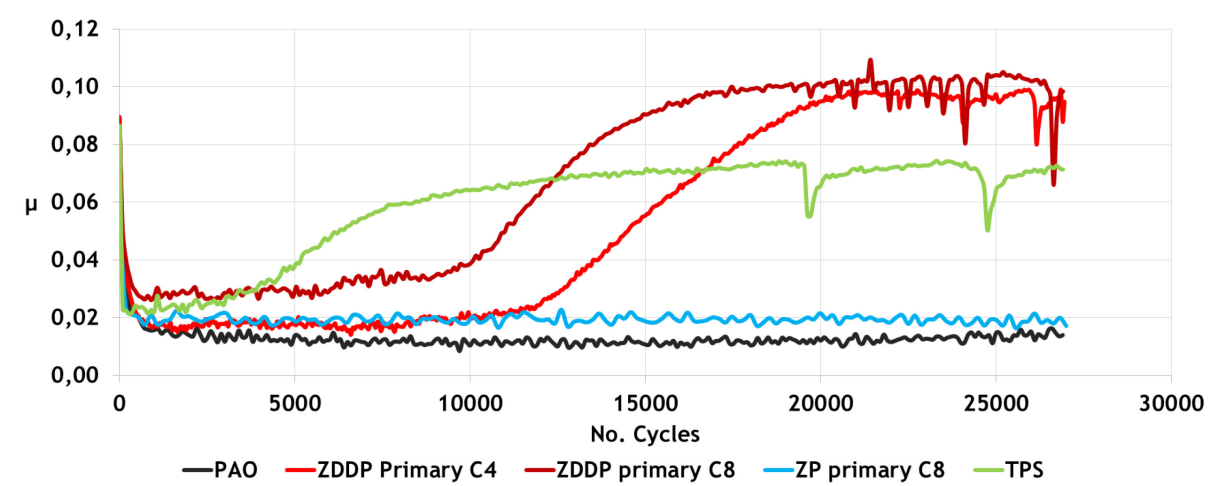


Figure 5. 17. Friction curves obtained from sliding tests of ta-C(66)/ta-C(66) tribopairs in PAO base oil and PAO + additives lubricants.

Optical images of the wear tracks are shown in **Figure 5. 18**. For ta-C, the wear tracks in PAO base oil and PAO + ZP ( $\mu = 0.02$ ) are barely visible on the cylinder and no scratches are seen

on the flat. For the other additives that exhibited a rise of  $\mu$  during the sliding tests (ZDDP primary-C4, primary-C8 and TPS), the wear tracks on the flats and cylinders exhibit large horizontal scratches and increased surface roughnesses (as shown in the optical interferometer images, see **Figure 5. 19**). For a-C:H, the wear tracks are much smaller and exhibit no horizontal scratches. The cylinders wear tracks have a width of 70 – 115  $\mu\text{m}$  (initial contact area  $\approx 70 \mu\text{m}$ ) and seem very smooth, except for the cylinder in ZP that shows small horizontal scratches.

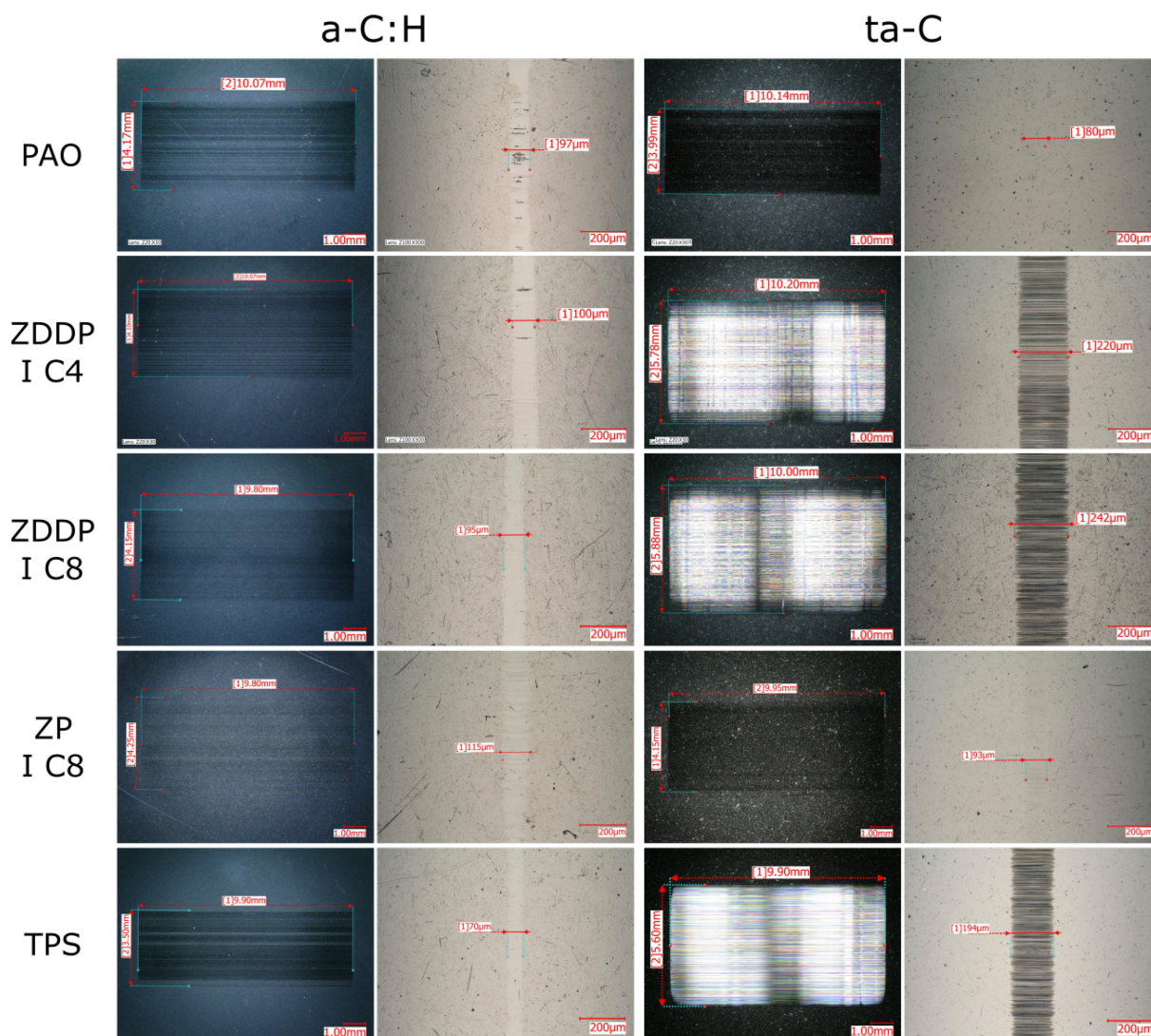


Figure 5. 18. Optical images of the wear tracks of a-C:H and ta-C(66) flats and cylinders after sliding tests in PAO base oil and PAO + additives lubricants.



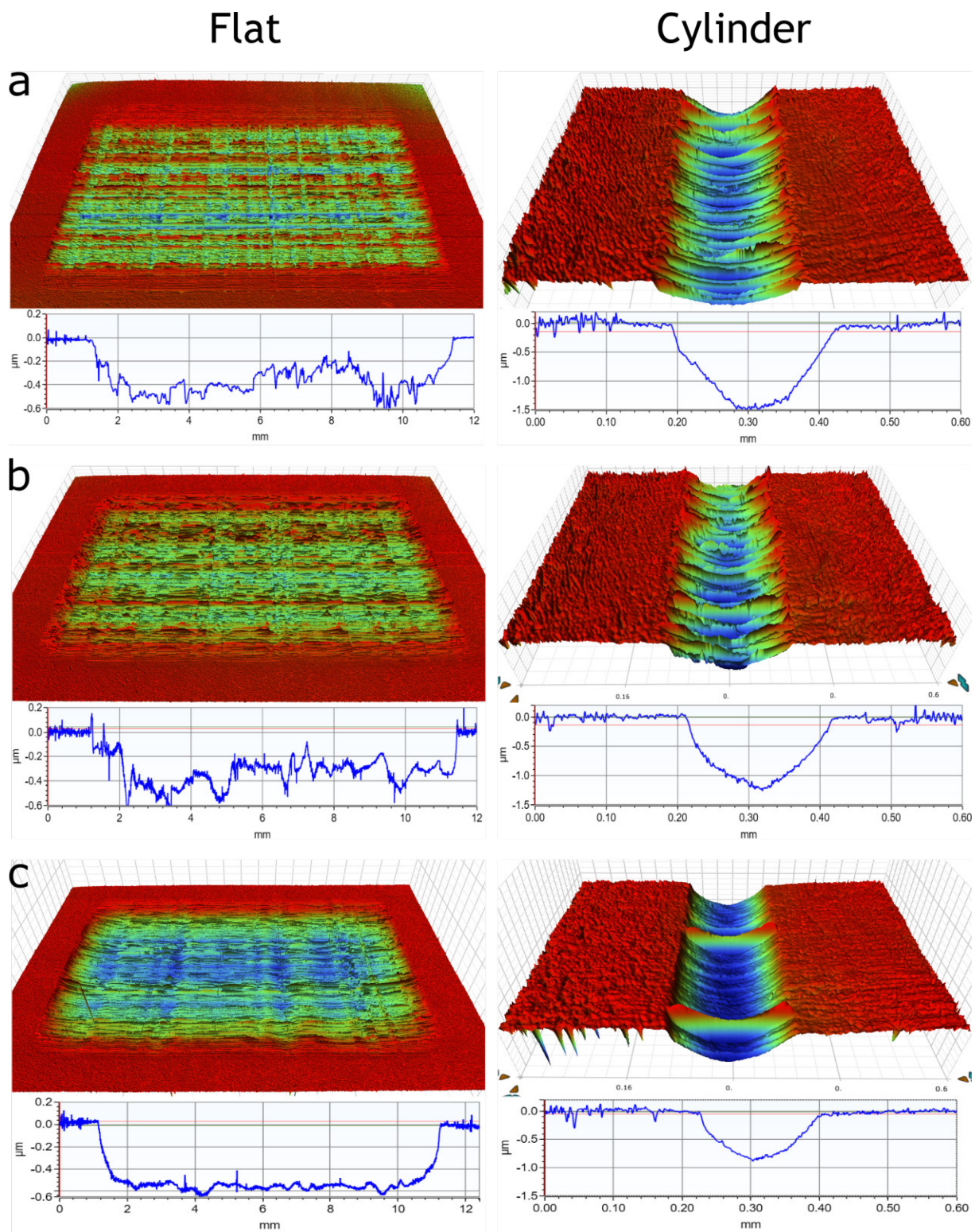


Figure 5. 19. Optical interferometer images of wear tracks of ta-C flats and cylinders after sliding tests in: (a) PAO + ZDDP primary-C4, (b) PAO + ZDDP primary-C8, and (c) PAO + TPS solutions.

The wear volumes measured by optical interferometry are shown in **Figure 5. 20**. For a-C:H, there was no measurable wear for the flats and mild wear for the cylinders (wear depth between 0.1-0.2  $\mu\text{m}$ ). The ta-C coatings exhibited severe wear in ZDDP primary-C4, ZDDP

primary-C8, and TPS solutions. The wear depths on the flats and cylinders are approximately 0.5-0.6 and 1.0 -1.5  $\mu\text{m}$  deep, which equals to about 25% and 75% of the coating thickness, respectively. It is worth noticing that the wear volumes of the flats are one order of magnitude greater than those of the cylinders, despite a much larger kinematic distance (150 times larger). This is indicative of tribochemical wear due to chemical reactions of sulphur at the sliding interfaces and not mechanical or abrasive wear.

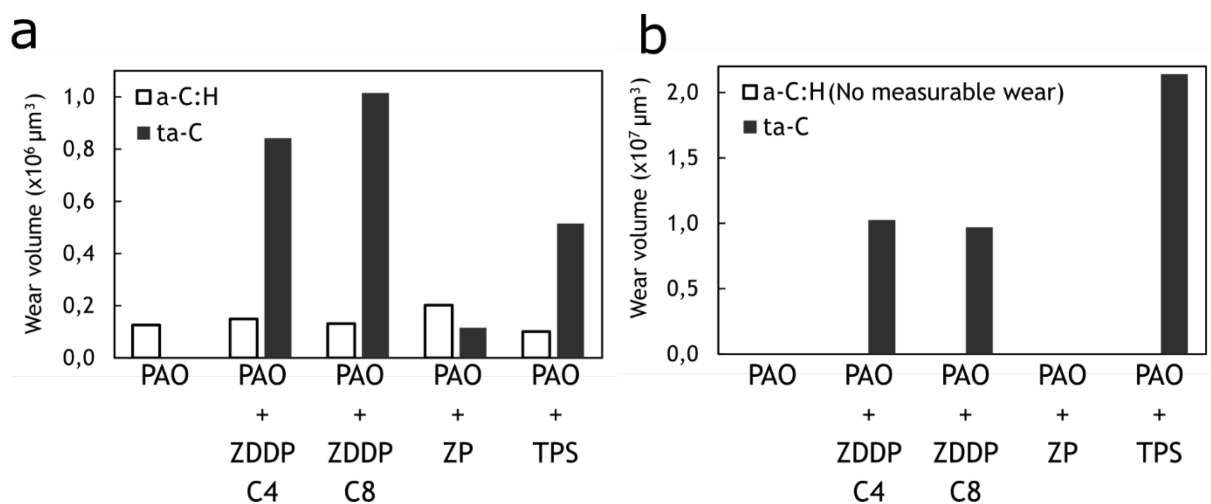


Figure 5. 20. Wear volumes of a-C:H and ta-C cylinders (a) and flats (b) after sliding tests in PAO base oil and PAO + additives lubricants.

### 5.4.3 Surface analysis techniques

Surface chemical analysis were performed by XPS on the flat coupons after sliding tests in PAO + additives lubricants to study the chemical compositions of the surfaces. **Figure 5. 21** shows the relative chemical compositions of P, S, and Zn elements for: (a) a-C:H and (b) ta-C. The atomic concentrations including C and O are given in **Table 5. 6**. Their concentrations are three to five times greater for a-C:H than ta-C. For a-C:H the concentration decreases in the order: ZDDP primary-C4  $\approx$  ZDDP primary-C8 > TPS > ZP. It should be noted that the sulphur content is equivalent between the ZDDP and the TPS additives (S = 2400 ppm) and so is the phosphorus content between ZDDP and ZP (P = 1200 ppm), as presented in the **methods section 3.2**. For ta-C, the atomic concentrations are barely above 1 % and in the case of the ZP additive the P and Zn concentrations are between 0.1 – 0.2 %. The same amounts are found outside of the wear tack due to physical adsorption.

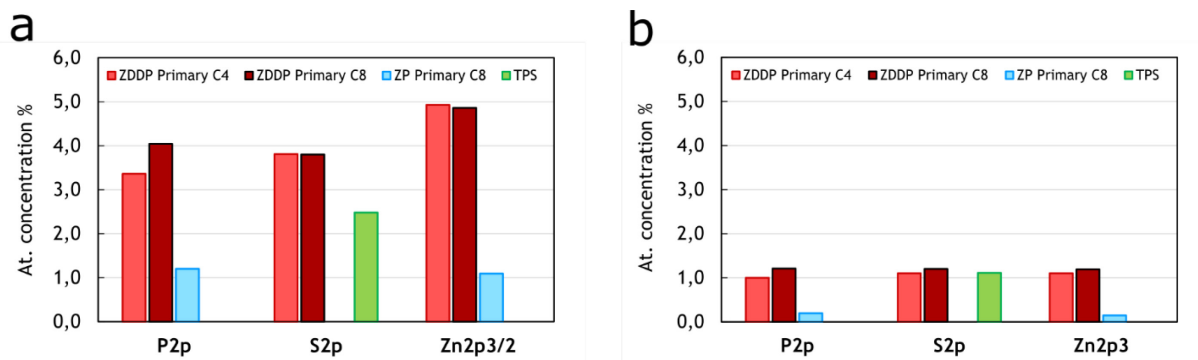


Figure 5. 21. XPS atomic quantification results of a-CH (a) and ta-C(66) (b) after sliding tests in PAO base oil and PAO + additives lubricants.

Table 5. 6. Relative chemical composition obtained from XPS spectra on the a-C:H and ta-C flat coupons after sliding tests in PAO + additives lubricants.

a-C:H					
Additive	C1s (at. %)	O1s (at. %)	P2p (at. %)	S2p (at. %)	Zn2p <sub>3/2</sub> (at. %)
ZDDP I C4	73.6	14.3	3.4	3.8	4.9
ZDDP I C8	71.0	16.4	4.0	3.8	4.9
ZP	83.2	14.6	1.2	0.0	1.1
TPS	81.4	16.1	0.0	2.5	0.0
ta-C-66					
Additive	C1s (at. %)	O1s (at. %)	P2p (at. %)	S2p (at. %)	Zn2p <sub>3/2</sub> (at. %)
ZDDP I C4	87.5	9.3	1.0	1.1	1.1
ZDDP I C8	87.4	9.0	1.2	1.2	1.2
ZP	92.9	6.8	0.2	0.0	0.1
TPS	91.5	7.4	0.0	1.1	0.0

One of the main reasons for testing these additives was to study the effect of sulphur on the friction and wear properties of a-C:H and ta-C. In Chapter 4, it was evidenced that in PAO + ZDDP primary-C4 lubrication, there is a correlation between wear and the presence of C-S bonds for hard taCs and no wear on one side, and lack of S-C bonds for soft and moderate hard DLCs (a-C:H, a-C, and ta-C(52)) on the other side. In this section, those results are compared with the other ZDDP (primary-C8) and the TPS additive to further investigate this phenomenon.

For this reason, particular attention is once again paid to the S2p spectra shown in **Figure 5. 22** obtained inside the flat wear tracks of a-C:H (a) and ta-C (b). They are fitted using a

doublet due to spin-coupling with a separation of 1.2 eV and an intensity ratio of 0.5. Each peak is identified by a color and corresponds to a specific chemical state. The blue peak at B.E. =  $163,3 \pm 0,1$  eV corresponds to S-Zn, and S-P or S=P bonds in thiophosphates. The red peak at B.E. =  $163,3 \pm 0,1$  eV corresponds to S-C bonds. Next, the yellow peak at B.E. =  $164 \pm 0,1$  eV is attributed to the S(0) oxidation state of S-S-S<sup>35</sup> bonds in long polysulphides or the central and terminating sulphur atoms in shorter polysulphides such as S<sub>3</sub><sup>2-</sup> as in [S-S-S]<sup>2-</sup> where the terminating sulphur atoms do not exhibit strong chemical shifts<sup>105</sup>. Lastly, the green peak at B.E. =  $168,4 \pm 0,1$  eV is attributed to oxidized sulphur species such as sulphates.

In the case of a-C:H, there are no S-C bonds (in red) formed with any of the additives. As where for ta-C, the S-C peak is the dominant chemical state of all three spectra. It is also noteworthy to observe that the sulphate peak (in green) is relatively larger in TPS, and very little or no sulphates are found with ZDDP.

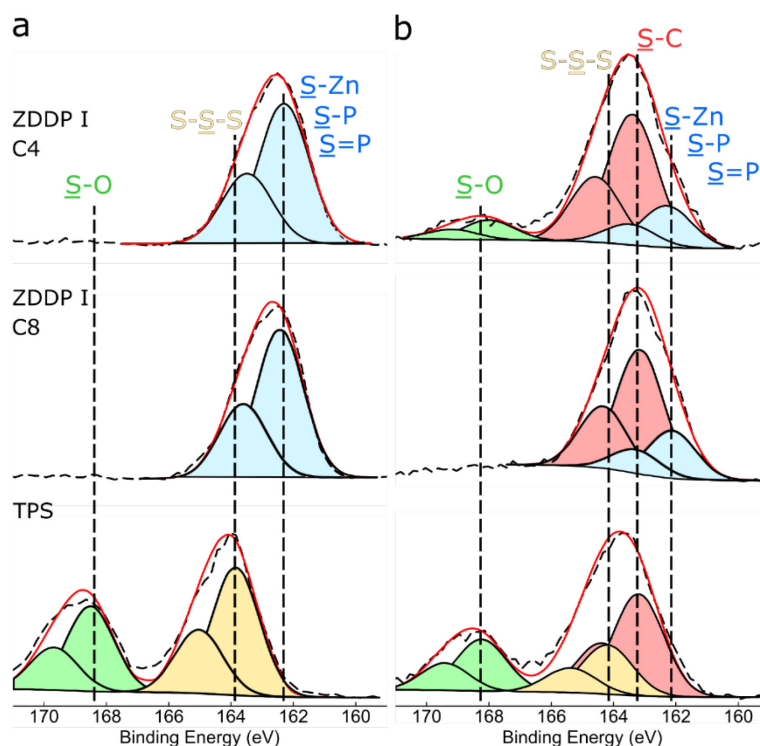


Figure 5. 22. S2p spectra obtained inside the flats wear tracks of a-C:H (a) and ta-C (b) after sliding tests in PAO + additives.

**Figure 5. 23** shows the C1s, O1s, P2p, and Zn2p<sub>3/2</sub> spectra for a-C:H (a-d) and ta-C (e-h). As it can be observed, there are no significant chemical shifts between the spectra obtained with the different additives for a-C:H and ta-C. The C1s XPS spectra show the contribution of three types of chemical bonds: the first peak at B.E. = 284.8 eV is attributed to both *sp*<sup>2</sup> and *sp*<sup>3</sup> carbon bonds in DLC as well as to adsorbed aliphatic carbon. The second and third peaks



at B.E. = 286.5 and 288.3 eV correspond to C–O and O–C=O bonds, respectively. The O1s XPS spectra is fitted using two peaks: the first one at B.E. = 531.7 eV, is attributed to non-bridging oxygen (NBO) and the second one, at B.E. = 533.0 eV, is attributed to bridging oxygen (BO). The P2p spectra are fitted with one doublet with a separation of 0.84 eV and intensity ratio of 0.5. The P2p<sub>3/2</sub> peak located at B.E. = 133.4 eV corresponds to phosphates. The Zn2p<sub>3/2</sub> peak at B.E. = 1022.3 eV corresponds to ZnS or Zn<sup>2+</sup> in zinc phosphates. A small peak corresponding to Zn–O bonds is found for the a-C:H in ZP additive at B.E. = 1024.3 eV. The parameters used for the fitting procedure of all the spectra are given in **Table A. 2** and **Table A. 3** for a-C:H and ta-C, respectively.

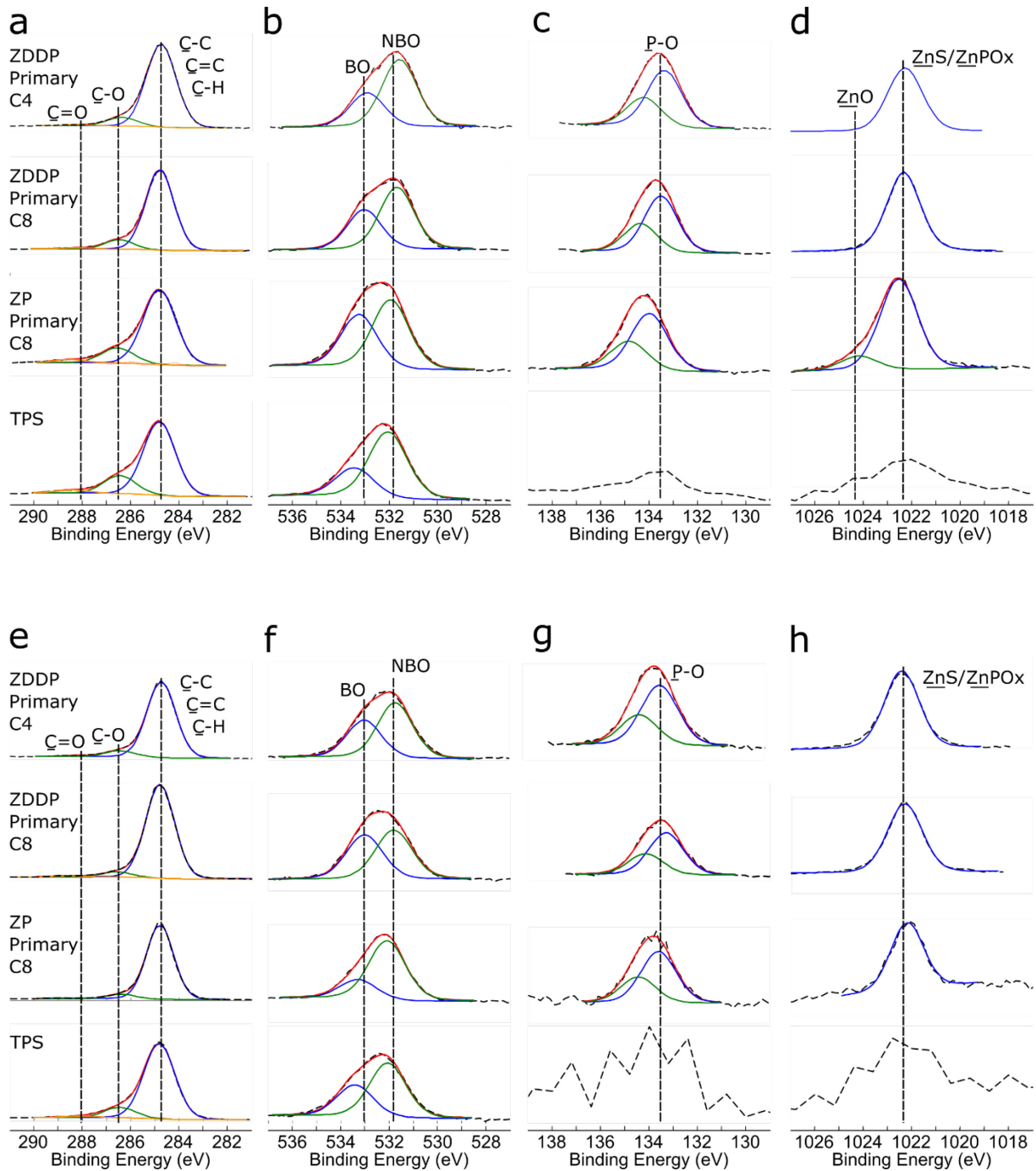


Figure 5. 23. C1s, O1s, P2p, and Zn2p<sub>3/2</sub> spectra obtained on the flat coupons of a-C:H (a-d) and ta-C (e-h) after sliding tests in PAO + additives lubricants.

In order to investigate whether or not these additives form tribofilms on the a-C:H and ta-C surfaces, SEM + EDX analysis were performed on the flat coupons. **Figure 5. 24** shows representative SEM images of a-C:H and ta-C surfaces after sliding tests in PAO + additives. Tribofilms were formed on the a-C:H surfaces (**Figure 5. 24a-c**) under lubrication with ZDDP primary-C4, ZDDP primary-C8, and ZP (marked with green-dashed circles). Their chemical composition was checked by EDX analysis, see **Table 5. 7**. The tribofilms formed

with both ZDDP molecules (**Figure 5. 24a and b**) consist of tribopatches that have an average diameter of about 1  $\mu\text{m}$  and up to 5  $\mu\text{m}$  for the largest ones. The tribopatches formed with ZP (**Figure 5. 24c**) have a diameter smaller than 1  $\mu\text{m}$ , but are more homogenous in size and more densely packed. The ta-C surfaces show horizontal scratches (in agreement with the wear results) and no tribofilms were observed. Only small particles containing traces of the additive-derived elements were found (marked by green-dashed circles).

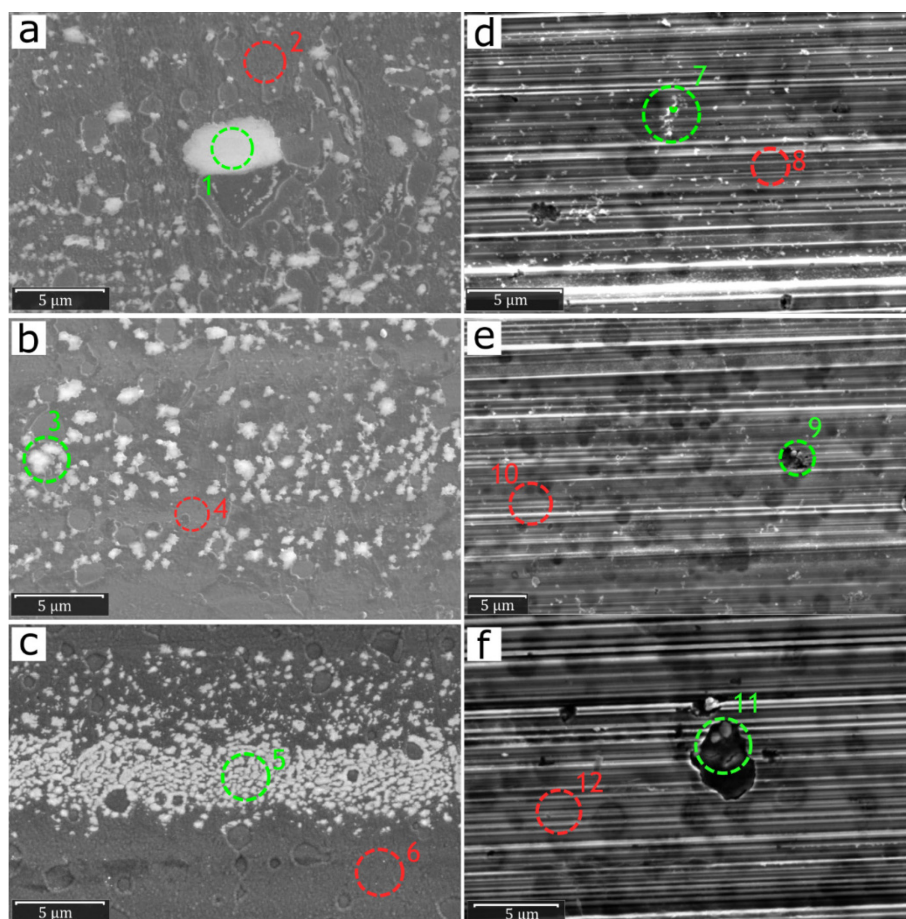


Figure 5. 24. Representative SEM images (SE detection mode) of a-C :H in (a) ZDDP primary-C4, (b) ZDDP primary-C8, (c) ZP and ta-C in (d) ZDDP primary-C4, (e) ZDDP primary-C8 and (f) TPS.

Table 5. 7. Elemental quantification obtained by EDX spectra recorded on the a-C:H and ta-C flats indicated by green and red dashed circles in Figure 5. 24

		Chemical composition (at.%)					
		Spectrum #	C	O	P	S	Zn
a-C:H	ZDDP I	01	84.3	5.0	2.8	1.9	6.0
	C4	02	99.3	0.7	0.0	0.0	0.0
	ZDDP I	03	88.3	3.3	1.6	1.9	4.9
	C8	04	99.7	0.3	0.0	0.0	0.0
	ZP	05	91.7	3.5	1.6	0.0	3.2
		06	99.8	0.2	0.0	0.0	0.0
ta-C	ZDDP	07	98.8	0.2	0.3	0.6	0.1
	I C4	08	99.8	0.2	0.0	0.0	0.0
	ZDDP	09	98.8	0.2	0.2	0.7	0.1
	I C8	10	99.8	0.2	0.0	0.0	0.0
	TPS	11	90.1	8.6	0.0	1.3	0.0
		12	99.6	0.4	0.0	0.0	0.0

#### 5.4.4 Summary and Conclusions

In summary, four different additives, namely ZDDP primary-C4, ZDDP primary-C8, ZP, and TPS, were studied on a-C:H and ta-C coatings. The a-C:H coatings exhibit no wear, and  $\mu$  varies between 0.07 – 0.12 (lowest  $\mu$  with longer alkyl chains). MEB and XPS analysis revealed the formation of ZDDP-derived patches on the surfaces. Ta-C exhibits no wear in PAO, with sulphurless additive lubrication, PAO + ZP, there was no change in its friction and wear properties as the ZP molecule did not react with the ta-C surface. However, with sulphur-containing additives, severe wear and a rise of  $\mu$  occur in PAO + ZDDP (both primary-C4 and C8) and PAO + TPS. The correlation observed in Chapter 4 between the formation of S-C bonds and severe wear of hard ta-C coatings continues to apply. SEM and XPS analysis revealed that ZDDP-derived tribofilms do not form on the ta-C surfaces, only a very small amount (about 1%) of additive-derived elements were detected.

---

## Chapter 6: Contribution of controlled environment lubrication to the comprehension of the tribochemistry of S-containing additives on DLC surfaces.

---


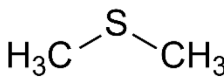
In the previous chapters, liquid lubricants used in the automotive and other mechanical applications were used to study the tribological behavior of DLC systems. In this chapter, sliding tests are performed using an Analytical Tribometer in Controlled Environment (ATCE), which allows the introduction of gas additives in a wide range of pressures to study specific molecules. In this way, a specific chemical function of a complex additive molecule can be targeted to obtain a simpler tribological system.

## 6.1 Ta-C in controlled gas environments

### 6.1.1 Introduction

For this study, ball-on-disk sliding tests were performed with an ATCE system described in the **Methods section 3.3.4**. XPS analysis are carried out after the sliding tests without the samples being exposed to air. This allows a better analysis of the tribochemical reactions taking place at the sliding interface. The testing conditions used were as follows: applied load  $F_N = 5$  N (corresponding to an initial maximum Hertzian contact pressure  $P_{\text{Hertz}} = 800$  MPa), temperature  $T = 20^\circ\text{C}$ , average speed  $v = 0.2$  mm  $\text{s}^{-1}$ , stroke length  $l = 2$  mm for a total of 100 passages (50 cycles). The tests were performed in three different controlled environments: first, in UHV to study the tribological behavior of self-mated ta-Cs without any lubrication as reference; second, in  $\text{O}_2$  environment to investigate the effect of oxygen, which is an element present in many additives and oils; and third in di-methyl sulfide (DMS) environment to study the tribochemistry of sulphur-containing molecules and its effect on the friction and wear properties of ta-Cs. The tested environments are summarized in **Table 6. 1**.

Table 6. 1. Tested environments during the sliding friction tests.

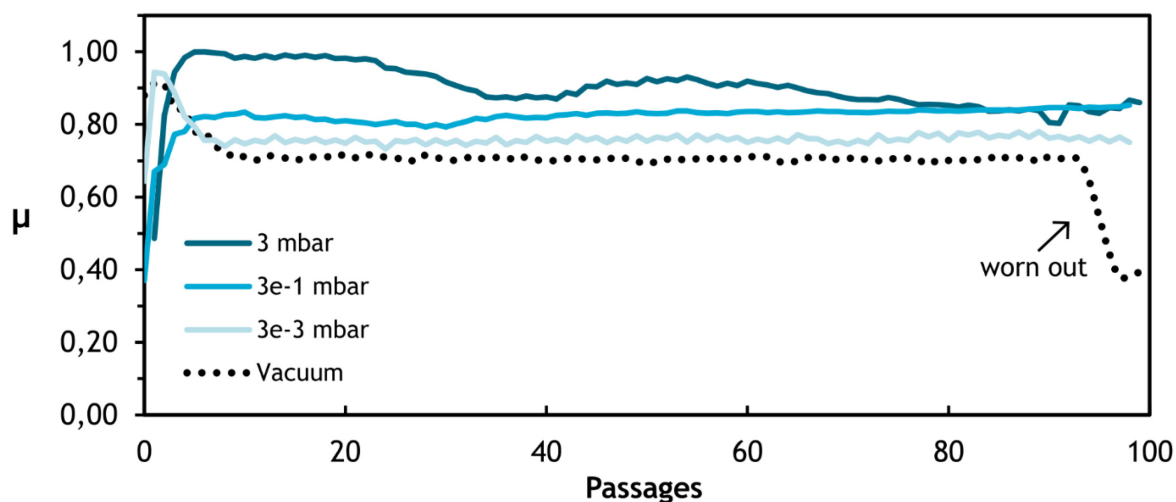
 el	Conditions
UHV	$P = 1 \times 10^{-9}$ mbar
$\text{O}_2$	$P_1 = 3.10^{-3}$ mbar $P_2 = 3.10^{-1}$ mbar $P_3 = 3$ mbar
DMS 	$P_1 = 3.10^{-3}$ mbar $P_2 = 3.10^{-1}$ mbar $P_3 = 3$ mbar

### 6.1.2 Friction and wear results

The friction curves of ta-C(66)/ta-C(66) tribopairs obtained from sliding tests in UHV,  $\text{O}_2$  and DMS environments at different pressures are shown in **Figure 6. 1 a and b**. In UHV the friction coefficient  $\mu$  was about 0.70 throughout the test. After 95 passages the ta-C flat was completely worn out and the steel substrate was exposed, which caused  $\mu$  to decrease. The test was stopped shortly afterwards at 100 passages. In  $\text{O}_2$  environment,  $\mu$  is close to 0.75 at

the lowest pressure ( $P = 3 \cdot 10^{-3}$  mbar) and  $\mu = 0.80 - 1.00$  at the intermediate and highest pressure ( $P = 3 \cdot 10^{-1}$  mbar and  $P = 3$  mbar). In DMS at low and intermediate pressures ( $P = 3 \cdot 10^{-3}$  mbar and  $P = 3 \cdot 10^{-1}$  mbar),  $\mu$  oscillates between  $0.80 - 1.00$ . At the highest pressure ( $P = 3$  mbar), there is an incredible friction reduction.  $\mu = 0.05$  and is steady throughout the whole test.

a



b

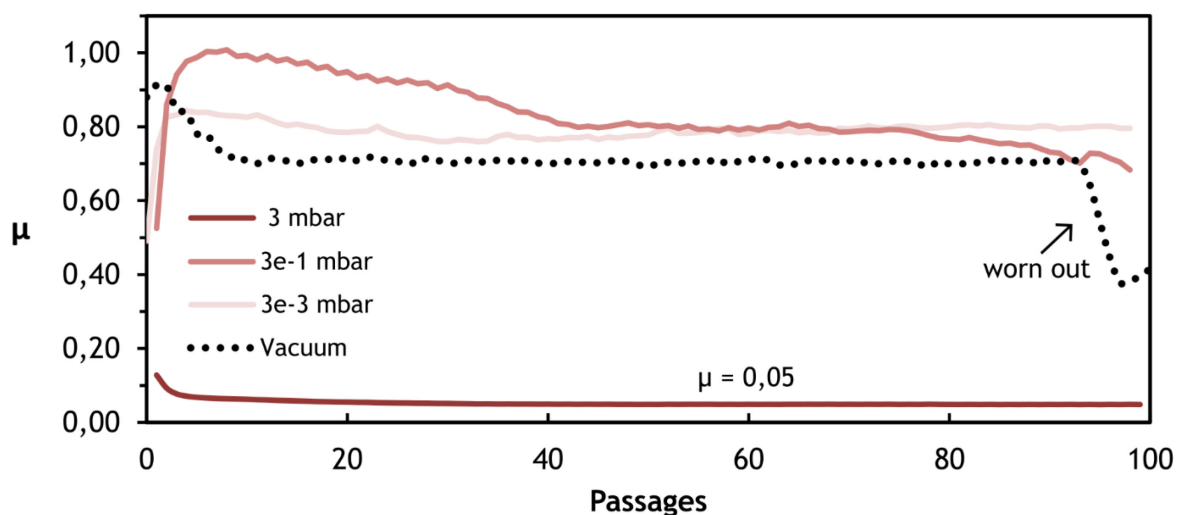


Figure 6. 1. Evolution of friction coefficient of ta-C(66) during sliding tests in controlled environments: (a)  $O_2$  and (b) DMS at 3 mbar,  $3 \cdot 10^{-1}$  mbar, and  $3 \cdot 10^{-3}$  mbar. The dotted black line is the reference test in UHV.

Stick-slip phenomena (indicative of adhesive wear) was observed during the friction tests for all the curves where  $\mu > 0.7$ . The only case where this was not observed was for DMS at high pressure ( $P = 3$  mbar), where  $\mu = 0.05$ . Images of the instantaneous friction coefficient for one and a half cycles are shown in **Figure 6. 2**.



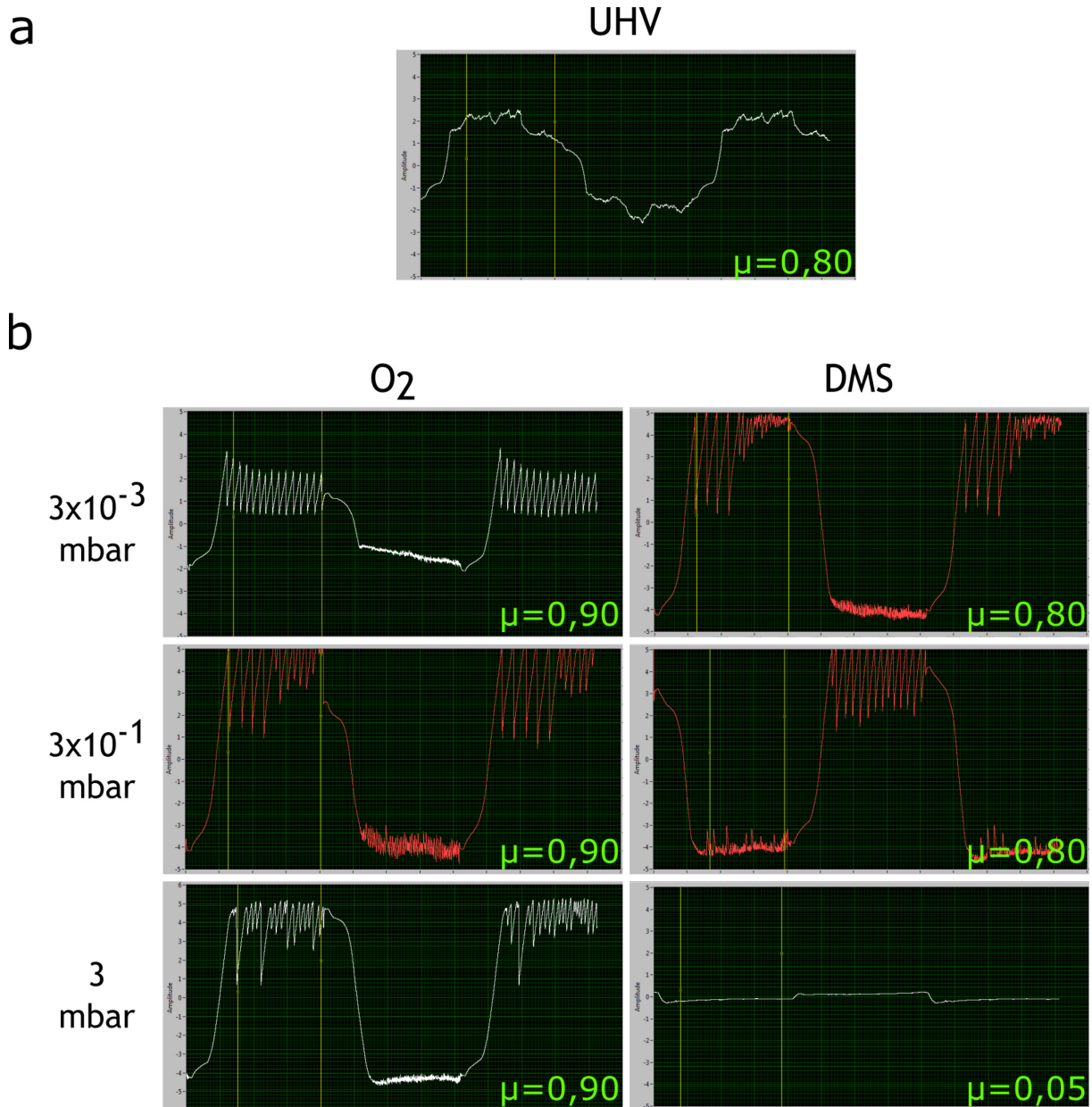


Figure 6. 2. Tangential force signals of one and a half cycles of ta-C sliding in: (a) UHV, and (b) O<sub>2</sub>, and DMS environments.

Optical images of the wear tracks after sliding in UHV are shown in **Figure 6. 3**. In these tests, there is no oil to evacuate the wear debris generated during sliding so they remain on the surface of the wear tracks. The images were taken before cleaning the samples to observe the wear debris (that resemble black smeared stains). Such wear particles have already been observed during sliding tests of different DLCs in various atmospheres<sup>106–108</sup>. In UHV the ta-C flat was completely worn out and the steel substrate was exposed. The ta-C coating on the ball also underwent severe wear, but was not fully removed.



vacuum

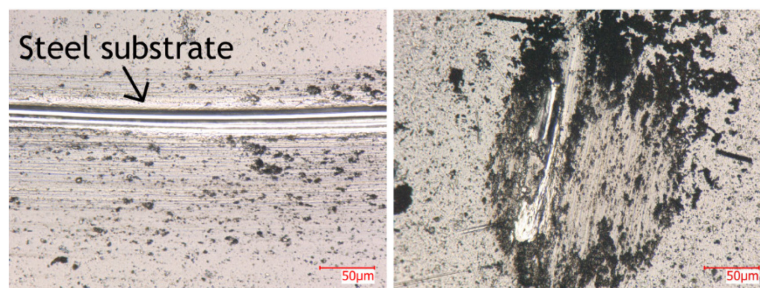


Figure 6. 3. Optical images of the ta-C flat (left) and ball (right) after sliding tests in UHV. The images were taken before cleaning the samples to avoid removing the black wear debris.

The wear tracks after sliding tests in O<sub>2</sub> and DMS are shown in **Figure 6. 4a and b**, respectively. It can be observed that black wear debris are found on the wear tracks of the tests that exhibited high friction ( $\mu > 0.7$ ), which is the case for O<sub>2</sub> environment at the three tested pressures and in DMS at the lowest ( $P = 3 \cdot 10^{-3}$  mbar) and intermediate pressures ( $P = 3 \cdot 10^{-1}$  mbar). In the only case where friction was low ( $\mu = 0.05$ ), in DMS at  $P = 3$  mbar, the wear tracks are not even visible under the observed conditions and no wear debris were found.

Figure 6. 4. Optical images of the ta-C flats (top) and balls (bottom) after sliding tests in: (a) O<sub>2</sub> and (b) DMS at low, intermediate, and high pressures ( $P = 3 \cdot 10^{-3}$  mbar,  $P = 3 \cdot 10^{-1}$  mbar, and  $P = 3$  mbar, respectively). The images were taken before cleaning the samples to avoid removing the black wear debris particles.

Optical interferometer images of the ta-C flats and balls after sliding in UHV are shown in **Figure 6. 5**. The ta-C coating on the flat was completely worn out and the maximum wear depth went beyond 3  $\mu\text{m}$  (the coating thickness is 2.0  $\mu\text{m}$ ). Similarly, the ball also exhibited severe wear although the wear depth was  $\approx 1.0 \mu\text{m}$  (50% of the coating thickness).

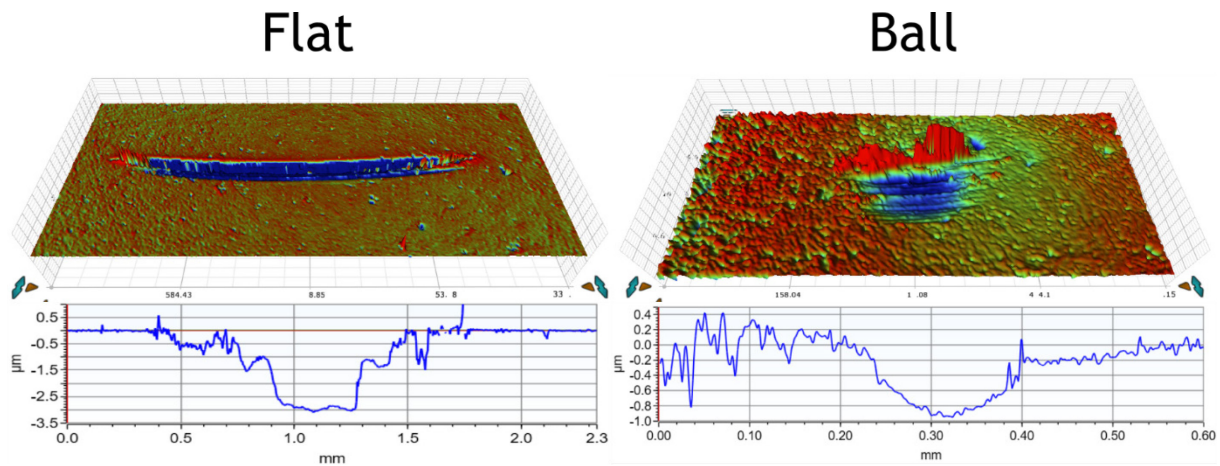


Figure 6. 5. Optical interferometer images of the wear tracks of ta-C(66) flat and ball after sliding in UHV. The image of the ball is flattened to observe the wear scar.

The wear tracks after sliding tests in  $\text{O}_2$  are shown in **Figure 6. 6**. At the lowest pressure ( $P = 3 \cdot 10^{-1}$  mbar), the flat and ball have a wear depth of approximately 1.0  $\mu\text{m}$ . At the intermediate and highest pressures ( $P = 3 \cdot 10^{-1}$  and  $P = 3$  mbar) the flat wear depth is greatly reduced (less than 0.1  $\mu\text{m}$ ), and the ball wear depth decreases to 0.6  $\mu\text{m}$ .

The wear tracks in DMS are shown in **Figure 6. 7**. At the lowest and intermediate pressures ( $P = 3 \cdot 10^{-3}$  and  $3 \cdot 10^{-1}$  mbar), the flats exhibit very little wear (wear depth  $< 0.1 \mu\text{m}$ ) while the balls wear depth is between 0.5 – 0.8  $\mu\text{m}$ . At the highest pressure ( $P = 3$  mbar), there is no measurable wear and the wear tracks are barely visible.

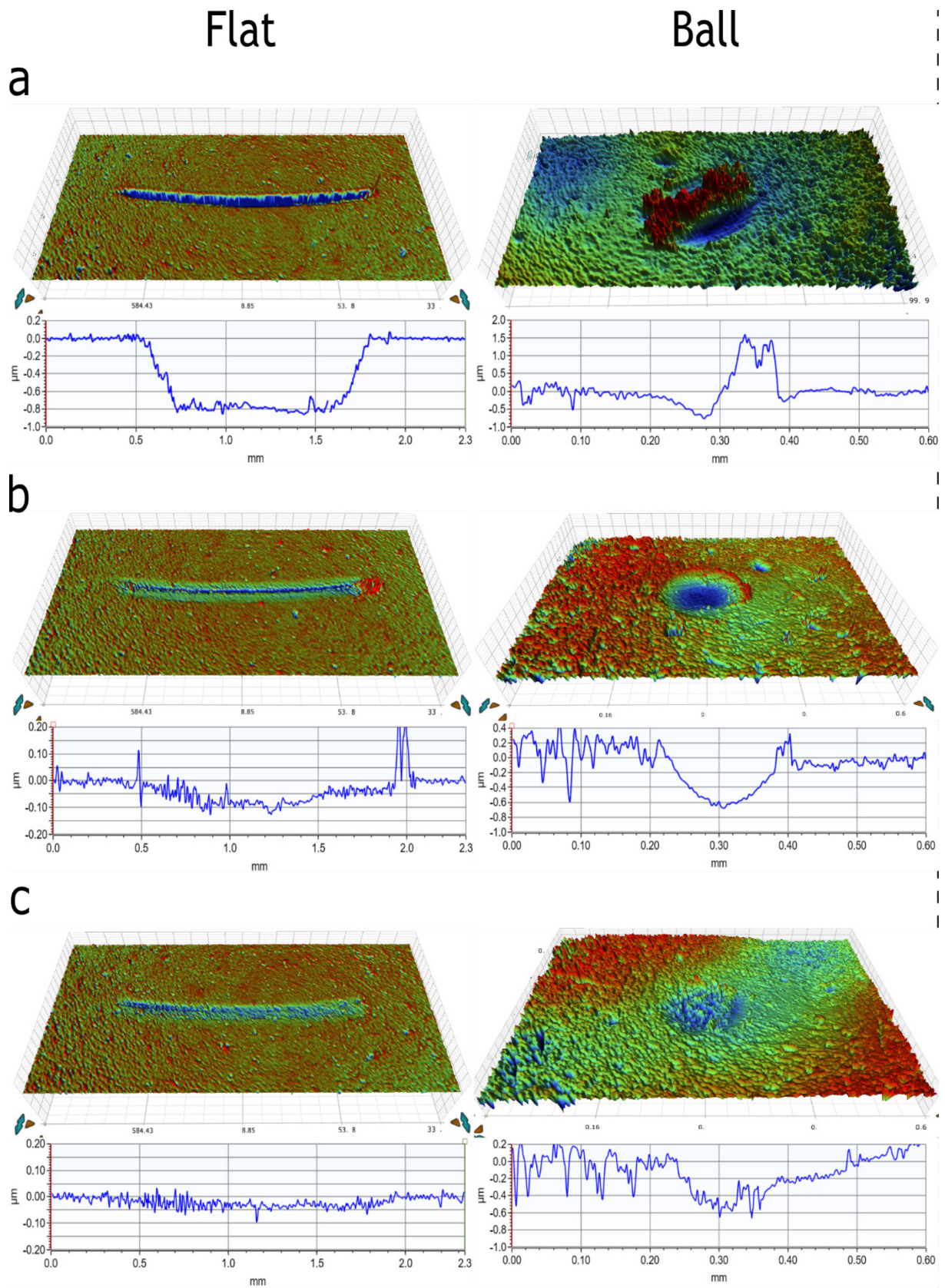


Figure 6. 6. Optical interferometer images of the wear tracks of ta-C(66) flats and balls after sliding tests in O<sub>2</sub> environment at different pressures: (a)  $3 \cdot 10^{-3}$  mbar, (b)  $3 \cdot 10^{-1}$  mbar, and (c) 3 mbar.



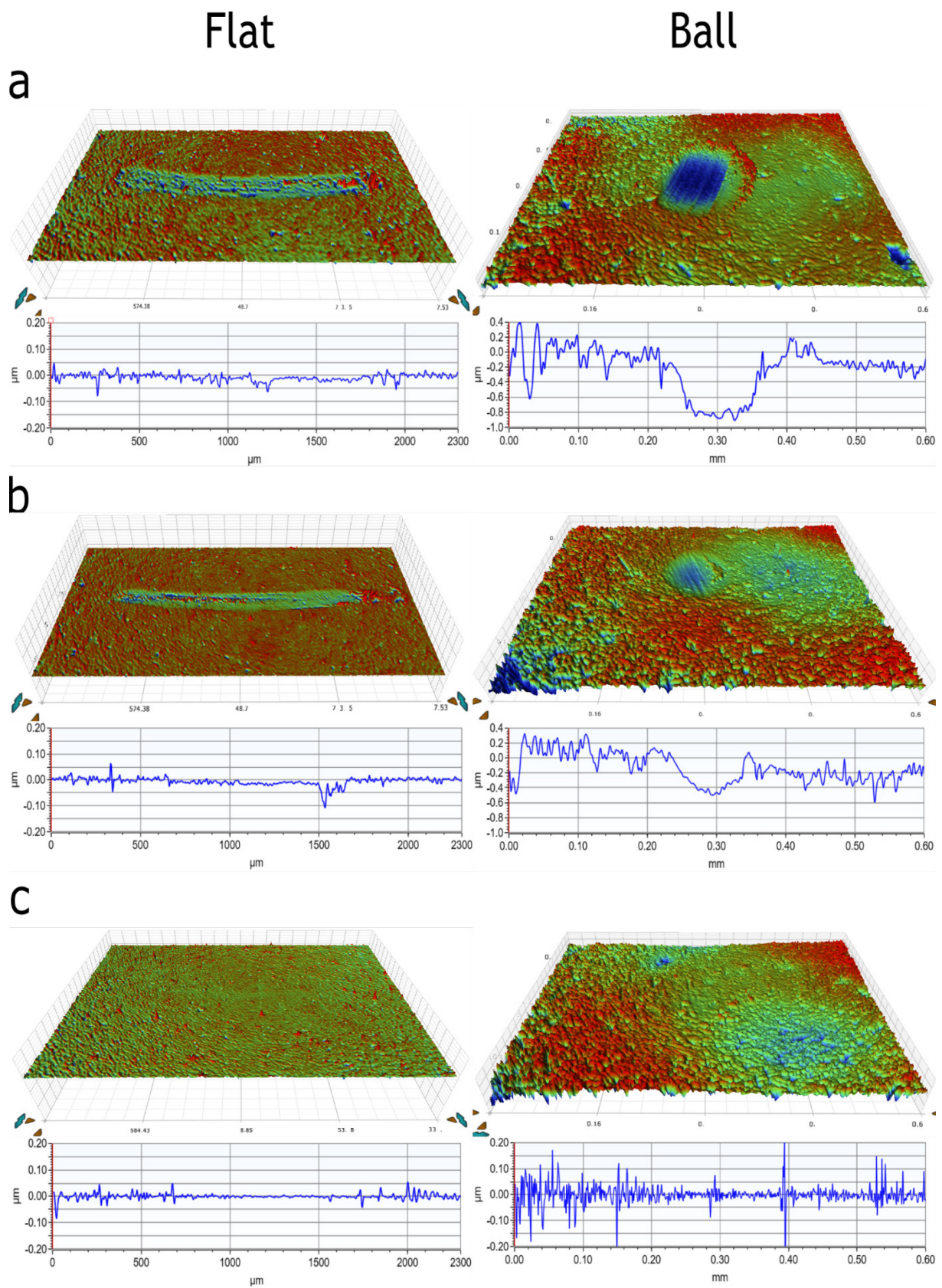


Figure 6. 7. Optical interferometer images of the wear tracks of ta-C(66) flats and balls after sliding tests in DMS environment at different pressures: (a)  $3 \cdot 10^{-3}$  mbar, (b)  $3 \cdot 10^{-1}$  mbar, and (c) 3 mbar.

The wear volumes were calculated from the optical interferometer measurements and are shown in **Figure 6. 8**. At intermediate and high O<sub>2</sub> pressures, wear is greatly reduced compared to UHV and O<sub>2</sub> at low pressure. In DMS, even at the lowest and intermediate pressures wear is greatly inhibited, and at the highest pressure it is completely avoided.

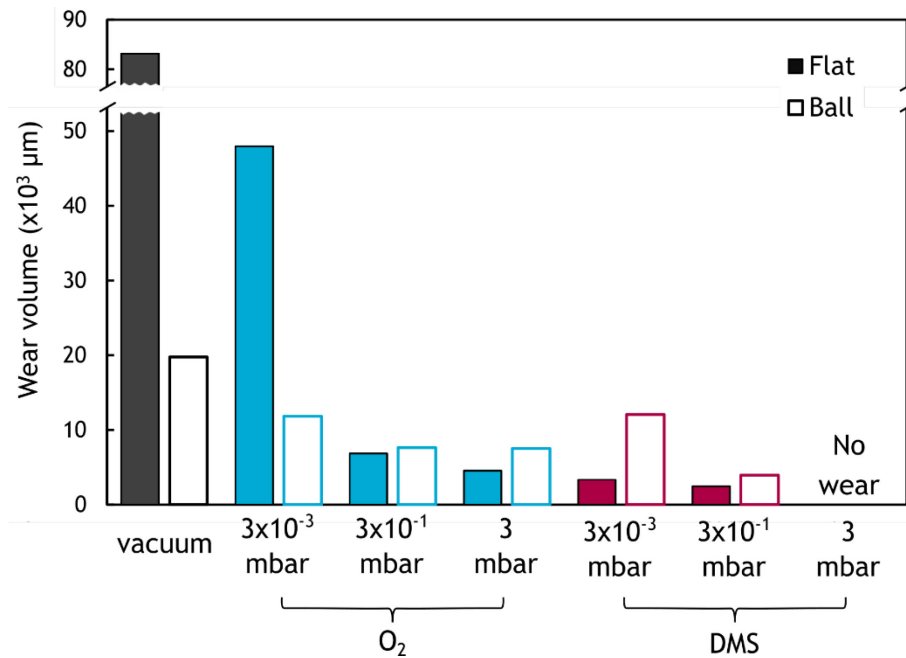


Figure 6. 8. Wear volumes of the ta-C(66) flats and balls measured by optical interferometer after sliding tests in UHV, O<sub>2</sub>, and DMS environments at different pressures.

### 6.1.3 Raman spectroscopy

The black wear debris were analyzed by Raman Spectroscopy (see **Methods section 3.4.2** for analysis conditions) on the ta-C flat after sliding tests in O<sub>2</sub> environment at low pressure ( $P = 3.10^{-3}$  mbar). This test showed the second largest amount of wear after the vacuum test. The Raman spectra are shown in **Figure 6. 9**. Three zones (indicated by red points) were analyzed to compare their ratios between the intensities of the G and D peaks at different laser energies to look for indications of graphitization. At laser power = 5%, the spectra obtained outside the wear track (a) and inside the wear track on the white region (b) are identical. However, the spectra on the black wear debris exhibit a very slight increase of the intensity of the D peak, suggesting graphitization occurred. At higher laser energy (100%), there is no change on spectra (a) and (b), but spectrum (c) shows an even higher increase in intensity of the D peak. It is obvious that the laser energy has an effect on the obtained spectra. Therefore, with the current experimental evidence, it is not very clear how to prove that graphitization indeed occurred. In the future, TEM observations could be performed to study the structure of the black wear debris and study if graphitic structures are observed.

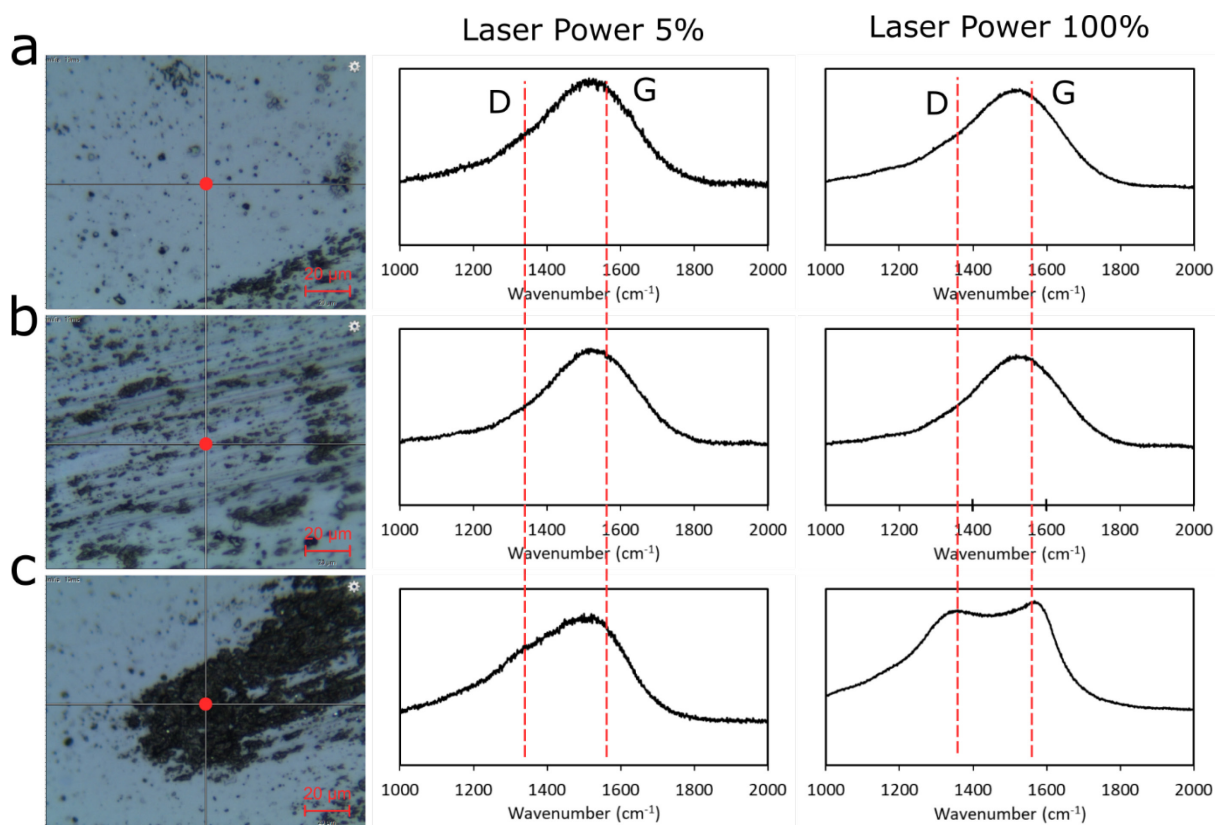


Figure 6. 9. Raman spectra at different laser powers recorded on the ta-C flat after sliding test in  $O_2$  environment at  $P = 3 \cdot 10^{-3}$  mbar on different regions of interest: (a) outside of the wear track, (b) inside the wear track on the white region, (c) inside the wear track on the black wear debris.

#### 6.1.4 XPS analysis

After the sliding tests, the disks and balls were transferred to the XPS analysis chamber without being exposed to air. The surface chemical composition were analyzed in order to study their chemical states and understand the different wear and friction results obtained. The atomic concentrations of sulphur and oxygen in DMS and  $O_2$  environments on the flats and balls are shown in **Figure 6. 10 a and b**, respectively. The atomic concentrations including carbon are given in **Table 6. 2**. In DMS, the highest amount of sulphur found on the wear tracks was at the lowest pressure ( $P = 3 \cdot 10^{-3}$  mbar), which is counter-intuitive as higher amounts of sulphur were expected at higher pressure. This matter will be addressed in the discussion section. The sulphur concentration on the disk decreases in the order:  $3 \cdot 10^{-3} > 3 \cdot 10^{-1}$  mbar  $>$  3 mbar. For the balls, it decreases in the order:  $3 \cdot 10^{-3} >$  3 mbar  $>$   $3 \cdot 10^{-1}$  mbar. In  $O_2$  environment, the oxygen concentration was similar or slightly higher outside the wear tracks compared to the inside. Before introducing the samples to the ATCE system, they were exposed to air while being stored. Thus oxygen is always found on samples exposed to air due to adventitious contamination, oxidation, water etc.... However, the chemical state between t

outside and inside of the wear tracks was different, and will be shown in the XPS spectra below. The wear tracks on the balls in O<sub>2</sub> were not visible on the acquired picture. Indeed, there was no chemical contrast compared to the outside where oxygen is also present. Therefore the wear tracks could not be analyzed.

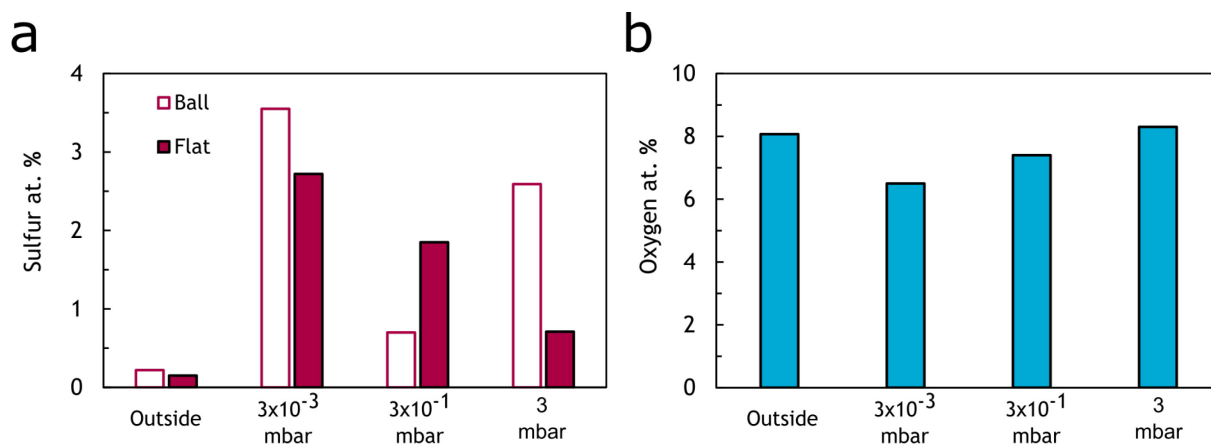


Figure 6. 10. XPS elemental quantification obtained from: (a) ta-C balls and flats in DMS and (b) ta-C flats in O<sub>2</sub>.

Table 6. 2. Relative chemical composition obtained from XPS spectra on ta-C flats and balls after sliding tests in O<sub>2</sub> and DMS environments.

Environment	Pressure (mbar)	Sample	C1s (at. %)	O1s (at. %)	S2p (at. %)
O <sub>2</sub>	3.10 <sup>-3</sup>	flat	93.5	6.5	0.0
	3.10 <sup>-1</sup>	flat	92.6	7.4	0.0
	3.10 <sup>0</sup>	flat	91.7	8.3	0.0
	Outside	flat	91.9	8.1	0.0
DMS	3.10 <sup>-3</sup>	ball	92.7	3.8	3.6
		flat	93.9	3.3	2.7
	3.10 <sup>-1</sup>	ball	90.5	8.8	0.7
		flat	92.9	5.3	1.9
	3.10 <sup>0</sup>	ball	92.8	4.6	2.6
		flat	97.2	2.1	0.7
	Outside	ball	92.7	7.1	0.2
		flat	93.9	6.0	0.2



The S2p spectra obtained from inside the wear tracks of the ta-C balls and disks are shown in Figure 6. 11. XPS S2p spectra obtained after sliding tests in DMS environment from inside the wear tracks of: (a) ta-C balls (b) ta-C disks. **Figure 6. 11.** They are fitted using a doublet due to spin-coupling with a separation of 1.2 eV and an intensity ratio of 0.5. The spectra recorded outside the wear tracks are not shown as there were only very small traces of sulphur ( $\approx 0.2$  at. %). The S2p photopeak obtained on the disks are composed of one main contribution (in red) at B.E. = 163.2 eV, which corresponds to organic sulphur species (C-S-X bonds). As already mentioned in Chapter 4, it is difficult to distinguish between C-S-C, C-S-S, and C-S-H chemical states as the shifts in B.E. are close to 0.1-0.2 eV from each other. For the balls, there was a slight difference between the low and intermediate pressure compared to the high pressure. At high pressure ( $P = 3$  mbar), the peak is shifted (+ 0.4 eV) towards higher B.E. = 163.6 eV. This shift is larger than the error measurement which is considered to be 0.1 eV, indicating that the shift is significant and representative of a different chemical state. It could explain the decrease in friction coefficient  $\mu = 0.05$  compared to the tests in low and intermediate pressures where  $\mu$  was higher than 0.8. This matter will be addressed in the discussion section ahead. It should be noted that no peak was observed at B.E. = 164.0 eV, which corresponds to the S(0) oxidation state in S-S-S bonds in long polysulphides. There is a second small contribution of oxidized sulphur species between 166.0 eV – 166.8 eV corresponding to sulphites and sulphates, respectively.

The C1s and O1s spectra acquired at different pressures show no significant difference and are not shown here. The C1s spectra is composed as usual of three contributions: the first peak at B.E. = 284.8 eV is attributed to both  $sp^2$  and  $sp^3$  carbon bonds in DLC as well as to adsorbed aliphatic carbon. The second and third peaks at B.E. = 286.5 and 288.1 eV correspond to C-O and O-C=O bonds, respectively. The O1s XPS spectra is fitted using only two peaks: the first one at B.E. = 531.7 eV is attributed to O=C bonds and the second one at B.E. = 533.0 eV is attributed to O-C bonds. The full detail of the parameters use for the fitting procedure of the spectra are given in **Table A. 4.**

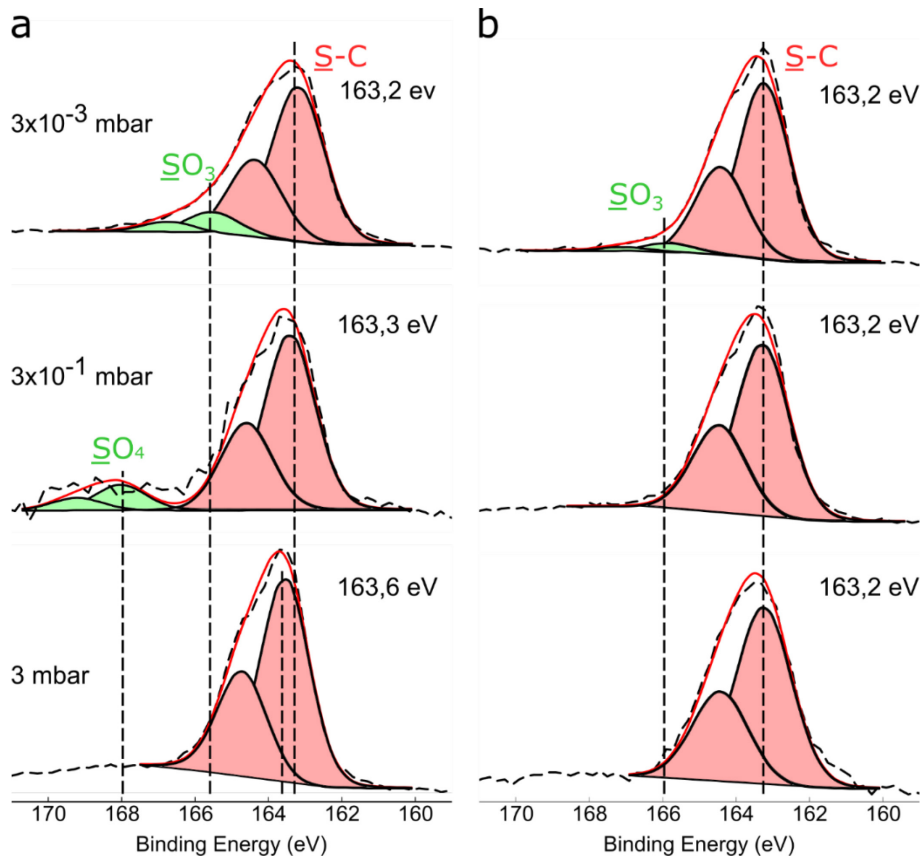


Figure 6. 11. XPS S2p spectra obtained after sliding tests in DMS environment from inside the wear tracks of: (a) ta-C balls (b) ta-C disks.

The O1s spectra obtained from the ta-C flats are shown in **Figure 6. 12**. The spectrum outside the wear tracks is made up of oxygen derived from adventitious contamination and water. There is no difference between the spectra recorded at the three different pressures: in all cases the O1s photopeak is composed of two contributions. The first one at B.E. = 531.4 eV and the second one at B.E. = 532.9 eV, corresponds to O=C and O-C bonds<sup>109-111</sup>, respectively. Similarly, there is no difference in the C1s which are composed of three contributions, as usual: the first peak at B.E. = 284.8 eV is attributed to  $sp^2$  and  $sp^3$  carbon bonds in DLC and adsorbed aliphatic carbon. The second and third peaks at B.E. = 286.5 and 288.1 eV correspond to C-O and O-C=O bonds, respectively. The full details of the parameters used for the fitting procedure of the spectra are given in **Table A. 5**.

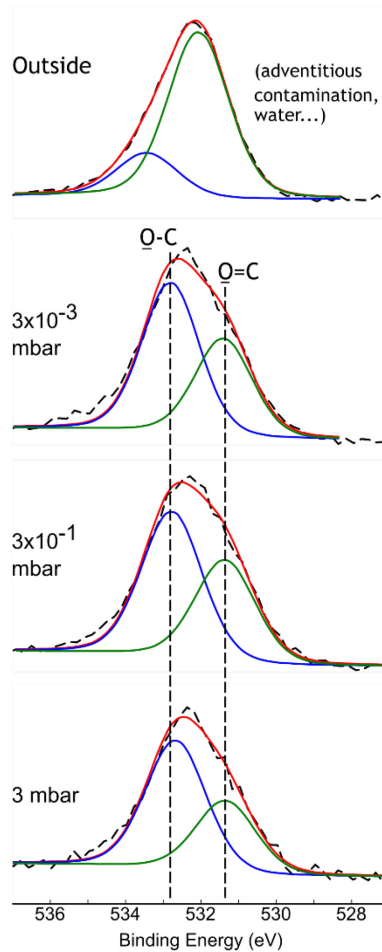


Figure 6. 12. XPS O1s spectra obtained after sliding tests in O<sub>2</sub> environment from inside and outside the wear tracks of: (a) ta-C balls and (b) ta-C disks.

### 6.1.5 Discussion

In the previous chapters, it was shown that hard ta-Cs exhibited wear in the presence of sulphur-containing additives in liquid lubrication, while softer DLCs did not. The results presented in this chapter seem contradictory, as in DMS environment at sufficiently high pressure ( $P = 3$  mbar), the ta-C surface is passivated and wear is avoided. The tests were conducted with another tribometer and different testing conditions had to be used. There are two main differences between the tests conducted in the previous and present chapter that could explain the discrepancy in the results. First, in the sliding tests in controlled atmosphere, the temperature inside the tribometer chamber is 20°C, while in the tests conducted with liquid lubricants the temperature is 110°C. It is possible that the sulphur-induced wear mechanism of ta-Cs is temperature dependent; this remains to be investigated. Second, the DMS molecule already contains C-S-C bonds in its structure so the C-S-X bonds detected by XPS on the ta-C surface could come from this fragment of the molecule, and not necessarily from ta-C carbon atoms bonded to the sulphur atoms from the DMS molecule. If the DMS

molecule decomposes into small fragments or entirely (breaking its C-S-C fragment) then the released sulphur atoms could react with the ta-C surface. To explain the low friction coefficient observed ( $\mu = 0.05$ ), it is reasonable to assume that a sulphur tribofilm was formed on the ta-C surface, and not diffused into the ta-C matrix as in the previous chapters. In the S2p spectra, there was no peak detected at 164.0 eV corresponding to S-S-S bonds in long polysulfides. This suggests that a very thin sacrificial sulphur tribofilm (perhaps only a few monolayers thick) is formed.

In the previous chapters, there was a correlation between severe wear and the presence of C-S bonds at B.E. = 163.3 eV. In this chapter, when wear is observed, at low and intermediate pressures, the C-S bonds are also observed at B.E. = 163.2 eV, while at high pressure ( $P = 3$  mbar) when there was no wear, the C-S bonds were observed at B.E. = 163.6 eV. This chemical shift to higher energy is significant as the error measurement is considered to be 0.1 eV. It could represent a different chemical state such as C-S-S or C-S-H bonds which could be expected from a thin sulphur tribofilm and low friction. This aspect remains unclear as it is difficult to distinguish between C-S-C, C-S-S, and C-S-H chemical states. Performing tests with other molecules such as dimethyl disulfide (DMDS), dimethyl trisulfide (DMTS) which contain C-S-S-C and C-S-S-S-C fragments, respectively, or other organic polysulfides could help to shed more light in this matter.

### **6.1.6 Summary and Conclusions**

The tribological properties of ta-C were investigated by reciprocating sliding test in UHV, O<sub>2</sub>, and DMS environments at low ( $P = 3 \cdot 10^{-3}$  mbar), intermediate ( $P = 3 \cdot 10^{-1}$  mbar) and high pressure ( $P = 3$  mbar). High friction ( $\mu > 0.70$ ), stick-slip phenomena, and severe to mild wear was observed in UHV, O<sub>2</sub> (all three pressures), and DMS at low and intermediate pressures. However, in DMS at high pressure ( $P = 3$  mbar)  $\mu$  is reduced to 0.05 and wear is completely inhibited by passivation of the ta-C surface by the DMS additive. Presumably, passivation occurs by the formation of a thin sulphur film which acts as lubricant. Although, complementary tests with other polysulphide molecules and analyses are needed to check. This subject will be further addressed in the suggestion for future works sections at the end of this work.

## 6.2 DLCs lubricated in neat ZDDP film.

### 6.2.1 Introduction

In Chapters 4 and 5, the tribological properties of DLCs in liquid lubrication with ZDDP-containing solutions were studied. The decomposition and reaction mechanisms of ZDDP were investigated for various DLCs by Quantum Chemical Simulations, where ZDDP-molecules were introduced between two modelled DLC asperities under an applied normal pressure  $P_z$  and shear stress.

In this chapter, reciprocating sliding tests were conducted using the same analytical tribometer under controlled environment (ATCE) as in Chapter 6.1. Before introducing the disk into the tribometer chamber, a thin layer of neat ZDDP was applied on its surface. The procedure consists of applying a small drop of liquid ZDDP using a micropipette and spreading the drop across the surface while removing the excess using aluminum sheet foils. The resulting ZDDP film can be observed in **Figure 6. 13**. The optical interference suggest the ZDDP layer has a thickness of a few hundreds of nm and is not perfectly homogenous.

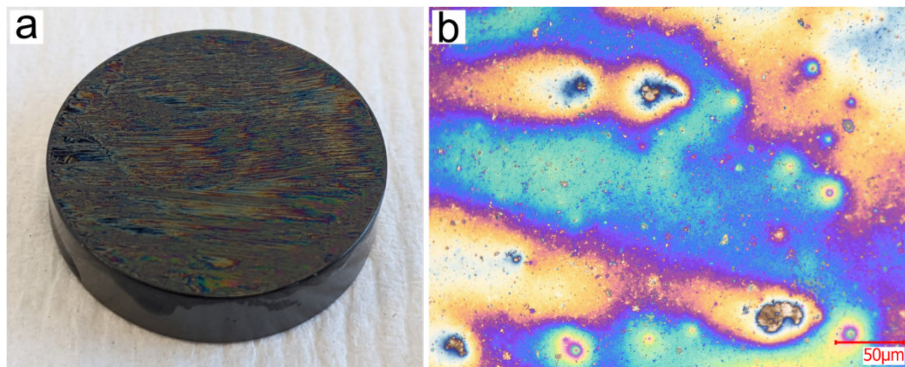


Figure 6. 13. (a) picture and (b) optical image of the neat ZDDP layer on DLC surface.

The ZDDP-coated disk and the ball samples were introduced into the tribometer chamber where the reciprocating sliding tests are conducted in UHV using the same test parameters as the ones given in **Table 6. 1**. For this study, two DLC coatings were tested: a-C:H, and ta-C(66) to study the tribochemistry of DLC/ZDDP interfaces without the influence of a base oil or outside air contamination.

### 6.2.2 Friction and wear results

Friction curves of a-C:H and ta-C(66) in UHV (without ZDDP layer) used as reference are shown in **Figure 6. 14a**. The a-C:H coating exhibits a friction coefficient  $\mu = 0.01$  at the beginning of the tests, but after 10 passages ( 5 cycles),  $\mu$  rises and stabilizes at 0.75. The low

friction regime is obtained when the a-C:H surface is still terminated with H, but after initial wear and H depletion at the surface,  $\mu$  rises. For ta-C,  $\mu = 0.70$  throughout the test, as observed already in Chapter 6.1 (shown here again to facilitate comparison). **Figure 6. 14b** shows the friction curves obtained from a-C:H and ta-C(66) with the applied layer of neat ZDDP on the flat sample (shown in **Figure 6. 13**). In pure ZDDP lubrication without base oil, friction is incredibly reduced by 10 times compared to UHV, and  $\mu = 0.075$  for both a-C:H and ta-C(66). After a few hundreds of passages, the ZDDP film is completely depleted (290 and 390 passages for ta-C(66) and a-C:H, respectively) and  $\mu$  starts to rise due to direct contact of the DLC surfaces (the depletion time depends on the thickness of the ZDDP layer, which is not homogenous and varies in each test).

Shorter tests were performed and stopped after 50 and 145 passages to obtain analysis points at different moments of the friction curve (beginning, middle, and end). The wear tracks of the a-C:H and ta-C(66) flats are shown in **Figure 6. 15**. As it can be seen, at the beginning of the test after only 50 cycles (**Figure 6. 15a and d**), there is still liquid ZDDP on the center of the wear track. At the middle and at the end of the tests (**Figure 6. 15b-c and e-f**) the liquid ZDDP layer has been mostly depleted inside the wear tracks. During the low friction regime (when  $\mu = 0.075$ ) there is still ZDDP lubrication and no wear is generated on the flat or ball on neither a-C:H nor ta-C.

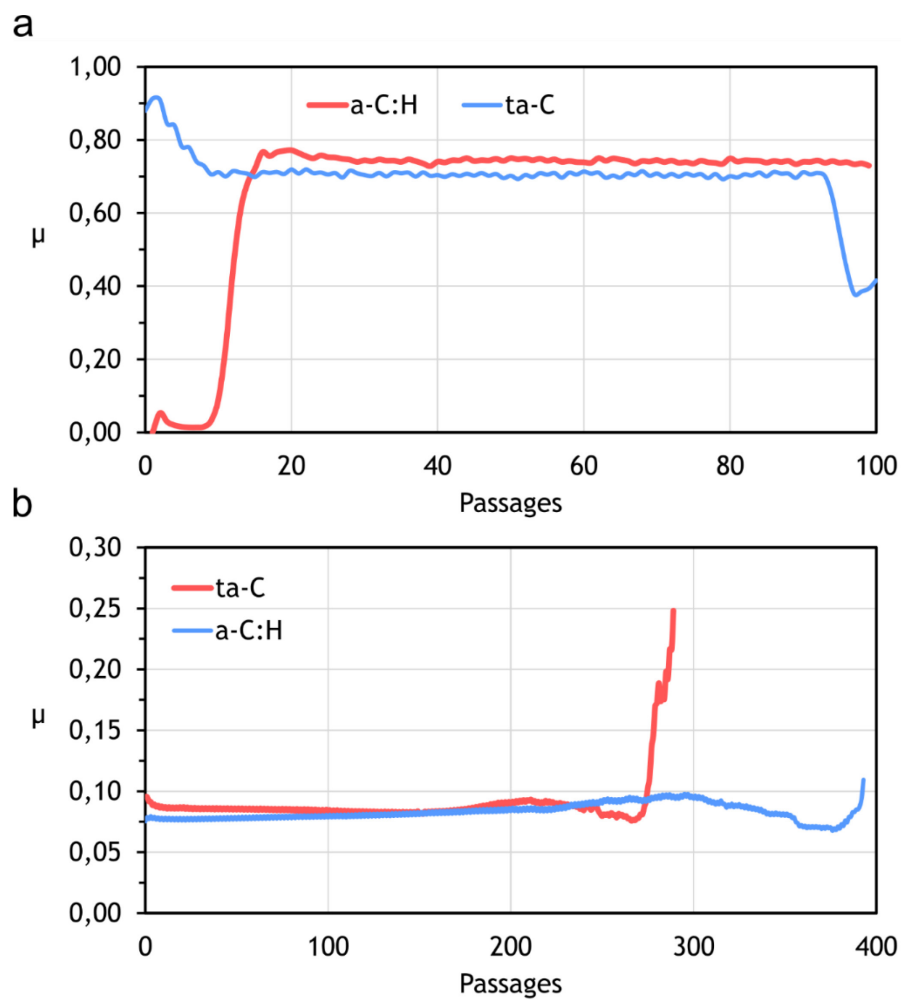


Figure 6. 14. Friction curves of a-C:H and ta-C(66) obtained from sliding tests in: (a) vacuum and (b) ZDDP thin layer.



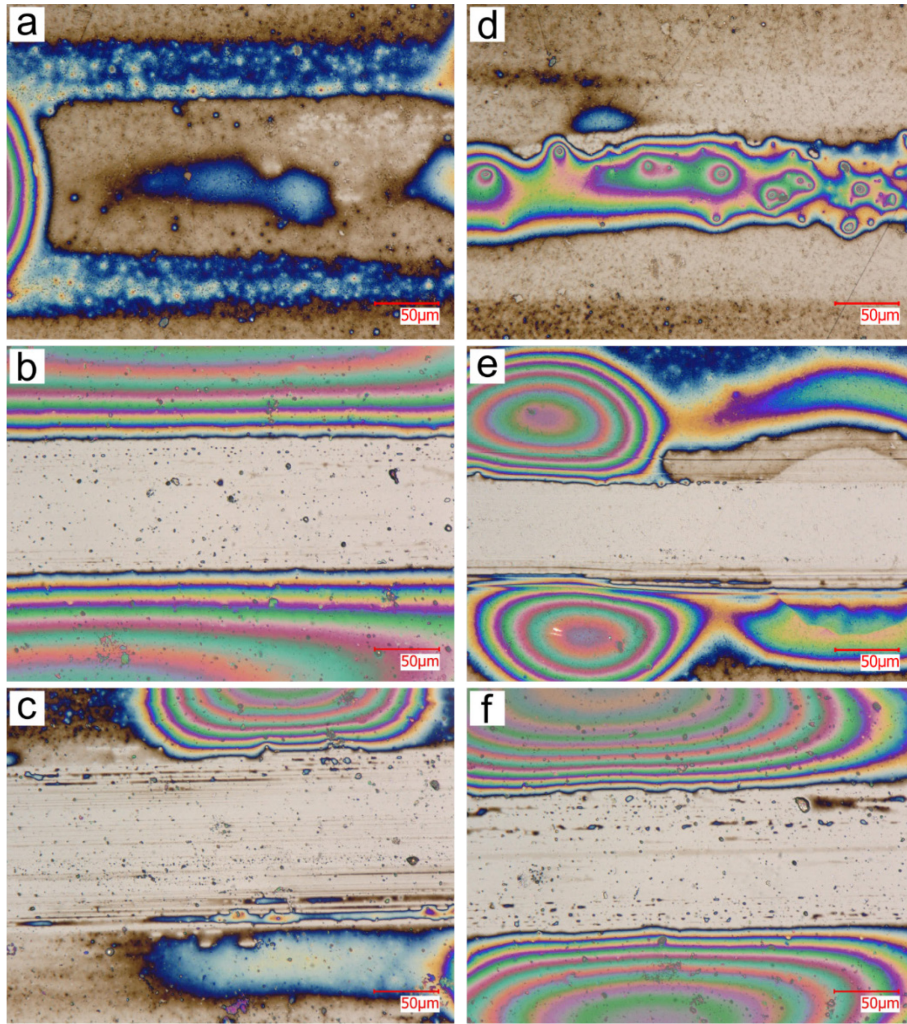


Figure 6. 15. Optical images of the wear tracks of ta-C flats after: (a) 50 passages, (b) 145 passages, and (c) 290 passages and a-C:H flats after: (d) 50 passages, (e) 145 passages, and (f) 390 passages.



### 6.2.3 XPS analysis

After the sliding tests, the flat samples were directly transferred to the XPS analysis chamber for analysis without being exposed to the outside air environment. XPS spectra were recorded inside of the wear tracks of the a-C:H and ta-C flats after individual sliding tests performed for 50, 145, 290, and 390 passages. Additionally, spectra were recorded outside of the wear tracks on the neat ZDDP layer to have a reference value of the B.E. (binding energy) and chemical state of each element. The elemental quantification results are presented in **Figure 6. 16**. As it can be observed, the highest amount of ZDDP-derived elements (P, S, and Zn) can be found on the spectra corresponding to neat ZDDP and decreases as the number of passages increases (as the ZDDP layer starts to be depleted). The quantities are practically the same between ta-C and a-C:H; the precise values including C and O are given in **Table 6. 3**.

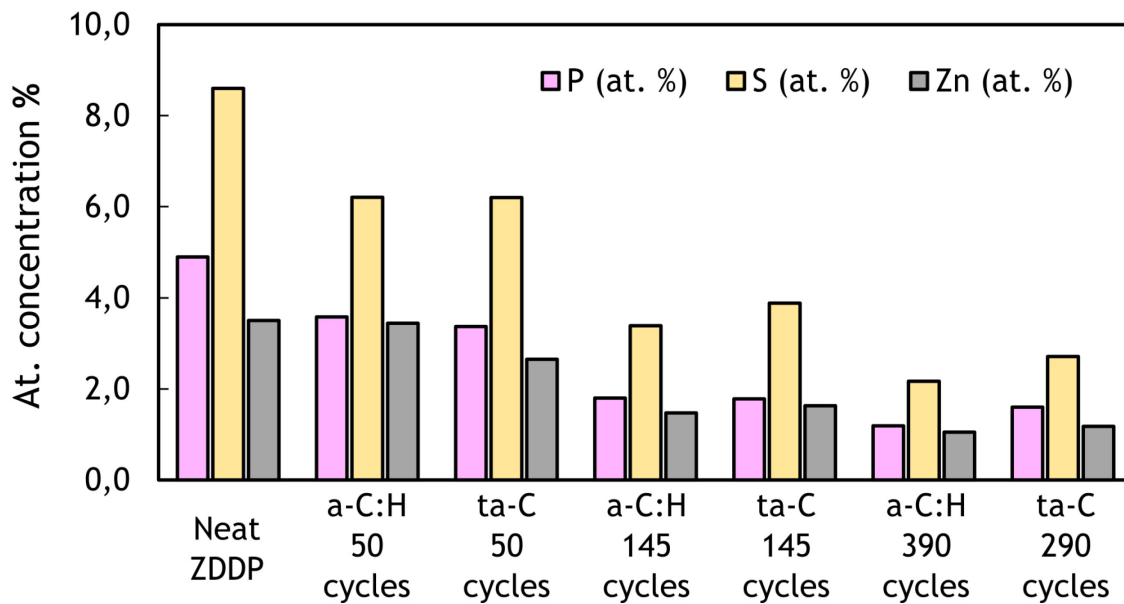


Figure 6. 16. XPS elemental quantification obtained from a-C:H and ta-C(66) disks after short tests when  $\mu = 0.08$  (50 cycles) and long tests when the friction coefficient  $\mu$  starts to rise (290 and 390 cycles for ta-C and a-C:H, respectively).

Table 6. 3. XPS elemental quantification obtained from a-C:H and ta-C(66) disks after short (50 cycles) and long sliding tests (290 and 390 cycles for ta-C and a-C:H, respectively).

Additive	C (at. %)	O (at. %)	P (at. %)	S (at. %)	Zn (at. %)
Neat ZDDP	73.0	10.0	4.9	8.6	3.5
a-C:H 50 cycles	78.8	8.0	3.6	6.2	3.4
ta-C 50 cycles	80.3	7.5	3.4	6.2	2.7
a-C:H 145 cycles	88.7	4.7	1.8	3.4	1.5
ta-C 145 cycles	87.8	4.9	1.8	3.9	1.6
a-C:H 390 cycles	92.4	3.2	1.2	2.2	1.1
ta-C 290 cycles	90.3	4.2	1.6	2.7	1.2

The C1s and O1s XPS spectra obtained on neat ZDDP and inside the wear tracks of a-C:H and ta-C flats at the beginning and end of the friction tests (50 passages and 390/290 passages, respectively) are shown in **Figure 6. 17**. The P2p, S2p, and Zn2p<sub>3/2</sub> spectra are shown in **Figure 6. 18**. The B.E.s obtained from neat ZDDP and in the inside of the wear tracks are practically identical, indicating that there was no change in the chemical states of the elements found on the wear tracks after sliding.

The C1s spectra are composed of two contributions: the first one at  $284.8 \pm 0.1$  eV, is assigned to aliphatic carbon and C-C, and C-H bonds in ZDDP and the DLC coatings. The second one, at  $286.5 \pm 0.1$  eV, corresponds to -C-O bonds in ZDDP. The O1s spectra consists of two peaks: the first and smallest one, at B.E. =  $531.7 \pm 0.2$  eV, is assigned to O-Zn bonds and the second at  $533.1 \pm 0.2$  eV to the C-O-P fragment of ZDDP. The P2p spectra are fitted with one doublet due to spin-coupling with a separation of 0.84 eV and intensity ratio of 0.5. The only P2p<sub>3/2</sub> peak at B.E. =  $133.5 \pm 0.2$  eV is assigned to the (-CO)<sub>2</sub>P=S fragment in ZDDP. The S2p spectra are fitted using a doublet with a separation of 1.2 eV and an intensity ratio of 0.5. They consist of two contributions: the first one, at  $162.4 \pm 0.2$  eV, is assigned to the P-S-Zn fragment in ZDDP and the second one, at  $164.0 \pm 0.2$  eV, is assigned to the S=P bond in ZDDP. Finally, the Zn2p<sub>3/2</sub> spectra are composed of two peaks: the first one at  $1022.3 \pm 0.2$  eV is assigned to Zn-S and the second and smallest one at B.E. =  $1023.8 \pm 0.3$  eV is assigned to Zn-O bonds (in agreement with the O1s spectra). The parameters used for the fitting procedure of the spectra are given in **Table A. 6**.

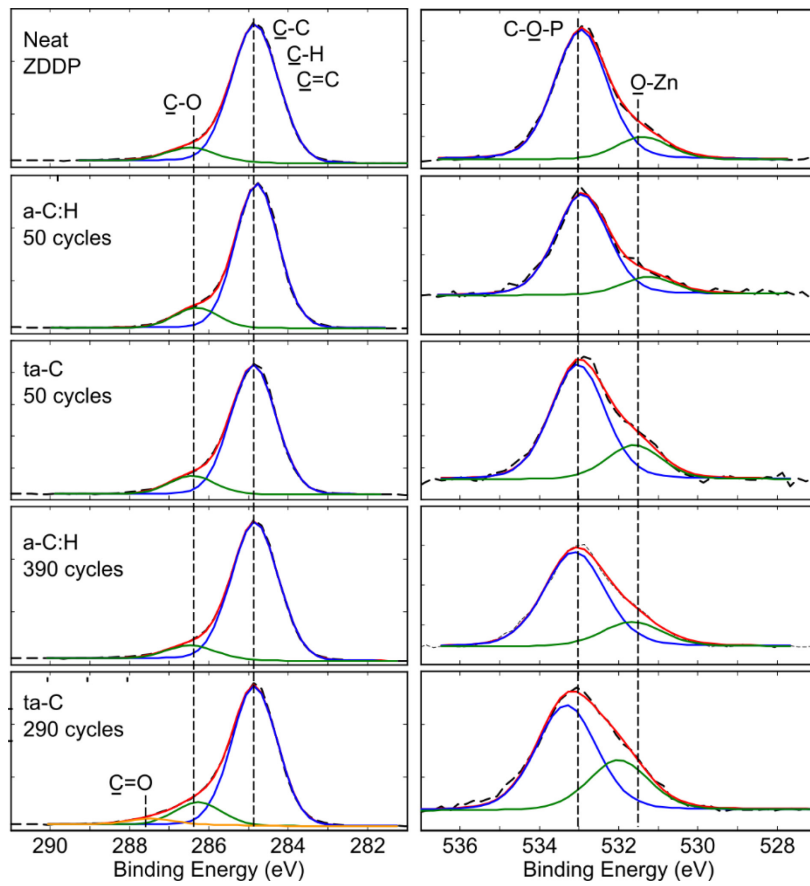


Figure 6. 17. C1s (left) and O1s (right) XPS spectra obtained from neat ZDDP (row 1 top to bottom), a-C:H and ta-C disks after sliding tests for different durations: 50 cycles (row 2 and 3), a-C:H after 390 cycles (row 4) and ta-C after 290 cycles (row 5).

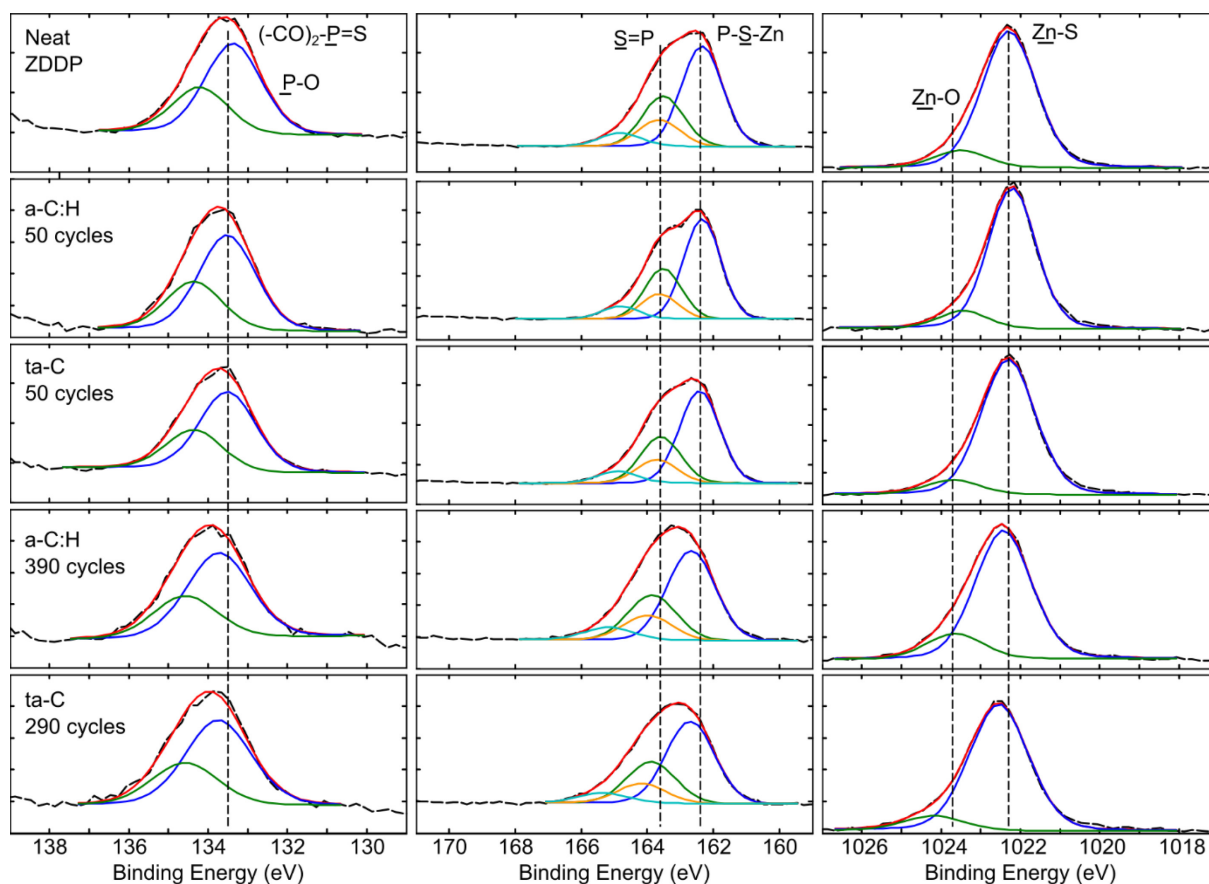


Figure 6. 18. P2p (left), S2p (middle), and Zn2p<sub>3/2</sub> (right) XPS spectra obtained from neat ZDDP (row 1 top to bottom), a-C:H and ta-C disks after sliding tests for different durations: 50 cycles (row 2 and 3), a-C:H after 390 cycles (row 4) and ta-C after 290 cycles (row 5).

## 6.2.4 Discussion

From the results of the previous chapters it was expected that in ZDDP lubrication, ta-C would undergo severe wear accompanied by S-C bonds and sulphur diffusion into the ta-C, but this was not observed. As discussed in Chapter 6.1, the sliding tests performed inside the test chamber of the ATCE apparatus were performed at 20°C. There was no observable difference between the chemical states of the ZDD-derived elements from the spectra obtained on neat ZDDP and the ones inside the wear tracks. This suggests that the ZDDP molecule was not decomposed, thus no S-C bonds and sulphur doping could occur. The effect of temperature on the tribochemistry of DLC/ZDDP systems still needs to be investigated.

## 6.2.5 Summary and Conclusions

A thin layer of neat ZDDP was applied onto a-C:H and ta-C disks and sliding tests were performed in UHV to study a simplified system that resembles the conditions in atomic simulations performed of ZDDP molecules between DLC asperities. In UHV without a ZDDP layer,  $\mu = 0.70 - 0.75$  and severe wear occurred for ta-C and a-C:H coatings. When the thin

ZDDP layer is applied, friction was reduced by 10 times, with  $\mu = 0,075$  and no wear. This low friction regime lasts for a few hundred cycles until the ZDDP liquid film is completely depleted and direct contact between the DLC surfaces occurs. The chemical states of the ZDDP-derived elements (P, S, and Zn) were practically identical between neat ZDDP and the inside of the DLC's wear tracks, suggesting that in the tested conditions the ZDDP molecules do not decompose nor react with the ta-C or a-C:H surfaces.

---

## Chapter 7: General conclusions and suggestions for future work

---

In this chapter, the main findings and conclusions of this work are summarized. Suggestions for future work are given to follow-up on certain results that could benefit from complementary experiments.

## 7.1 General Conclusions

The main objective of this work was to study the tribological effect and interactions between low-friction-inducing materials, such as DLC, and traditional engine oils additives, such as ZDDP. This is of important relevance towards the goal of improving fuel efficiency in passenger cars by reducing energy losses due to friction and wear in ICE.

Based on the experimental, analytical, and simulation results, it can be concluded that the tribological behavior of DLC/DLC tribopairs in ZDDP lubrication is governed by their mechanical (hardness, elastic modulus) and chemical (hydrogen content, carbon  $sp^3/sp^2$  ratio) properties. Their surface topography ( $h_{rms}$  and  $h'_{rms}$ ) plays a crucial role in inter-asperity contacts which leads to different local asperity pressures between the DLCs and influence their tribochemical reactions with the ZDDP molecule. Even though thin ZDDP-derived patchy tribofilms grown on soft and moderate-hard DLCs, ZDDP has very little, or no effect on their tribological behavior. An optimal combination of ultralow friction ( $\mu = 0.02$ ) and negligible wear was achieved with moderate hard ta-C(51). However, ZDDP has a catastrophic effect on hard ta-Cs which exhibit severe wear, increased surface roughness, and rise of friction coefficient. The newly proposed wear mechanism of hard ta-Cs can be summarized as follows:

- The high stiffness and surface topography of hard ta-Cs lead to effective local pressures  $P_1 = 10$  GPa. The high pressures at contacting asperities lead to cold welding and increase the defragmentation of the ZDDP molecule.
- Free sulphur atoms are released into the sliding interface, causing chemical mixing. The released sulphur atoms diffuse into the sub-surface of the ta-C coating and weaken the material (decreasing the shear strength).
- Plastic deformation, and the formation of graphitic regions and onion-like structures are observed in the weakened, sulphur-rich zones.
- In ta-C/steel tribopairs, wear was avoided and in this case ZDDP fulfilled its role as AW agent, preventing tribochemical wear of the ta-C counterpart due to the transfer of carbon atoms onto the steel surface.
- In ta-C/steel tribopairs, ZDDP does not cause any wear. Indeed, in this asymmetric configuration it protects the ta-C counterpart from tribochemical wear that occurs in PAO base oil lubrication by limiting the diffusion of carbon atoms onto the steel surface. Thus, fulfilling its role as AW agent.



The effect of sulphur was further investigated by testing other sulphur-containing and sulphur-free additives. Similar tribochemical wear and high friction were observed for hard ta-Cs lubricated with sulphur containing molecules (ZDDP primary-C4, ZDDP primary-C8, and TPS). On the contrary, no wear was observed with the sulphur-free, ZP additive, which does not react with the ta-C surfaces in the tested experimental conditions. For a-C:H surfaces, wear did not occur with any of the tested additives and the lowest friction coefficient ( $\mu = 0.07$ ) was obtained with additives containing longer alkyl chains.

Other mechanical parameters were studied to better understand the tribological behavior of DLC/ZDDP systems. In general, to minimize friction and wear, the DLC surfaces must be polished close to a mirror finish ( $R_a \approx 10$  nm). When lubricated with sulfur-containing compounds, this will reduce the effective local pressure at the asperity level and thus decrease the decomposition of the molecules trapped between them. Certain tribological phenomena, such as tribofilm formation, and wear initiation, are favored at the edges of the stroke, where the lubrication regime shifts from ML/EHL to BL.

Finally, sliding tests were performed in a controlled environment chamber to study simpler tribological systems and the tribochemical reactions taking place at the DLC surfaces. In this configuration, the working temperature was set at 20°C, while it was set at 110°C for the tests performed in liquid lubrication. This difference could be responsible for the differing results and still needs to be investigated.

In O<sub>2</sub> environment, wear of ta-C could be reduced to some extent, but high friction ( $\mu > 0.7$ ) and stick-slip phenomena was still observed. Similar results were observed in DMS environment, but when the partial pressure was sufficiently high, friction was greatly reduced ( $\mu = 0.05$ ), and wear was completely inhibited. Presumably due to passivation of the ta-C surface by a thin sulphur layer.

In neat ZDDP lubrication under UHV, both a-C:H and ta-C exhibited low friction ( $\mu = 0.075$ ) and no wear was observed during this low friction regime, while the ZDDP layer was not yet depleted. There was no change in the chemical states of the ZDDP-derived elements found on neat ZDDP and inside the wear tracks, suggesting that its defragmentation did not occur. It is possible that higher temperature is needed to active the molecule and still needs to be investigated.

In general, this study sheds light to the underlying micro/nano-scale mechanisms that are responsible for macroscopic tribological behaviour of DLC coatings lubricated in ZDDP and

similar additives. Practical solutions are given to optimize the friction and wear properties of DLC/ZDDP systems that can be directly applied to ICEs in passenger cars. The harmful effect of sulphur-containing additives will hopefully lead to the formulation and use of other additives that can protect steel surfaces, while not harming DLCs.

Furthermore, the multi-approached methodology used in this work can be used in future studies aiming at finding optimized tribological behaviours between different materials and lubricants. by controlling the mechanical and chemical parameters of the materials and fine-tuning the tribochemistry of the lubricants.

## 7.2 Suggestions for future works

There are a certain results presented in this work that still require more investigation to better understand them. Some suggestions are given below:

1. It is still not clear why soft a-C:H and a-C coatings exhibit higher friction coefficient ( $\mu=0.10$ ) in PAO base oil, while for harder ta-Cs  $\mu = 0.02$ . It is possible that the ta-C surfaces become smoother and the lubrication regime is predominantly EHL, while BL or ML could apply at larger portions of the stroke for softer DLCs. Similarly, low friction ( $\mu = 0.02$ ) is observed for ta-C/steel tribopairs where tribochemical wear leads to atomically smooth surfaces. A closer inspection of the surface roughness by AFM could shed some light in this matter. AFM topographies were already recorded in this work, but in PAO + ZDDP lubrication, and not in pure PAO.

Another possibility is the dehydrogenation of PAO and subsequent passivation of hard ta-Cs surfaces, where effective local pressures at contacting asperities are larger than those of softer DLCs. It has been shown, that H terminated nanocrystalline diamond surfaces (NCD), exhibit superlow friction<sup>112</sup>. Superlubricity has also been observed with ta-C and a-C:H coatings in low pressure hydrogen environment<sup>107</sup>. Sliding tests performed at low sliding speeds, in boundary lubrication (BL) regime, could be performed to eliminate the contribution of EHL regime.

2. The results in liquid lubrication (Ch. 4 and 5) and those obtained in controlled environment (Ch. 6) are divergent. In the former, wear of ta-C was observed with sulphur-containing additives, while for the latter, no wear was observed in DMS environment or lubricated with a layer of neat ZDDP. An important difference between

both configurations is the working temperature, which was set at 110°C in liquid lubrication (representative of ICE), and only at 20°C in controlled environment. This parameter can activate the diffusion process of the active elements like sulphur brought to the surface, causing them to penetrate further into the subsurface. The effect of temperature remains to be investigated to check if it can explain the results obtained in both different test conditions.

3. Finally, to study the reactivity of ta-C, a-C and a-C:H, tests could be performed with other sulphur-containing molecules besides DMS, such as, dimethyl disulphide (DMDS), and dimethyl trisulphide (DMTS). The idea is to introduce the DLCs into the test chamber in UHV and perform short sliding tests to generate wear and create reactive surfaces with carbon dangling bonds. Next, the contact between the samples is removed and the sulphur-containing molecules are introduced in gas phase for a given time, say 30 minutes. XPS spectra would be recorded in the reactive surface to study the decomposition of the gas molecules without sliding motion. Afterwards, in a new area of the surfaces, sliding tests could be performed in the presence of the gas molecules to record XPS spectra and compare them with the ones where there was no sliding after the gas molecules were introduced. And lastly, FIB + TEM analyses could be performed to study the sulphur diffusion in the samples.

---

## References

---

- (1) Holmberg, K.; Erdemir, A. Influence of Tribology on Global Energy Consumption, Costs and Emissions. *Friction* **2017**, *5* (3), 263–284. <https://doi.org/10.1007/s40544-017-0183-5>.
- (2) Holmberg, K.; Erdemir, A. The Impact of Tribology on Energy Use and CO<sub>2</sub> Emission Globally and in Combustion Engine and Electric Cars. *Tribol. Int.* **2019**, *135*, 389–396. <https://doi.org/10.1016/j.triboint.2019.03.024>.
- (3) Statista. Worldwide number of electric cars <https://www.statista.com/statistics/270603/worldwide-number-of-hybrid-and-electric-vehicles-since-2009/> (accessed 2021 -04 -01).
- (4) Holmberg, K.; Andersson, P.; Erdemir, A. Global Energy Consumption Due to Friction in Passenger Cars. *Tribol. Int.* **2012**, *47*, 221–234. <https://doi.org/10.1016/j.triboint.2011.11.022>.
- (5) Climate Action, European Commission. Road Transport: Reducing CO<sub>2</sub> emissions from passenger cars before 2020 [https://ec.europa.eu/clima/policies/transport/vehicles/cars\\_en](https://ec.europa.eu/clima/policies/transport/vehicles/cars_en) (accessed 2021 -04 -01).
- (6) Schmellenmeier, H. *Exp. Technik der Physik*. 1st ed. 1954, p 49.
- (7) Aisenberg, S.; Chabot, R. Ion-Beam Deposition of Thin Films of Diamondlike Carbon. *J. Appl. Phys.* **1971**, *42* (7), 2953–2958. <https://doi.org/10.1063/1.1660654>.
- (8) Aisenberg, S.; Chabot, R. W. Physics of Ion Plating and Ion Beam Deposition. *J. Vac. Sci. Technol.* **1973**, *10* (1), 104–107. <https://doi.org/10.1116/1.1317915>.
- (9) Holland, L.; Ojha, S. M. Deposition of Hard and Insulating Carbonaceous Films on an r.f. Target in a Butane Plasma. *Thin Solid Films* **1976**, *38* (2), L17–L19. [https://doi.org/10.1016/0040-6090\(76\)90214-5](https://doi.org/10.1016/0040-6090(76)90214-5).
- (10) Weissmantel, Chr.; Bewilogua, K.; Schürer, C.; Breuer, K.; Zscheile, H. Characterization of Hard Carbon Films by Electron Energy Loss Spectrometry. *Thin Solid Films* **1979**, *61* (2), L1–L4. [https://doi.org/10.1016/0040-6090\(79\)90451-6](https://doi.org/10.1016/0040-6090(79)90451-6).
- (11) Enke, K.; Dimigen, H.; Hübsch, H. Frictional Properties of Diamondlike Carbon Layers. *Appl. Phys. Lett.* **1980**, *36* (4), 291–292. <https://doi.org/10.1063/1.91465>.
- (12) Enke, K. Some New Results on the Fabrication of and the Mechanical, Electrical and Optical Properties of i-Carbon Layers. *Thin Solid Films* **1981**, *80* (1–3), 227–234. [https://doi.org/10.1016/0040-6090\(81\)90226-1](https://doi.org/10.1016/0040-6090(81)90226-1).
- (13) Memming, R.; Tolle, H. J.; Wierenga, P. E. Properties of Polymeric Layers of Hydrogenated Amorphous Carbon Produced by a Plasma-Activated Chemical Vapour Deposition Process II: Tribological and Mechanical Properties. *Thin Solid Films* **1986**, *143* (1), 31–41. [https://doi.org/10.1016/0040-6090\(86\)90144-6](https://doi.org/10.1016/0040-6090(86)90144-6).
- (14) Robertson, J. Diamond-like Amorphous Carbon. *Mater. Sci. Eng. R Rep.* **2002**, *37* (4–6), 129–281. [https://doi.org/10.1016/S0927-796X\(02\)00005-0](https://doi.org/10.1016/S0927-796X(02)00005-0).
- (15) Vengudusamy, B. Behaviour of Lubricant Additives on DLC Coatings. **2011**. <https://doi.org/10.25560/11734>.
- (16) Ohtake, N.; Hiratsuka, M.; Kanda, K.; Akasaka, H.; Tsujioka, M.; Hirakuri, K.; Hirata, A.; Ohana, T.; Inaba, H.; Kano, M.; Saitoh, H. Properties and Classification of Diamond-Like Carbon Films. *Materials* **2021**, *14* (2), 315. <https://doi.org/10.3390/ma14020315>.

- (17) *Carbon Based Films -- Classification and Designations ISO 20523:2017*; The International Organization for Standardization: Geneva, Switzerland, 2017.
- (18) Vetter, J. 60 Years of DLC Coatings: Historical Highlights and Technical Review of Cathodic Arc Processes to Synthesize Various DLC Types, and Their Evolution for Industrial Applications. *Surf. Coat. Technol.* **2014**, *257*, 213–240. <https://doi.org/10.1016/j.surfcoat.2014.08.017>.
- (19) Weiler, M.; Sattel, S.; Jung, K.; Ehrhardt, H.; Veerasamy, V. S.; Robertson, J. Highly Tetrahedral, Diamond-like Amorphous Hydrogenated Carbon Prepared from a Plasma Beam Source. *Appl. Phys. Lett.* **1994**, *64* (21), 2797–2799. <https://doi.org/10.1063/1.111428>.
- (20) Stachowiak, G. W.; Batchelor, A. W. *Engineering Tribology*, Fourth edition.; Elsevier/Butterworth-Heinemann: Oxford, 2014.
- (21) Bin Mustafa, M. M.; Umehara, N.; Tokoroyama, T.; Murashima, M.; Shibata, A.; Utsumi, Y.; Moriguchi, H. Effect of Pillar and Mesh Structure of Tetrahedral Amorphous Carbon (Ta-C) Coatings on the Wear Properties and Fracture Toughness of the Coating. *Tribol. Online* **2019**, *14* (5), 388–397. <https://doi.org/10.2474/trol.14.388>.
- (22) Lin, Y.; Zia, A. W.; Zhou, Z.; Shum, P. W.; Li, K. Y. Development of Diamond-like Carbon (DLC) Coatings with Alternate Soft and Hard Multilayer Architecture for Enhancing Wear Performance at High Contact Stress. *Surf. Coat. Technol.* **2017**, *320*, 7–12. <https://doi.org/10.1016/j.surfcoat.2017.03.007>.
- (23) Sui, X.; Liu, J.; Zhang, S.; Yang, J.; Hao, J. Microstructure, Mechanical and Tribological Characterization of CrN/DLC/Cr-DLC Multilayer Coating with Improved Adhesive Wear Resistance. *Appl. Surf. Sci.* **2018**, *439*, 24–32. <https://doi.org/10.1016/j.apsusc.2017.12.266>.
- (24) Duminica, F.-D.; Belchi, R.; Libralesso, L.; Mercier, D. Investigation of Cr(N)/DLC Multilayer Coatings Elaborated by PVD for High Wear Resistance and Low Friction Applications. *Surf. Coat. Technol.* **2018**, *337*, 396–403. <https://doi.org/10.1016/j.surfcoat.2018.01.052>.
- (25) Lu, Y.; Huang, G.; Xi, L. Tribological and Mechanical Properties of the Multi-Layer DLC Film on the Soft Copper Substrate. *Diam. Relat. Mater.* **2019**, *94*, 21–27. <https://doi.org/10.1016/j.diamond.2019.02.019>.
- (26) Cao, H.; Ye, X.; Li, H.; Qi, F.; Wang, Q.; Ouyang, X.; Zhao, N.; Liao, B. Microstructure, Mechanical and Tribological Properties of Multilayer Ti-DLC Thick Films on Al Alloys by Filtered Cathodic Vacuum Arc Technology. *Mater. Des.* **2021**, *198*, 109320. <https://doi.org/10.1016/j.matdes.2020.109320>.
- (27) NISSAN'S HYDROGEN-FREE DLC COATING WINS METI AWARD <https://global.nissannews.com/en/releases/070829-02-e> (accessed 2021 -04 -19).
- (28) Kano, M. Super Low Friction of DLC Applied to Engine Cam Follower Lubricated with Ester-Containing Oil. *Tribol. Int.* **2006**, *39* (12), 1682–1685. <https://doi.org/10.1016/j.triboint.2006.02.068>.
- (29) Robertson, J. Comparison of Diamond-like Carbon to Diamond for Applications. *Phys. Status Solidi A* **2008**, *205* (9), 2233–2244. <https://doi.org/10.1002/pssa.200879720>.
- (30) Tasdemir, H. A.; Tokoroyama, T.; Kousaka, H.; Umehara, N.; Mabuchi, Y. Friction and Wear Performance of Boundary-Lubricated DLC/DLC Contacts in Synthetic Base Oil. *Procedia Eng.* **2013**, *68*, 518–524. <https://doi.org/10.1016/j.proeng.2013.12.215>.
- (31) Long, Y.; Bouchet, M.-I. D. B.; Lubrecht, T.; Onodera, T.; Martin, J. M. Superlubricity of Glycerol by Self-Sustained Chemical Polishing. *Sci. Rep.* **2019**, *9* (1), 6286. <https://doi.org/10.1038/s41598-019-42730-9>.
- (32) Johnson, K. L. The Correlation of Indentation Experiments. *J. Mech. Phys. Solids* **1970**, *18* (2), 115–126. [https://doi.org/10.1016/0022-5096\(70\)90029-3](https://doi.org/10.1016/0022-5096(70)90029-3).

- (33) Guibert, M.; Nauleau, B.; Kapsa, P.; Rigaud, E. CONCEPTION ET REALISATION D'UN TRIBOMETRE ALTERNATIF LINEAIRE. **2006**, 11.
- (34) Moes, H. Optimum Similarity Analysis with Applications to Elastohydrodynamic Lubrication. *Wear* **1992**, *159*, 57–66.
- (35) Tallian, T. E. On Competing Failure Modes in Rolling Contact. *ASLE Trans.* **1967**, *10*, 418–439. <https://doi.org/10.1080/05698196708972201>.
- (36) Jaeger, J. C. Moving Sources of Heat and the Temperature at Sliding Contacts. *J. Proc. R. Soc. New South Wales* **1942**, *76*, 203–224. <https://doi.org/10.1126/science.ns-20.493.39-b>.
- (37) Gaus, M.; Cui, Q.; Elstner, M. DFTB3: Extension of the Self-Consistent-Charge Density-Functional Tight-Binding Method (SCC-DFTB). *J. Chem. Theory Comput.* **2011**, *7* (4), 931–948. <https://doi.org/10.1021/ct100684s>.
- (38) Tian, X.; Kennedy, F. E. Temperature Rise at the Sliding Contact Interface for a Coated Semi-Infinite Body. *J. Tribol.* **1993**, *115*, 1–9.
- (39) Ferrari, A. C. Diamond-like Carbon for Magnetic Storage Disks. *Surf. Coat. Technol.* **2004**, *180–181*, 190–206. <https://doi.org/10.1016/j.surfcoat.2003.10.146>.
- (40) Casiraghi, C.; Piazza, F.; Ferrari, A. C.; Grambole, D.; Robertson, J. Bonding in Hydrogenated Diamond-like Carbon by Raman Spectroscopy. *Diam. Relat. Mater.* **2005**, *14*, 1098–1102. <https://doi.org/10.1016/j.diamond.2004.10.030>.
- (41) Hakovirta, M.; Vuorinen, J. E.; He, X. M.; Nastasi, M.; Schwarz, R. B. Heat Capacity of Hydrogenated Diamond-like Carbon Films. *Appl. Phys. Lett.* **2000**, *77*, 2340–2342. <https://doi.org/10.1063/1.1290387>.
- (42) Shamsa, M.; Liu, W. L.; Balandin, A. A.; Casiraghi, C.; Milne, W. I.; Ferrari, A. C. Thermal Conductivity of Diamond-like Carbon Films. *Appl. Phys. Lett.* **2006**, *89*, 161921. <https://doi.org/10.1063/1.2362601>.
- (43) Blok, H. Theoretical Study of Temperature Rise at Surfaces of Actual Contact under Oiliness Lubricating Conditions. *Proc. Gen. Discuss. Lubr. Lubr.* **1937**, *2*, 222–235.
- (44) Persson, B. N. J. Theory of Rubber Friction and Contact Mechanics. *J. Chem. Phys.* **2001**, *115*, 3840–3861.
- (45) Weber, B.; Suhina, T.; Junge, T.; Pastewka, L.; Brouwer, A. M.; Bonn, D. Molecular Probes Reveal Deviations from Amontons' Law in Multi-Asperity Frictional Contacts. *Nat. Commun.* **2018**, *9*, 888.
- (46) Stanley, H. M.; Kato, T. An FFT-Based Method for Rough Surface Contact. *J. Tribol.* **1997**, *119*, 481–485. <https://doi.org/10.1115/1.2833523>.
- (47) Campañá, C.; Müser, M. H. Practical Green's Function Approach to the Simulation of Elastic Semi-Infinite Solids. *Phys. Rev. B* **2006**, *74*, 075420. <https://doi.org/10.1103/PhysRevB.74.075420>.
- (48) Pastewka, L.; Sharp, T. A.; Robbins, M. O. Seamless Elastic Boundaries for Atomistic Calculations. *Phys. Rev. B* **2012**, *86*, 075459. <https://doi.org/10.1103/PhysRevB.86.075459>.
- (49) Polonsky, I. A.; Keer, L. M. A Numerical Method for Solving Rough Contact Problems Based on the Multi-Level Multi-Summation and Conjugate Gradient Techniques. *Wear* **1999**, *231*, 206–219. [https://doi.org/10.1016/S0043-1648\(99\)00113-1](https://doi.org/10.1016/S0043-1648(99)00113-1).
- (50) Pastewka, L.; Robbins, M. O. Contact Area of Rough Spheres: Large Scale Simulations and Simple Scaling Laws. *Appl. Phys. Lett.* **2016**, *108*, 221601. <https://doi.org/10.1063/1.4950802>.
- (51) Wang, F.; Wang, Y.; Li, Y. Study of Influencing Factors and the Mechanism of Preparing Triazinedithiol Polymeric Nanofilms on Aluminum Surfaces. *Int. J. Mol. Sci.* **2010**, *11* (11), 4715–4725. <https://doi.org/10.3390/ijms11114715>.
- (52) <http://www.atomistica.org/>.

- (53) Moras, G.; Klemenč, A.; Reichenbach, T.; Gola, A.; Uetsuka, H.; Moseler, M.; Pastewka, L. Shear Melting of Silicon and Diamond and the Disappearance of the Polyamorphic Transition under Shear. *Phys. Rev. Mater.* **2018**, *2*, 083601. <https://doi.org/10.1103/PhysRevMaterials.2.083601>.
- (54) Kunze, T.; Posselt, M.; Gemming, S.; Seifert, G.; Konicek, A. R.; Carpick, R. W.; Pastewka, L.; Moseler, M. Wear, Plasticity, and Rehybridization in Tetrahedral Amorphous Carbon. *Tribol. Lett.* **2014**, *53* (1), 119–126. <https://doi.org/10.1007/s11249-013-0250-7>.
- (55) Bitzek, E.; Koskinen, P.; Gähler, F.; Moseler, M.; Gumbsch, P. Structural Relaxation Made Simple. *Phys. Rev. Lett.* **2006**, *97*, 170201.
- (56) Lees, A. W.; Edwards, S. F. The Computer Study of Transport Processes under Extreme Conditions. *J. Phys. C Solid State Phys.* **1972**, *5*, 1921–1929.
- (57) Peters, E. A. J. F. Elimination of Time Step Effects in DPD. *Europhys. Lett.* **2004**, *66*, 311–317. <https://doi.org/10.1209/epl/i2004-10010-4>.
- (58) Frenkel, D.; Smit, B. *Understanding Molecular Simulations: From Algorithms to Applications*, 2nd ed.; Academic Press: New York, 1996.
- (59) Berendsen, H. J. C.; Postma, J. P. M.; van Gunsteren, W. F.; DiNola, A.; Haak, J. R. Molecular Dynamics with Coupling to an External Bath. *J. Chem. Phys.* **1984**, *81*, 3684–3690.
- (60) Kuwahara, T.; Moras, G.; Moseler, M. Friction Regimes of Water-Lubricated Diamond (111): Role of Interfacial Ether Groups and Tribo-Induced Aromatic Surface Reconstructions. *Phys. Rev. Lett.* **2017**, *119*, 096101. <https://doi.org/10.1103/PhysRevLett.119.096101>.
- (61) Kuwahara, T.; Moras, G.; Moseler, M. Role of Oxygen Functional Groups in the Friction of Water-Lubricated Low-Index Diamond Surfaces. *Phys. Rev. Mater.* **2018**, *2* (7). <https://doi.org/10.1103/PhysRevMaterials.2.073606>.
- (62) Reichenbach, T.; Mayrhofer, L.; Kuwahara, T.; Moseler, M.; Moras, G. Steric Effects Control Dry Friction of H- and F-Terminated Carbon Surfaces. *ACS Appl. Mater. Interfaces* **2020**, *12*, 8805–8816.
- (63) Kuwahara, T.; Romero, P. A.; Makowski, S.; Weihnacht, V.; Moras, G.; Moseler, M. Mechano-Chemical Decomposition of Organic Friction Modifiers with Multiple Reactive Centres Induces Superlubricity of Ta-C. *Nat. Commun.* **2019**, *10*, 151. <https://doi.org/10.1038/s41467-018-08042-8>.
- (64) Bullen, A. J.; O'Hara, K. E.; Cahill, D. G.; Monteiro, O.; von Keudell, A. Thermal Conductivity of Amorphous Carbon Thin Films. *J. Appl. Phys.* **2000**, *88*, 6317–6320. <https://doi.org/10.1103/PhysRevB.65.140201>.
- (65) Kano, M.; Martin, J. M.; Yoshida, K.; De Barros Bouchet, M. I. Super-Low Friction of Ta-C Coating in Presence of Oleic Acid. *Friction* **2014**, *2* (2), 156–163. <https://doi.org/10.1007/s40544-014-0047-1>.
- (66) De Barros Bouchet, M. I.; Martin, J. M.; Avila, J.; Kano, M.; Yoshida, K.; Tsuruda, T.; Bai, S.; Higuchi, Y.; Ozawa, N.; Kubo, M.; Asensio, M. C. Diamond-like Carbon Coating under Oleic Acid Lubrication: Evidence for Graphene Oxide Formation in Superlow Friction. *Sci. Rep.* **2017**, *7* (April), 46394. <https://doi.org/10.1038/srep46394>.
- (67) Shinyoshi, T.; Fuwa, Y.; Ozaki, Y. Wear Analysis of DLC Coating in Oil Containing Mo-DTC. *SAE Tech. Pap.* **2007**, SAE 2007-01-1969.
- (68) Vengudusamy, B.; Green, J. H.; Lamb, G. D.; Spikes, H. A. Tribological Properties of Tribofilms Formed from ZDDP in DLC/DLC and DLC/Steel Contacts. *Tribol. Int.* **2011**, *44*, 165–174. <https://doi.org/10.1016/j.triboint.2010.10.023>.

- (69) Vengudusamy, B.; Green, J. H.; Lamb, G. D.; Spikes, H. A. Influence of Hydrogen and Tungsten Concentration on the Tribological Properties of DLC/DLC Contacts with ZDDP. *Wear* **2013**, *298*, 109–119. <https://doi.org/10.1016/j.wear.2013.01.020>.
- (70) Vengudusamy, B.; Green, J. H.; Lamb, G. D.; Spikes, H. A. Durability of ZDDP Tribofilms Formed in DLC/DLC Contacts. *Tribol. Lett.* **2013**, *51*, 469–478. <https://doi.org/10.1007/s11249-013-0185-z>.
- (71) Tasdemir, H. A.; Tokoroyama, T.; Kousaka, H.; Umehara, N.; Mabuchi, Y. Influence of Zinc Dialkyldithiophosphate Tribofilm Formation on the Tribological Performance of Self-Mated Diamond-like Carbon Contacts under Boundary Lubrication. *Thin Solid Films* **2014**, *562*, 389–397.
- (72) Okubo, H.; Watanabe, S.; Tadokoro, C.; Sasaki, S. Effects of Structure of Zinc Dialkyldithiophosphates on Tribological Properties of Tetrahedral Amorphous Carbon Film under Boundary Lubrication. *Tribol. Int.* **2016**, *98*, 26–40.
- (73) Spikes, H. The History and Mechanisms of ZDDP. *Tribol. Lett.* **2004**, *17* (3), 469–489.
- (74) Spikes, H. Low- and Zero-Sulphated Ash, Phosphorus and Sulphur Anti-Wear Additives for Engine Oils. *Lubr. Sci.* **2008**, *20*, 103–136. <https://doi.org/10.1002/ls>.
- (75) Qu, J.; Truhan, J. J.; Dai, S.; Luo, H.; Blau, P. J. Ionic Liquids with Ammonium Cations as Lubricants or Additives. *Tribol. Lett.* **2006**, *22* (3), 207–214. <https://doi.org/10.1007/s11249-006-9081-0>.
- (76) Martin, J. M.; Onodera, T.; Minfray, C.; Dassenoy, F.; Miyamoto, A. The Origin of Anti-Wear Chemistry of ZDDP. *Faraday Discuss.* **2012**, *156*, 311–323. <https://doi.org/10.1039/c2fd00126h>.
- (77) Zhang, J.; Spikes, H. On the Mechanism of ZDDP Antiwear Film Formation. *Tribol. Lett.* **2016**, *63*, 24. <https://doi.org/10.1007/s11249-016-0706-7>.
- (78) Zhang, J.; Ewen, J. P.; Ueda, M.; Wong, J. S. S.; Spikes, H. A. Mechanochemistry of Zinc Dialkyldithiophosphate on Steel Surfaces under Elastohydrodynamic Lubrication Conditions. *ACS Appl. Mater. Interfaces* **2020**, *12*, 6662–6676.
- (79) Gosvami, N. N.; Bares, J. A.; Mangolini, F.; Konicek, A. R.; Yablon, D. G.; Carpick, R. W. Mechanisms of Antiwear Tribofilm Growth Revealed in Situ by Single-Asperity Sliding Contacts. *Science* **2015**, *348* (6230), 102–106.
- (80) De Barros Bouchet, M. I.; Martin, J. M.; Le-Mogne, T.; Vacher, B. Boundary Lubrication Mechanisms of Carbon Coatings by MoDTC and ZDDP Additives. *Tribol. Int.* **2005**, *38*, 257–264. <https://doi.org/10.1016/j.triboint.2004.08.009>.
- (81) Tasdemir, H. A.; Wakayama, M.; Tokoroyama, T.; Kousaka, H.; Umehara, N.; Mabuchi, Y.; Higuchi, T. Ultra-Low Friction of Tetrahedral Amorphous Diamond-like Carbon (Ta-C DLC) under Boundary Lubrication in Poly Alpha-Olefin (PAO) with Additives. *Tribol. Int.* **2013**, *65*, 286–294.
- (82) Ueda, M.; Kadiric, A.; Spikes, H. ZDDP Tribofilm Formation on Non-Ferrous Surfaces. *Tribol. Online* **2020**, *15*, 318–331. <https://doi.org/10.2474/TROL.15.318>.
- (83) Aboua, K. A. M.; Umehara, N.; Kousaka, H.; Tokoroyama, T.; Murashima, M.; Tasdemir, H. A.; Mabuchi, Y.; Higuchi, T. Effect of ZnDTP Tribofilm's Morphology on Friction Behaviors of DLC Coatings: Tribofilm Characterization by 3D Scanning Electron Microscope Observation. *J. Adv. Mech. Des. Syst. Manuf.* **2018**, *12*, 1–12. <https://doi.org/10.1299/jamdsm.2018jamdsm0129>.
- (84) Mosey, N. J.; Müser, M. H.; Woo, T. K. Molecular Mechanisms for the Functionality of Lubricant Additives. *Science* **2005**, *307*, 1612–1615.
- (85) Mohammadtabar, K.; Eder, S. J.; Dörr, N.; Martini, A. Heat-, Load-, and Shear-Driven Reactions of Di-Tert-Butyl Disulfide on Fe(100). *J. Phys. Chem. C* **2019**, *123*, 19688–19692. <https://doi.org/10.1021/acs.jpcc.9b05068>.



- (86) Loehle, S.; Righi, M. C. Ab Initio Molecular Dynamics Simulation of Tribochemical Reactions Involving Phosphorus Additives at Sliding Iron Interfaces. *Lubricants* **2018**, *6*, 31. <https://doi.org/10.3390/lubricants6020031>.
- (87) Rossi, A.; Piras, F. M.; Kim, D.; Gellman, A. J.; Spencer, N. D. Surface Reactivity of Tributyl Thiophosphate: Effects of Temperature and Mechanical Stress. *Tribol. Lett.* **2006**, *23* (3), 197–208. <https://doi.org/10.1007/s11249-006-9051-6>.
- (88) Wang, F.; Wang, Y.; Li, Y. Study of Influencing Factors and the Mechanism of Preparing Triazinedithiol Polymeric Nanofilms on Aluminum Surfaces. *Int. J. Mol. Sci.* **2010**, *11*, 4715–4725. <https://doi.org/10.3390/ijms11114715>.
- (89) Eglin, M.; Rossi, A.; Spencer, N. D. X-Ray Photoelectron Spectroscopy Analysis of Tribostressed Samples in the Presence of ZnDTP: A Combinatorial Approach. *Tribol. Lett.* **2003**, *15* (3), 199–209.
- (90) Haack, L.; Simko, S. Neat Zinc Bis[O,O-Bis(2-Ethylhexyl)] Dithiophosphate (ZDDP), by XPS. *Surf. Sci. Spectra* **2011**, *18*, 1–8.
- (91) Berman, D.; Narayanan, B.; Cherukara, M. J.; Sankaranarayanan, S. K. R. S.; Erdemir, A.; Zinovev, A.; Sumant, A. V. Operando Tribochemical Formation of Onion-like-Carbon Leads to Macroscale Superlubricity. *Nat. Commun.* **2018**, *9*, 1164. <https://doi.org/10.1038/s41467-018-03549-6>.
- (92) Guzmán de la Mata, B.; Dowsett, M. G.; Twitchen, D. Sputter Yields in Diamond Bombarded by Ultra Low Energy Ions. *Appl. Surf. Sci.* **2006**, *252*, 6444–6447. <https://doi.org/10.1016/j.apsusc.2006.02.067>.
- (93) Gaus, M.; Cui, Q.; Elstner, M. DFTB3: Extension of the Self-Consistent-Charge Density-Functional Tight-Binding Method (SCC-DFTB). *J. Chem. Theory Comput.* **2011**, *7*, 931–948.
- (94) Joly-Pottuz, L.; Matta, C.; De Barros Bouchet, M. I.; Vacher, B.; Martin, J. M.; Sagawa, T. Superlow Friction of Ta-C Lubricated by Glycerol: An Electron Energy Loss Spectroscopy Study. *J. Appl. Phys.* **2007**, *102*, 064912. <https://doi.org/10.1063/1.2779256>.
- (95) Mosey, N. J.; Woo, T. K. Finite Temperature Structure and Dynamics of Zinc Dialkyldithiophosphate Wear Inhibitors: A Density Functional Theory and Ab Initio Molecular Dynamics Study. *J. Phys. Chem. A* **2003**, *107*, 5058–5070. <https://doi.org/10.1021/jp034085c>.
- (96) Manners, W.; Greenwood, J. A. Some Observations on Persson's Diffusion Theory of Elastic Contact. *Wear* **2006**, *261*, 600–610.
- (97) Pastewka, L.; Moser, S.; Gumbsch, P.; Moseler, M. Anisotropic Mechanical Amorphization Drives Wear in Diamond. *Nat. Mater.* **2011**, *10* (1), 34–38. <https://doi.org/10.1038/nmat2902>.
- (98) Lafon-Placette, S.; Fontaine, J.; De Barros Bouchet, M.-I.; Heau, C. Critical Role of a Metallic Counterpart on the Tribochemical Wear of Ta-C Coatings in Base Oil. *Wear* **2018**, *402–403*, 91–99. <https://doi.org/10.1016/j.wear.2018.02.006>.
- (99) Abdullah Tasdemir, H.; Wakayama, M.; Tokoroyama, T.; Kousaka, H.; Umehara, N.; Mabuchi, Y.; Higuchi, T. The Effect of Oil Temperature and Additive Concentration on the Wear of Non-Hydrogenated DLC Coating. *Tribol. Int.* **2014**, *77*, 65–71. <https://doi.org/10.1016/j.triboint.2014.04.015>.
- (100) Okubo, H.; Tadokoro, C.; Hirata, Y.; Sasaki, S. In Situ Raman Observation of the Graphitization Process of Tetrahedral Amorphous Carbon Diamond-Like Carbon under Boundary Lubrication in Poly-Alpha-Olefin with an Organic Friction Modifier. *Tribol. Online* **2017**, *12* (5), 229–237. <https://doi.org/10.2474/trol.12.229>.

- (101) Makowski, S.; Schaller, F.; Weihnacht, V.; Englberger, G.; Becker, M. Tribochemical Induced Wear and Ultra-Low Friction of Superhard Ta-C Coatings. *Wear* **2017**, *392–393*, 139–151. <https://doi.org/10.1016/j.wear.2017.08.015>.
- (102) Tasdemir, H. A.; Wakayama, M.; Tokoroyama, T.; Kousaka, H.; Umehara, N.; Mabuchi, Y.; Higuchi, T. Ultra-Low Friction of Tetrahedral Amorphous Diamond-like Carbon (Ta-C DLC) under Boundary Lubrication in Poly Alpha-Olefin (PAO) with Additives. *Tribol. Int.* **2013**, *65*, 286–294. <https://doi.org/10.1016/j.triboint.2013.03.014>.
- (103) Okubo, H.; Watanabe, S.; Tadokoro, C.; Sasaki, S. Effects of Concentration of Zinc Dialkyldithiophosphate on the Tribological Properties of Tetrahedral Amorphous Carbon Films in Presence of Organic Friction Modifiers. *Tribol. Int.* **2016**, *94*, 446–457. <https://doi.org/10.1016/j.triboint.2015.10.008>.
- (104) Fantauzzi, M.; Elsener, B.; Atzei, D.; Rigoldi, A.; Rossi, A. Exploiting XPS for the Identification of Sulfides and Polysulfides. *RSC Adv.* **2015**, *5* (93), 75953–75963. <https://doi.org/10.1039/C5RA14915K>.
- (105) Lacey, M. J.; Yalamanchili, A.; Maibach, J.; Tengstedt, C.; Edström, K.; Brandell, D. The Li-S Battery: An Investigation of Redox Shuttle and Self-Discharge Behaviour with LiNO<sub>3</sub>-Containing Electrolytes. *RSC Adv.* **2016**, *6* (5), 3632–3641. <https://doi.org/10.1039/C5RA23635E>.
- (106) Fontaine, J.; Belin, M.; Le Mogne, T.; Grill, A. How to Restore Superlow Friction of DLC: The Healing Effect of Hydrogen Gas. *Tribol. Int.* **2004**, *37* (11–12), 869–877. <https://doi.org/10.1016/j.triboint.2004.07.002>.
- (107) Okubo, H.; Tsuboi, R.; Sasaki, S. Frictional Properties of DLC Films in Low-Pressure Hydrogen Conditions. *Wear* **2015**, *340–341*, 2–8. <https://doi.org/10.1016/j.wear.2015.03.018>.
- (108) Zhang, W.; Tanaka, A.; Wazumi, K.; Koga, Y. Effect of Environment on Friction and Wear Properties of Diamond-like Carbon Film. *Thin Solid Films* **2002**, *413* (1–2), 104–109. [https://doi.org/10.1016/S0040-6090\(02\)00351-6](https://doi.org/10.1016/S0040-6090(02)00351-6).
- (109) Menapace, I.; Yiming, W.; Masad, E. Chemical Analysis of Surface and Bulk of Asphalt Binders Aged with Accelerated Weathering Tester and Standard Aging Methods. *Fuel* **2017**, *202*, 366–379. <https://doi.org/10.1016/j.fuel.2017.04.042>.
- (110) Ávila-Torres, Y.; Huerta, L.; Barba-Behrens, N. XPS-Characterization of Heterometallic Coordination Compounds with Optically Active Ligands. *J. Chem.* **2013**, *2013*, 1–9. <https://doi.org/10.1155/2013/370637>.
- (111) XPS Interpretation of Oxygen <https://xpssimplified.com/elements/oxygen.php> (accessed 2021-05-20).
- (112) Wang, Y.; Hayashi, K.; Ootani, Y.; Bai, S.; Shimazaki, T.; Higuchi, Y.; Ozawa, N.; Adachi, K.; De Barros Bouchet, M.-I.; Martin, J. M.; Kubo, M. Role of OH Termination in Mitigating Friction of Diamond-like Carbon under High Load: A Joint Simulation and Experimental Study. *Langmuir* **2021**, *37* (20), 6292–6300. <https://doi.org/10.1021/acs.langmuir.1c00727>.

# Appendix A

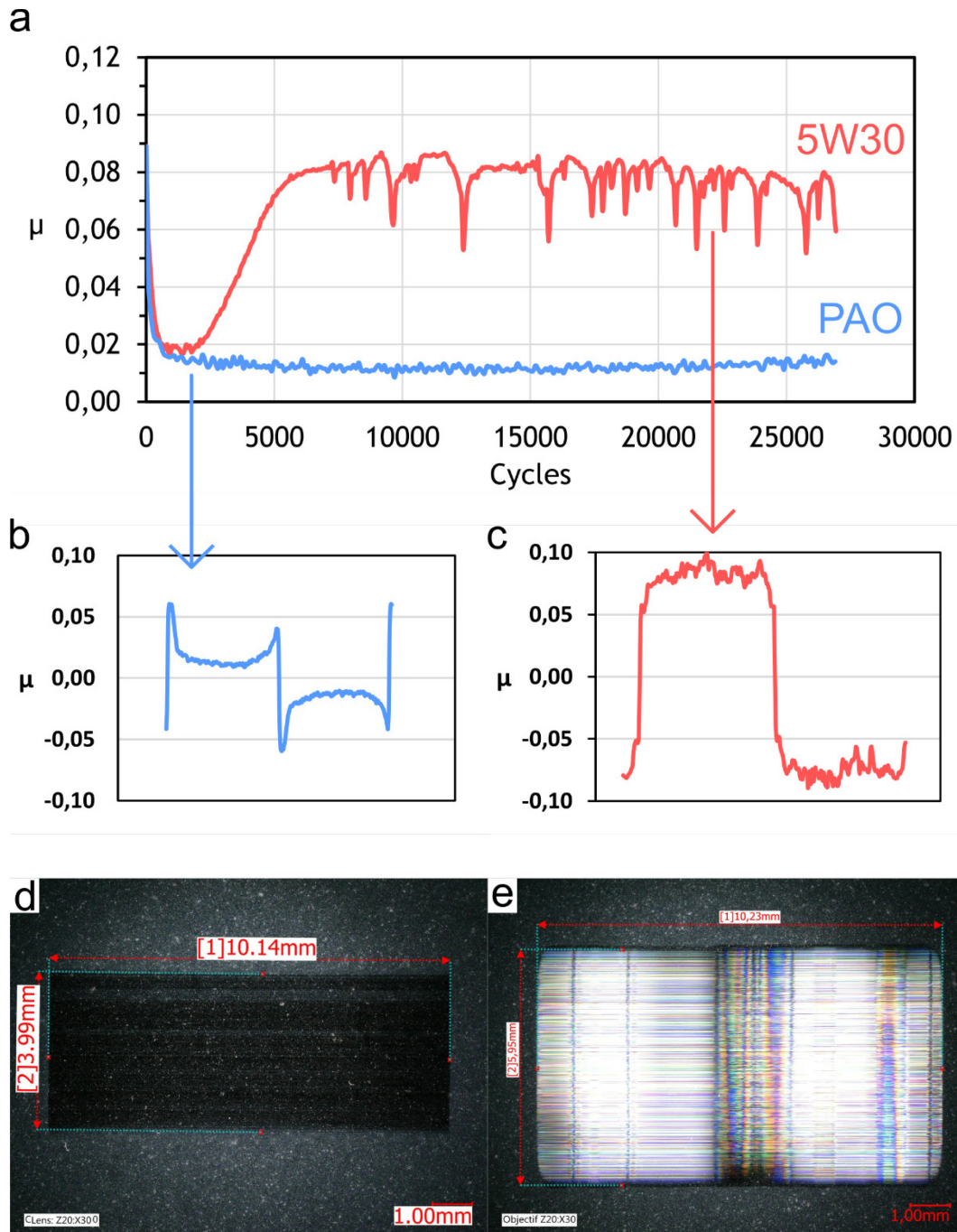


Figure A. 1. (a) Friction curves of ta-C(66) in PAO base oil (blue curve) and 5W30 (red curve) lubrication. Instantaneous friction coefficient for one cycle in (b) PAO and (c) 5W30. Optical images of the wear tracks of the flats after sliding tests in (d) PAO and (e) 5W30.

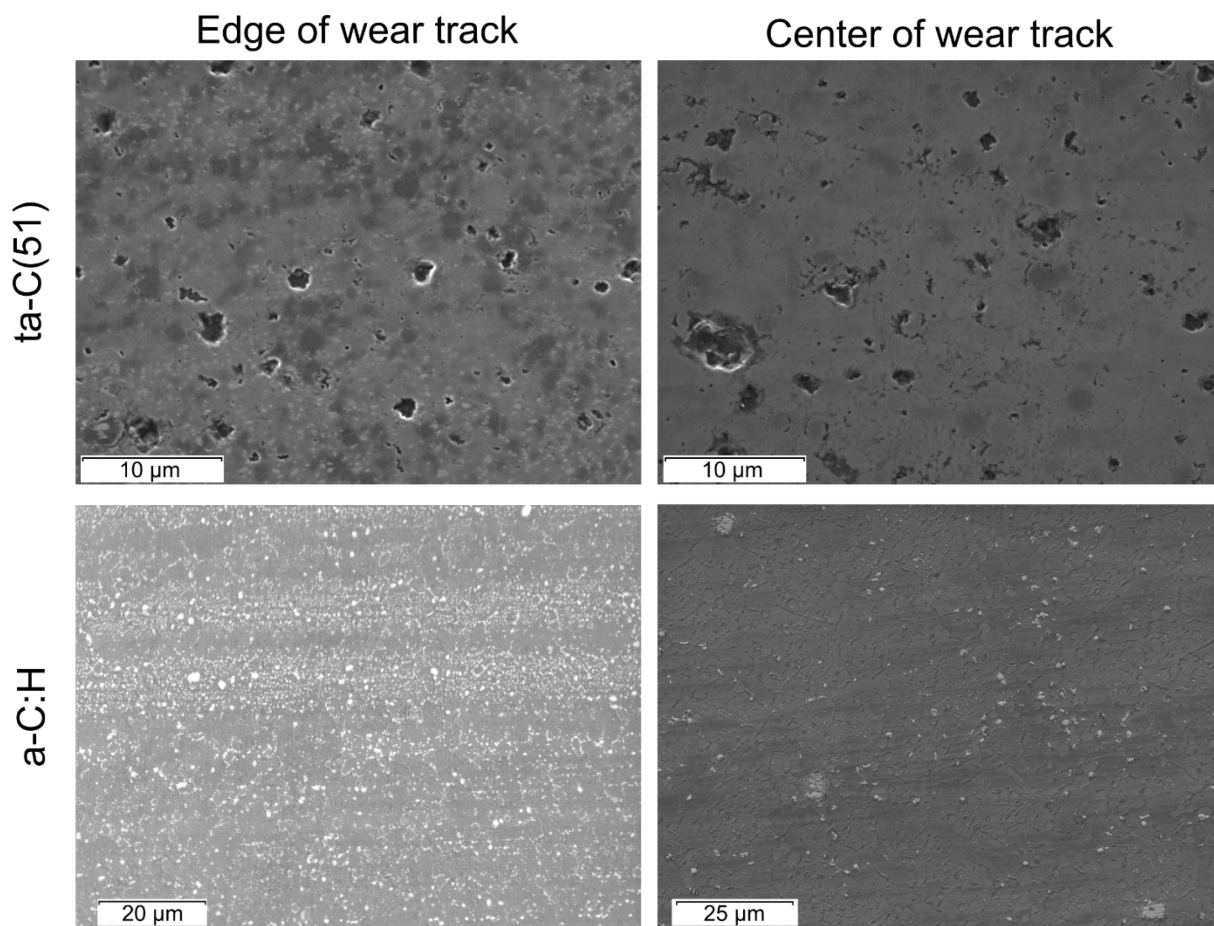


Figure A. 2. SEM images in SE detection mode at the edge (left) and center (right) of the wear track for ta-C(51) (top) and a-C:H (bottom).

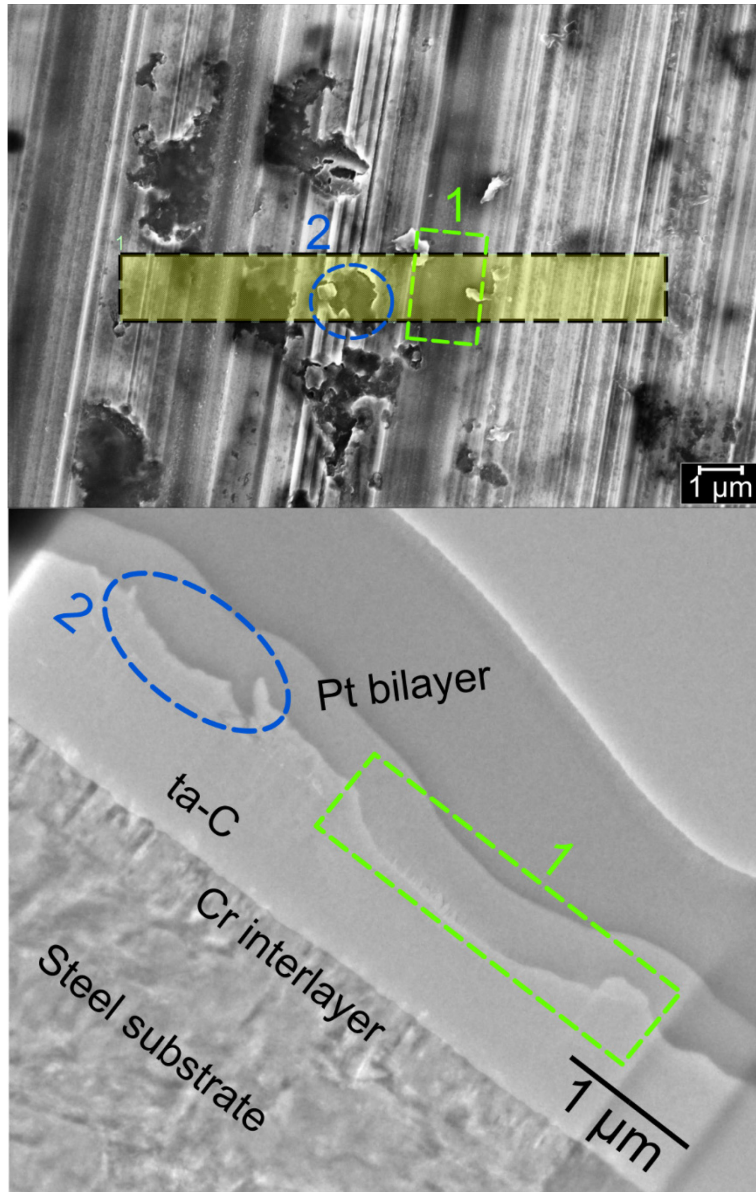


Figure A. 3. SEM images of the preparation zone for the ta-C(66) FIB cross-section sample.



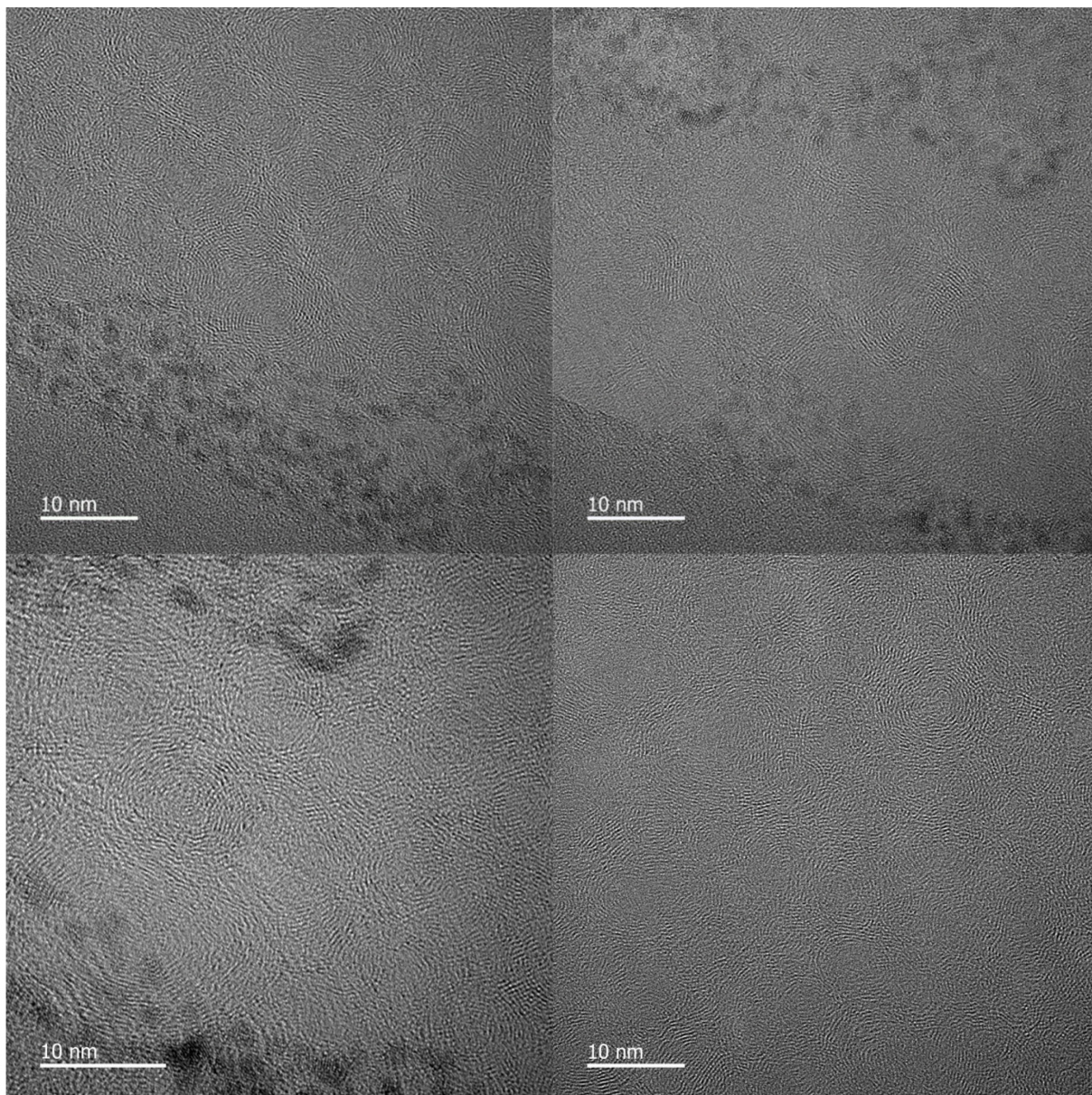


Figure A. 4. BF-TEM images of the graphitic-like (onions) structures observed on the cross-section sample of ta-C(66).

After 5 min sputtering

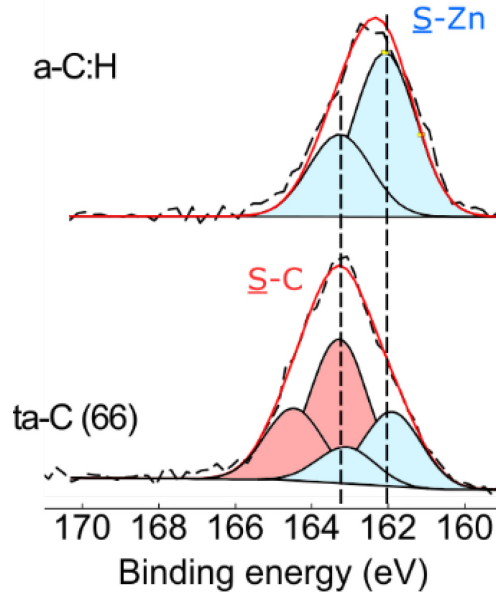


Figure A. 5. S2p XPS profiles obtained from a-C:H (top) and ta-C(66) (bottom) after 5 minutes of sputtering.

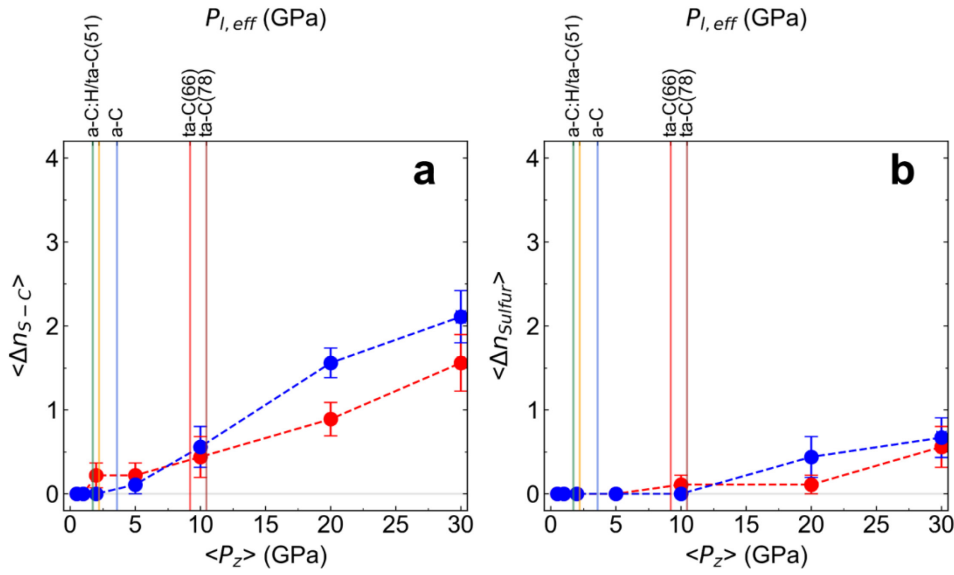


Figure A. 6. Quasi-static contact-closing/reopening simulations for hydrogen-passivated a-C:H with  $\rho = 2.0 \text{ g cm}^{-3}$  and  $C_H = 20 \text{ at.}\%$  and for hydrogen-passivated a-C with  $\rho = 2.0 \text{ g cm}^{-3}$  in contact with a ZDDP molecule using DFTB3 quantum chemical calculations. Averaged numbers of (a) S-C bonds  $\langle \Delta n_{S-C} \rangle$  formed between ZDDP sulphur and DLC carbon atoms as well as (b) sulphur atoms released from ZDDP  $\langle \Delta n_{Sulphur} \rangle$  to the DLC after opening the contact as a function of the contact pressure  $P_z$  for a-C:H (red) and a-C (blue). The error bars represent standard error of the means. The vertical lines mark the effective local contact pressures  $P_{l,eff}$  for the five experimental coatings (reported in **Figure 4.5b**).



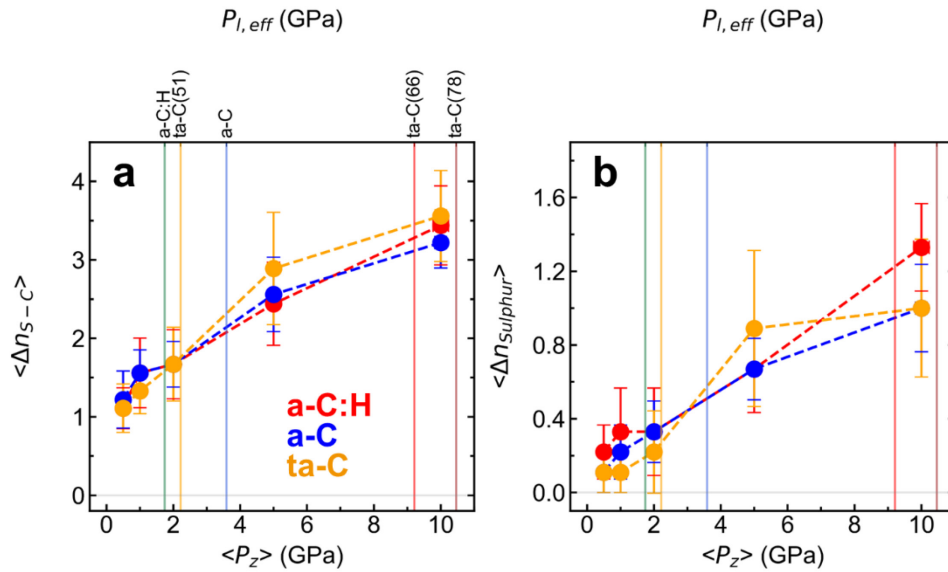


Figure A. 7. Quasi-static contact-closing/reopening simulations for  $sp^3$ -rich ta-C with  $\rho = 3.0 \text{ g cm}^{-3}$  (orange) in contact with a ZDDP molecule using DFTB3 quantum chemical calculations. Averaged numbers of (a) S-C bonds  $\langle \Delta n_{S-C} \rangle$  formed between ZDDP sulphur and DLC carbon atoms as well as (b) sulphur atoms released from ZDDP  $\langle n_{Sulphur} \rangle$  to the DLC after opening the contact as a function of the contact pressure  $P_z$ . The plots for a-C:H (red) and a-C (blue) are the same as in Figure A. 6. The error bars represent standard error of the means. The vertical lines mark the effective local contact pressures  $P_{l,eff}$  for the five experimental coatings (Figure 4.5b).

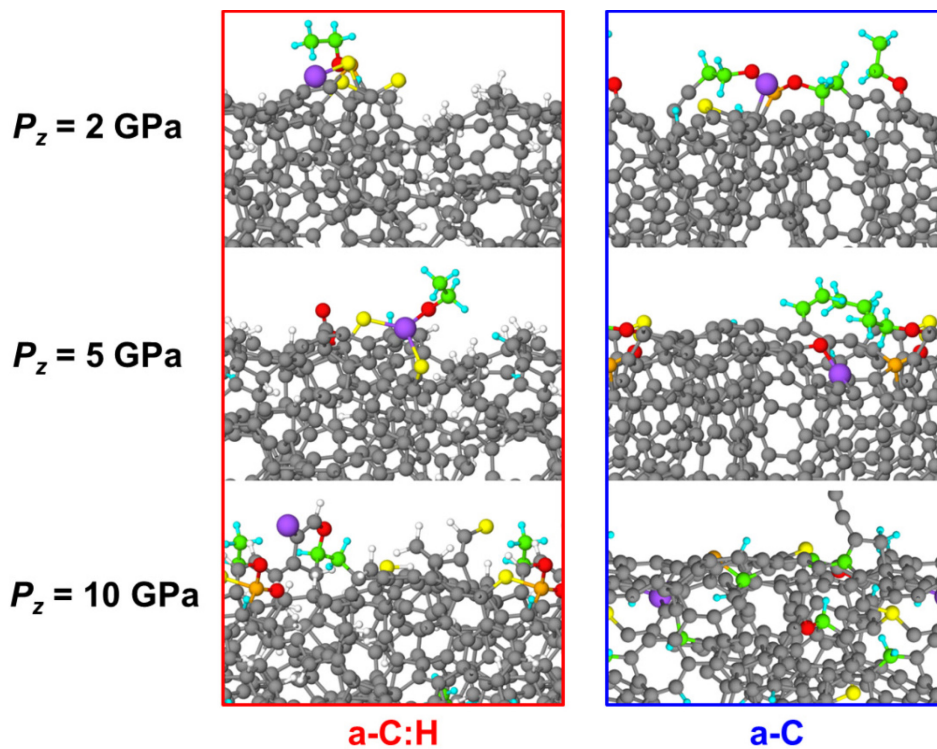


Figure A. 8. Representative pictures of DLC surfaces functionalized with ZDDP-derived atoms/fragments at three different contact pressures ( $P_z = 2, 5,$  and  $10 \text{ GPa}$ ) after surface separation for a-C:H and a-C.



Table A. 1. XPS fitting parameters used for the spectra presented in Figure 5. 11-13.

Sample	Assignment	Chemical state	B.E. (eV)	FWHM (eV)	Gauss %
ta-C disk vs. steel cylinder	C1s (1)	C-C, C=C, C-H	284.8	1.6	95
	C1s (2)	C-O	286.5	1.6	95
	C1s (3)	O-C=O	288.3	1.6	95
	O1s (1)	NBO	531.8	1.9	80
	O1s (2)	BO	533.2	1.9	80
	P2p <sub>3/2</sub>	P-O	133.5	1.6	85
	S2p <sub>3/2</sub> (1)	S-Zn	162.3	1.9	100
	S2p <sub>3/2</sub> (2)	SO <sub>4</sub>	168.9	1.8	100
	Zn2p <sub>3/2</sub> (1)	ZnS, ZnPO <sub>x</sub>	1022.1	1.7	85
	Zn2p <sub>3/2</sub> (2)	ZnO	-	-	-
steel disk vs. ta-C cylinder	C1s (1)	C-C, C=C, C-H	284.8	1.6	95
	C1s (2)	C-O	286.4	1.6	95
	C1s (3)	O-C=O	288.5	1.6	95
	O1s (1)	NBO	531.4	1.9	80
	O1s (2)	BO	533.0	1.9	80
	P2p <sub>3/2</sub>	P-O	133.5	1.9	85
	S2p <sub>3/2</sub> (1)	S-Zn, S-P, S=P	162.0	1.9	100
	S2p <sub>3/2</sub> (2)	SO <sub>4</sub>	168.0	1.9	100
	Zn2p <sub>3/2</sub> (1)	ZnS, ZnPO <sub>x</sub>	1022.1	1.8	85
	Zn2p <sub>3/2</sub> (2)	ZnO	1023.8	1.8	85
steel disk vs. steel cylinder	C1s (1)	C-C, C=C, C-H	284.8	1.5	95
	C1s (2)	C-O	286.3	1.5	95
	C1s (3)	O-C=O	288.2	1.5	95
	O1s (1)	NBO	531.4	1.9	80
	O1s (2)	BO	532.0	1.9	80
	P2p <sub>3/2</sub>	P-O	133.5	1.8	85
	S2p <sub>3/2</sub> (1)	S-Zn, S-P, S=P	162.0	1.9	100
	S2p <sub>3/2</sub> (2)	SO <sub>4</sub>	168.4	1.9	100
	Zn2p <sub>3/2</sub> (1)	ZnS, ZnPO <sub>x</sub>	1022.0	1.8	85
	Zn2p <sub>3/2</sub> (2)	ZnO	1023.8	1.8	85

Table A. 2. Parameters used for the fitting procedure of the spectra shown in Figure 5. 23 of a-C:H.

Lubricant	Contribution	Assignment	B.E. (eV)	FWHM (eV)	Gauss (%)
ZDDP I C4	C1s (1)	C-C, C=C, C-H	284,8	1,4	95
	C1s (2)	C-O	286,4	1,4	95
	C1s (3)	O-C=O	288,3	1,4	95
	O1s (1)	NBO	531,7	1,7	80
	O1s (2)	BO	533,0	1,7	80
	P2p <sub>3/2</sub> (1)	P-O	133,4	1,7	85
	S2p <sub>3/2</sub> (1)	S-Zn, S-P, S=P	162,3	1,9	100

	S2p <sub>3/2</sub> (2)	S-C	-	-	-
	S2p <sub>3/2</sub> (3)	S-S-S	-	-	-
	S2p <sub>3/2</sub> (4)	S-O	-	-	-
	Zn2p <sub>3/2</sub> (1)	ZnS, ZnPO <sub>x</sub>	1022,3	1,7	85
	Zn2p <sub>3/2</sub> (2)	ZnO	-	-	-
ZDDP I C8	C1s (1)	C-C, C=C, C-H	284,8	1,4	95
	C1s (2)	C-O	286,5	1,4	95
	C1s (3)	O-C=O	288,3	1,4	95
	O1s (1)	NBO	531,7	1,7	80
	O1s (2)	BO	533,0	1,7	80
	P2p <sub>3/2</sub> (1)	P-O	133,5	1,6	85
	S2p <sub>3/2</sub> (1)	S-Zn, S-P, S=P	162,4	1,8	100
	S2p <sub>3/2</sub> (2)	S-C	-	-	-
	S2p <sub>3/2</sub> (3)	S-S-S	-	-	-
	S2p <sub>3/2</sub> (4)	S-O	-	-	-
	Zn2p <sub>3/2</sub> (1)	ZnS, ZnPO <sub>x</sub>	1022,3	1,7	75
	Zn2p <sub>3/2</sub> (2)	ZnO	-	-	--
ZP I C8	C1s (1)	C-C, C=C, C-H	284,8	1,6	95
	C1s (2)	C-O	286,5	1,6	95
	C1s (3)	O-C=O	288,3	1,6	95
	O1s (1)	NBO	532,1	1,9	80
	O1s (2)	BO	533,4	1,9	80
	P2p <sub>3/2</sub> (1)	P-O	134,0	1,8	85
	S2p <sub>3/2</sub> (1)	S-Zn, S-P, S=P	-	-	-
	S2p <sub>3/2</sub> (2)	S-C	-	-	-
	S2p <sub>3/2</sub> (3)	S-S-S	-	-	-
	S2p <sub>3/2</sub> (4)	S-O	-	-	-
	Zn2p <sub>3/2</sub> (1)	ZnS, ZnPO <sub>x</sub>	1022,5	1,9	85
	Zn2p <sub>3/2</sub> (2)	ZnO	1024,3	1,9	85
TPS	C1s (1)	C-C, C=C, C-H	284,8	1,6	95
	C1s (2)	C-O	286,5	1,6	95
	C1s (3)	O-C=O	288,4	1,6	95
	O1s (1)	NBO	532,1	1,9	80
	O1s (2)	BO	533,6	1,9	80
	P2p <sub>3/2</sub> (1)	P-O	-	-	-
	S2p <sub>3/2</sub> (1)	S-Zn	-	-	-
	S2p <sub>3/2</sub> (2)	S-C	-	-	-
	S2p <sub>3/2</sub> (3)	S-S-S	163,9	1,8	100
	S2p <sub>3/2</sub> (4)	S-O	168,5	1,8	100
	Zn2p <sub>3/2</sub> (1)	ZnS, ZnPO <sub>x</sub>	-	-	-
	Zn2p <sub>3/2</sub> (2)	ZnO	-	-	-

Table A. 3. Parameters used for the fitting procedure of the spectra shown in Figure 5. 23 of ta-C(66).

Lubricant	Contribution	Assignment	B.E. (eV)	FWHM (eV)	Gaussian (%)
ZDDP I C4	C1s (1)	C-C, C=C, C-H, C-S	284.8	1.4	95
	C1s (2)	C-O	286.5	1.4	95
	C1s (3)	O-C=O	288.3	1.4	95
	O1s (1)	NBO	531.9	1.7	80
	O1s (2)	BO	533.0	1.7	80
	P2p <sub>3/2</sub> (1)	P-O	133.3	1.9	85
	S2p <sub>3/2</sub> (1)	S-Zn	162.3	1.9	100
	S2p <sub>3/2</sub> (2)	S-C	163.3	1.9	100
	S2p <sub>3/2</sub> (3)	S-S-S	-	-	-
	S2p <sub>3/2</sub> (4)	S-O	167.9	1.9	100
	Zn2p <sub>3/2</sub> (1)	ZnS/ZnPO <sub>x</sub>	1022.4	1.8	85
	Zn2p <sub>3/2</sub> (2)	ZnO	-	-	-
ZDDP I C8	C1s (1)	C-C, C=C, C-H, C-S	284,8	1,4	95
	C1s (2)	C-O	286,6	1,4	95
	C1s (3)	O-C=O	288,6	1,4	95
	O1s (1)	NBO	531,8	1,8	80
	O1s (2)	C-O	533,0	1,8	80
	P2p <sub>3/2</sub> (1)	P-O	133,3	1,7	85
	S2p <sub>3/2</sub> (1)	S-Zn	162,1	1,8	100
	S2p <sub>3/2</sub> (2)	S-C	163,3	1,8	100
	S2p <sub>3/2</sub> (3)	S-S-S	-	-	-
	S2p <sub>3/2</sub> (4)	S-O	-	-	-
	Zn2p <sub>3/2</sub> (1)	ZnS, ZnPO <sub>x</sub>	1022,3	1,7	85
	Zn2p <sub>3/2</sub> (2)	ZnO	-	-	-
ZP I C8	C1s (1)	C-C, C=C, C-H	284,8	1,3	95
	C1s (2)	C-O	286,4	1,3	95
	C1s (3)	O-C=O	288,6	1,3	95
	O1s (1)	NBO	532,1	1,8	80
	O1s (2)	BO	533,3	1,8	80
	P2p <sub>3/2</sub> (1)	P-O	133,6	1,7	85
	S2p <sub>3/2</sub> (1)	S-Zn, S-P, S=P	-	-	-
	S2p <sub>3/2</sub> (2)	S-C	-	-	-

	S2p <sub>3/2</sub> (3)	S-S-S	-	-	-
	S2p <sub>3/2</sub> (4)	S-O	-	-	-
	Zn2p <sub>3/2</sub> (1)	ZnS, ZnPO <sub>x</sub>	1022,2	1,6	85
	Zn2p <sub>3/2</sub> (2)	ZnO	-	-	-
TPS	C1s (1)	C-C, C=C, C-H, C-S	284,8	1,5	95
	C1s (2)	C-O	286,5	1,5	95
	C1s (3)	O-C=O	288,0	1,5	95
	O1s (1)	NBO	532,1	1,8	80
	O1s (2)	BO	533,3	1,8	80
	P2p <sub>3/2</sub> (1)	P-O	-	-	-
	S2p <sub>3/2</sub> (1)	S-Zn, S-P, S=P	-	-	-
	S2p <sub>3/2</sub> (2)	S-C	163,2	1,9	100
	S2p <sub>3/2</sub> (3)	S-S-S	164,1	1,9	100
	S2p <sub>3/2</sub> (4)	S-O	168,4	1,9	100
	Zn2p <sub>3/2</sub> (1)	ZnS, ZnPO <sub>x</sub>	-	-	-
	Zn2p <sub>3/2</sub> (2)	ZnO	-	-	-

Table A. 4. Parameters used for the fitting procedure of the spectra recorded in ta-C flats and balls after sliding tests in DMS environment at different pressures.

Pressure (mbar)	Sample	Contribution	Assignment	B.E. (eV)	FWHM (eV)	Gaussian (%)
3.10 <sup>-3</sup>	ball	C1s (1)	C-C, C=C, C-H, C-S	284.8	1.5	95.0
		C1s (2)	C-O	286.5	1.5	95.0
		C1s (3)	O-C=O	288.0	1.5	95.0
		O1s (1)	C=O	531.7	1.9	80.0
		O1s (2)	C-O	533.1	1.9	80.0
		S2p <sub>3/2</sub> (1)	S-C	163.2	1.7	90.0
	S2p <sub>3/2</sub> (2)	S-O	165.5	1.7	0.0	
	flat	C1s (1)	C-C, C=C, C-H, C-S	284.8	1.5	95.0
		C1s (2)	C-O	286.4	1.5	95.0
		C1s (3)	O-C=O	287.9	1.5	95.0
		O1s (1)	C=O	531.6	1.9	80.0
		O1s (2)	C-O	533.0	1.9	80.0
		S2p <sub>3/2</sub> (1)	S-C	163.2	1.7	90.0
	S2p <sub>3/2</sub> (2)	S-O	165.9	1.7	90.0	

3.10 <sup>-1</sup>	ball	C1s (1)	C-C. C=C. C-H. C-S	284.8	1.5	95.0
		C1s (2)	C-O	286.5	1.5	95.0
		C1s (3)	O-C=O	287.9	1.5	95.0
		O1s (1)	C=O	531.6	1.9	80.0
		O1s (2)	C-O	533.0	1.9	80.0
		S2p <sub>3/2</sub> (1)	S-C	163.3	1.8	90.0
		S2p <sub>3/2</sub> (2)	S-O	-	0.0	0.0
	flat	C1s (1)	C-C. C=C. C-H. C-S	284.8	1.5	95.0
		C1s (2)	C-O	286.4	1.5	95.0
		C1s (3)	O-C=O	287.9	1.5	95.0
		O1s (1)	C=O	531.7	1.8	80.0
		O1s (2)	C-O	533.2	1.8	80.0
		S2p <sub>3/2</sub> (1)	S-C	163.2	1.7	90.0
		S2p <sub>3/2</sub> (2)	S-O	0.0	0.0	0.0
3.10 <sup>0</sup>	ball	C1s (1)	C-C. C=C. C-H. C-S	284.8	1.5	95.0
		C1s (2)	C-O	286.4	1.5	95.0
		C1s (3)	O-C=O	288.1	1.5	95.0
		O1s (1)	C=O	531.7	1.9	80.0
		O1s (2)	C-O	532.8	1.9	80.0
		S2p <sub>3/2</sub> (1)	S-C	163.6	1.7	90.0
		S2p <sub>3/2</sub> (2)	S-O	166.6	1.7	90.0
	flat	C1s (1)	C-C. C=C. C-H. C-S	284.8	1.4	95.0
		C1s (2)	C-O	286.5	1.4	95.0
		C1s (3)	O-C=O	-	-	-
		O1s (1)	C=O	531.7	1.9	80.0
		O1s (2)	C-O	532.9	1.9	80.0
		S2p <sub>3/2</sub> (1)	S-C	163.2	1.8	90.0
		S2p <sub>3/2</sub> (2)	S-O	0.0	0.0	0.0

Table A. 5. Parameters used for the fitting procedure of the spectra recorded in ta-C flats after sliding tests in O<sub>2</sub> environment at different pressures.

Pressure (mbar)	Contribution	Assignment	B.E. (eV)	FWHM (eV)	Gaussian (%)
P = 3.10 <sup>-3</sup>	C1s (1)	C-C, C=C, C-H	284,8	1,5	95,0
	C1s (2)	C-O	286,5	1,5	95,0
	C1s (3)	O-C=O	288,1	1,5	95,0
	O1s (1)	C=O	531,4	1,9	80,0
	O1s (2)	C-O	532,8	1,9	80,0
P = 3.10 <sup>-1</sup>	C1s (1)	C-C, C=C, C-H	284,8	1,5	95,0
	C1s (2)	C-O	286,5	1,5	95,0
	C1s (3)	O-C=O	288,0	1,5	95,0
	O1s (1)	C=O	531,4	1,9	80,0
	O1s (2)	C-O	532,8	1,9	80,0
P = 3.10 <sup>0</sup>	C1s (1)	C-C, C=C, C-H	284,8	1,5	95,0
	C1s (2)	C-O	286,6	1,5	95,0
	C1s (3)	O-C=O	288,1	1,5	95,0
	O1s (1)	C=O	531,5	1,9	80,0
	O1s (2)	C-O	532,9	1,9	80,0

Table A. 6. Parameters used for the fitting procedure of the spectra recorded in ta-C flats after sliding tests in UHV and neat ZDDP layer.

Position	Contribution	Assignment	B.E. (eV)	FWHM (eV)	% Gauss
Neat ZDDP	C1s (1)	C-C, C-H	284.8	1.4	95
	C1s (2)	C-O	286.5	1.4	95
	C1s (3)	C=O	-	-	95
	O1s (1)	O-Zn	531.4	1.6	80
	O1s (2)	C-O-P	533.0	1.6	80
	P2p <sub>3/2</sub> (1)	(-CO) <sub>2</sub> -P=S	133.4	1.6	85
	S2p <sub>3/2</sub> (1)	P-S-Zn	162.4	1.5	100
	S2p <sub>3/2</sub> (2)	S=P	163.7	1.5	100

	Zn2p <sub>3</sub> (1)	Zn-S	1022.3	1.6	85
	Zn2p <sub>3</sub> (2)	Zn-O	1023.5	1.6	85
a-C:H 50 cycles	C1s (1)	C-C. C-H	284.8	1.4	95
	C1s (2)	C-O	286.5	1.4	95
	C1s (3)	C=O	-	-	95
	O1s (1)	O-Zn	531.4	1.6	80
	O1s (2)	C-O-P	532.9	1.6	80
	P2p <sub>3/2</sub>	(-CO) <sub>2</sub> -P=S	133.5	1.7	85
	S2p <sub>3/2</sub> (1)	P-S-Zn	162.4	1.5	100
	S2p <sub>3/2</sub> (2)	S=P	163.7	1.5	100
	Zn2p <sub>3</sub> (1)	Zn-S	1022.2	1.6	85
	Zn2p <sub>3</sub> (2)	Zn-O	1023.4	1.6	85
ta-C 50 cycles	C1s (1)	C-C. C-H	284.8	1.4	95
	C1s (2)	C-O	286.5	1.4	95
	C1s (3)	C=O	-	1.4	95
	O1s (1)	O-Zn	531.6	1.6	80
	O1s (2)	C-O-P	533.0	1.6	80
	P2p <sub>3/2</sub> (1)	(-CO) <sub>2</sub> -P=S	133.5	1.7	85
	S2p <sub>3/2</sub> (1)	P-S-Zn	162.4	1.4	100
	S2p <sub>3/2</sub> (2)	S=P	163.8	1.4	100
	Zn2p <sub>3</sub> (1)	Zn-S	1022.3	1.6	85
	Zn2p <sub>3</sub> (2)	Zn-O	1023.7	1.6	85
a-C:H 390 cycles	C1s (1)	C-C. C-H	284.8	1.4	95
	C1s (2)	C-O	286.5	1.4	95
	C1s (3)	C=O	-	-	95
	O1s (1)	O-Zn	531.7	1.8	80
	O1s (2)	C-O-P	533.1	1.8	80
	P2p <sub>3/2</sub> (1)	(-CO) <sub>2</sub> -P=S	133.7	1.9	85
	S2p <sub>3/2</sub> (1)	P-S-Zn	162.7	1.7	100
	S2p <sub>3/2</sub> (2)	S=P	164.0	1.7	100
	Zn2p <sub>3</sub> (1)	Zn-S	1022.4	1.7	85
	Zn2p <sub>3</sub> (2)	Zn-O	1023.7	1.7	85
ta-C	C1s (1)	C-C. C-H	284.8	1.4	95



50 cycles	C1s (2)	C-O	286.3	1.4	95
	C1s (3)	C=O	287.5	1.4	95
	O1s (1)	O-Zn	532.0	1.8	80
	O1s (2)	C-O-P	533.4	1.8	80
	P2p <sub>3/2</sub> (1)	(-CO) <sub>2</sub> -P=S	133.7	1.9	85
	S2p <sub>3/2</sub> (1)	P-S-Zn	162.7	1.7	100
	S2p <sub>3/2</sub> (2)	S=P	164.2	1.7	100
	S2p <sub>3/2</sub> (3)	Zn-S	1022.5	1.7	85
	Zn2p <sub>3</sub> (1)	Zn-O	1024.2	1.7	85